Editor:

Assoc. Prof. Dr. Sıtkı KOCAOĞLU

Asst. Prof. Dr. Harun GEZİCİ

INNOVATION, SCIENCE & TECHNOLOGY CONFERENCE

InnoSciTech'26

E-ISBN:

978-605-4929-47-4

PROCEEDINGS BOOK

INTERNATIONAL INNOVATION, SCIENCE, AND TECHNOLOGY CONFERENCE
(InnoSciTech'26)

May 15–18, 2026
Akyaka-Muğla, Türkiye

Editors
Assoc. Prof. Dr. Sıtkı KOCAOĞLU
Asst. Prof. Dr. Harun GEZİCİ

Published by
InnoSciTech'26 Organizing Committee

E-ISBN: 978-605-4929-47-4

CONGRESS ID

CONFERENCE TITLE

INTERNATIONAL INNOVATION, SCIENCE, AND TECHNOLOGY CONFERENCE

DATE AND PLACE

May 15-18, 2026

MUĞLA, TÜRKİYE

ORGANIZATION

InnoSciTech'26 Organizing Committee

LANGUAGE

ENGLISH

T.C.
ANKARA YILDIRIM BEYAZIT ÜNİVERSİTESİ REKTÖRLÜĞÜ
Mühendislik ve Doğa Bilimleri Fakültesi Dekanlığı

2025 AİLE YILI

Sayı : E-60708718-903.07.02-419531 31.10.2025
Konu : Görevlendirme (Dr. Öğr. Üyesi Sıtkı KOCAOĞLU)

PERSONEL DAİRE BAŞKANLIĞINA

İlgi : Enerji Sistemleri Mühendisliği Bölüm Başkanlığının 30.10.2025 tarihli ve 97697016-903.07.02-419442 sayılı yazısı.

İlgi yazı gereği Fakültemiz Enerji Sistemleri Mühendisliği Bölümü Dr. Öğr. Üyesi Sıtkı KOCAOĞLU'un 14 – 18 Mayıs 2025 tarihleri arasında Muğla Akyaka'da düzenlenmesi planlanan "International Innovation, Science and Technology Conference (InnoSciTech'26)" Düzenleme Kurulu Başkanı olarak 2547 sayılı Kanunun 39. Maddesi 1. fıkrası gereğince ilgili tarihler arasında yolluksuz yevmiyesiz maaşlı izinli olarak görevlendirilmesi Dekanlığımızca uygun görülmüştür.

Gereğini bilgilerinize rica ederim.

Prof. Dr. Ergün ERASLAN
Dekan

Adres: Ayvalı Mh. Takdir Cad.150 Sk. No:5 Etlik-Keçiören / ANKARA
Telefon: 0 312 906 2202
Faks: 0 312 906 29 55
KEP Adresi : yildirimbeyazituniversitesi@hs01.kep.tr

Bilgi için:Ramazan AVCI
Bilgisayar İşletmeni
Telefon No:(312) 906 22 85

T.C.
KIRKLARELİ ÜNİVERSİTESİ REKTÖRLÜĞÜ
Teknik Bilimler Meslek Yüksekokulu Müdürlüğü

2025 AİLE YILI

Sayı : E-57145752-903.07-189718 12.01.2026
Konu : Görevlendirme Hk.

Sayın Dr. Öğr. Üyesi Harun GEZİCİ

İlgi : Elektronik ve Otomasyon Bölüm Başkanlığı'nın 08.01.2026 tarihli ve E-16223361-903.07-189339 sayılı yazısı.

İlgi yazıya istinaden, 16-18 Mayıs 2026 tarihleri arasında Akyaka/MUĞLA'da gerçekleştirilecek olan "International Innovation Science and Technology Conference (InnoSciTech'26)" adlı konferansın düzenlenmesinde Konferans Başkanı olarak görevlendirilme talebiniz uygun bulunmuştur.

Bilgilerinize rica ederim.

Dr. Öğr. Üyesi Gülcan İNER
Müdür V.

Bu belge, güvenli elektronik imza ile imzalanmıştır.

Belge Doğrulama Kodu : 2EE0-ZZTT-876I Belge Doğrulama Adresi : https://www.turkiye.gov.tr/kirklareli-universitesi-ebys

Adres: Kırklareli Üniversitesi Teknik Bilimler Meslek Yüksek Okulu Müdürlüğü/Karahıdır Mahallesi Okul Yolu Sokak No:34/1
Telefon No : 0 288 214 18 45 Fax No : 0 288 214 1495
e-Posta : tbmyo@klu.edu.tr İnternet Adresi : http://www.klu.edu.tr
Kep Adresi : kirklareliuniversitesirektorlugu@hs01.kep.tr

Bilgi İçin :Simge CELEP
Memur
Dahili No:5208

HONORARY COMMITTEE

Prof. Dr. Ali Cengiz KÖSEOĞLU
- *Ankara Yıldırım Beyazıt University*

Prof. Dr. Rengin AK
- *Kırklareli University*

CONFERENCE CHAIR

Assoc. Prof. Dr. Sıtkı KOCAOĞLU
- *Ankara Yıldırım Beyazıt University*

Asst. Prof. Dr. Harun GEZİCİ
- *Kırklareli University*

ORGANIZING COMMITTEE

Prof. Dr. Bülent YEŞİLATA
- *Ankara Yıldırım Beyazıt University*

Prof. Dr. Haydar LİVATYALI
- *Yıldız Technical University*

Assoc. Prof. Dr. Uğur DEMİR
- *Marmara University*

Asst. Prof. Dr. Özcan ŞİMŞEK
- *Çanakkale Onsekiz Mart University*

Asst. Prof. Dr. Gazi AKGÜN
- *University of Tennessee at Chattanooga*

Asst. Prof. Dr. Aydın GÜLLÜ
- *Trakya University*

Asst. Prof. Dr. Mehmet Emin AKTAN
- *Bartın University*

Dr. Ömer Faruk MURATHAN
- *Ankara University*

TECHNICAL COMMITTEE

Assoc. Prof. Dr. Furkan SOYSAL
- *Ankara Yıldırım Beyazıt University*

Assoc. Prof. Dr. Burhan COŞKUN
- *Kırklareli University*

Assoc. Prof. Dr. Murat TUNA
- *Kırklareli University*

Asst. Prof. Dr. Halil KILIÇ
- *Kırklareli University*

Asst. Prof. Dr. Ercan COŞGUN
- *Kırklareli University*

Asst. Prof. Dr. Eray YILMAZLAR
- *Kırklareli University*

Asst. Prof. Dr. Yılmaz GÜVEN
- *Kırklareli University*

Asst. Prof. Dr. Mehmet Remzi ABUL
- *Ankara Yıldırım Beyazıt University*

Asst. Prof. Dr. Yunus YALMAN
- *Ankara Yıldırım Beyazıt University*

Asst. Prof. Dr. Ahmet UÇAR
- *Ankara Yıldırım Beyazıt University*

Asst. Prof. Dr. Mehmet Zahid EREL
- *Ankara Yıldırım Beyazıt University*

Asst. Prof. Dr. Metin ÖZTÜRK
- *Ankara Yıldırım Beyazıt University*

Asst. Prof. Dr. Döndü SARIŞEN
- *Ankara Yıldırım Beyazıt University*

MSc. Mustafa Yasir AYDIN
- *Ankara Yıldırım Beyazıt University*

MSc. Ümran Özge ÇAĞIRIR
- *Ankara Yıldırım Beyazıt University*

MSc. Ömer Önder ERAT
- *Ankara Yıldırım Beyazıt University*

MSc. Nepse Seda BOZKURT
- *Ankara Yıldırım Beyazıt University*

MSc. Şeymanur BAŞLIK
- *Ankara Yıldırım Beyazıt University*

INTERNATIONAL INNOVATION, SCIENCE, AND TECHNOLOGY CONFERENCE

InnoSciTech'26

15-18 MAY 2026

AKYAKA-MUĞLA

CONFERENCE PROGRAM

FACE TO FACE PROGRAM

OPENING CEREMONY

DATE:

16.05.2026 Saturday

Time:10.00

CONFERENCE PLACE

Hotel Lotus Spa&Sport Akyaka

Conference Place:

Hotel Lotus Spa&Sport Akyaka

Conference Registration:

09:00-10:00

Opening Ceremony:

10:00-10:30

Assoc. Prof. Dr. Sıtkı KOCAOĞLU

Conference Chair

Asst. Prof. Dr. Harun GEZİCİ

Conference Chair

Invited Speaker:

10:30-11:00

Prof. Dr. Erhan Akdoğan

Yıldız Technical University

Topic:

Biomechatronic Systems and Their Future in the Age of Human-Centered Technologies

16/05/2026 – Saturday

Session 1 / 11.00-12.30

Chair: Asst. Prof. Dr. Yılmaz GÜVEN

Authors	University/Institution	Topic Title
• Yılmaz GÜVEN	• Kırklareli University	Digital Filter Design Using Artificial Neural Networks
• Aydın GÜLLÜ • Aylin SATILMIŞ	• Trakya University • Multigrain Grain Technologies A.Ş	Comparative Analysis of Grain Measurement Systems Used in Industrial Grain Plants and an Application of a Discrete Weighing-Based Yield Scale
• Ali BEKTAŞ	• Hidromek A.Ş	Structural Analysis and Experimental Validation of an Excavator Chassis
• Eray YILMAZLAR	• Kırklareli University	Comparison of Reducer Types for Robotic Applications and Cycloid Reducer Design
• Ekin Can KAYAR • Mustafa YILDIZ	• Hidromek A.Ş • Ankara Yıldırım Beyazıt University	CFD Analysis of the Hydrogen Tank Filling
• Selin DEKSİZLER • İdris Tuğrul GÜLENÇ	• Ankara Yıldırım Beyazıt University -Turkish Patent and Trademark Office • Ankara Yıldırım Beyazıt University	Patent Landscape Analysis of LPBF and WAAM for Functionally Graded Metal Additive Manufacturing

16/05/2026 – Saturday

Session 2 / 13.30-15.15

Chair: Assoc. Prof. Dr. Uğur DEMİR

Authors	University/Institution	Topic Title
• Uğur DEMİR • Alper Nabi AKPOLAT • Sıtkı KOCAOĞLU	• Marmara University • Marmara University • Ankara Yıldırım Beyazıt University	Micro Stewart Platform for Vertebra Model and Motion Simulation in Posture Disorders
• Merve BOZDAĞ • Ahmet UÇAR	• Ankara Yıldırım Beyazıt University	Performance, Exergy and Economic Impacts of Green Hydrogen Blending in NGCC Power Plants in Türkiye
• Osman TOKLUOĞLU • Emin KERESTECI	• Ankara Yıldırım Beyazıt University • TOBB	Deep Learning-Based Automatic Modulation Classification Using GRU Networks
• Ömer Faruk MURATHAN • Mehmet Remzi ABUL	• Ankara University • Ankara Yıldırım Beyazıt University	Altering Microstructure of High Boron Steels by Conducting Different Heat Treatment Procedures
• Mustafa Akif YILDIRIM • Osman TOKLUOĞLU	• Ankara Yıldırım Beyazıt University	Comparative Performance Analysis of NIST PQC Standards: From STM32 Software Limitations to FPGA-SoC Acceleration
• Ercan COŞGUN • Nahide ÖNER COŞGUN	• Kırklareli University • Independent Researcher	Decision Tree-Based Classification of Textile Production Productivity and Its Implementation on ESP32
• Büşra Erkömek ATEŞ • Elif Nihan YILDIZ • Mahmut ULUSOY • Uğur DEMİR	• FLO Group • FLO Group • FLO Group • Marmara University	CNN and PINN based CFD Approach for Sneakers

17/05/2026 – Sunday

Session 3 / 10.00-12.00

Chair: Assoc. Prof. Dr. Furkan SOYSAL

Authors	University/Institution	Topic Title
• Mohamed FARAH ABDILAHI • Yunus YALMAN	• Ankara Yıldırım Beyazıt University	A Genetic Algorithm-Based Framework for Inertia Estimation in Power Systems with Grid-Scale BESS
• Alperen ÖZCAN • Selahattin ÇELİK	• Ankara Yıldırım Beyazıt University	Performance Evaluation of High-Speed Air Cycle Machine Architectures for Aerospace Cooling Applications
• Mohammed ALOBEİD • Merve MENTEŞ • Furkan ÇETINER • Selahattin ÇELIK	• Ankara Yıldırım Beyazıt University	Numerical Performance Analysis of Flow Field Designs for Large-Area PEM Fuel Cells in Heavy-Duty Vehicle Applications
• Ümran Özge ŞEBİK • Sıtkı KOCAOĞLU	• Ankara Yıldırım Beyazıt University	Smart De-Icing of Wind Turbine Blades: A Review of Machine Learning and Power Electronics-Based Approaches
• Şeymanur BAŞLIK • Ömer Önder ERAT • Furkan SOYSAL • Ahmet UÇAR • Bülent YEŞILATA	• Ankara Yıldırım Beyazıt University	A Comparative Analysis on Energy Consumption, Economic Growth and Carbon Dioxide Emissions
• Kaan Berk ÇELIK • Mustafa ÇELIK • Ruhican DÜRLÜ • Ömer Önder ERAT • Furkan SOYSAL • Sıtkı KOCAOĞLU • Bülent YEŞILATA	• Ankara Yıldırım Beyazıt University	Experimental Investigation of Density and Apparent Viscosity Evolution Across Multi-Compartment Sedimentation Tanks Under Varying Total Suspended Solid Contents
• Kazım YEL • Mehmet Zahid EREL	• Ankara Yıldırım Beyazıt University	An Overview of Interleaved Buck Converters and Modern Control Approaches
• Batuhan YURTDAN • Selahattin ÇELIK • Kamil ARSLAN	• Ankara Yıldırım Beyazıt University	Geometric Design and Numerical Analysis of Jet Stretcher in Supersonic Free-Jet Tests

17/05/2026 – Sunday

Session 4 / 13.00-15.00

Chair: Prof. Dr. Fatih Vehbi ÇELEBİ

Authors	University/Institution	Topic Title
• Mahmut Cihat YILMAZ	• Ankara Yıldırım Beyazıt University	Vibroacoustic Optimization of Porous Kelvin Cell Metamaterials for Washing Machine Mounts: A Computational Approach
• Ali ÇOBAN • Zeynep Huri ÖZKUL BİRGÖREN	• Ankara Yıldırım Beyazıt University	Design Considerations and Geotechnical Challenges for Subsea Shallow Foundations
• Ahmed MERZE • Fatih Vehbi ÇELEBİ	• Ankara Yıldırım Beyazıt University	Cooperative Trajectory Planning for Large-Scale Additive Manufacturing: A Multi-Agent Reinforcement Learning Approach
• Sefa ŞAHİN • Hasan ÖZCAN • Ahmet Talha TOPCU • Mustafa KAYMAK	• Ankara Yıldırım Beyazıt University	Design and Experimental Investigation of a Membrane-Free Flow-through Electrolyzer for Hydrogen Production
• Harun GEZİCİ	• Kırklareli University	An Improved Sine-Cosine Algorithm for Solving the Reactor Network Design Problem: ANELS-SCA
• Özcan ŞIMŞEK • Ece KAZANCI • Özge ÖZER • İrem KIVRAK	• Çanakkale Onsekiz Mart University	The Climate–Fire Nexus: Assessing The Impact of Global Climate Change on Forest Fires in Türkiye
• Ahmed Emin KILIÇ • Selahattin ÇELIK • Meryem Sena AKKUŞ • Cihangir DURAN • Erol ARCAKLIOĞLU	• Ankara Yıldırım Beyazıt University	Suppression of Delamination in Tape-Cast Planar YSZ Electrolytes via Multi-Step Lamination and Thermal Conditioning for rSOC Applications
• İnci Nur ATALAY • Sıtkı KOCAOĞLU	• Ankara Yıldırım Beyazıt University	Efficiency Comparison of Bifacial Photovoltaic Panels Under Various Ground Conditions

CONTENTS

Digital Filter Design Using Artificial Neural Networks

Yılmaz GÜVEN[1,*]

[1] *Department of Electronics and Automation, Kırklareli University, Kırklareli, TÜRKİYE*

***Contact:** ylmzguven@hotmail.com

Abstract—Digital filter design using artificial neural networks is a highly powerful field where traditional signal processing methods intersect with machine learning. Whilst traditional filters rely on pre-calculated coefficients to pass or block specific frequency bands, artificial neural network-based filters learn these coefficients from the data. This approach demonstrates significantly superior performance to traditional methods, particularly in the filtering of non-linear noise, acoustic signal analysis, or complex signal classification problems. In this study, the design of an adaptive digital filter utilizing the data-learning capability of artificial neural networks will be examined. Furthermore, an example application will be presented, demonstrating their training in the Python environment and implementation on a microcontroller-based embedded system using the C programming language.

Keywords: Digital Filters, Artificial Neural Networks, Signal Processing, Adaptive Filters

I. INTRODUCTION

Finite-impulse response (FIR) and infinite-impulse response (IIR) digital filters can be designed using mathematical methods such as linear difference equations and the z-transform. They can be adapted to different scenarios using specific coefficients and are easily implemented in software. At this point, the similarity between adaptive digital filters and artificial neural networks is striking. Thanks to similarities such as transfer functions and optimization methods, the use of artificial neural networks for digital filter design has emerged as an effective method. FIR filters, which use only current and past input values, are structurally similar to feedforward networks or one-dimensional convolutional neural networks (CNNs) [1]. IIR filters, which also take past output values (back-feed) into account, exhibit structural similarities to recurrent neural networks (RNNs) [2].

$$y[n] = \sum_{k=0}^{M} b_k . x[n-k] \tag{1}$$

$$y = f(\sum_{i=1}^{N} w_i . x_i + b) \tag{2}$$

Mathematically, the FIR filter (1) and the model of a single neuron in an artificial neural network (2) are very similar [3]. Here, if the activation function is chosen to be linear and delayed samples are applied to the input, the learning weights of the artificial neural network will correspond to the filter coefficients [4]. On the other hand, the use of non-linear activation functions enables the analysis of more complex signals. Furthermore, one-dimensional convolutional neural networks (1D CNNs) can also be used in the analysis of sequential time series. Here, the convolutional layer can learn frequency and time features at different positions, much like a window function. Each filter kernel obtained serves to suppress or emphasize a specific type of noise.

The process for designing digital filters using artificial neural networks consists of four main steps. Firstly, the necessary data must be collected and labelled. Subsequently, the specified model must be trained using this data to obtain the weights and bias values. Finally, the digital filter is implemented via a microcontroller or embedded system using a programming language.

II. FILTER DESIGN

To design a digital filter using feedforward artificial neural networks, the weights and error values must first be determined. Methods such as backpropagation and the gradient descent approach can be used during the training process. Based on the predictions generated by the feedforward layer, the training process is carried out by updating the weights via backpropagation (4) until the desired output values are obtained, following an error calculation (3) [5].

$$L = \frac{1}{N}\sum_{i=1}^{N}(y_i - \hat{y_i})^2 \tag{3}$$

$$w_i = w_j - \propto \frac{\partial L}{\partial w} \tag{4}$$

In this study, the design of a basic artificial neural network filter will be carried out, which takes three delayed inputs, passes them through a hidden layer with four neurons, and filters them with a single output. The topology of the artificial neural network is shown in Fig. 1.

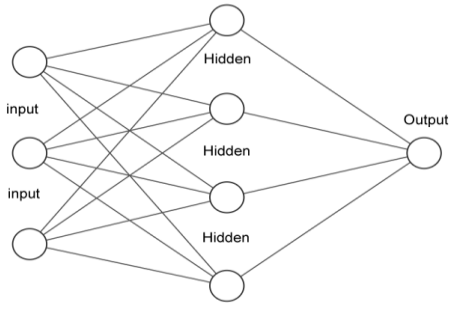

Fig. 1. Network topology

The *PyTorch* library was used for training [6], and 100 samples of a randomly generated noise signal were taken. Using the Adaptive Moment Estimation (Adam) optimization method, the learning rate was set to 0.01. The Adam (Adaptive Moment Estimation) optimization algorithm combines the advantages of the Momentum (5) and *RMSprop* (6) (Root Mean Square Propagation) techniques to adjust learning rates during training [7].

$$m_t = \beta m_{t-1} + (1 - B_1)\frac{\partial L}{\partial w_t} \quad (5)$$

$$v_t = \beta_2 v_{t-1} + (1 - \beta_2)(\frac{\partial L}{\partial w_t})^2 \quad (6)$$

The rectified linear unit (ReLU) activation function (7) was selected as the activation function. This function both eliminates negative values and provides better optimization convergence [8].

$$ReLU(x) = \max(0, x) = \frac{x+|x|}{2} \quad (7)$$

Pseudocode:

```
import torch
class NeuralFilter(nn.Module):
    self.hidden = nn.Linear(3, 4)
    self.output = nn.Linear(4, 1)
    self.relu = nn.ReLU()
model = NeuralFilter()
criterion = nn.MSELoss()
optimizer = optim.Adam(model.parameters(), lr=0.01)
x_train = torch.randn(100, 3)
y_train = torch.randn(100, 1)
epochs = 500
for epoch in range(epochs):
    optimizer.zero_grad()
    predictions = model(x_train)
    loss = criterion(predictions, y_train)
    loss.backward()
    optimizer.step()
```

At the end of the training process described in the pseudocode above, the weights (w) and biases (b) of the artificial neural network are obtained. These numbers replace the coefficients obtained from the difference equations of digital filters.

TABLE I
Weight and Bias Values

Hidden Layer Input	**w1[4][3]** = [[-0.228824645280838, -0.027164718136191368, -0.7032652497291565], [-0.7069176435470581, -0.4474407136440277, 0.4501200318336487], [-0.5639817714691162, 0.707327663898468, 0.7530871033668518], [0.14024488627910614, -0.9331445693969727, 0.35165131092071533]];
	b1[4] = [-0.7103489637374878, -0.1328185498714447, -0.449463814496994, -0.0219586081802845];
Hidden Layer Output	**w2[4]** = [0.6533299684524536, -0.6605104207992554, 0.763785183429718, 0.7044501900672913];
	b2 = -0.3730510473251343;

III.APPLICATION

Once training is complete, the resulting weight (w) and bias (b) matrices are embedded as fixed arrays into C code that will run in real time on a microcontroller or DSP. For efficient signal processing on the hardware, past signal samples must be managed using multi-dimensional arrays or pointers [9].

As an example, the filtered results of values obtained from a sensor are shown in Table 2. The relevant C code is also provided below. Using the filter coefficients and bias values obtained here, the desired output values are calculated based on the input values via the previously trained artificial neural network.

TABLE II
Test Results

Input	Output
1.23	0.27
0.92	0.37
0.53	0.27
2.11	0.30
1.81	0.05

C code:

```
#include <stdio.h>
#define INPUT_SIZE 3
#define HIDDEN_SIZE 4

// Model parameters transferred from Python
const float W1[HIDDEN_SIZE] [INPUT_SIZE] ={
{-0.228824645280838,-0.027164718136191368,0.7032652497291565},
{-0.7069176435470581, -0.4474407136440277, 0.4501200318336487},
{-0.5639817714691162,0.707327663898468,0.7530871033668518},
{0.14024488627910614,-0.9331445693969727,0.35165131092071533}
 };

const float b1[HIDDEN_SIZE] = {
-0.7103489637374878, -0.1328185498714447,
-0.449463814496994, -0.0219586081802845};

const float W2[HIDDEN_SIZE] = {
0.6533299684524536, -0.6605104207992554,
```

```
0.763785183429718, 0.7044501900672913};

const float b2 = -0.3730510473251343;

float relu(float x){return(x > 0.0f) ? x : 0.0f;}

float neural_filter_process(float*input_window){
      float hidden_layer_out[HIDDEN_SIZE];
      float output = 0.0f;

// Hidden Layer (Matrix Multiplication and Activation)
for (int i = 0; i < HIDDEN_SIZE; i++) {
          float sum = 0.0f;

    for (int j=0; j<INPUT_SIZE; j++) sum += W1[i][j] *
input_window[j];
          hidden_layer_out[i] = relu(sum + b1[i]);
       }

// Output Layer
for (int i = 0; i < HIDDEN_SIZE; i++) output += W2[i] *
hidden_layer_out[i];
       return output + b2;
    }

    int main() {

       float raw_signal[]={1.23,0.92,0.53,2.11,1.81};
       // Sample sensor data
       float input_window[INPUT_SIZE] = {0};

    for (int n=0;n<5;n++) {
        // Moving window update
          input_window[2] = input_window[1];
          input_window[1] = input_window[0];
          input_window[0] = raw_signal[n];

float filtered_value = neural_filter_process(input_window);

printf("Input: %5.2f->Output:%5.2f\n", raw_signal[n], filtered_value);
       }

       return 0;
}
```

IV. RESULT

Artificial neural networks offer a data-driven solution by overcoming the analytical challenges of digital filter design. Models trained in the Python environment using high computing power can be successfully run on low-power embedded devices by converting the weight matrices into C code. This approach makes signal analysis in modern electrical engineering applications more flexible, adaptable and more robust against noise.

TABLE III
Comparison of classical and ANN filters

	Conventional Digital Filters	**ANN-Based Filters**
Processing	Linear	Linear and Non-linear
Design	Mathematical	Machine Learning
Adaptability	Fixed coefficients	Variable weights
Hardware	Low processing power	High processing power

Artificial neural network-based adaptive filters are used in many fields such as Active Noise Cancellation, Biomedical Signal Processing and Channel Equalization. Although their only disadvantage compared to classical digital filters is more complex hardware and high processing power, these filters offer numerous advantages. Some of these advantages are summarized in Table 3.

REFERENCES

[1] S. Sharma, A. Goen. Review on Digital Filter Design Using Artificial Neural Network. Journal of Communication Engineering & Systems. 2016; 6(2): 9–15p.

[2] T. Sinjanakhom and S. Chivapreecha, "Real-Time Zero-Phase Digital Filter Using Recurrent Neural Network," 2023 IEEE Asia Pacific Conference on Circuits and Systems (APCCAS), Hyderabad, India, 2023, pp. 348–352, doi: 10.1109/APCCAS60141.2023.00084.

[3] D. A. Alwahaba, D. R. Zagharb, S. Lakic, Proceedings of the 10th International Conference on Applied Informatics, Eger, Hungary, 30 January–1 February 2017, pp. 5–13, doi: 10.14794/ICAI.10.2017.5

[4] T. Xue, "Design of FIR digital filter based on improved neural network," 2021 International Symposium on Computer Technology and Information Science (ISCTIS), Guilin, China, 2021, pp. 406–410, doi: 10.1109/ISCTIS51085.2021.00088.

[5] Peter Sadowski, Notes on Backpropagation, University of California Irvine, https://www.ics.uci.edu/~pjsadows/notes.pdf Accessed: 11 May 2025

[6] https://github.com/pytorch/pytorch, Accessed: 23 February 2026

[7] D. P. Kingma, J. Lei Ba, Adam: A Method for Stochastic Optimization, Published as a conference paper at ICLR 2015, https://arxiv.org/pdf/1412.6980

[8] S. Kılıçarslan, K. Adem & M. Çelik, An overview of the activation functions used in deep learning algorithms. Journal of New Results in Science, 10(3), 2021, 75–88. https://doi.org/10.54187/jnrs.1011739

[9] https://www.geeksforgeeks.org/c/pointer-array-array-pointer/ Accessed: 23 February 2026

Comparative Analysis of Grain Measurement Systems Used in Industrial Grain Plants and an Application of a Discrete Weighing-Based Yield Scale

Aydın GÜLLÜ[1,*] and Aylin SATILMIŞ[2]

[1]*Trakya University İpsala Vocational School, Mechatronics Programme, Edirne/İpsala, TÜRKİYE*

[2]*Multigrain Grain Technologies A.Ş., Edirne/İpsala, TÜRKİYE*

***Contact:** aydingullu@trakya.edu.tr*

Abstract— Accurate measurement of production quantity in grain processing plants is critical for reliable yield calculations and monitoring process efficiency. This study examines the technical principles, advantages, and limitations of grain measurement systems commonly used in factories; continuous and intermittent measurement systems (yield scales). In the application section of the study, the design, production, and field application results of a yield scale with a capacity of measuring 10 tons of rice per hour and performing intermittent weighing every 50 kg are presented. The developed system consists of a load cell-based weighing chamber, a pneumatically controlled input-output mechanism, and a PLC-supported control algorithm. The system reaches its target capacity with approximately 200 weighing cycles per hour and automatically calculates the total daily production quantity. In the performance tests conducted, it was determined that the system achieved a measurement accuracy of ±0.8% and gave results consistent with reference scale measurements. The findings show that intermittent weighing-based yield scales offer a highly accurate and economical solution, especially in medium-capacity grain facilities. This study presents a technical comparison of measurement systems in grain mills and evaluates the industrial applicability of a domestically produced yield scale.

Keywords: Grain measurement systems, yield scales, batch weighing, rice processing, production efficiency.

I. INTRODUCTION

. Accurate measurement of production quantity in grain processing plants is of great importance for production planning, inventory management, and monitoring process efficiency. Especially in mills, rice processing plants, and feed factories, accurate measurement of raw material input and product output directly affects the reliability of yield calculations. Therefore, weighing systems used in grain factories are a critical component of the production process. Various systems based on different principles are used in the industry for measuring grain quantity. These systems are generally categorized into two main groups: continuous measurement systems and intermittent measurement systems. Continuous measurement systems typically measure instantaneous flow rate during product flow via conveyor belt scales or pulse-based flowmeters, while intermittent measurement systems determine the total production quantity by measuring a specific amount of product in a weighing hopper. In this study, different measurement systems used in grain factories are examined and compared from a technical perspective. Furthermore, the application section of the study presents the design and application results of a 10-ton/hour capacity yield scale with 50 kg intermittent weighing, developed for use in rice processing plants.

II. LITERATURE BACKGROUND

Yield sensing principles in industrial/commercial systems; in field and laboratory validation studies, strong correlations between yield monitor outputs and reference scales have been demonstrated. For example, a reported R^2 of 0.99 between a load-cell–based yield monitor and an electronic scale, with average differences around 2% (or a few percent across flow ranges), supports the viability of mass-flow/scale–based yield estimation at high flow rates, while acknowledging degradation in instantaneous measurements at low or highly dynamic flow [1, 2].

A widely cited on-farm comparison shows very high correlations between combine-mounted yield sensors and weigh wagons for total yield, with R around 0.98–0.99 for yield and weight, illustrating that, when properly calibrated and aggregated, modern yield monitors can replace weigh-wagon assessments for planning and breeding trials [3].

Calibration quality strongly governs yield monitor performance. Arslan emphasizes that the smallest errors are achieved when grain flow is averaged over longer segments (IS, 30–60 m), and field and laboratory tests indicate that instantaneous fluctuations in grain flow cause yield monitor errors, which can be mitigated by temporal averaging and robust calibration strategies [2]. Burks, Shearer [4]; show that a yield monitor's accumulated mass flow can be very accurate at calibration flow rates, but instantaneous flow rates at low flows can exhibit substantial relative error and that there is a weak correlation between yield monitor estimates and hand samples for local yield variation ($R^2 \approx 0.203$) [4].

In a comprehensive review by Chung et al., mass-flow sensors (including load-cell–based and radiometric approaches) can achieve error levels below 5% with high R^2

values, while volume-flow sensors (e.g., paddle wheels or optical) show lower precision in some configurations, highlighting that sensor selection and mounting dramatically influence accuracy [1].

Correia (2025), discuss that the accuracy of yield sensors is sensitive to flow rate dynamics, with lowest errors occurring at steady state and increases in transient flow[5]. Averaging over 4–10 seconds in laboratory settings was suggested to improve instantaneous yield signal reliability, reinforcing the theme that discrete or highly dynamic flow conditions require data processing to reach field-useful accuracy [2].

The discrete weighing based approach (a weigh-scale/weigh wagon–like reference on a dedicated path or a discrete weighing tank) provides a robust reference for end-of-harvest total mass and can yield high correlation with continuous yield monitor data when properly synchronized in time and space. Nelson et al., 2015; show that yield monitor data can be highly concordant with weigh wagon measurements for plot-level evaluations, with correlation coefficients near 0.98–0.99 for yield and strong agreement in weight and moisture content, depending on experimental design and data processing [6].

In industrial contexts, discrete weighing scales integrated into a grain handling line (e.g., weigh tanks or weigh wagons used alongside a continuous flow sensor) can function as a calibration/validation backbone, helping to correct bias in real-time yield estimates and to quantify end-of-line yield with high accuracy. The test facility work by Burks et al. demonstrates the value of a weigh scale system for accumulating mass flow independently of instantaneous flow rate, providing a credible reference for calibrating and validating yield monitoring sensors [4].

Marcelo Augusto da Silva, Silva [7] and Krishnan, Kumar [8]; illustrate that accurate TGW estimation and image-based counting can complement mass-flow–based yield estimates by providing independent yield components (grain count, weight, and size) that can cross-validate a discrete weigh-scale–based approach, though TGW estimation is not a primary yield measurement in industrial flow paths. These references emphasize the broader ecosystem of yield-related metrics beyond cumulative mass, which can be leveraged to improve the robustness of a discrete weighing based yield scale [8, 9].

Conceptual design: A discrete weigh scale can be implemented as a separate weighing module positioned along the grain flow path where accumulated mass can be accurately captured, such as a weigh tank or a belt/drag conveyor with a calibrated load cell, similar to a conventional weigh wagon but integrated into the processing line. This arrangement provides a reference measurement for total mass flow over defined segments and can serve as the baseline against which continuous yield monitor data are cross-validated and corrected [2, 4].

Calibration strategy: A robust calibration protocol should combine static flow calibration across a range of expected grain flow rates with dynamic flow tests to characterize response under transients. The literature indicates that calibration accuracy improves with averaging over moderate to longer time windows and with calibration against an independent mass reference. Calibration targets include end-of-harvest total mass and short-interval accumulations, ensuring the scale tracks cumulative mass flow with errors well below 4% in both steady and slowly varying flows [2, 4].

Data processing and fusion: The discrete weigh scale data can be fused with the continuous yield monitor output using statistical calibration models (e.g., regression-based bias correction, Kalman filter blending) to reduce instantaneous errors and improve spatial yield mapping. This approach aligns with the findings of Correia et al. that combined sensor data can improve yield estimation, especially when flow dynamics are non-stationary, by leveraging multiple data streams to stabilize yield estimates [2].

Practical considerations: When integrating a discrete weigh scale into an industrial line, one must account for grain properties (moisture variability, bulk density changes), sensor nonlinearity, tank vibrations, and environmental conditions that affect load cell readings. Burks et al. note that tank vibration and load cell sensitivity can confound instantaneous measurements at low flow rates, underscoring the need for mechanical isolation and careful dynamic calibration in an industrial setting (Burks et al., 2003; . In practice, averaging over 4–10 seconds (laboratory-like guidance) can help mitigate transient fluctuations, while field validation against weigh wagons or laboratory scales remains essential for credibility and regulatory/trust reasons [2].

Accuracy and reliability: A discrete weigh scale provides a robust, independent mass reference that is less sensitive to transient flow fluctuations than some continuous sensing methods. When properly calibrated and used to constrain the end-of-line yield statistic, it can reduce systematic biases in yield monitor data and improve overall accuracy, particularly for end-user decision-making and on-farm evaluations where long-term stability is critical. This aligns with the evidence that weigh-wagon comparisons and integrated scales yield high correlations with continuous monitors in field conditions [3, 6].

Calibration and validation backbone: The discrete scale serves as a crucial calibration reference to reconcile continuous monitor signals with true accumulated mass, addressing concerns about low-flow, transient flow, and spatial yield variability highlighted in the literature [1, 2, 4].

Yield mapping implications: By providing segment-wise total mass flow measured via the discrete scale, the system supports more accurate yield maps when combined with flow rate data and regionally averaged calibrations. The review and empirical studies suggest that yield mapping accuracy improves when sensor data are corrected using reliable

references and appropriate averaging windows, particularly across yield strata in the field [1, 2].

Component yield insights: Although TGW and kernel-level attributes (e.g., grain weight, kernel count) are not direct substitutes for mass flow, combining a discrete weigh scale with yield sensor data and grain quality measurements can enable richer yield accounting and quality-linked yield mapping, consistent with the broader literature on yield components and their relationships to total yield [3, 9, 10].

Instantaneous versus accumulated yield: Several sources emphasize that instantaneous flow measurements can exhibit larger errors at low or highly dynamic flow rates, whereas accumulated mass over a calibration interval is more reliable. Burks et al. report low accuracy for instantaneous flow at low rates (1–4 kg/s) despite good static calibration, highlighting a potential mismatch between instantaneous yield sensing and accumulated mass constructs (Burks et al., 2003; . Das and others emphasize path-dependent correlations and the importance of averaging to stabilize estimates in variable conditions [11].

Sensor type performance variance: Mass-flow sensors (weighing, load cells) generally show high correlation with reference scales in ideal conditions, while volume-flow sensors can be more prone to error depending on flow pattern and sensor mounting. This variability motivates the use of a discrete weigh scale as a stabilizing reference in conjunction with a continuous flow sensor, rather than relying on one sensor type alone [1].

Use a calibrated weigh scale installed on a discrete segment of the flow path (e.g., a weigh tank or a belt/drag conveyor segment) to accumulate total mass over predefined collection windows, ensuring mechanical isolation from vibrations and consistent mounting to minimize measurement drift [2, 4].

Establish a comprehensive calibration protocol that spans static and dynamic flow regimes, includes cross-validation against a separate reference (e.g., a weigh wagon or laboratory electronic scale), and accounts for grain-specific factors (moisture content, bulk density) that influence mass readings [2, 4].

Integrate the discrete scale data with the continuous yield monitor via a data fusion framework (e.g., regression-based bias correction, Kalman filtering) to improve instantaneous yield estimates and deliver more accurate yield maps and batch summaries for process optimization [2].

Consider extending the system to also collect grain quality proxies (e.g., TGW via image-based counting or periodic sampling) to enable cross-validation of mass-flow data with grain size/weight distributions and to support richer yield accounting and product quality management [8, 9].

A discrete weighing-based yield scale, when properly integrated and calibrated, provides a robust mass-reference that complements continuous yield monitoring systems in industrial grain plants. The evidence indicates that while yield monitors can achieve high accuracy in aggregated measurements, instantaneous flow measurements are susceptible to errors under dynamic flow or low-flow conditions, making an independent weigh-scale reference valuable for calibration, validation, and bias correction [1, 2, 4]. A discrete weigh scale thus serves as an essential component in a hybrid yield measurement strategy that blends robust reference data with continuous sensing to yield more accurate, stable yield maps and decision-support insights for industrial grain handling and on-farm evaluations [2, 3, 6].

III.MASS MEASUREMENT APPROACHES IN GRAIN FACTORIES

Systems used to determine product quantity in grain processing plants are generally divided into two groups: continuous measurement systems and batch measurement systems. Continuous measurement systems determine the mass flow rate of the product in motion, while batch measurement systems calculate the total mass by weighing a specific amount of product.

A. Rotary Flow Meter

Rotating impeller flowmeters offer compact, volumetric-based solutions for flow measurement of grains and fine-grained products. A constant volume of material is conveyed with each impeller rotation, and the mass flow rate is calculated based on the number of revolutions, providing high repeatability in low-to-medium flow rate ranges (typically 1-50 tons/hour). While advantages include PLC integration and minimal space requirements, abrasive particles can wear down the impeller surface, leading to long-term calibration losses; therefore, they are preferred for products such as soft flour or bran[12, 13].

B. Loss-in-Weight Systems

Lost weight systems are among the most accurate examples of gravimetric measurement and calculate flow rate by monitoring weight changes over time via load cells placed under a feed bunker (Flow Rate = ΔWeight / ΔTime). They stand out with ±0.1% accuracy, especially in dosing and mixer feeding applications with capacities of 0.1-50 tons/hour, and operate continuously with stock replenishment cycles in continuous flow. Their disadvantage is that they require reset periods due to susceptibility to vibration or air currents, and vibration isolation is critical in industrial environments[14, 15].

C. Coriolis Flowmeter (Granular)

Coriolis effect-based granule flowmeters provide multi-parameter data by simultaneously measuring the mass flow and density of the material in a vibrating tube. Their fluid-focused design adaptations for granule processing have been developed. While they provide reliable results over wide flow rate ranges (1-100+ tons/hour) with ±0.1-0.5% accuracy, their high initial investment cost and economic inefficiency in

large-scale installations are major limitations. Their superior performance across density variations makes them suitable for quality control integration[16].

D. Magnetic/Capacitive Sensors

Magnetic and capacitive flow sensors are non-invasive technologies for relative flow detection rather than precise mass measurement; they generate flow presence, fill rate, and trend data via magnetic field changes or dielectric properties. Their low cost and maintenance-free nature make them common in flow control or alarm systems (e.g., silo emptying monitoring), although their accuracy is limited to ±5-10%. A disadvantage is that they do not provide absolute flow rate values, limiting these sensors to a supporting role only, and they are sensitive to density/moisture changes.

E. Impact Flow Meter

Real-time flow measurement of bulk solid materials is critical for in-line monitoring and instantaneous dosing control in industrial automation processes. In this context, the 'Impact Flow Meter' is a non-contact but dynamic measurement technology that measures the mechanical impact force generated when material in free fall passes through a vertical plane and hits an inclined plate. Based on Newton's second law of motion (F=m·a) and the principles of momentum change, these systems convert the kinetic energy of particulate material into electrical signals via load cells or LVDT sensors, producing instantaneous flow rate information. Unlike discrete weighing systems, these devices provide continuous data without stopping or interrupting the flow; they offer highly accurate mass flow monitoring without disrupting operational continuity, especially in processes requiring high speed, in confined spaces, and in dusty environments[17].

In impact type flowmeters, the product in free fall strikes a measuring plate positioned at a specific angle. The force resulting from the change in momentum of the product is measured by load cells. The mass flow rate is calculated using the measured force value. The working structure is shown in Figure 1 [18].

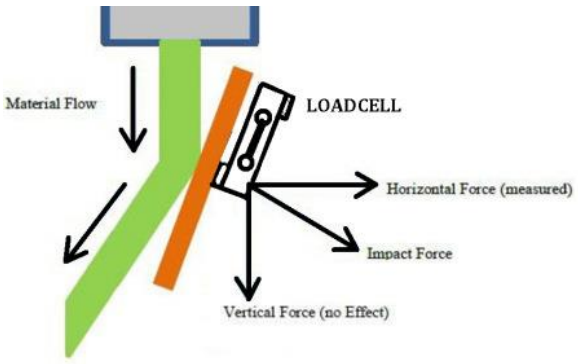

Fig. 1 Impact Flow Meter Working Principle

According to the principle of momentum: $F = \dot{m}\ x\ v$
Where;

- F : Measured force (N)
- v : Impact velocity of the product (m/s)
- $\dot{m}$: Mass flow rate (kg/s)

Flow Rate Calculation: The mass flow rate value is usually converted to tons/hour.

$$Q = \dot{m}\ x\ 3{,}6$$

Where;

- Q : Flow Rate (ton/saat)

Total Mass Calculation: The total amount of product is calculated by time integral.

$$M = \int \dot{m}\ dt$$

In practical applications, this calculation in PLC systems is performed as follows:

$$M = \sum (\dot{m} x \Delta t)$$

Where;

- Δt: measurement time interval

Advantages

- Continuous measurement is possible
- Can operate at high flow rates
- Relatively simple mechanical structure
- Provides instantaneous flow rate information

Disadvantages

- Can be affected by changes in density and product velocity
- Accuracy may decrease at low flow rates
- Requires calibration with reference weighing

F. Efficiency Scale (Discrete Weighing System)

In industrial bulk material processing, precise control of operational efficiency and raw material management constitutes one of the cornerstones of a sustainable production economy. In this context, discontinuous totalizing automatic weighing instruments, also called 'Efficiency Scales', are critical automation components that calculate the total mass with high accuracy by weighing the material in specific batches. Unlike continuous flow systems, these mechanisms, which operate on the principle of static weighing, minimize the margin of error through load cell technology and advanced control algorithms, and are used especially in the grain, feed, and chemical industries for incoming-outgoing inventory control and plant efficiency analysis. Efficiency scales operate on the principle of discontinuous weighing. The product is filled into a weighing hopper, and when the target weight is reached, the weighing is completed and the product is discharged. This process is repeated continuously, and the total amount of product is calculated based on the number of weighings. Single Weighing Mass

The mass measured in each weighing cycle: m = W (kg). In the system used in this study: W = 50 kg was used.

Total production quantity: M = n × W

Where;

- M: total mass (kg)
- n: number of weighings
- W: weight of a single weighing

Hourly flow rate:

$$Q = \frac{n \times W}{t}$$

Where;

- Q: flow rate (kg/hour or tons/hour)
- t: measurement time

For 50 kg weighing and 200 weighings per hour:

$$Q = 200 \times 50 = 10000\, kg/hour\ Q = 10\, ton/hour$$

Advantages

• Very high measurement accuracy
• Unaffected by density changes
• Easy calibration
• Suitable for commercial measurements

Disadvantages

• Intermittent measurement instead of continuous measurement
• Requires a mechanical flap and drain mechanism
• The tank size increases at very high capacities

A comparative summary of all measurement systems is given in Table 1.

TABLE I
COMPARISON TABLE OF MEASUREMENT SYSTEMS

System	Working Principle	Suitability / Capacity	Accuracy	Advantages	Disadvantages
1 Impact Flow Meter	Grain hits the measuring plate, force is measured by load cell	Vertical pipe, elevator outlet, free fall 5–200 tons/hour	±05–1%	Does not require a conveyor belt, works in closed systems, ideal for medium-high flow rates	Accuracy may decrease at low flow rates
2 Rotary Flow Meter	Rotating impeller carries a constant volume, flow rate is calculated from the revolutions	Low-medium flow rate, flour/bran/fine grains low-medium tons/hour	High (not specified)	Compact, easy PLC integration	Prone to wear, requires maintenance with hard particles
3 Loss-in-Weight	Load cell under the bunker, flow rate is calculated with Weight / Time	Additive dosage, mixer feed 01–50 tons/hour	Very high	Very precise, ideal for dosing	Requires continuous feeding, can be affected by vibration
4 Coriolis	Mass flow rate + density measurement from vibrating tube (granule version)	Granule applications various flow rates	±01–05%	Density and flow rate simultaneously, very accurate	High cost, not economical for large diameters
5 Magnetic/Capacitive	Flow present/absent, fill rate, flow rate trend (relative measurement)	Flow control, trend tracking	Low (relative)	Inexpensive, simple installation, low maintenance	Does not perform full flow rate measurement, only indicator
6 Dynamic Screw Conveyor	Load cell + speed sensor under the screw Fill level × Speed ??× Volume × Density	Medium-sized factories medium flow rate	Medium	Integrated screw conveyor system, practical	Sensitive to density changes, calibration required
7 Yield Scale	Analyzes grain sample in terms of moisture, volume and yield (IR/Microwave) integrated with flow rate	Grain silo inlet 10–100+ tons/hour	±02–05%	Calculates moisture/storage loss, provides quality control, fast (sec/min)	Requires cleaning, may have sampling bias

IV. SYSTEM DESIGN

In products with relatively fragile grain structures, such as rice, measurement accuracy and minimizing product loss are important criteria. While impact type flowmeters offer continuous measurement at high flow rates, measurement accuracy depends on product velocity and flow stability. In contrast, yield scales, based on the direct weighing principle, provide higher accuracy. Therefore, it is considered that yield scales based on the intermittent weighing principle offer a more suitable solution for determining production quantity and performing yield calculations in medium-capacity rice processing plants.

In this study, a yield scale based on the intermittent weighing principle was designed and implemented for use in rice processing plants. The system is sized to measure approximately 10 tons of product per hour.

The developed system basically consists of the following components and is shown in Figure 2:

• Weighing chamber
• Load cells

- Product inlet flap
- Product discharge flap
- PLC-based control system
- Operator interface (HMI)

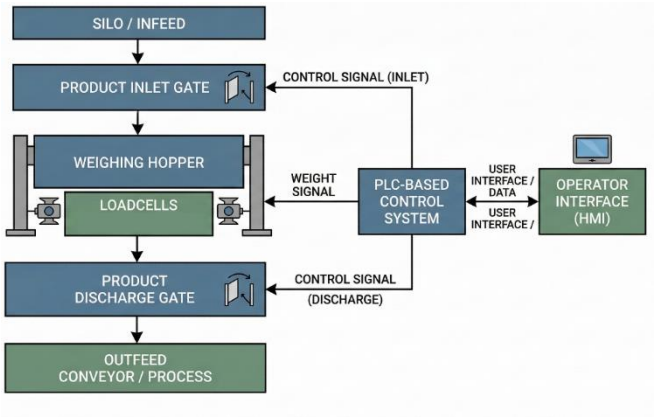

Fig. 2 developed system components

In the system, the weighing chamber is placed on three load cells. The product is loaded into the weighing chamber via the upper inlet flap, and when the target weight of 50 kg is reached, the inlet flap closes automatically. After the weighing process is completed, the lower discharge flap opens, the product is discharged from the system, and a new weighing cycle begins.

To reach a capacity of 10 tons per hour, the system performs approximately 200 weighing cycles per hour.

The total production quantity is calculated using the following equation:

Total Product Quantity = Number of Weighings × Single Weighing Weight

The PLC control system records each weighing cycle and automatically calculates the total daily production quantity. Time required for one weighing cycle:

$$tc = \frac{3600}{n}$$

$$tc = 18\ s$$

This time consists of the following stages:

- Filling time
- Stabilization time
- Weighing time
- Discharege time

Rice density for the Weighing Hopper Volume is approximately:

$$\rho \approx 750\ kg/m^3$$

Hopper volume is calculated from this:

$$V = m/\rho = 50/750 = 0.066 m^3 \approx 0.07\ m^3$$

This value is used in the hopper design.

Loadcell capacity is selected with a safety factor:

$$C = m \times S_f$$

Here;

C: loadcell capacity

m: maximum load

S_f safety factor (1.5–2)

$$C = 50 \times 2 = 100 kg$$

Three loadcells are used, and each sensor is selected with a capacity of 100 kg. The mechanical design of the system is as shown in Figure 3.

Fig. 3 Mechanical design of the system

For this study, a GMT 396T PLC and a GMT 7" HMI were used. The screen design for the measurement is shown in Figure 4. The PLC's operating algorithm is shown in Figure 5.

Fig. 4 HMI Design

Calculations and experimental results show that the developed yield scale can operate reliably at a capacity of 10 tons/hour. Thanks to the intermittent weighing principle, the measurement accuracy is high, and the system offers a suitable solution for determining the production quantity in rice processing plants. In repeated measurements, an average

error rate of ±0.8% was detected using the system when a product with a known weight of 50 tons was sent. It is anticipated that this inaccuracy will be reduced with mechanical improvements to prevent the system from swaying on the mechanical chassis.

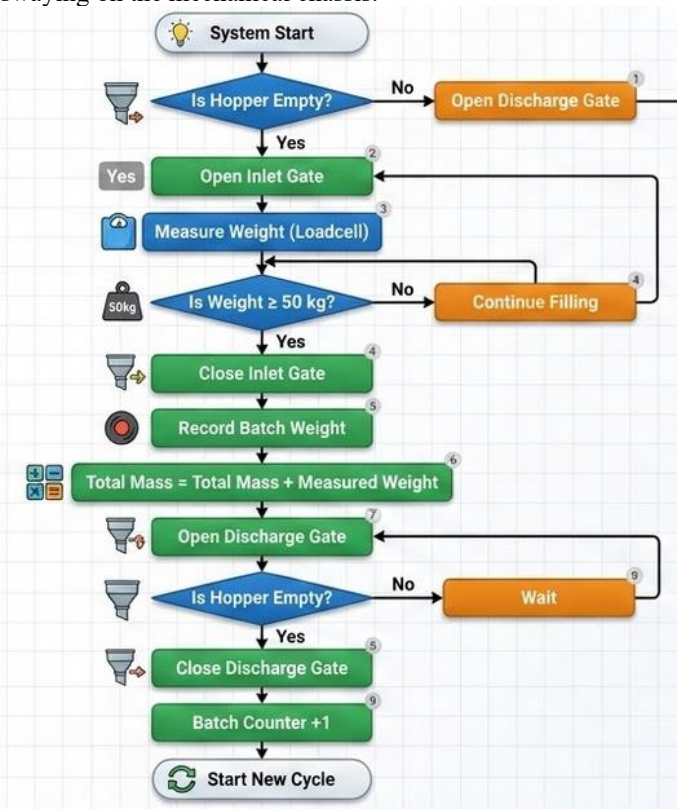

Fig. 5 PLC algorithm

V. FINDINGS AND DISCUSSION

The developed yield scale was tested and its performance evaluated in a rice processing plant. During the test studies, the system was compared with a reference scale. Experimental results showed that the system has an approximate measurement accuracy of ±0.8%. It was also determined that the system can perform approximately 200 weighing cycles per hour, thus achieving the target capacity of 10 tons/hour. While the measurement accuracy is high thanks to the system's batch weighing principle, it was observed that the mechanical flap and unloading times affect the cycle time. However, the ease of maintenance and calibration of the system provides a significant advantage for the operation. The results obtained show that batch weighing systems offer a reliable and economical solution, especially in medium-capacity grain processing plants.

VI. CONCLUSIONS

This study examines the measurement systems used in grain mills and presents the design and implementation of a yield scale based on the batch weighing principle. The developed system has a capacity to measure 10 tons of rice per hour and operates using a 50 kg batch weighing method.

Test results showed that the system operates with high accuracy and provides results consistent with reference measurements. Furthermore, the developed system was found to offer an economical and feasible solution for medium-sized grain facilities. Future studies plan to improve the system's data collection infrastructure, integrate it with remote monitoring systems, and conduct performance evaluations on different grain types..

REFERENCES

[1] Chung, S.O., et al., (2016), *Sensing Technologies for Grain Crop Yield Monitoring Systems: A Review*. Journal of Biosystems Engineering, 41(4): p. 408-417.

[2] Arslan, S., (2000), *Evaluation of Yield Sensors for Site-Specific Management*. *Iowa State University*.

[3] Nelson, B.P., R.W. Elmore, and A.W. Lenssen, (2015), *Comparing Yield Monitors With Weigh Wagons for On-farm Corn Hybrid Evaluation*. Crop Forage & Turfgrass Management, 1(1): p. 1-7.

[4] Burks, T.F., et al., (2003), *Combine Yield Monitor Test Facility Development and Initial Monitoring Test*. Applied Engineering in Agriculture, 19(1).

[5] Correia, L.V., R.J. Hoover, and D.R. Carrijo, (2025), *Winter Wheat Straw and Grain Production in Response to Trinexapac-ethyl and Nitrogen Fertilizer*. Crop Forage & Turfgrass Management, 11(1).

[6] Verdi, C.A., et al., (2019), *Path Analysis on Traits Associated With Oat Milling Yield*. Communications in Plant Sciences, 9(1).

[7] Marcelo Augusto da Silva, S., et al., (2019), *Production Components and Agricultural Productivity of Corn Under Nitrogen Doses and Planting Times*. Journal of Experimental Agriculture International: p. 1-9.

[8] Krishnan, J.N., et al., (2023), *Development of a Novel Image-Based Grain Counting Setup for Thousand-Grain Weight Estimation in Wheat*. Indian Journal of Genetics and Plant Breeding (The), 83(04): p. 469-475.

[9] Fernandez, C.W., et al., (2020), *Effects of Nitrogen Fertilization and Planting Density on Intermediate Wheatgrass Yield*. Agronomy Journal, 112(5): p. 4159-4170.

[10] Scott, W.R., C.T. Dougherty, and R.H.M. Langer, (1977), *Development and Yield Components of High-yielding Wheat Crops*. New Zealand Journal of Agricultural Research, 20(2): p. 205-212.

[11] Das, P.K., (1972), *Studies on Selection for Yield in Wheat. An Application of Genotypic and Phenotypic Correlations, Path-Coefficient Analysis and Discriminant Functions*. The Journal of Agricultural Science, 79(3): p. 447-453.

[12] Perekopskiy, A., et al., (2006), *Effect of initial moisture content of wheat grain on its drying time in a rotary dryer*.

[13] Marczuk, A., et al., (2019), *Studies of a Rotary–Centrifugal Grain Grinder Using a Multifactorial Experimental Design Method*. Sustainability, 11(19): p. 5362.

[14] Olorunfemi, B.J. and S.E. Kayode, (2018), *Computer-Aided Method: An Improved Procedure for Assessing Weight Loss in Stored Grains*. Biosystems Engineering, 3(1): p. 27-37.

[15] Engelbrecht, M.L., (2008), *Assessment of variance in measurement of hectolitre mass of wheat and maize, using equipment from different grain producing and exporting countries*. *Stellenbosch: University of Stellenbosch*.

[16] Dimaczek, G., et al., (1994), *High-precision Coriolis mass flowmeter for bulk material two-phase flows*. Flow Measurement and Instrumentation, 5(4): p. 295-302.

[17] Wei, X., et al., (2014), *Signal processing method of impact-based grain flow sensor for predicted yield***.** Transactions of the Chinese Society of Agricultural Engineering, 30(15): p. 222-228.
[18] E-Tartı.(2026), *E. Impact Flow Meter.* 2026; Available from: https://www.etarti.com/info/tr_003_carpmali.php.

Structural Analysis and Experimental Validation of an Excavator Chassis

Ali BEKTAŞ[1,*]

[1]*Hidromek A.Ş*

***Contact:** Ali.Bektas@hidromek.com.tr

Accurate representation of operating conditions is of critical importance when performing finite element analysis, as the reliability of the results strongly depends on how well the real working conditions are reflected in the numerical model. If the analysis model is defined with boundary conditions that are either more constrained or more free than the actual operating conditions, it can lead to significant differences in the results. In this study, the differences between various modeling techniques of the excavator chassis are evaluated through a comparison of experimental test results and finite element analysis results.

In finite element analysis, various assumptions and acceptance criteria are often introduced during the modeling process. However, an increased number of assumptions may lead to deviations from the actual structural behavior. Such assumptions are typically adopted to reduce computational time and manage model size. In this study, simplified modeling assumptions, detailed modeling approaches, and experimental test results are compared to evaluate the extent to which these assumptions influence the analysis outcomes.

Within the scope of this study, models constrained at the attachment points and models including track–ground contact are validated through comparison with experimental test results. The obtained analysis outputs and their comparisons are presented in the study.

The main motivation of this study originates from the operational behavior of excavators under real working conditions. During field operations, excavators can operate within a 360-degree working range, meaning that the loading direction acting on the chassis continuously changes. If track–ground contact is not represented in the numerical model, the influence of the working direction on the chassis cannot be accurately transferred to the structure. Consequently, both the stress distribution and the magnitude of stresses may deviate from the actual structural response. Moreover, when additional operating conditions, such as the tipping condition of the machine, are considered, it is observed that simplified finite element models may produce stress responses that differ significantly from the real working behavior.

Keywords: *Excavator, FEA, Chasis*

Comparison of Reducer Types for Robotic Applications and Cycloid Reducer Design

Eray YILMAZLAR[1,*]

[1]*Department of Electronics and Automation, Kırklareli University, Kırklareli, TÜRKİYE*

***Contact:** eray.yilmazlar@klu.edu.tr

Abstract—In robotic systems, the need for precision, reliability, and high torque in the motors that provide motion makes the design and selection of reducers crucial. Reducers are mechanical components that convert the high-speed, low-torque motion produced by motors into low-speed, high-torque motion. Today, many types of reducers exist that perform this conversion. Reducers have critical performance parameters such as efficiency, precision, gear ratio, and torque capacity. This study examines the operating principles of different reducer types and compares their basic characteristics. As a result of this comparison, the most suitable gearbox types for use in robotic systems have been identified. Based on these evaluations, a sample reducer design was produced using a 3D printer, and its performance was analysed.

Keywords: Reducer, Cycloid Reducer, Reducer selection

I. Introduction

With the advancement of robot technology and the increasing capabilities of robots, their use in our daily lives is becoming increasingly widespread. It is predicted that humanoid, four-legged robots and robotic arms will be widely used in our daily lives in the coming years. When examining the structure of these robots, the motors that perform the motion are one of the most important components. These motors are required to have a high torque structure at low rotational speeds. In addition to these characteristics, they are required to be precise, capable of rapid control, and to operate with high response times. Motors that meet these criteria include brushless (BLDC), servo and stepper motors. Whilst these motors offer high controllability, response times and speed, their torque values are low. Torque reducers are used to increase the low torque output. Motor torque reducers convert high-speed (RPM) and low-torque motors into slower, high-torque motors. In this study, the types of reducers used, their characteristics and applications were examined, and the characteristics of the different reducer types were compared. Based on the comparison results, the aim was to design a sample reducer using a 3D printer, and the design results were compared.

II. Torque Reducers

Torque reducers, which increase motor torque, reduce speed, facilitate the rotation of the load, and enhance the system's precision and control stability, generally consist of a gear mechanism. This gear mechanism transmits the torque received from the motor shaft to the output shaft via a closed housing. Different types of reducers emerge with various gear mechanism designs. Consequently, each reducer has a distinct torque-speed relationship. The types of reducers are explained in the subheadings.

A. Planetary Gearboxes

Planetary gearboxes consist of a mechanism comprising a central sun gear, planetary gears and an internal gear. In Fig. 1(a), the even distribution of load between the gears in the planetary gear system has increased the system's strength[1]. Quiet operation and high reduction ratios can be achieved.

B. Worm Gear Reducers

As shown in Fig. 1(b), this type of gearbox transfers the torque from the motor to a worm gear, which is rotated by 90 degrees via a spur gear. They achieve high reduction ratios depending on the gear ratios [2]. They operate quietly and with precision.

C. Helical Gearboxes

Helical gearboxes consist of a helical gear structure rather than a spur gear for torque transmission. They operate quietly due to the helical structure shown in Fig. 1(c). Different reduction ratios can be achieved depending on the gear ratios and stages [3]. They operate with high efficiency and quietly.

D. Cycloidal Reducers

A disc rotating on an eccentric shaft performs cycloidal motion between pins. As shown in Fig. 1(d), cycloidal reducers produce significant speed reduction and high torque [4]. They are resistant to high impacts and shocks [5].

Fig. 1: Internal structures of reducers

E. Harmonic Reducers

A flexible gear is shaped using an elliptical wave generator to enable movement. It provides a very high reduction ratio due to the tooth difference [6]. It offers high precision and a high reduction ratio [7].

III. Comparison of Gear Reducer Types

The selection of gearboxes, designed with different internal structures, varies according to application requirements. The factors to be considered in these selections are presented in a comparative table in Table 1. In robotic applications, torque capacity, reduction ratio, load-carrying capacity, service life, cost and response time are key considerations when selecting a gearbox. Planetary gearboxes are preferred in automation systems due to their high efficiency and torque values. Worm gearboxes can be designed for high reduction ratios, but their efficiency is lower compared to other types. Helical gearboxes operate quietly and are highly efficient, but their reduction ratios are lower than those of other types. Cycloidal gearboxes offer advantages in precise movements due to their resistance to high impact loads and low shaft backlash, but they operate noisier than other gearboxes. Their construction is complex and costly. Harmonic reducers possess very high positional accuracy. They are preferred in robotics and applications requiring precise control. They are expensive. They are not as resistant to sudden impacts and shocks as cycloidal reducers.

When examining reducers used in the field of robotics, Roozing et al. ensured that the robotic joint moved more lightly and with higher torque through their cycloidal reducer design [8]. Lee et al. designed a cycloidal reducer for robotic legs and based on their analyses, highlighted the advantages of the cycloidal reducer [9]. Zhu et al. investigated the effect of planetary gears and cycloidal reducers on robotic legs, noting that planetary reducers are less prone to vibration, larger in size, and have lower torque values. They noted that the cycloidal reducer, however, achieved higher torque and load capacity[10]. Park compared the use of harmonic and cycloidal reducers in robotic arm design. The harmonic reducer yielded relatively low efficiency and high inertia. With the cycloidal reducer, he encountered manufacturing and assembly difficulties but achieved high reduction ratios and torque capacity[11]. When literature reviews and the reducer characteristics in Table 1 are compared, cycloidal and harmonic reducers stand out in humanoid, legged robots.

TABLE 1

Types and characteristics of reducers

Feature / Type	Planetary Reducer	Worm Gearbox	Helical Gearbox	Cycloidal Gearbox	Harmonic Reducer
Reduction Ratio	Medium-High	Very high possible	Medium	Very high	Very high
Yield	High	Low to Medium	Very high	High	Medium-High
Gap	Low	Medium	Low	Very low	Almost zero
Torque Density	Very high	Medium	High	Very high	High
Sensitivity	High	Low	Medium	Very high	Very high
Quiet operation	Good	Very good	Very good	Average	Good
Impact Resistance	Good	Average	Good	Very high	Low - Medium
Compactness	Very good	Good	Average	Average	Very good
Maintenance requirements	Low	Low	Low	Medium	Delicate use
Cost	Medium-High	Low to medium	Medium	High	High
Typical Applications	Servo systems, robotics, automation	Conveyors, lifts	Industrial machinery	Robotics, precision motion	Robotics, aerospace, medical
Key Advantages	High torque and efficiency	High speed and quiet operation	Quiet and durable	Precision and impact resistance	Seamless and precise
Main disadvantage	Relatively high cost	Low efficiency / heating	Limited scale	Complex structure	Limited torque capacity

IV. CYCLOIDAL REDUCER DESIGN

A cycloidal reducer is a type of reducer that operates based on cycloidal geometry and the principle of rolling. Torque conversion in rotational motion is achieved through the rolling of circular gears. The components forming the cycloidal reducer are shown in Fig. 2. Fig. 2(a) shows the pins in contact with the disc. These pins, fixed to the lower housing, transmit the rotational motion to the outer housing via free-running cylindrical nuts. Fig. 2(b) shows the outer housing, which performs the rotational motion and torque transmission. Torque transmission is achieved via the teeth within the housing. Fig. 2(c) shows the cycloidal discs that transmit the rotational motion to the housing. Fig. 2(d) shows the shaft and housing retainer that convert the rotational motion from the motor into eccentric motion. The components of the cycloidal reducer design were manufactured using a 3D printer, and the motion transmissions are supported by bearings. The reduction ratio of the designed cycloidal reducer is(i) 26:1, and the reducer efficiency is(η) 0.915. The cycloidal reducer has been connected to the motor shown in Fig. 3. When this design is connected to a NEMA 17 stepper motor with a torque of$T_{\mathrm{m}} = 0.45\ Nm$ and a motor speed of$n_{\mathrm{m}} = 300\ rpm$, the motor angular speed(ω_m) , output speed(n_{out}) and output angular speed(ω_{out}) were calculated using Equations 1–3 [12].

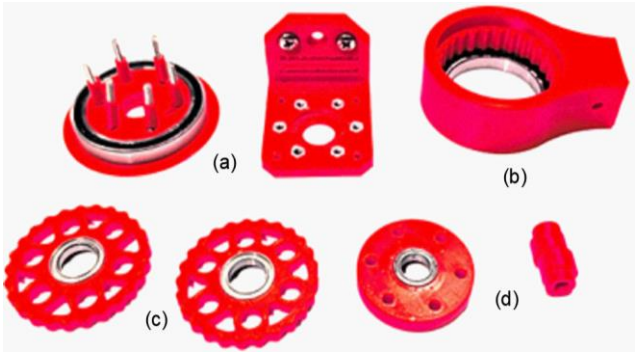

Fig. 2 Cycloidal reducer components

$$\omega_m = \frac{2\pi \times n_m}{60} = 31.42\ \mathrm{rad/s} \quad (1)$$

$$n_{out} = \frac{n_m}{i} = 11.54 rpm \quad (2)$$

$$\omega_{out} = \frac{\omega_m}{i} = 1.208 rad/d \quad (3)$$

The ideal output torque(T_{ideal}) and the actual output torque(T_{out}) are explained by Equations 4–5. The motor power(P_{in}) and the motor output power(P_{out}) are calculated in Equations 6–7.

$$T_{ideal} = T_m \times i = 11.7 Nm \quad (4)$$

$$T_{out} = T_m \times i \times \eta = 10.71 Nm \quad (5)$$

$$P_{in} = T \times \omega_m = 14.14 W \quad (6)$$

$$P_{out} = P_{in} \times \eta = 12.94 W \quad (7)$$

As a result of the speed-torque conversion performed by the cycloidal reducer, the speed has been reduced from 340 rpm to 11.54 rpm. In terms of torque, an increase from 0.45 Nm to 10.71 Nm has been achieved. In terms of power conversion, a loss has occurred in accordance with the efficiency ratio.

Fig. 3 Cycloidal reducer connection to NEMA 17 stepper motor

V. RESULTS

The aim of the gearbox comparisons was to examine the characteristics of the gearboxes used. Through this analysis, a sample cycloidal gearbox design was developed, and speed-torque variations were presented according to the reduction ratio.

Based on the results of these studies, when evaluating reducer choices for robotic systems according to the fundamental characteristics sought, the following are desired: being lightweight and compact; being able to withstand sudden impacts such as walking, jumping and running; and distributing impacts via multiple contact surfaces. At the same time, low internal friction and high efficiency are desired. The aim is to achieve error-free precise position control by ensuring that the backlash is close to zero. With these characteristics, cycloidal reducers stand out among other types of reducers. Another type of reducer with similar characteristics is the harmonic reducer. Due to the harmonic reducer's lower efficiency, limited torque capacity and low resistance to sudden impacts, it is preferred in applications requiring low torque. Whilst gearboxes commonly used in industry, such as planetary, worm and helical gearboxes, perform well in terms of impact resistance, torque density,

precision and shaft play, they fall short of cycloidal gearboxes when it comes to robotic systems.

The torque of a Nema 17 stepper motor has been converted using a cycloidal reducer design prototyped with a 3D printer. With a reduction ratio of 26:1, the torque value of 0.45 Nm has been converted to 10.71 Nm. This will enable precise position control and powerful limb movement in robotic applications.

This study highlights the key considerations for selecting motor reducers used in robotic applications, emphasises the advantages of different reducer types in specific fields, and compares the characteristics of the reducers. It also presents a design suitable for robotic applications using an example gearbox design. It is anticipated that this study will contribute to the gearbox selection process in future robotic applications.

REFERENCES

[1] "Planetary gear reducer," https://www.neugart.com/en/planetary-gear-reducer.

[2] "Worm gear reducers," https://www.ystendustri.com/urun/liming-we-serisi-sonsuz-disli-reduktorler-54319.

[3] "Helical gearboxes," https://varvel.com/en/blog/in-line-helical-gearboxes-and-gearmotors/.

[4] "Cycloidal Reducer," https://www.hakayrulman.com/sumitomo-fine-cyclo/.

[5] W. Roozing and J. Volbeda, "Anti-Backlash Mechanisms for Cycloidal Drive Robotic Actuators: Design and Evaluation," *IEEE Robotics and Automation Letters, Autom. Lett.*, vol. 10, no. 11, pp. 12221–12228, 2025, doi: 10.1109/LRA.2025.3619805.

[6] "Harmonic drive gear reducer," https://www.hanzh.com/harmonic-drive-gear-reducer-XB1-BS-CF-p.html.

[7] M. S. Islam, K. Kim, and H. Y. Kim, "Data-Driven Approach for Fault Diagnosis of Harmonic Drives Using Wireless Acceleration Sensors and Machine Learning," *International Journal of Precision Engineering and Manufacturing - Green Technology*, vol. 12, no. 3, pp. 951–968, May 2025, doi: 10.1007/s40684-025-00728-x.

[8] W. Roozing and G. Roozing, "3D-printable low-reduction cycloidal gearing for robotics," in *IEEE International Conference on Intelligent Robots and Systems*, Institute of Electrical and Electronics Engineers Inc., 2022, pp. 1929–1935. doi: 10.1109/IROS47612.2022.9982006.

[9] K. K. Lee, S. Hong, and J. H. Oh, "Development of a Lightweight and High-efficiency Compact Cycloidal Reducer for Legged Robots," *International Journal of Precision Engineering and Manufacturing*, vol. 21, no. 3, pp. 415–425, Mar. 2020, doi: 10.1007/s12541-019-00215-9.

[10] A. Zhu, Y. Tanaka, F. Rafeedi, and D. Hong, "Cycloidal Quasi-Direct Drive Actuator Designs with Learning-based Torque Estimation for Legged Robotics," Mar. 2025, [Online]. Available: http://arxiv.org/abs/2410.16591

[11] M.-W. Park, "A Study on the Conceptual Design of a Planocentric Involute Reducer for a Modular Robot," in *the 19th International Conference on Control, Automation and Systems (ICCAS) 2019*, 2019, pp. 1412–1414. doi: 10.23919/ICCAS47443.2019.8971607.

[12] H. Tariq, Z. Galym, A. Amrin, and C. Spitas, "Assessment of contact forces and stresses, torque ripple and efficiency of a cycloidal gear drive and its involute kinematic equivalent," *Mechanics Based Design of Structures and Machines*, vol. 52, no. 3, pp. 1304–1323, 2024, doi: 10.1080/15397734.2022.2144885.

CFD Analysis of the Hydrogen Tank Filling

Ekin Can KAYAR[1,*], Mustafa YILDIZ[2]

[1]*Hidromek A.Ş., Ankara, TÜRKİYE*

[2]*Department of Mechanical Engineering, Ankara Yıldırım Beyazıt University, Ankara, TÜRKİYE*

***Contact:** ekin.kayar@hidromek.com.tr

Abstract— In this study, the filling process of a high-pressure hydrogen tank is investigated using a transient Computational Fluid Dynamics (CFD) approach. The continuity, momentum, and energy equations are solved simultaneously, and the Redlich–Kwong real gas equation of state is employed to accurately represent the thermodynamic behaviour of hydrogen under high-pressure conditions. The tank is modelled as a two-dimensional axisymmetric domain under the assumption of axial symmetry, and the computational domain includes both the inlet nozzle and the internal volume of the tank. The results demonstrate the transient evolution of the pressure, temperature, and velocity fields inside the tank during the filling process. The pressure field exhibits a continuously increasing trend and gradually becomes more uniform, while the temperature field rises and spreads throughout the tank volume. The velocity field is dominated by a high-momentum jet at the inlet during the early stages of filling, and as the process progresses, the velocity levels decrease and the flow transitions toward a more quiescent regime. The findings indicate that the hydrogen filling process is a complex and strongly time-dependent problem that requires the coupled evaluation of flow dynamics and thermodynamic behaviour. This study shows that a CFD-based approach incorporating real gas effects provides a physically consistent and reliable framework for analysing the filling processes of high-pressure hydrogen storage tanks.

Keywords: Hydrogen Tank, High-Pressure Storage, Hydrogen Filling Process, CFD, Real Gas Redlich–Kwong

I. INTRODUCTION

With the increasing global demand for clean and sustainable energy systems, hydrogen has emerged as a promising energy carrier due to its high energy density and environmentally friendly characteristics. When used in fuel cells, hydrogen produces only water as a by-product, making it an attractive alternative to conventional fossil fuels, particularly in transportation and energy storage applications. Therefore, the development of safe and efficient hydrogen storage systems has become a critical requirement for the widespread adoption of hydrogen-based technologies [1].

Among various hydrogen storage methods, high-pressure compressed hydrogen tanks are widely preferred due to their technological maturity and applicability. However, the hydrogen filling process in such systems involves complex and strongly coupled phenomena, including rapid pressure increase, temperature rise due to gas compression, transient flow behaviour, and real gas effects. These factors significantly influence the safety, performance, and durability of hydrogen storage systems. Therefore, a detailed understanding of the filling process is essential for the design and optimization of high-pressure hydrogen tanks [2].

Experimental investigations of hydrogen filling processes are often associated with high costs, safety risks, and measurement limitations, especially under extreme pressure conditions. In this context, Computational Fluid Dynamics (CFD) has become a powerful tool for analysing hydrogen storage systems. CFD enables detailed investigation of the temporal and spatial evolution of pressure, temperature, and velocity fields within the tank, providing insights that are difficult to obtain experimentally [3].

A considerable number of studies in the literature have focused on both experimental and numerical analysis of hydrogen tank filling processes. Heitsch et al. experimentally investigated the thermal effects during fast hydrogen filling and demonstrated that temperature rise is a critical parameter for system safety [4]. Melideo et al. conducted CFD simulations of hydrogen tank filling and emptying processes, highlighting the transient evolution of pressure, temperature, and velocity fields [5]. Bourgeois et al. numerically analysed the influence of tank geometry and inlet conditions on temperature distribution and showed that these parameters significantly affect thermal stratification and peak temperature levels [6].

More recent studies have emphasized the importance of real gas effects in accurately predicting hydrogen filling behaviour under high-pressure conditions. Zhao et al. investigated the fast-filling process using both experimental and numerical approaches and highlighted the limitations of ideal gas assumptions [7]. Monteiro et al. performed CFD simulations using different equations of state and demonstrated that real gas models, such as Redlich–Kwong and Peng–Robinson, provide significantly improved accuracy in predicting thermodynamic properties compared to ideal gas models [8].

Despite these advancements, many studies focus on experimental observations or use simplified models that do not fully capture the coupled transient and thermodynamic nature of hydrogen filling. In this study, the filling process of a high-pressure hydrogen tank is analysed using a transient CFD approach, where the governing equations of mass, momentum, and energy are solved with the Redlich–Kwong real gas model. The tank is modelled as a two-dimensional

axisymmetric domain to ensure computational efficiency while preserving essential physics. The results provide a comprehensive representation of the coupled flow and thermodynamic behaviour, offering insights for the design and safety assessment of high-pressure hydrogen storage systems.

II. Materials And Methods

A. Model Description

The hydrogen tank filling process was investigated using a transient Computational Fluid Dynamics (CFD) framework to accurately capture the coupled interaction between flow dynamics and thermodynamic effects. The numerical model was constructed based on the physical configuration of a high-pressure hydrogen storage system, including both the inlet nozzle and the internal tank volume. The adopted modelling approach enables the analysis of time-dependent variations in pressure, temperature, and velocity fields throughout the filling process. Particular attention was given to the selection of appropriate assumptions, boundary conditions, and thermodynamic models in order to ensure a physically consistent and reliable representation of high-pressure hydrogen behaviour.

Figure 1 presents the real physical configuration of the high-pressure hydrogen storage tank modelled in this study. This image illustrates the geometric features and overall structure of the system that form the basis of the numerical model. The cylindrical shape of the tank, the inlet nozzle connection, and the flow development along the axial direction support the suitability of the two-dimensional axisymmetric approach adopted in the CFD model. This consistency between the real system and the numerical model strengthens the validity of the assumptions and enhances the engineering interpretability of the obtained results.

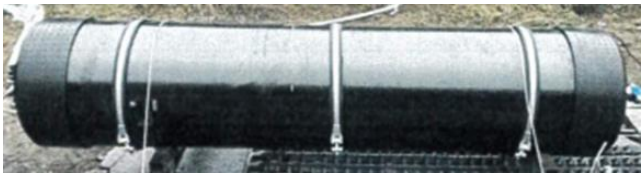

Fig. 1 Hydrogen Tank

Figure 2 presents the geometric model of the hydrogen tank employed in the CFD analysis. The model was constructed by simplifying the real system into a two-dimensional axisymmetric domain, which enables a significant reduction in computational cost while retaining the dominant physical characteristics of the filling process. The computational domain encompasses both the inlet nozzle and the internal tank volume, allowing accurate representation of the inflow conditions and the development of the flow field within the tank. This geometric representation provides a reliable and efficient basis for capturing the transient behaviour of pressure, temperature, and velocity fields during the hydrogen filling process.

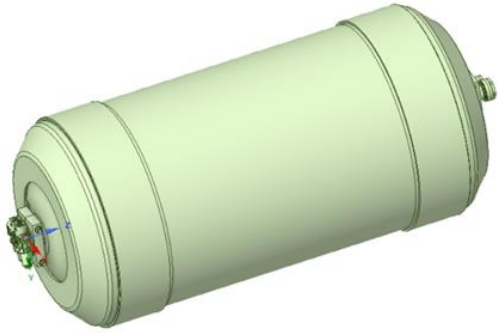

Fig. 2 The Geometric Model

Figure 3 presents the numerical model used in the CFD analysis of the hydrogen tank filling process. The computational domain was defined to include both the internal volume of the tank and the inlet nozzle region, and the hydrogen filling was modelled using a mass flow rate boundary condition. A constant mass flow rate of 8 g/s was specified at the inlet, while the initial conditions inside the tank were defined as 20 bar pressure and 25°C temperature. Appropriate thermal boundary conditions were applied to the tank walls, and the energy equation was activated to accurately capture the temperature variations resulting from gas compression. The solution was carried out in a transient manner, and at each time step, the continuity, momentum, and energy equations were solved simultaneously. In order to accurately represent the real gas behaviour of hydrogen under high-pressure conditions, the Redlich–Kwong equation of state was employed. All simulations were performed using ANSYS Fluent, and the visualization results were obtained from the sectional plane shown in Figure 3.

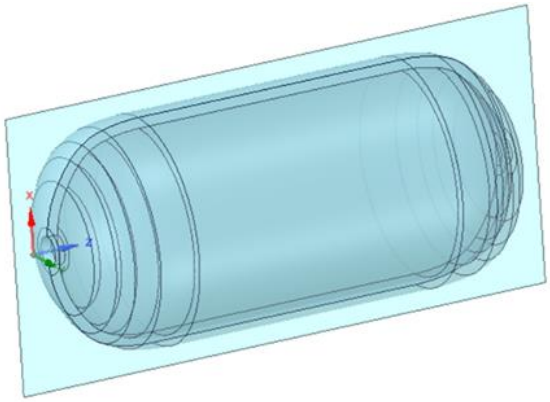

Fig. 3 The Numerical Model

B. Governing Equations

Conservation of Mass:

The principle of conservation of mass states that the difference between the mass entering and leaving a control volume is equal to the rate of change of mass within that control volume. This principle constitutes one of the fundamental laws of fluid mechanics and forms the basis of all physical and numerical models used to describe fluid flow. Mass can neither be created nor destroyed within a flow field; it can only be transported in space and time. The mathematical expression of this principle is given by the continuity equation, which in its general form is written as [9]:

$$\frac{\partial \rho}{\partial t} + \nabla \cdot (\rho v) = 0 \qquad (1)$$

where:

- ρ denotes the fluid density (kg/m³),
- v represents the velocity vector (m/s),
- t is the time (s).

This equation states that the temporal variation of density within a control volume is balanced by the net mass flux due to fluid motion across its boundaries. The first term accounts for the local (time-dependent) change in density, while the second term represents the convective transport of mass through the flow field. Together, these terms ensure that mass is conserved both locally and globally [9].

The continuity equation is solved simultaneously with the momentum and energy conservation equations to determine the flow field variables in a physically consistent manner. Its accurate satisfaction is a prerequisite for the reliability of the computed velocity, pressure, and density fields. Therefore, the continuity equation occupies a central position in the theoretical formulation of fluid flow problems and constitutes an essential component of all CFD-based modelling approaches [9].

Conservation of Momentum:

The principle of conservation of momentum is based on Newton's second law and states that the rate of change of momentum of a fluid element is equal to the sum of the forces acting on it. In fluid flow, these forces arise mainly from pressure gradients and viscous stresses. The momentum equation provides the fundamental relationship that governs the motion of the fluid and describes how the velocity field evolves in space and time. In its general vector form, the momentum conservation equation is written as [10]:

$$\frac{\partial (\rho v)}{\partial t} + \nabla \cdot (\rho v v) = -\nabla p + \nabla \cdot \tau \qquad (2)$$

where:

p denotes the pressure (Pa),

τ represents the viscous stress tensor (Pa),

$\rho v v$ represents the convective flux of momentum (N/m³).

This equation represents the balance between inertial effects, pressure forces, and viscous forces within the flow field. The left-hand side accounts for the temporal and convective transport of momentum, while the right-hand side includes the forces acting on the fluid element [10].

For a Newtonian fluid, the viscous stress tensor τ is expressed as [10]:

$$\tau_{ij} = \mu \left(\frac{\partial v_i}{\partial x_j} + \frac{\partial v_j}{\partial x_i} \right) - \frac{2}{3} \mu (\nabla \cdot v) \delta_{ij} \qquad (3)$$

where:

- μ is the dynamic viscosity (Pa·s),
- δ_{ij} is the Kronecker delta.

This formulation relates the viscous stresses to the velocity gradients and ensures that the effects of internal friction within the fluid are properly accounted for in the momentum balance [10].

The momentum equation is solved simultaneously with the continuity and energy equations to obtain a complete description of the flow field. It determines the velocity and pressure distributions and plays a central role in predicting the dynamic behaviour of the fluid. The accurate representation of momentum transport is essential for ensuring the physical consistency and reliability of the numerical solution [10].

Conservation of Energy:

The principle of conservation of energy describes how the total energy within a system varies with time and constitutes the fundamental basis of the thermal and mechanical interactions in a flow field. Since the temperature distribution in a fluid is directly related to the pressure and velocity fields, the energy equation represents one of the most important governing equations for describing the thermodynamic behaviour of the flow. For a compressible flow, the energy equation is expressed in the following general form [11]:

$$\frac{\partial (\rho E)}{\partial t} + \nabla \cdot \big(v(\rho E + p) \big) = \nabla \cdot (k \nabla T) + \Phi \qquad (4)$$

where:

- E denotes the total energy per unit mass (J/kg),
- k denotes the thermal conductivity (W/m·K),
- T denotes the temperature (K),
- Φ represents the viscous dissipation term (W/m³).

This equation accounts simultaneously for the temporal variation of the total energy, the convective transport of energy due to fluid motion, the heat transfer by thermal conduction, and the conversion of mechanical energy into thermal energy caused by viscous effects. The terms on the left-hand side represent the time-dependent change and convective transport of energy, whereas the terms on the right-hand side correspond to heat conduction and viscous dissipation, respectively [11].

The total energy per unit mass is defined as the sum of the internal energy, the flow work, and the kinetic energy, and is given by [11]:

$$E = h - \frac{p}{\rho} + \frac{|v|^2}{2} \quad (5)$$

This formulation enables the energy balance in the flow field to be evaluated by simultaneously considering both thermal and mechanical contributions. The energy equation makes it possible to account for the temperature rise caused by gas compression, the kinetic energy associated with fluid motion, and the heat transfer occurring through conduction and convection mechanisms. Therefore, it plays a central role in the accurate and physically consistent prediction of the temperature field and heat distribution within the system [11].

First Law of Thermodynamics and Energy Balance:

The first law of thermodynamics is based on the principle of conservation of energy and states that the change in the total energy of a system is determined by the energy exchange between the system and its surroundings. This law provides the fundamental framework for describing any physical process from an energy perspective. When a control volume approach is adopted, the energy balance is formulated in terms of the energy transported by mass flow and the heat transfer between the system and the environment. The general form of the energy balance can be written as [12]:

$$\frac{dU}{dt} = \dot{m}_{in} h_{in} + \dot{Q} \quad (6)$$

where:

- U denotes the total internal energy stored within the control volume [J],
- m_{in} represents the mass flow rate entering the control volume [kg/s],
- h_{in} is the specific enthalpy of the incoming flow [J/kg],
- Q denotes the rate of heat transfer between the system and its surroundings [W].

This expression indicates that the time rate of change of the internal energy within a system is governed by the energy carried by the incoming mass flow and by the heat exchanged with the environment. The energy balance provides a macroscopic description of the thermodynamic behaviour of the system and clarifies the mechanisms through which energy is transported and transformed during a given process [12].

This integral form of the energy balance constitutes the thermodynamic foundation of the differential energy equation used in Computational Fluid Dynamics. In CFD, the energy equation represents the localized and time-dependent form of this balance, applied at every point of the flow domain. In other words, the numerical solution of the energy equation ensures that the first law of thermodynamics is satisfied locally and instantaneously throughout the computational domain [12].

Therefore, the first law of thermodynamics, together with the energy balance formulation, plays a central role in establishing a physically consistent description of the thermal behaviour of the system. It provides the theoretical basis for predicting temperature fields, energy transport, and heat distribution in fluid flow problems [12].

Real Gas Redlich–Kwong:

The Redlich–Kwong real gas equation of state is a semi-empirical thermodynamic model developed to account for the deviations of real gases from ideal gas behaviour, particularly under moderate and high-pressure conditions. It provides a more realistic relationship between pressure, temperature, and density by incorporating the effects of intermolecular interactions and the finite volume occupied by gas molecules. Owing to its simplicity and reasonable accuracy over a wide range of operating conditions, the Redlich–Kwong model has been widely used in engineering and thermodynamic applications. The Redlich–Kwong equation of state is expressed as [13]:

$$p = \frac{RT}{v - b} - \frac{a}{\sqrt{T} v (v + b)} \quad (7)$$

where:

- p is the pressure $[Pa]$,
- T is the temperature $[K]$,
- v is the specific volume $[m^3/kg]$,
- R is the specific gas constant of the fluid $[J/(kg \cdot K)]$,
- a and b are substance-specific constants determined experimentally.

In this formulation, the first term represents the ideal gas contribution, while the second term introduces a correction that accounts for intermolecular attractive forces and real gas effects. As a result, the Redlich–Kwong equation provides a more physically accurate description of gas behaviour compared to the ideal gas law [13].

The relationship between the specific volume and the density is given by [13]:

$$v = \frac{1}{\rho} \quad (8)$$

which allows the equation of state to be expressed in terms of pressure, temperature, and density [13].

Real gas behaviour is commonly characterized using the compressibility factor Z, defined as [13]:

$$Z = \frac{p}{\rho R T} \quad (9)$$

For an ideal gas, Z=1, whereas for real gases Z deviates from unity depending on the pressure and temperature. At elevated pressure levels, this deviation becomes significant and the ideal gas assumption may lead to considerable inaccuracies in the prediction of thermodynamic properties. The Redlich–Kwong equation of state implicitly accounts for these deviations by incorporating real gas corrections, thereby improving the accuracy of density, enthalpy, and internal energy predictions [13].

Therefore, the Redlich–Kwong real gas model provides a reliable and practical framework for representing the

thermodynamic behaviour of gases in regimes where ideal gas assumptions are no longer valid, and it is particularly well suited for applications involving high-pressure gas systems [13].

III. RESULTS

In this section, the numerical results of the hydrogen tank filling process are presented, and the time-dependent evolution of pressure, temperature, and velocity fields is analysed in detail. The results indicate that the filling process is strongly transient in nature and that flow dynamics and thermodynamic effects are closely coupled. In particular, the variations in pressure, temperature, and velocity fields are evaluated together to provide a comprehensive understanding of the system behaviour.

Figure 4 shows the time-dependent variation of pressure inside the tank. The results indicate that the pressure increases continuously and monotonically throughout the filling process. Starting from an initial value of approximately 20 bar, the pressure reaches nearly 350 bar at the end of the process. A good agreement between the numerical results and experimental data is observed, which supports the accuracy of the developed model. As the filling progresses, the rate of pressure increase slightly changes, indicating a transition toward a more stable regime.

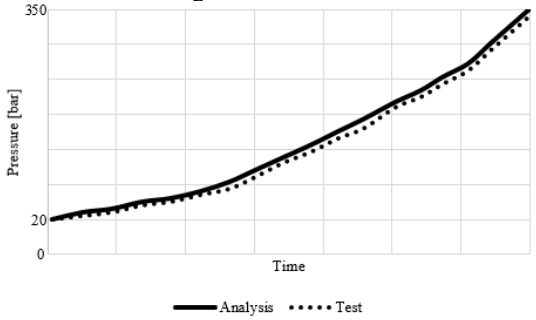

Fig. 4 Comparison of Pressure Evolution Inside the Hydrogen Tank

Figure 5 presents the time-dependent variation of temperature inside the tank. The results show a rapid temperature increase during the initial stage of the filling process. This behaviour is mainly attributed to gas compression under high-pressure conditions. As the process continues, the rate of temperature increase decreases, and the system exhibits a more stable thermal behaviour. A reasonable agreement between the numerical and experimental results is observed, indicating that the model successfully captures the thermodynamic behaviour of hydrogen.

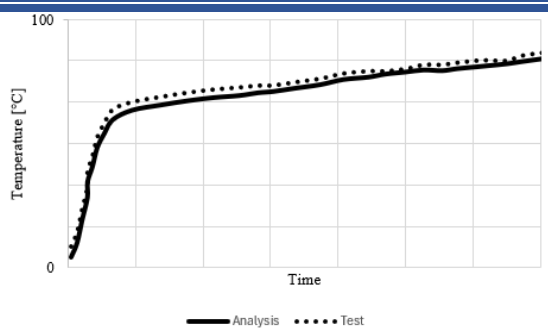

Fig. 5 Comparison of Temperature Evolution Inside the Hydrogen Tank

Figure 6 illustrates the pressure distribution inside the tank at three different time steps. At the initial stage (1), the pressure levels are relatively low, and localized effects near the inlet region are dominant. At the intermediate stage (2), the pressure increases and spreads over a larger portion of the tank volume. At the final stage (3), the pressure distribution becomes nearly uniform throughout the tank, indicating that the system approaches equilibrium conditions as the filling process progresses.

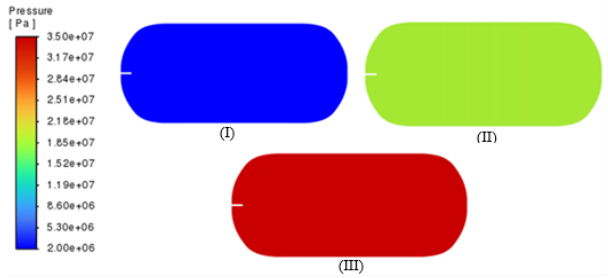

Fig. 6 Time-Dependent Pressure Distribution Inside the Hydrogen Tank

Figure 7 shows the temperature distribution inside the tank at three different time steps. At the initial stage (1), the temperature remains relatively low, with slight increases near the inlet region. At the intermediate stage (2), the temperature rises significantly due to compression effects and begins to spread throughout the tank. At the final stage (3), the temperature distribution becomes more uniform, reaching its maximum levels across the tank volume. These results clearly demonstrate the impact of gas compression and energy transport mechanisms during the filling process.

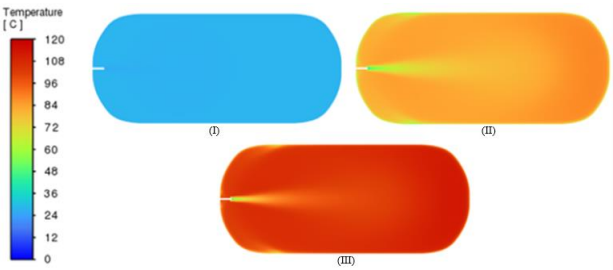

Fig. 7 Time-Dependent Temperature Distribution Inside the Hydrogen Tank

Figure 8 presents the velocity distribution inside the tank at three different time steps. At the initial stage (1), a high-momentum jet is formed at the inlet, leading to maximum velocity levels. At the intermediate stage (2), as the internal tank pressure increases, the driving force at the inlet decreases, resulting in a reduction in velocity levels. At the final stage (3), the flow becomes significantly damped, and the system transitions toward a low-velocity, quasi-stagnant regime. This behaviour indicates that the system evolves from a flow-dominated regime at the beginning to a thermodynamically controlled regime in the later stages of the filling process.

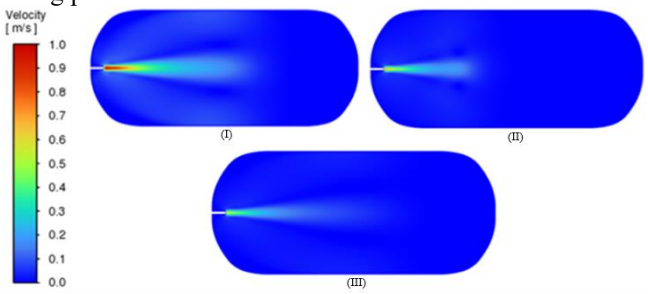

Fig. 8 Time-Dependent Velocity Distribution Inside the Hydrogen Tank

IV. Conclusions

In this study, the hydrogen tank filling process was investigated using a transient Computational Fluid Dynamics (CFD) approach, incorporating the Redlich–Kwong real gas equation of state to accurately represent hydrogen behaviour under high-pressure conditions. The developed numerical model successfully captured the coupled evolution of pressure, temperature, and velocity fields during the filling process, providing a comprehensive understanding of the underlying physical mechanisms.

The results showed that the pressure inside the tank increases continuously and reaches approximately 350 bar at the end of the filling process, while the pressure distribution gradually becomes more uniform throughout the tank volume. Similarly, the temperature rises significantly due to gas compression, reaching values close to 100°C, and evolves toward a more homogeneous distribution over time. These findings are consistent with the expected behaviour of compressible gases and highlight the importance of considering real gas effects for accurate thermodynamic predictions.

The velocity field is initially dominated by a high-momentum jet at the inlet, resulting in strong local gradients. However, as the internal pressure increases, the driving force decreases, leading to a gradual reduction in velocity levels. In the final stage, the flow transitions into a low-velocity, quasi-stagnant regime, indicating a shift from a flow-dominated to a thermodynamically controlled process during filling.

Overall, the results demonstrate that the hydrogen filling process is strongly transient and governed by the coupled interaction between flow dynamics and thermodynamic effects. The use of a real gas model plays a crucial role in accurately predicting pressure and temperature evolution under high-pressure conditions. The proposed CFD approach provides a reliable and physically consistent framework for analysing hydrogen tank filling processes and offers valuable insights for the design, optimization, and safety assessment of high-pressure hydrogen storage systems. Furthermore, the presented methodology can serve as a reference for future studies aiming to improve the accuracy of hydrogen storage modelling under realistic operating conditions.

Acknowledgment

I would like to thank HİDROMEK for its contribution to this study.

References

[1] Schlapbach, Louis, and Andreas Züttel. "Hydrogen-storage materials for mobile applications." nature 414.6861 (2001): 353-358.

[2] Züttel, Andreas. "Materials for hydrogen storage." Materials today 6.9 (2003): 24-33.

[3] Versteeg, Henk Kaarle. An introduction to computational fluid dynamics the finite volume method, 2/E. Pearson Education India, 2007.

[4] Heitsch, Matthias, Daniele Baraldi, and Pietro Moretto. "Numerical investigations on the fast filling of hydrogen tanks." International Journal of Hydrogen Energy 36.3 (2011): 2606-2612.

[5] Melideo, Daniele, et al. "CFD simulations of filling and emptying of hydrogen tanks." international journal of hydrogen energy 42.11 (2017): 7304-7313.

[6] Bourgeois, Thomas, et al. "Evaluating the temperature inside a tank during a filling with highly-pressurized gas." international journal of hydrogen energy 40.35 (2015): 11748-11755.

[7] Zhao, Bin, et al. "Experimental and numerical research on temperature evolution during the fast-filling process of a type III hydrogen tank." Energies 15.10 (2022): 3811.

[8] Monteiro, José Miguel, et al. "Computational fluid dynamics simulation of filling a hydrogen type 3 tank at a constant mass flow rate." Energies 17.6 (2024): 1375.

[9] White, Frank M., and Joseph Majdalani. Viscous fluid flow. Vol. 3. New York: McGraw-Hill, 2006.

[10] Pritchard, Philip J. "Introduction to Fluid Mechanics 8th Edition. Fox and McDonald." (2011).

[11] Incropera, Frank P., et al. Fundamentals of heat and mass transfer. Vol. 6. New York: Wiley, 1996.

[12] Moran, Michael J., et al. Fundamentals of engineering thermodynamics. John Wiley & Sons, 2010.

[13] Bruce E.. Poling, John M. Prausnitz, and O'Connell John Paul. The properties of gases and liquids. New York: McGraw-Hill, 2001.

Patent Landscape Analysis of LPBF and WAAM for Functionally Graded Metal Additive Manufacturing

Selin Deksizler[1,2], İdris Tuğrul Gülenç[1,*]

[1]*Department of Metallurgical and Materials Engineering, Ankara Yıldırım Beyazıt University, Ankara, TÜRKİYE*

[2]*Turkish Patent and Trademark Office, Ankara, TÜRKİYE*

*Contact: idristugrul.gulenc@aybu.edu.tr

Metal additive manufacturing (AM) has experienced significant growth in recent years, with patents serving as an important source for tracking technological developments and emerging research directions. In particular, Laser Powder Bed Fusion (LPBF) and Wire Arc Additive Manufacturing (WAAM) are increasingly explored for the production of functionally graded materials (FGMs), owing to their distinct processing capabilities and potential for tailored material properties.

This study presents a patent-based framework for assessing developments in LPBF and WAAM systems, with a focus on multi-material processing, gradient control, and system integration. It examines how patent data can be systematically analyzed to map technological trends, identify key areas of innovation, and reveal the distribution of research efforts across different application domains and material systems.

The presentation discusses the types of engineering challenges addressed in existing patents, including process stability, thermal management, material compatibility, and defect mitigation. It also considers how these challenges influence the design and evolution of AM systems intended for FGM production. Particular attention is given to the contrasting characteristics of LPBF and WAAM, highlighting differences in resolution, deposition rate, and scalability, as well as their respective implications for gradient fabrication.

Overall, the work provides a structured overview of the current patent landscape and contributes to a broader understanding of how intellectual property trends align with technical challenges in metal AM. The study also establishes a foundation for further investigation into the role of patent analysis in guiding research and development strategies for FGM-enabled manufacturing systems.

Keywords: *Metal Additive Manufacturing, Functionally Graded Materials (FGMs), Patent Analysis (IP), Laser Powder Bed Fusion (LPBF), Wire Arc Additive Manufacturing (WAAM)*

Micro Stewart Platform for Vertebra Model and Motion Simulation in Posture Disorders

Uğur Demir[1,*], Alper Nabi Akpolat[1], and Sıtkı Kocaoğlu[2]

[1]*Marmara University Department of Electrical and Electronics Engineering, İstanbul, TÜRKİYE*

[2]*Ankara Yıldırım Beyazıt University, Department of Biomedical Engineering, Ankara, TÜRKİYE*

*Contact: udemir@marmara.edu.tr

In the treatment of spinal deformities, there is a need for well-trained personnel with high-level technology in software and hardware. Especially in the physiotherapy and rehabilitation section, pre-surgical interventions such as Concrete Learning and Interactive Experience, Research and Data Collection, Treatment Planning, Personalization and Feedback, Simulation-Supported Therapy and Rehabilitation, New Approaches in Spinal Stability and Posture Analysis, Differentiated Treatment Recommendations Based on Age Groups, Predictive Analyses for Early Diagnosis and Intervention, Ergonomics and Office Worker Training, and Pre-Therapeutic and Surgical Education Simulations constitute the rationale and objectives of this work. Therefore, this study will be able to meet the necessary hardware and software components for a robotic vertebra device, suitable for the required technology levels and trained personnel education. It will feature a three-dimensional physical model capable of real-time, one-to-one simulation, fully mimicking the natural anatomical structure and movement ability of the spine, thus enabling the creation of a personalized spinal model that is perfectly aligned with real case data.

The application and training platform developed for digital twin-based robotic spine simulation allows for the creation of a digital twin model of either a patient or a healthy individual. This model can physically update vertebra positions on a robotic spine device, enabling visual and haptic (tactile) 3D training and analysis on the robotic spine device. It demonstrates to both the patient and the student where the problematic areas are and how they can be corrected. Additionally, it allows for diagnosis of the potential outcomes of applying necessary physiotherapy movements during the treatment process on the simulator.

For the cervical, thoracic, and lumbar vertebrae, an interface design with movement control arrangements such as axis-centered rotation, lateral bending, and extension/flexion will be used. Position data received by the robotic spine device via communication protocols like Wi-Fi/Bluetooth will physically shape and position the spine accordingly. This allows both educators and students to perform visual and tactile diagnostics on the robotic spine device. Essentially, to mimic the necessary positions on the robotic spine device, micro Stewart platforms placed within different vertebrae provide up to six degrees of freedom for positioning.

Keywords: *Robotic Spine, Digital Twin, Convolutional Neural Network, Experiment Design, Configurable Spinal Deformities, Model-Based Control, Physical Therapy and Rehabilitation Education*

Performance, Exergy and Economic Impacts of Green Hydrogen Blending in NGCC Power Plants in Türkiye

Merve Bozdağ[1], Ahmet Uçar[1,*]

[1]*Ankara Yıldırım Beyazıt University, Faculty of Engineering and Natural Sciences, Department of Energy Systems Engineering, 06010, Ankara, TÜRKİYE*

*Contact: ahmet.ucar@aybu.edu.tr

The decarbonization of electricity generation has become a strategic necessity under regulatory frameworks such as the European Green Deal and the Carbon Border Adjustment Mechanism (CBAM). In Türkiye, Natural Gas Combined Cycle Power Plants (NGCCPPs) play a key role in grid stability, making their low-carbon conversion a priority. Green hydrogen integration offers a promising pathway to reduce emissions while preserving existing power generation infrastructure.

This study presents a comprehensive thermodynamic, exergy, and techno-economic assessment of green hydrogen integration into NGCCPPs in Türkiye. A reference combined cycle power plant equipped with a GE 9F-class gas turbine is analyzed under hydrogen blending scenarios of 0%, 20%, 50%, and 100% by volume. A validated MATLAB-based thermodynamic model is used to evaluate turbine inlet temperature, mass flow rates, net power output, and energy and exergy efficiencies. Environmental impacts are quantified through CO_2 and NO_x emission analyses.

The results indicate that increasing hydrogen content leads to substantial reductions in direct CO_2 emissions, reaching near-zero emissions under full hydrogen operation. Partial blending scenarios achieve significant emission reductions with moderate impacts on efficiency and power output. Exergy analysis confirms that the combustion chamber remains the main source of irreversibility, with hydrogen enrichment modifying the distribution of exergy losses. A techno-economic evaluation performed using RETScreen Expert shows that hydrogen blending can mitigate CBAM-related carbon costs and improve long-term economic performance under realistic carbon pricing scenarios. The findings demonstrate that green hydrogen integration is a technically feasible and economically relevant decarbonization pathway for existing NGCCPPs, supporting Türkiye's net-zero targets while reducing the risk of stranded assets.

Keywords: *Green hydrogen, NGCC power plants, hydrogen blending, exergy analysis, techno-economic assessment, energy transition*

Deep Learning-Based Automatic Modulation Classification Using GRU Networks

Osman Tokluoglu[1*], Emin Keresteci[2]

[1]*Department of Electrical and Electronics Engineering, AYBU, Ankara, TÜRKİYE*

[2]*Department of Computer Engineering, TOBB ETU, Ankara, TÜRKİYE*

***Contact:** otokluoglu@aybu.edu.tr

Abstract— Automatic modulation classification (AMC) plays a critical role in modern wireless communication systems, particularly in non-cooperative scenarios where prior knowledge of the transmitted signal is unavailable. In this study, a gated recurrent unit (GRU)-based deep learning framework is investigated for the classification of digital modulation schemes by exploiting the temporal characteristics of received signals. The proposed approach operates directly on in-phase and quadrature (I/Q) signal representations and aims to learn discriminative features in a data-driven manner without relying on handcrafted feature extraction. The performance of the proposed model is evaluated for BPSK, QPSK, and 16PSK modulation schemes under additive white Gaussian noise (AWGN) channel conditions across a wide range of signal-to-noise ratio (SNR) levels. The obtained results demonstrate that the GRU-based model achieves reliable classification performance, with overall accuracy improving from 55.3% at −10 dB SNR to 98.5% at 15 dB SNR. In particular, the model exhibits strong performance at moderate and high SNR levels, while maintaining reasonable accuracy even under challenging low SNR conditions. These findings suggest that GRU-based architectures provide a promising and computationally efficient solution for modulation classification tasks. The presented results represent an initial step toward more comprehensive studies, including extensions to fading channel environments, additional modulation schemes, and real-time implementations using hardware platforms.

Keywords: Automatic modulation classification (AMC), Automatic Modulation Identification (AMI), Gated Recurrent Unit (GRU), Deep Learning, Modulation Classification, In-Phase/Quadrature (I/Q) Signals, Wireless Communications, Signal Processing, Time-Series Analysis

I. INTRODUCTION

Automatic modulation classification (AMC) is a fundamental component in modern wireless communication systems, enabling adaptive transmission, spectrum monitoring, cognitive radio, and signal intelligence applications [1]. In scenarios where prior information about the transmitted signal is unavailable, accurate identification of the modulation scheme becomes essential for reliable demodulation and efficient spectrum utilization. Traditional AMC techniques can be broadly categorized into likelihood-based and feature-based approaches. Likelihood-based methods, such as maximum likelihood (ML) classifiers, offer optimal performance under ideal conditions but suffer from high computational complexity and sensitivity to model mismatches [2], [3]. On the other hand, feature-based methods rely on expert-designed statistical features, including higher-order cumulants and cyclostationary properties, which reduce computational burden but often exhibit degraded performance in low signal-to-noise ratio (SNR) environments and under channel impairments [4], [5].

In recent years, the rapid advancement of deep learning has led to a paradigm shift in AMC, where data-driven models automatically learn discriminative features directly from raw or minimally processed signals. Early works demonstrated the effectiveness of convolutional neural networks (CNNs) in extracting spatial features from in-phase and quadrature (I/Q) samples [6]. Subsequent studies further improved classification performance by employing deeper CNN architectures and hybrid models combining convolutional and fully connected layers [7]. However, while CNN-based approaches are effective at capturing local patterns, they are inherently limited in modeling long-range temporal dependencies present in communication signals [8].

To address this limitation, recurrent neural networks (RNNs) have been introduced for AMC tasks. These models are designed to capture sequential dependencies in time-series data, making them well-suited for communication signals where temporal correlations carry important modulation-specific information. For instance, a long short-term memory (LSTM)-based AMC framework that extracts robust features from noisy radio signals to efficiently and accurately classify modulation schemes and communication technologies is proposed in [9]. In another study, a hybrid approach employing a dual-stream CNN–LSTM framework for automatic modulation classification that jointly exploits spatial–temporal features and feature interactions from I/Q and amplitude–phase representations to improve performance is proposed in [10].

In this context, gated recurrent unit (GRU)-based architectures offer a promising alternative for modulation classification due to their ability to model temporal dependencies with a relatively simpler structure compared to other recurrent models. Motivated by these advantages, this study investigates the use of a GRU-based framework for automatic modulation identification. By leveraging the sequential characteristics of communication signals, the

proposed approach aims to effectively capture temporal patterns relevant to different modulation schemes while maintaining computational efficiency.

The remainder of this paper is organized as follows: Section II presents the system model and problem formulation. Section III describes the proposed GRU-based modulation identification framework. Section IV provides the simulation setup and discusses the obtained results. Finally, Section V concludes the paper and outlines potential directions for future work.

II. System Model

In this study, the AMC problem is formulated as a supervised classification task, where the objective is to determine the modulation scheme of a received signal from a predefined set of candidates. Specifically, the considered modulation types are Binary Phase Shift Keying (BPSK), Quadrature Phase Shift Keying (QPSK), and 16-Phase Shift Keying (16PSK), which represent commonly used phase modulation techniques with increasing constellation complexity.

A. Transmitted Signal Model

Let $\{a_k\}$ denote the sequence of transmitted symbols drawn from the corresponding modulation constellation. For BPSK, QPSK, and 16PSK, the symbols are defined as complex-valued points on the unit circle, expressed as $a_k = e^{j\theta_k}$, where θ_k represents the phase associated with the selected modulation scheme. Specifically, the phase sets are given by:

- BPSK: $\theta_k \in \{0, \pi\}$,
- QPSK: $\theta_k \in \left\{0, \frac{\pi}{2}, \pi, \frac{3\pi}{2}\right\}$,
- 16PSK: $\theta_k \in \left\{\frac{2\pi m}{16} \mid m = 0,1,\dots,15\right\}$.

The transmitted baseband signal can be written as

$$s(t) = \sum_k a_k g(t - kT), \tag{1}$$

where $g(t)$denotes the pulse shaping filter and $T$is the symbol duration.

B. Channel Model

The transmitted signal propagates through a wireless channel and is impaired by additive noise. In this study, the channel is modeled as an additive white Gaussian noise (AWGN) channel, and the received signal is given by

$$r(t) = s(t) + n(t), \tag{2}$$

where $n(t)$represents complex-valued white Gaussian noise with zero mean and variance σ^2. After matched filtering and sampling at the symbol rate, the discrete-time received signal can be expressed as

$$r_k(t) = a_k(t) + w_k(t), \tag{3}$$

where $w_k \sim \mathcal{CN}(0, \sigma^2)$ denotes the discrete-time noise component.

C. Signal Representation

For deep learning-based processing, the received signal is represented in terms of its in-phase (I) and quadrature (Q) components. Specifically, each received symbol is decomposed as

$$r_k(t) = I_k + jQ_k, \tag{4}$$

where $I_k = \Re\{r_k\}$and $Q_k = \Im\{r_k\}$. A sequence of Nreceived samples is then organized into a two-dimensional input representation given by

$$\boldsymbol{X} = [I_1, Q_1, I_2, Q_2, \dots, I_N, Q_N], \tag{5}$$

or equivalently as an $N \times 2$matrix. This representation preserves the temporal structure of the signal and enables the model to learn modulation-specific patterns from the I/Q components.

D. Problem Formulation

Given the input sequence **X**, the goal of the modulation classifier is to estimate the corresponding modulation label $y \in$ {BPSK,QPSK,16PSK}. This can be formulated as a multi-class classification problem, where a neural network model $f(\cdot)$is trained to learn the mapping $y = f(\boldsymbol{X})$. The model is trained using labeled data generated under different SNR conditions to ensure robustness against noise variations.

III. Proposed GRU-Based Modulation Identification Framework

In this section, the proposed GRU-based modulation identification framework is presented. The overall objective is to exploit the temporal characteristics of the received signal to accurately classify different modulation schemes. The proposed model operates directly on the sequential in-phase and quadrature (I/Q) representation of the received signal and learns modulation-specific patterns in a data-driven manner.

A. Input Representation

As described in Section II, the received signal is represented using its in-phase (I) and quadrature (Q) components. For each sample, a sequence of Nsymbols is considered and arranged as

$$\boldsymbol{X} = \{[I_1, Q_1], [I_2, Q_2], \dots, [I_N, Q_N]\}, \tag{6}$$

which forms an $N \times 2$input matrix. This representation preserves both the amplitude and phase information of the signal while maintaining its temporal structure. Such a formulation is particularly suitable for recurrent neural networks, which are specifically designed to process sequential data by capturing temporal dependencies and correlations between successive samples, thereby enabling the model to effectively learn the underlying structure and dynamic behavior of time-varying communication signals.

B. GRU-Based Architecture

To model the temporal dependencies in the input signal, a neural network architecture based on GRUs is employed. Compared to conventional recurrent neural networks, GRUs incorporate gating mechanisms that help mitigate the vanishing gradient problem and enable more effective learning of long-range dependencies.

As illustrated in Fig. 1, the GRU unit consists of two main gates: the update gate and the reset gate [11]. These gates control the flow of information through the network and determine how much of the past information is retained or updated at each time step. Given an input sequence **X**, the GRU processes the data sequentially and produces a hidden representation that captures the temporal evolution of the signal.

In this study, the proposed architecture consists of one or more stacked GRU layers, followed by a fully connected layer for classification. The GRU layers extract temporal features from the I/Q sequence, while the dense layer maps these features to the corresponding modulation classes.

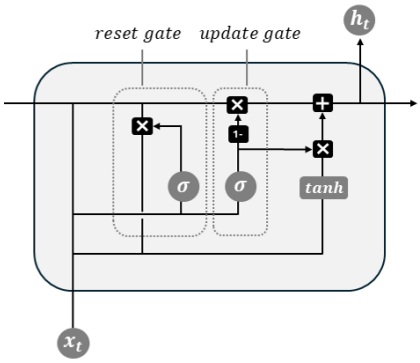

Fig. 1 Structure of a gated recurrent unit (GRU).

C. Classification Layer

The output of the final GRU layer is passed to a fully connected (dense) layer, which performs the classification task. A softmax activation function is used at the output layer to produce the probability distribution over the modulation classes, namely BPSK, QPSK, and 16PSK.

Let **h** denote the feature vector obtained from the GRU layers. The output of the classifier is given by

$$\hat{\mathbf{y}} = softmax(\mathbf{W}\mathbf{h} + \mathbf{b}), \quad (7)$$

where **W** and **b** represent the weights and bias of the dense layer, respectively, and $\hat{\mathbf{y}}$ denotes the predicted probability vector. The final decision is made by selecting the class with the highest probability, as determined by the output of the softmax layer, which assigns a likelihood value to each possible modulation class based on the learned feature representation.

D. Training Procedure

The model is trained in a supervised manner using labeled data generated according to the system model described in Section II. The training dataset includes signals corresponding to different modulation schemes under various SNR conditions to improve the robustness of the model.

The categorical cross-entropy loss function is employed to measure the discrepancy between the predicted and true labels. The network parameters are optimized using a gradient-based optimization algorithm such as Adam.

To enhance generalization performance, the dataset is divided into training and validation sets. The training process is carried out over multiple epochs until convergence is achieved.

IV. Simulation Results

In this section, the performance of the proposed GRU-based modulation identification framework is evaluated. The results are presented in terms of classification accuracy under different SNR conditions.

A. Simulation Setup

The dataset is generated according to the system model described in Section II. The considered modulation schemes include BPSK, QPSK, and 16PSK. For each modulation type, a large number of signal sequences are generated with random symbol realizations.

The transmitted signals are passed through an additive white Gaussian noise (AWGN) channel, and different SNR levels are considered to evaluate the robustness of the model. In this study, the SNR range is selected from $\mathrm{SNR}_{\min} = -10$ to $\mathrm{SNR}_{\max} = 15$ dB with a step size of $\Delta\mathrm{SNR}=5$ dB.

Each received signal is represented using its in-phase (I) and quadrature (Q) components and organized into sequences of length N. The dataset is divided into training, validation, and test sets. The model is trained using the Adam optimizer with categorical cross-entropy loss.

B. Performance Metric

The performance of the proposed model is evaluated using classification accuracy, defined as

$$\text{Accuracy} = \frac{\text{Number of correctly classified samples}}{\text{Total number of samples}}. \quad (8)$$

Accuracy is computed for each SNR level to analyze the behavior of the model under different noise conditions, allowing for a detailed evaluation of its robustness and classification performance as the signal quality varies from highly noisy to relatively clean scenarios, thereby providing a clearer understanding of its performance trends across different SNR regimes.

C. Results and Discussion

The classification accuracy of the proposed GRU-based model under different SNR conditions is presented in Table I.

TABLE I
CLASSIFICATION ACCURACY (%) OF THE PROPOSED GRU-BASED MODEL AT DIFFERENT SNR LEVELS

SNR (dB)	BPSK (%)	QPSK (%)	16PSK (%)	Overall Accuracy
-10	68.5	55.2	42.3	55.3
-5	82.7	71.4	58.6	70.9
0	92.8	85.3	73.9	84.0
5	97.6	93.8	86.5	92.6
10	99.1	97.5	92.8	96.5
15	99.8	99.1	96.7	98.5

As shown in Table I, the classification accuracy improves as the SNR increases, which is consistent with expectations since higher SNR values correspond to less noisy signal conditions and a clearer representation of the underlying modulation patterns. At low SNR levels, the performance degrades noticeably due to the increased difficulty in distinguishing modulation-specific features in the presence of strong noise. In such conditions, the noise components can significantly distort the amplitude and phase information of the received signal, leading to overlapping feature distributions among different modulation classes and consequently reducing classification accuracy.

Among the considered modulation schemes, BPSK generally achieves higher classification accuracy compared to QPSK and 16PSK, particularly at low SNR levels. This behavior can be attributed to the simpler constellation structure of BPSK, which consists of only two distinct symbols with maximum separation in the signal space, making it inherently more robust to noise and distortion. QPSK, while still relatively robust, exhibits slightly lower performance due to its increased constellation density. In contrast, 16PSK demonstrates comparatively lower accuracy, especially in low and moderate SNR regimes, due to its densely packed constellation points. The smaller angular separation between symbols in 16PSK makes it more susceptible to noise and phase variations, thereby increasing the likelihood of misclassification.

As the SNR increases, the performance gap between the modulation schemes gradually decreases, and all classes achieve high classification accuracy at moderate to high SNR levels. This indicates that the model is able to effectively learn and exploit distinguishing features when the signal quality is sufficiently high. Overall, the proposed GRU-based model demonstrates reliable classification performance across a wide range of SNR conditions. The results suggest that the model effectively captures temporal dependencies and modulation-specific patterns, highlighting the potential of GRU-based architectures for modulation classification in practical communication systems.

V. CONCLUSIONS

In this paper, a GRU-based framework for automatic modulation identification has been investigated, focusing on the exploitation of temporal characteristics of communication signals. The obtained results demonstrate that the proposed approach is capable of achieving reliable classification performance for BPSK, QPSK, and 16PSK modulation schemes under AWGN channel conditions. These findings can be considered as an initial step toward understanding the potential of GRU-based models in modulation classification tasks. Future work will focus on extending the proposed framework to more realistic communication scenarios. In particular, the performance of the model under fading channel conditions will be investigated, along with its applicability to a wider range of modulation schemes. Additionally, practical implementations using software-defined radio (SDR) platforms, such as Universal Software Radio Peripheral devices, as well as hardware-oriented solutions including FPGA-based realizations, will be considered to evaluate the feasibility of the approach in real-world environments, with particular attention to real-time processing capabilities, computational efficiency, and deployment constraints in practical communication systems.

REFERENCES

[1] O. A. Dobre, A. Abdi, Y. Bar-Ness, and W. Su, “Survey of automatic modulation classification techniques: Classical approaches and new trends,” *IET Commun.*, vol. 1, no. 2, pp. 137–156, Apr. 2007.

[2] W. Wei and J. M. Mendel, “Maximum-likelihood classification for digital amplitude-phase modulations,” *IEEE Trans. Commun.*, vol. 48, no. 2, pp. 189–193, Feb. 2000.

[3] J. L. Xu, W. Su, and M. Zhou, “Likelihood-ratio approaches to automatic modulation classification,” *IEEE Trans. Syst., Man, Cybern. C, Appl. Rev.*, vol. 41, no. 4, pp. 455–469, Jul. 2011.

[4] A. Swami and B. M. Sadler, “Hierarchical digital modulation classification using cumulants,” *IEEE Trans. Commun.*, vol. 48, no. 3, pp. 416–429, Mar. 2000.

[5] F. -X. Socheleau, “Cyclostationarity of communication signals in underwater acoustic channels,” *IEEE J. Ocean. Eng.*, vol. 50, no. 2, pp. 425–447, Apr. 2025.

[6] T. J. O’Shea, J. Corgan, and T. C. Clancy, “Convolutional radio modulation recognition networks,” arXiv:1602.04105, Feb. 2016.

[7] S. Rajendran, W. Meert, D. Giustiniano, V. Lenders, and S. Pollin, “Deep learning models for wireless signal classification with distributed low-cost spectrum sensors,” *IEEE Trans. Cogn. Commun. Netw.*, vol. 4, no. 3, pp. 433–445, Sept. 2018.

[8] O. Tokluoglu, E. Cavus, E. Bedeer, and H. Yanikomeroglu, "A novel CNN-based standalone detector for faster-than-Nyquist signaling," *IEEE Trans. Commun.*, vol. 73, no. 12, pp. 14316–14331, Dec. 2025.

[9] Z. Ke and H. Vikalo, "Real-time radio technology and modulation classification via an LSTM auto-encoder," *IEEE Trans. Wireless Commun.*, vol. 21, no. 1, pp. 370–382, Jan. 2022.

[10] Z. Zhang, H. Luo, C. Wang, C. Gan, and Y. Xiang, "Automatic modulation classification using CNN-LSTM based dual-stream structure," *IEEE Trans. Veh. Technol.*, vol. 69, no. 11, pp. 13521–13531, Nov. 2020.

[11] O. Tokluoglu, A. Cicek, E. Cavus, E. Bedeer, and H. Yanikomeroglu, "GRU-based sequence detection for faster-than-Nyquist signaling," *IEEE Open J. Veh. Technol.*, vol. 7, pp. 565–581, 2026

Altering Microstructure of High Boron Steels by Conducting Different Heat Treatment Procedures

Ömer Faruk Murathan[1,*], Mehmet Remzi Abul[2]

[1] *Ankara University 1st Organized Industrial Zone Vocational School, Ankara University, Ankara/Sincan, TÜRKİYE*

[2]*Metallurgical and Materials Engineering, Ankara Yıldırım Beyazıt University, Ankara/Keçiöğren, TÜRKİYE*

***Contact:** ofmurathan@ankara.edu.tr

Abstract— Large amount of boron in steels causes extreme hardness (65 HRC or higher) but low toughness (as low as 2J) as a drawback. This prevents the usability of high boron steels in the industry. In order to enhance the toughness, heat treatment is the fastest and cheapest method. In this paper; estimation of austenitizing temperature, effect of quenching, full annealing and isothermal heat treatments conducted separately on boron added as cast steels that contains 0.48, 1.18, 2.05 and 4.75 wt.% boron. Scanning Electron Microscope (SEM) was used in order to characterize microstructure of the constituents; matrix and secondary phases. X-ray diffraction method was used in order to differentiate the difference between as-cast and heat treated secondary phases. Finally; macrohardness, Charpy impact test and dry sliding wear tests conducted to evaluate the mechanical properties of the samples. Experimental results showed that; the mechanical properties of the boron steels directly controlled by microstructure of the constituents. While the matrix can be modified by the heat treatment methods, secondary phases remained intact. Depending on the volume fraction of boron, the shape and distribution of the borides/carboborides changes. Up to 1200ºC, as the austenitizing temperature increases, the macrohardness of the specimens increases as well. When compared with each other; quenching, full annealing and isothermal heat treatments, macrohardness and Charpy toughness results showed 10% difference and dry sliding wear resistance results were identical since the unaltered borides/carboborides control the wear resistance of the alloys. In addition, specimens were as-cast condition, therefore residual stresses formed during casting and machining steps were relieved after every heat treatment step which explains the enhancement of toughness results as well.

Keywords: Carboboride, Grain Size**,** High Boron Steel, Heat Treatment,

I. INTRODUCTION

The main aim of boron addition (ppm) in steels is to increase hardenability without the need of known alloying elements (wt. %). While boron blocks the formation of ferrite which helps the formation of martensite, the solubility of boron is extremely low as well. In addition, boron forms secondary phases called borides/carboborides that are extremely hard and fragile [1, 2]. As the amount of boron increases; volume fraction, shape of the borides/carboborides change. However, toughness lowered drastically while the hardness keeps rising.

High boron steels do not have a place in steel standards due to lack of toughness and extremely high hardness drawbacks. In addition, not many researchers conducted different heat treatments as well as different secondary manufacturing procedures. Most researchers focused on the wear properties of high boron steels [3, 4], while other researchers [5-9] conducted researches on the formation of microstructure and its compounds.

This paper focuses on the effect of different heat treatments on high boron steels. For this aim; estimation of austenitizing temperature, quenching, full annealing and isothermal heat treatments conducted separately. X-Ray diffraction, Scanning Electron Microscopy (SEM) and Optical Microscopy was utilized for microstructure identification. In order to understand the effect on the mechanical properties, the specimens were subjected to Charpy test, macrohardness test, and dry sliding wear test.

II. EXPERIMENTAL

The chemical composition of the as cast boron free specimens is shown in Table 1, results obtained by using Bruker Q4-Tasman spectrometer.

TABLE 1
CHEMICAL COMPOSITION OF BORON FREE SPECIMEN (WT.%)

C	Si	Mn	Cr	Cu	Ti	Ni	S	P	Fe
0.485	0.434	1.024	11.15	0.436	0.178	0.141	0.0048	0.0075	Rem.

Table 2 shows the results of boron content of the as cast specimens by analysing with ICP-OES in METU Laboratory. Before casting, melt was fed by aluminium wires and Fe-Ti in order to prevent formation of BN and TiB phases.

TABLE 2
CHEMICAL COMPOSITION OF BORON ADDED SPECIMENS

Designed wt.% B	Final Result
0.5	0.48 ± 0.01
2.0	2.05 ± 0.02
5.0	4.75 ± 0.10

A. Austenitizing, Quenching and Full Annealing Heat Treatments

Since the cast composition is not standard, some pilot tests were conducted in order to decide the austenitizing temperature. For this purpose, specimens containing 1.18 wt.% B was used. Between 800-1200ºC for 60 minutes, by increasing 50ºC, microstructure analysis and macrohardness tests conducted in order to obtain optimal austenitizing temperature. Lowest and highest points were chosen after conducting DTA analysis. After deciding austenitizing temperature, quenching (cooling in water) and full annealing (cooling in furnace) heat treatments conducted.

B. Isothermal Heat Treatment

In order to obtain the temperature of the bainite transformation, quench dilatometer was used on the specimen that contains 2.05 wt.% B. To create CCT and TTT diagrams, JMatPro was utilised. For this calculation, chemical composition and austenite grain size was required.

C. Sample Preparation

As cast samples obtained from the bottom of Y blocks having DIN1683 –GTB18/5 standard. Before cutting with EDM, chill zones were eliminated by machining 2mm in depth. According to ASTM A23 [10], Charpy impact specimens were prepared having non-notched with 10x10x55mm size specifications. After mechanical tests, specimens were cut from non-deformed parts having 10x10x10mm in size. Heat treatment procedure were conducted; after austenitizing (at 1150ºC for 60 minutes), specimens cooled in water (quenching), specimens cooled in furnace (full annealing) and held in salt bath for prolonged times (isothermal heat treatment, 380ºC for 96 hours).

For both as cast and heat treated specimens grinded up to 1200 mesh grit, polished to 3µm single crystal diamond suspension and etched by RALPH [11] etchant.

Hardness tests (Emco Test Duravision 2000, 5 different spots), Charpy impact tests (Instron-WolpertPW30) and pin on disc wear tests (10 N load, 220 mesh alumina sandpaper, 40 m sliding distance with 1.5 m/s sliding speed) according to ASTM G99 were conducted.

III. RESULTS AND DISCUSSION

Figure 1 shows the microstructure of the as cast specimens. As cast matrix is martensite + unknown amount of retained austenite as it was not possible to calculate by using metallurgical methods only. However, X-RD showed the presence of retained austenite (Figure 2). As the boron content increases more than 2.05 wt.% B, shape (fishbone to rodlike) and the distribution (network to irregular) of the secondary phases changes as well (Figure 1). Similar results were obtained by different researchers as well [1, 2 and 6-9].

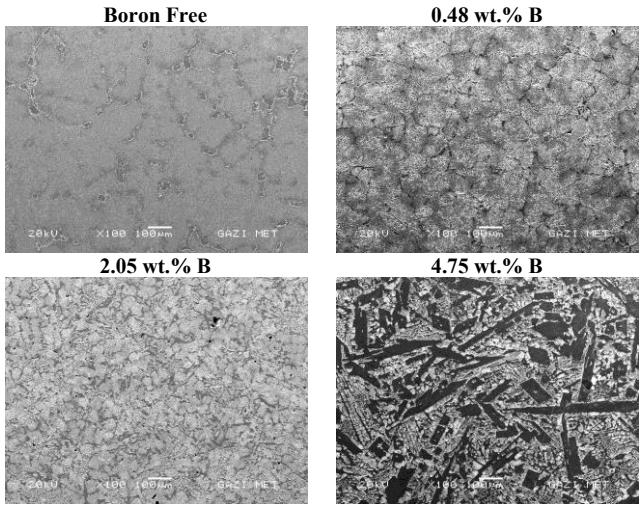

Fig. 1 SEM micrographs of as cast specimens

In addition, higher boron contents changed the matrix-secondary phase phenomenon as 4.75 wt.% B specimen consists of 69% ± 4 secondary phases distributed over the matrix (five different micrographs analysed by Leica Application Suit). Moreover, X-RD peaks showed that boron/borides embedded in chromium carbides as well.

Table 3 shows the mechanical properties of as cast specimens. As the boron content increases, the macrohardness and wear resistance of the boron added specimen increases while the Charpy results affected negatively. Boron has a low solubility (ppm) in microstructure (for both in ferrite and austenite) which causes the formation of borides, carboborides (chromium carbide + boron/boride) having sharp corners which were embedded in matrix. Those secondary phases alters the microstructure and hence the mechanical properties.

TABLE 3
MECHANICAL TEST RESULTS OF AS CAST SPECIMENS

Boron (wt.%)	HRC	Charpy Test (J)	Wear Loss (mg)
-	51.8 ± 1.4	7.6 ± 0.6	0.21 ± 0.02
0.48	54.6 ± 1.1	4.3 ± 0.6	0.19 ± 0.03
2.05	60.2 ± 0.1	3.3 ± 0.6	0.12 ± 0.00
4.75	66.3 ± 0.5	2.0 ± 0.2	0.06 ± 0.01

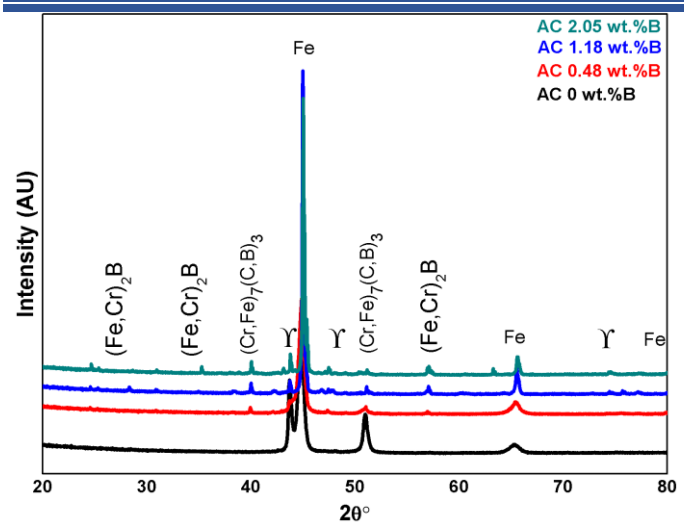

Fig. 2 X-RD results of as cast specimens

A. Austenitizing Heat Treatment

Figure 3 shows the hardness results of austenitization of 1.18 wt.% B specimen. As the austenitizing temperature increases, the hardness increases as well. However at 1200ºC specimen starts to deform due to extreme heat. In addition, DTA showed that, specimen starts to melt at 1400ºC. This shows that, austenitizing temperature should not exceed 1200 ºC.

While the detection of retained austenite (RA) is not possible, it is well known that amount of RA lowers the mechanical properties of steels therefore increase in hardness is directly controlled by the elimination of RA in the matrix. Higher austenitizing temperatures eliminated RA which affected the hardness positively [12, 13].

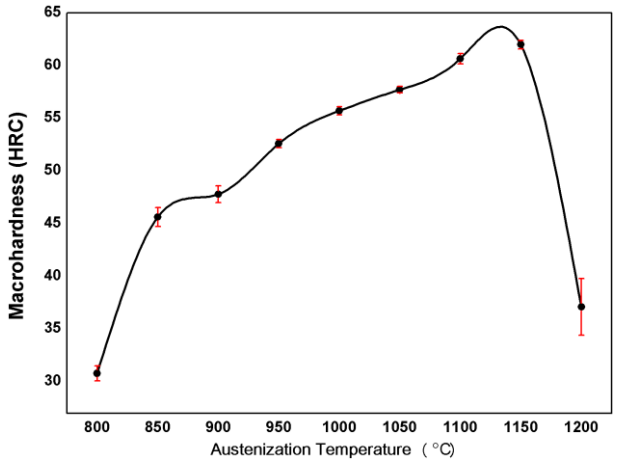

Fig. 3 Macrohardness values of austenized 1.18 wt.% B specimen

B. Quenching Heat Treatment

Figure 4 shows the microstructure of the as cast and quenched (austenized at 1150ºC for 60 minutes) specimen having 1.18 wt.% B. It is obvious that, shape and distribution of secondary phases unchanged. In addition, matrix is also martensite as well. However when the macrohardness results compared, quenched specimen (61.99 ± 0.39 HRC) showed more than 10% improvement when compared with as cast specimen (55.38 ± 1.59 HRC). After quenching, it is believed that the change in the RA fraction, elimination of residual stresses formed during casting and machining steps is the main reason for this improvement.

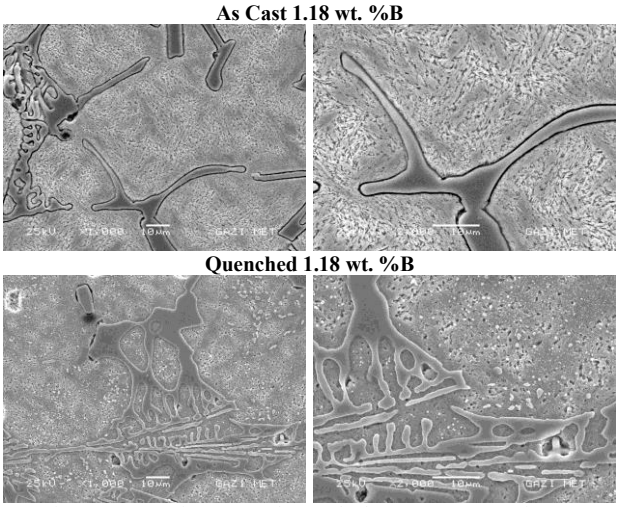

Fig. 4 Microstructure of as cast and quenched 1.18 wt. %B specimens

C. Isothermal Heat Treatment

Table 4 shows mechanical properties of isothermal heat treated boron added specimens. When compared with as cast specimens: hardness and impact toughness values were increased however there is no significant change on wear resistance of the specimens.

TABLE 4
MECHANICAL TEST RESULTS OF ISOTHERMAL HEAT TREATED SPECIMENS

Boron (wt.%)	HRC	Charpy Test (J)	Wear Loss (mg)
-	58.3 ± 0.3	12.0 ± 1.4	0.23 ± 0.04
0.48	59.0 ± 0.0	8.00 ± 0.7	0.20 ± 0.01
2.05	61.2 ± 0.6	7.00 ± 0.7	0.12 ± 0.03
4.75	65.8 ± 0.8	4.00 ± 0.0	0.06 ± 0.01

Previous heat treatment results showed that, martensitic matrix and secondary phases (chromium carbides, borides and carboborides) unaltered however RA and their percentages to each other could not be calculated. Therefore, this results shows that change in RA, microstructure fractions and residual stresses has an effect on the mechanical properties not more than 10%. In addition, this also shows that the wear properties of high boron steel controlled by secondary phases as the soft phase which is

martensite when compared with grinding paper oxide layer and secondary phases, worn out first and while the test continues much more harder secondary phases almost unchanged.

D. Full Annealing

After full annealing, matrix of the specimens changed martensite to ferrite while the secondary phases were unchanged (Figure 5).

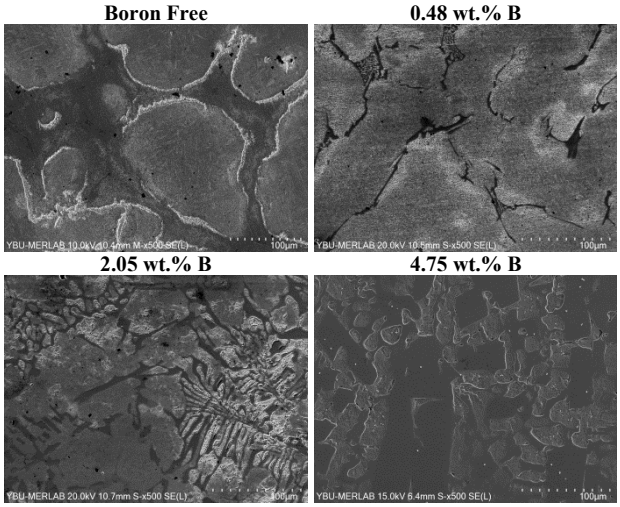

Fig. 5 Microstructure of full annealed specimens

Due to this change; depending on the boron content, macrohardness values majorly altered however impact toughness and wear resistance were identical when compared with isothermally heat treated samples (Table 5).

Ferritic matrix, which is softer than martensitic matrix did not have a major drawback on the wear resistance of the specimens. This also shows that, secondary phases mainly control this mechanical property.

As the boron content increases, secondary phases act as a matrix due to higher distribution which also controls the macrohardness as well. Because of this, 25% loss in hardness for the specimen having 4.75 wt.% B observed while rest of the specimens lowered more than 50%.

As cast or heat treated specimens (including full annealing), fracture type was cleavage fracture due to unmodified, extremely hard, sharp/fragile secondary phases. In addition, wear type was abrasive as well.

TABLE 5
MECHANICAL TEST RESULTS OF FULL ANNEALED SPECIMENS

Boron (wt.%)	HRC	Charpy Test (J)	Wear Loss (mg)
-	19.7 ± 2.2	11.0 ± 0.7	0.22 ± 0.01
0.48	25.8 ± 0.6	7.00 ± 0.6	0.21 ± 0.01
2.05	27.0 ± 1.3	6.40 ± 0.7	0.16 ± 0.01
4.75	50.4 ± 1.1	4.50 ± 0.7	0.12 ± 0.03

IV. CONCLUSIONS

Following conclusions can be drawn from the estimation of austenitizing temperature, effect of quenching, full annealing and isothermal heat treatments applied on high boron steels.

As cast boron added specimens having 11.65 wt.% Cr matrix consists of martensite while the borides embedded in chromium carbides which formed carboborides.

Up to 2.05 wt.% boron, secondary phases having fishbone structure distributed in networks over the matrix, above that boron content secondary phases changed their shape to rodlike with irregular distribution over the matrix.

Specimen having 1.18 wt.% B starts to melt at 1400ºC from DTA results and the austenitization temperature should not exceed 1200ºC as the alloy starts deforming due to extreme heat.

As the austenitization temperature increases, macrohardness of the specimen increases as well. This is attributed to elimination of retained austenite and residual stresses formed during manufacturing the alloy/specimens.

Microstructure and mechanical properties after normalizing (air cooling after austenitization), quenching and isothermal heat treatments were identical when compared each other however improvements were obvious when compared with as cast condition.

Full annealing negatively affected the macrohardness results however wear properties almost unchanged which shows that wear resistance is directly controlled by secondary phases as the applied heat treatments had no effect on secondary phases.

All specimens showed cleavage fracture, even full annealing did not alter this which was caused by sharp/fragile secondary phases. Wear type was abrasive.

ACKNOWLEDGMENT

The authors gratefully acknowledge financial support from the Gazi University (07/2018-06) and Ankara University (FBA_2024_3064) Scientific Research Projects (BAP). The authors are grateful to Caner Şimşir for Quench Dilatometer/JMatPro analysis and Middle East Technical University (METU) for ICP-OES analysis.

REFERENCES

[1] Staff, I.S.o.B.S., S.K. Banerji, and J.E. Morral, Boron in Steel: Proceedings of the International Symposium on Boron Steels - Sponsored by the TMS-AIME Heat Treatment and Ferrous Metallurgy Committees at the Fall Meeting of the Metallurgical Society of AIME, Milwaukee, Wisconsin, September 18, 1979. Books on Demand.

[2] Llewellyn, D. and W. Cook, *Metallurgy of boron-treated low-alloy steels.* Metals Technology, 1974. **1**(1): p. 517-529.

[3] Fu, H., Z. Wu, and J. Xing, Investigation of quenching effect on mechanical property and abrasive wear behaviour of high boron cast steel. materials science and Technology, 2007. **23**(4): p. 460-465.

[4] Fu, H.-g., D.-m. Fu, and J.-d. Xing, *Investigations on the cast boron steel guide roller and its application in steel wire-rod mill.* Materials and Manufacturing Processes, 2008. **23**(2): p. 123-129.
[5] Fu, H.-g., et al., *A Study on the Wear Behavior of Cast Boron Steel.* Journal of materials engineering and performance, 2011. **20**(9): p. 1665-1670.
[6] Egorov, M., Y.L. Sapozhnikov, and Y.V. Shakhnazarov, *Effect of carbon content on the structure, hardness, and thermal stability of boron-chromium cast steels.* Metal Science and Heat Treatment, 1989. **31**(5): p. 387-391.
[7] Ma, S., et al., *Effect of chromium concentration on microstructure and properties of Fe–3.5 B alloy.* Materials Science and Engineering: A, 2010. **527**(26): p. 6800-6808.
[8] Lentz, J., A. Röttger, and W. Theisen, *Solidification and phase formation of alloys in the hypoeutectic region of the Fe–C–B system.* Acta Materialia, 2015. **99**: p. 119-129.
[9] Lv, Z., et al., *Microstructure and crystallography of borides and mechanical properties of Fe–B–C–Cr–Al alloys.* Journal of Alloys and Compounds, 2016. **662**: p. 54-62.
[10] Standard, A., E23-09: Standard Test Method for Notched Bar Impact Testing of Metallic Materials, Annual Book of ASTM Standards. 2009.
[11] E407-07, A., *Standard practice for microetching metals and alloys*. 2015, ASTM International West Conshohocken, PA.
[12] Bhadeshia, H. and R. Honeycombe, *Steels: microstructure and properties*. 2017: Butterworth-Heinemann.
[13] Krauss, G., *Steels: processing, structure, and performance*. 2015: Asm International.

Comparative Performance Analysis of NIST PQC Standards: From STM32 Software Limitations to FPGA-SoC Acceleration

Mustafa Akif Yildirim[1,*], Osman Tokluoglu[1]

[1] *Department of Electrical and Electronics Engineering, AYBU, Ankara, TÜRKİYE*

***Contact:** yildirim.makif20@gmail.com

***Abstract*—The rapid advancement of quantum computing poses a significant threat to classical public-key cryptographic systems, necessitating the transition to Post-Quantum Cryptography (PQC). This study investigates the implementation challenges of NIST-standardized signature schemes on resource-constrained embedded hardware. We present a comparative analysis of SPHINCS+ and CRYSTALS-Dilithium on an ARM Cortex-M4 (STM32F407G) microcontroller. Our findings reveal that SPHINCS+ is practically unusable in this software-only environment, with impractical execution times. Furthermore, the reference Dilithium implementation failed to execute entirely on the MCU due to severe RAM and timing constraints. To overcome these hardware limitations, we integrated a hardware-accelerated Dilithium core onto a Xilinx Zynq-7000 ZedBoard SoC. By implementing a specialized Number Theoretic Transform (NTT) accelerator in the FPGA fabric, we achieved successful execution with performance rates for key generation and signature generation at millisecond levels. These results demonstrate that while pure software PQC is non-viable for standard microcontrollers, a hardware-software co-design approach provides the necessary efficiency for quantum-resistant embedded systems.

Keywords: *CRYSTALS-Dilithium, Embedded Security, FPGA Acceleration, Hardware-Software Co-design, Lattice-Based Signatures, Number Theoretic Transform (NTT), Post-Quantum Cryptography (PQC), SoC, SPHINCS+, STM32*

I. Introduction

Large-scale Quantum Computing has the potential to pose a threat to the current global cryptographic infrastructure, as theorized by Nielsen and Chuang [1]. The mathematical backbone of RSA and ECC can be solved via Shor's algorithm utilizing integer factorization and discrete logarithm problems in polynomial time by a powerful quantum processor [2], [3], [8]. This vulnerability has caused a paradigm shift toward Post-Quantum Cryptography (PQC), led by the National Institute of Standards and Technology (NIST) in 2016 [4].

In this paper, we focused on two digital signature schemes, CRYSTALS-Dilithium and SPHINCS+. These methods have different mathematical approaches: lattice-based and hash-based cryptography [5], [6]. These algorithms are resilient against "Store Now, Decrypt Later" (SNDL) attacks for post-Quantum era.

Nowadays, global cryptographic infrastructure relies on embedded solutions. PQC methods, on the other hand, are a new challenge for embedded systems. Platforms such as the ARM Cortex-M architecture often lack the necessary hardware requirements to manage high-degree polynomial multiplications of Dilithium or hypertree structures of SPHINCS+ [7].

This paper presents a comparative performance analysis of these NIST standards. We first documented the problems encountered when attempting software-only implementations on an STM32F407G MCU, where SPHINCS+ latencies reached around 10 minutes and Dilithium completely failed due to memory restrictions. Then, we demonstrated a successful new design based on hardware-software co-design, utilizing the Xilinx Zynq-7000 SoC for hardware acceleration [12]. Our results prove that for real-time embedded applications, hardware acceleration is not a mere optimization but a functional necessity.

This paper is organized as follows: Section II reviews the background of lattice-based and hash-based signature schemes, along with related work about hardware acceleration. Section III details the methodology and experimental setup for both the MCU and SoC platforms. Section IV provides the implementation details, and Section V presents the comparative results and discussion. At the end, Section VI concludes the paper.

II. Foundations of PQC and Hardware Implementations

This section outlines the mathematical foundations of the selected NIST standards, CRYSTALS-Dilithium and SPHINCS+, focusing specifically on the computational bottlenecks they introduce. Furthermore, it reviews the limitations of resource-constrained environments and the current landscape of hardware acceleration, highlighting why System-on-Chip (SoC) architectures are suited to address these cryptographic constraints.

A. CRYSTALS-Dilithium and Lattice-Based Security

CRYSTALS-Dilithium is a digital signature scheme based on the Module Learning with Errors (MLWE) problem [5]. Its security is derived from the shortest vector problem in

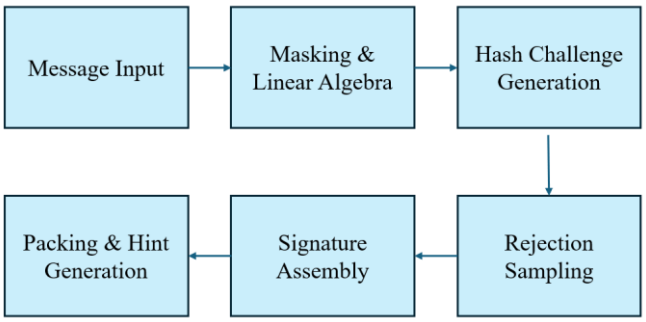

Fig. 1 Dilithium signing procedure.

lattices, which remains hard for both classical and quantum computing capabilities. The primary bottleneck in Dilithium is the multiplication of high-degree polynomials, typically optimized using the Number Theoretic Transform (NTT) to reduce complexity [12]. Despite these optimizations, the memory footprint remains significant; as documented in the NIST specifications, even Level 2 security requires substantial stack space for coefficient storage [5]. Fig. 1 is a schematic presenting the application steps of the CRYSTALS-Dilithium scheme.

The CRYSTALS-Dilithium signing process starts by taking the message and the private key, applying a random mask, and using the Number Theoretic Transform (NTT) to perform matrix-vector multiplications that hide the key. This masked data is combined with the message and hashed to generate a challenge string. To prevent the secret key from leaking, the algorithm uses rejection sampling—if the coefficient sizes fall outside strict security bounds, it throws them out and restarts the masking step. Once an iteration passes this check, the valid vectors are assembled into the signature and bit-packed with cryptographic "hints" so the verifier can reconstruct the matrices without needing the full uncompressed data.

B. SPHINCS+ and Stateless Hash-Based Frameworks

SPHINCS+ is a stateless hash-based signature scheme, evolving from the original SPHINCS design to improve security, reduce signature sizes, and optimize parameter sets for various performance trade-offs [6], [10]. It relies on a Merkle tree structure composed of Winternitz One-Time Signatures (WOTS+) and Forest of Random Subsets (FORS) few-time signatures [9]. Its primary advantage is its minimal security assumptions—requiring only a secure hash function—but this comes at the cost of high computational density. Research by Niederhagen et al. has explored "streaming" signatures to optimize memory constraints, yet the signing process remains prohibitively slow on low-power microcontrollers [7].

The SPHINCS+ signing process starts by heavily hashing the input message to create a digest and an index, which determines the exact path through its hyper-tree structure. The message digest is first signed at the bottom layer using the Forest of Random Subsets (FORS) scheme. The public key

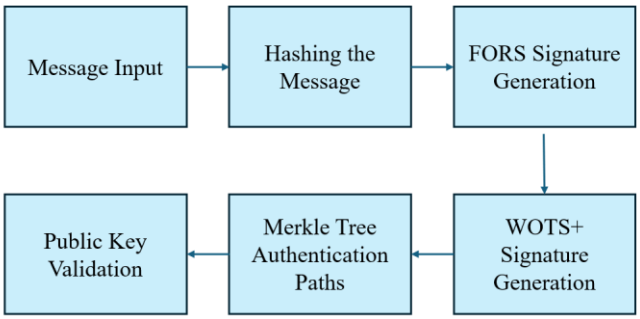

Fig. 2 SPHINCS+ signing procedure.

outputs from FORS are then signed using the Winternitz One-Time Signature (WOTS+) algorithm. Finally, the algorithm calculates the Merkle tree authentication paths to link these WOTS+ signatures all the way up to the main root node. The final signature package simply contains the FORS signature, the WOTS+ signatures, and the full sequence of authentication paths needed to verify it against the globally trusted public key.

C. Challenges in Resource-Constrained Environments

The use of PQC on MCUs is a rapidly growing field of research. Previous studies on ARM Cortex-M4 platforms have shown that while verification can often be performed within acceptable time bounds, key generation and signing frequently exceeded the capabilities of general-purpose MCUs [7]. Memory-restricted devices face a particular challenge with Dilithium, storing both the operating system/application stack and the large intermediate buffers required for polynomial arithmetic in their SRAMs.

D. Hardware Acceleration and the ZYNQ Architecture

Today's requirements demand not only high performance but also strong security guarantees, making the use of hardware accelerators increasingly essential in modern systems. Computationally intensive cryptographic operations such as hashing and Number Theoretic Transform (NTT) benefit significantly from parallel execution capabilities that are difficult to achieve efficiently on general-purpose processors alone. In this context, the use of Field Programmable Gate Arrays (FPGAs) provides a highly flexible and powerful solution for mitigating the bottlenecks of both lattice and hash-based schemes [13], as they enable the design of specialized hardware architectures tailored for parallelization and pipelining of these critical operations.

FPGAs allow designers to exploit fine-grained parallelism and optimize data paths, resulting in substantial improvements in throughput and latency. A notable example is the recent work on the CityUHK-CALAS architecture, which demonstrates an effective partitioning strategy between the Programmable Logic (PL) and the Processing System (PS) within a System-on-Chip (SoC) platform such as the

Xilinx Zynq-7000. In this approach, low-level computational primitives, including hashing and NTT operations, are offloaded to the PL, where they can be executed in parallel with high efficiency. Meanwhile, higher-level protocol logic and control mechanisms are handled by the PS, which provides greater flexibility and ease of implementation.

This division of responsibilities not only leverages the strengths of both hardware and software components but also significantly reduces overall system latency. By carefully balancing the workload between PL and PS, the architecture achieves a more efficient utilization of resources and enhances performance without compromising security. Consequently, such co-design approaches represent a promising direction for developing optimized platforms capable of meeting the stringent requirements of next-generation secure and high-performance applications [12].

III. Methodology and Experimental Setup

The assessment of NIST PQC standards was conducted across two distinct branches of hardware. This dual-phase approach revealed the performance complications on general purpose MCUs and the major gains on the specialized hardware acceleration.

A. Microcontroller Application: STM32F407G

In this stage, the STM32F407G-DISC1 board was utilized to evaluate an affordable embedded solution. The processor of this platform is 32-bit ARM Cortex-M4 core operating at 168 MHz. The memories of this microcontroller are 192 KB SRAM and 1 MB of FLASH memory.

Fig. 3 STM32F407G-DISC1 Board.

Target algorithms implemented here are the reference implementations for CRYSTALS-Dilithium and SPHINCS+ to establish a standard-compliant baseline. The objective was to assess the feasibility of the unmodified, software-only algorithms within strict memory boundaries, without applying any hardware-specific optimizations or algorithmic simplifications. The board that has been used in the setup can be seen in Fig. 3. This setup allows for a realistic evaluation of how such algorithms would perform in practical embedded environments under constrained resource conditions.

B. HW-SW Co-Design: ZYNQ-7000 SoC

In order to overcome the limitations encountered in the previous phase, the project was migrated to the Xilinx Zynq-7000 ZedBoard (XC7Z020) platform, which is illustrated in Fig. 4.

Fig. 4 Zedboard ZYNQ 7000 Board.

The architecture of this platform provides a Processor System (PS) –a dual core ARM Cortex-A9– and a Programmable Logic (PL) equivalent to an Artix-7 FPGA fabric. We adopted an architecture called CityUHK-CALAS, a high performance configurable HW-SW co-design developed for CRYSTALS-Dilithium [12]. The design has been partitioned as the PL to target the offloading of the computationally heavy side of the CRYSTALS-Dilithium like Number Theoretic Transform (NTT), Inverse NTT (INTT) and Keccak-based hashing operations. The PS was aimed at managing memory constraints and higher-level requirements.

IV. Implementation Details

This section details the execution of both testing phases. First, we examine the specific memory and timing bottlenecks encountered when porting the unmodified PQC algorithms to the bare-metal STM32 microcontroller. Following this failure analysis, we detail the hardware-software co-design strategy on the Zynq-7000, explaining how the AXI protocols were configured to successfully offload the heavy arithmetic from the ARM processor to the FPGA fabric.

A. Analysis of Software Implementation Failures on STM32

Porting the NIST standards to the Cortex-M4 revealed some mismatches between hardware resources and heavy algebraic requirements of PQC methods. Due to this it is shown that most of the standard microcontrollers cannot be used. It is also noteworthy that STM32 has a list of

cryptography methods that are implementable for STM platforms [11].

Stack Overflow (CRYSTALS-Dilithium): Dilithium relies on the Module Learning with Errors (MLWE) problem, which requires large local arrays for polynomial coefficients and intermediate transform buffers during key and signature generation [5]. On the other hand, STM32F4 had 192KB of SRAM which was not enough for Dilithium. It is noteworthy that algorithms working with the on-the-fly principle to reduce the RAM requirements are excluded.

Computational Latency (SPHINCS+): SPHINCS+ utilizes a Merkle tree structure composed of Winternitz One-Time Signatures (WOTS+) and Forest of Random Subset (FORS) [6]. The scheme successfully executed through signature and key generation without exceeding memory limits taking around 10 minutes for each step. On the verification process requiring thousands of hash function evaluations, the system collapsed. Lacking the dedicated hardware for hashing functions caused the SPHINCS+ execution to fail during the verification step. These findings prove that STM32F4 cannot run PQC algorithms as an embedded system, which is also shown on the website of ST Microelectronics [11].

B. FPGA Integration and AXI Logic

The successful acceleration on the ZYNQ-7000 relies on a module parallelization of the arithmetic primitives using the CityUHK-CALAS core [12].

Modular Acceleration: The hardware core features a highly optimized butterfly unit for NTT/INTT polynomial multiplication alongside a dedicated PRNG module with an SHA-3/Keccak core for sampling coefficients.

Inter-Processor Communication: To prevent data bottlenecks and synchronization issues between PS and PL, AXI protocols were used. The AXI4-Lite interface was used for transmitting control signals, while high-performance AXI4-Stream ports were used for the data transfer of public keys, messages and signature buffers.

Execution Flow: The system acts as a true co-processor model. The ARM core executes the top-level state machine, handling message formatting and high-level protocol logic. The FPGA side is triggered only when intensive mathematical blocks are required. Thereby, the latency of complex lattice arithmetic is masked.

Fig. 5 illustrates the top-level hardware-software co-design architecture implemented on the Zynq-7000 SoC [12]. The system is distinctly partitioned into two domains: the Processing System (PS) and the Programmable Logic (PL). The ARM-based PS acts as the master controller, managing the top-level state machine and message formatting. The computationally intensive cryptographic primitives—specifically the NTT/INTT polynomial multipliers and the Keccak/SHAKE hashing modules—are offloaded to the PL fabric as a dedicated hardware accelerator. To ensure efficient communication without bottlenecking the system, the architecture utilizes Advanced eXtensible Interface (AXI) protocols. AXI-Lite is employed for lightweight control signals and register configuration, while high-performance AXI-Stream interfaces, managed via Direct Memory Access (DMA), handle the rapid transfer of bulk data such as public keys and signature buffers.

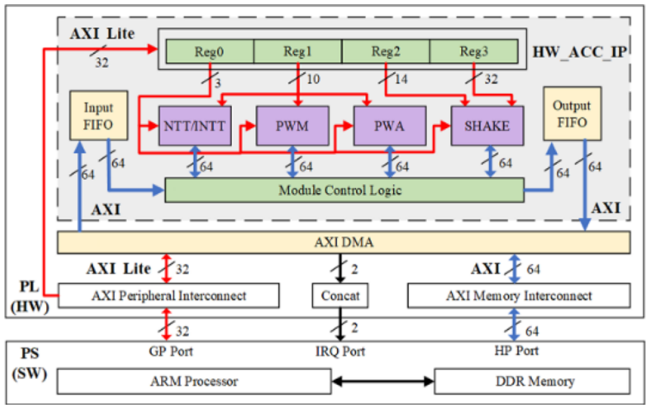

Fig. 5 The top-level SW/HW co-design SoC architecture.

V. Results and Performance Analysis

The evaluation and results clearly show that the operational boundaries of microcontroller-based PQC favor performance advantages of hardware acceleration. The metrics presented reflect the average execution times observed during testing.

As shown in the detailed results in Table I, both algorithms encountered critical bottlenecks related to hardware architecture.

TABLE I
PERFORMANCE RESULTS FOR STM32F407G-DISC1

PQC Method	Duration of		
	Key Generation	Signature Generation	Verification
SPHINCS+	~10 minutes	~10 minutes	N/A
Dilithium	N/A	N/A	N/A

The failure of CRYSTALS-Dilithium is directly caused by its MLWE foundation and 192 KB SRAM capacity. The memory footprint rapidly exceeded the SRAM capacity of the STM32F4 and resulted in a stack overflow situation at the initial stages. Also, while SPHINCS+ is a stateless scheme that avoids massive polynomial arrays, its reliance on thousands of iterative hash function calls for Merkle tree created a massive computational bottleneck [6]. Lacking hardware-level hashing acceleration, the Cortex M4 required approximately 20 minutes to generate signatures and keys, then collapsed during verification.

The migration to the ZYNQ-7000 SoC eliminates the memory overflows and computational bottlenecks observed in Phase 1. With an optimized approach, excellent results have been achieved compared to STM32F4. NTT and Keccak hashing have been offloaded to the FPGA fabric via the

CityUHK-CALAS architecture [12], resulting in the results given in Table II.

TABLE II
PERFORMANCE RESULTS FOR ZEDBOARD – ZYNQ-7000

PQC Method	Duration of		
	Key Generation	Signature Generation	Verification
Dilithium	1.109 ms	5.94 ms	1.17 ms

The results of this study clearly demonstrate that standard microcontroller architectures are under-equipped to handle the mathematical density and complexity of PQC methods. The STM32F407G suffered from immediate stack overflows during Dilithium execution due to its 192 KB SRAM limit, indicating that the available memory is insufficient for handling the intermediate data structures required by lattice-based computations. Similarly, the hash-heavy SPHINCS+ algorithm resulted in impractically long execution times of approximately 10 minutes, making it unsuitable for time-critical embedded applications.

On the other hand, offloading the Number Theoretic Transform (NTT) and Keccak hashing operations to the PL on the Zynq-7000 SoC radically changed system performance. By mitigating the computational bottlenecks of lattice-based schemes, execution times were reduced to the millisecond range. This stark performance gap indicates that software-only PQC implementations are insufficient for resource-constrained devices. Emerging quantum threats necessitate the adoption of these complex algorithms, and hardware dedicated cryptographic processors will become a necessity for secure embedded and larger systems.

VI. CONCLUSION

This study investigated the practical challenges associated with migrating to NIST Post-Quantum Cryptography standards within resource-constrained embedded systems. Our baseline implementation on the STM32F407G microcontroller demonstrated that conventional 32-bit architectures are vulnerable to issues such as stack overflows in lattice-based schemes like CRYSTALS-Dilithium and high computational latency in hash-based schemes such as SPHINCS+. These findings indicate that purely software-based approaches on low-power embedded platforms are insufficient to meet the stringent performance and reliability requirements of next-generation cryptographic standards. To overcome these limitations, a second implementation was performed on the Xilinx Zynq-7000 System-on-Chip, enabling a hardware-software co-design approach in which computationally intensive primitives—particularly the Number Theoretic Transform (NTT) and Keccak hashing functions—were offloaded to the FPGA fabric for parallel and pipelined execution, while higher-level protocol logic was handled by the processing system. This architecture effectively leveraged the strengths of both domains, eliminating memory bottlenecks and significantly reducing execution latency to the millisecond level. Overall, the results highlight the necessity of heterogeneous computing architectures for efficient deployment of post-quantum cryptographic algorithms in embedded systems, demonstrating that FPGA-accelerated solutions provide a scalable and high-performance alternative to traditional microcontroller-based implementations. As a direction for future work, further optimization of FPGA resource utilization and power consumption, extension of the framework to additional post-quantum schemes, and evaluation of side-channel attack resistance are important steps toward achieving more robust and practical implementations.

REFERENCES

[1] M. A. Nielsen and I. L. Chuang, *Quantum Computation and Quantum Information*. Cambridge, UK: Cambridge University Press, 2010.

[2] N. S. Yanofsky and M. A. Mannucci, *Quantum Computing for Computer Scientists*. Cambridge, UK: Cambridge University Press, 2008.

[3] S. Singh, *The Code Book: The Science of Secrecy from Ancient Egypt to Quantum Cryptography*. New York, NY, USA: Anchor Books, 2000.

[4] NIST, "PQC Standardization Process: Third Round Candidate Announcement," 2020. [Online]. Available: https://www.nist.gov/news-events/news/2020/07/pqc-standardization-process-third-round-candidate-announcement

[5] S. Bai et al., "CRYSTALS-Dilithium: Algorithm Specifications and Supporting Documentation," Version 3.1, 2021

[6] D. J. Bernstein et al., "The SPHINCS+ Signature Framework," Submission to the NIST Post-Quantum Project, 2019.

[7] R. Niederhagen et al., "Streaming SPHINCS+ for Embedded Devices," 13th International Conference on Cryptology in Africa,2022.

[8] A. J. Menezes, P. C. van Oorschot, and S. A. Vanstone, *Handbook of Applied Cryptography*. Boca Raton, FL, USA: CRC Press, 1996.

[9] A. Hülsing, M. Kudinov, E. Ronen, and E. Yogev, "SPHINCS+C: Compressing SPHINCS+ With (Almost) No Cost," in *Proc. IEEE Symp. Secur. Privacy (SP)*, 2023.

[10] S. Kölbl and J. Philipoom, "A note on SPHINCS+ parameter sets," in *Proc. 5th NIST PQC Standardization Conf.*, 2024.

[11] STMicroelectronics, "X-CUBE-PQC: Post-Quantum Cryptography expansion for STM32Cube," STMicroelectronics. [Online]. Available: https://www.st.com/en/embedded-software/x-cube-pqc.html

[12] G. Mao, D. Chen, G. Li, W. Dai, A. I. Sanka, Ç. K. Koç, and R. C. C. Cheung, "High-Performance and Configurable SW/HW Co-design of Post-Quantum Signature CRYSTALS-Dilithium," *ACM Transactions on Reconfigurable Technology and Systems*, vol. 16, no. 1, pp. 1–25, Dec. 2022.

[13] D. Amiet, L. Leuenberger, A. Curiger, and P. Zbinden, "FPGA-based SPHINCS+ Implementations: Mind the Glitch," in *Proc. 2020 23rd Euromicro Conference on Digital System Design (DSD)*, 2020, pp. 229–236.

Decision Tree-Based Classification of Textile Production Productivity and Its Implementation on ESP32

Ercan COŞGUN[1,*], Nahide ÖNER COŞGUN[2,*]

[1] *Kırklareli University, Department of Electronics and Automation, Kırklareli/TÜRKİYE*

[2] *Independent Researcher (Textile Finishing Technical Instructor), Kırklareli/TÜRKİYE*

***Contact:** ercancosgun@klu.edu.tr ,nahideoner@gmail.com

Abstract— In today's textile manufacturing enterprises, production planning is a critical process in terms of cost calculation. In particular, parameters such as production line downtime, overtime and workforce distribution have a direct impact on productivity. Traditional methods are insufficient for analysing the relationships between productivity and quality. This study aims to classify production line efficiency using machine learning methods based on textile production data. Within this scope, the 'Productivity Prediction of Garment Employees' database which contains real production data was utilised to classify production line efficiency using the Decision Tree algorithm, a machine learning method. In the study, the productivity variable, which has a continuous value structure, was divided into three classes: low, medium and high. Seven operational parameters related to the production process were provided as model inputs. For testing, the Decision Tree classifier model was loaded onto an ESP32 microcontroller and performance parameters were calculated. According to the results obtained, the model's overall accuracy rate was found to be 63.9%. When class-based performance was examined, sensitivity was calculated as 61.5% for the low efficiency class, 55.0% for the medium efficiency class, and 75.0% for the high efficiency class. These results indicate that the production parameters contain meaningful information for predicting efficiency levels and demonstrate that the proposed approach can be used to make decisions and intervene in production processes. Furthermore, it is assessed that this approach, which can operate with low-dimensional data, could form the basis for real-time applications on IoT-based data collection systems and embedded platforms.

Keywords: Textile productivity, Decision Trees, Classification, ESP32

I. INTRODUCTION

As in many countries, the ready-to-wear sector constitutes a significant portion of employment in Turkey [1]. In this sector, the effective planning and management of production processes demonstrate the competitiveness of businesses. Factors such as production line stoppages, model changes, workforce allocation and overtime can directly affect production efficiency [2]. Consequently, monitoring production processes and assessing efficiency are of paramount importance in the garment industry.

In traditional approaches, the monitoring of production performance is generally assessed using average values, ratio analyses or the examination of historical production records [3]. However, the large number of variables affecting the production process makes it difficult to identify the relationships between these variables. This situation necessitates the examination of production data using more systematic methods. In this context, a study analysed production processes in garment manufacturing facilities and conducted research aimed at identifying inefficient periods [4]. In another study, production efficiency was predicted using machine learning methods based on garment production data [5].

Nowadays, merely acquiring data from production lines is insufficient; making this data meaningful, measuring its performance and making predictions has become a necessity. In particular, rather than examining raw production data directly, categorising and analysing this data presents planners with an interpretable overview. In this context, [6] [7] and emphasise that in production environments, merely collecting data is insufficient; these data must be analysed to evaluate performance and draw conclusions for the future.

The use of databases in studies analysing production processes is important in terms of evaluating the methods employed and comparing them with other studies. Data sets obtained from real production environments contain numerous parameters that influence the production process. In the literature, studies on textile and production processes have been observed to utilise various datasets, such as garment production data, fabric defect datasets, and production line performance records [7], [8]. In particular, image-based datasets are preferred in studies involving fabric defect detection, whilst datasets comprising parameters derived from production are favoured in studies on production efficiency and planning [9]. These studies demonstrate that analysing production data can contribute to a better understanding of production performance and processes.

In recent years, the use of data-driven methods in the analysis of production data has become widespread. In particular, machine learning methods offer significant advantages in terms of identifying relationships between variables. There are studies in the literature where production efficiency has been estimated using garment production data. Sabuj et al. compared the performance parameters of various machine learning classifiers such as support vector machines, decision trees, and random forests to estimate the production efficiency of garment workers [10]. In another study, a system predicting the productivity performance of garment workers was developed using a hybrid approach involving multiple classifier models [11]. In yet another study, the MLP (Multilayer Perceptron) algorithm, an artificial intelligence algorithm, was used to estimate cycle times for a specific process in textile production [12].

In this study, using the Garment Worker Productivity Dataset [13], the continuous production efficiency value was first reduced to understandable categories such as 'low', 'medium' and 'high'. Subsequently, a classifier model was created using decision trees, a machine learning algorithm. The classifier model was then adapted to the ESP32 microcontroller and tested using the data set aside for testing. model performance was evaluated using accuracy and sensitivity metrics.

II. METHOD

This section describes the dataset used in the study, the data pre-processing steps, and the classification method applied. It also provides information on the model training, testing process, and performance evaluation metrics.

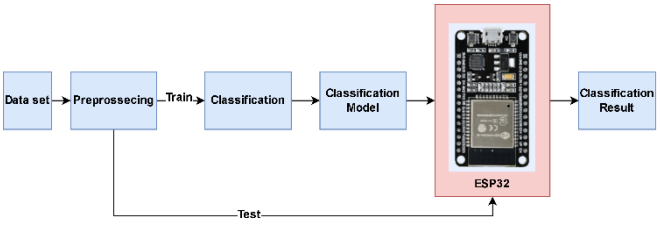

Fig. 1 . Block diagram of the proposed system

The general structure of the proposed system is shown in Fig. 1. Here, the dataset undergoes pre-processing, followed by classification, the creation of the classifier model, and finally, the testing of the data set aside for testing on the ESP32 microcontroller.

A. Dataset

In this study, the *Garment Worker Productivity* dataset, which contains data on garment manufacturing processes, was used [13]. The dataset consists of a total of fourteen features and a variable ranging from 0 to 1 representing productivity. The features presented in the dataset are shown in Table 1 at.

Table 1. Database description

Feature	Description
date	Date of production
quarter	Which part of the month it falls in
department	Production department
day	Day of the week
team	Production line team number
targeted_productivity	Target productivity value
smv	A product's standard production time
WIP	The amount of work currently in progress on the production line
overtime	Overtime hours
incentive	Incentives paid to workers
idle_time	Time the production line is idle
idle_men	Number of idle workers
no_of_style_change	Number of model changes
no_of_workers	Number of workers
actual_productivity	Actual productivity value

This dataset contains a total of 1,197 observations. It is used to estimate the actual productivity range between 0 and 1 or to classify data into different categories using the 14 features it contains. The features in the dataset vary in type, including categorical, continuous, integer and date fields. All other details regarding the dataset are presented in the study cited in [8].

B. Pre-processing

Pre-processing is the stage in machine learning algorithms where necessary operations are performed to organise and split the data in order to improve classification performance. The actual efficiency value, provided as a continuous value in the dataset, has been categorised into three classes in [8] to facilitate analysis and interpretation

Fig. 2. classification of actual efficiency values has been divided into three classes. Thus, the continuous values in the dataset have been converted into a classifiable format.

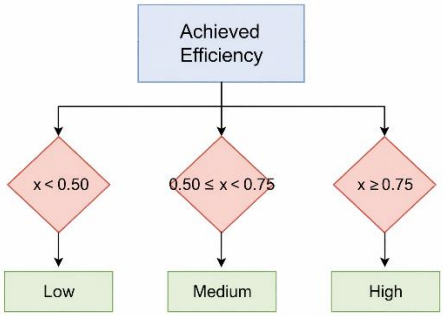

Fig 2 . Classification of actual efficiency values

After dividing the continuous values into levels, 716 observations were labelled as high, 348 as medium and 133 as low. This resulted in an imbalanced dataset. To resolve this issue, 133 observations were randomly selected from the entire dataset. The data was then split into training and test sets, as shown in Fig. 3 . 133 observations were obtained from each class.

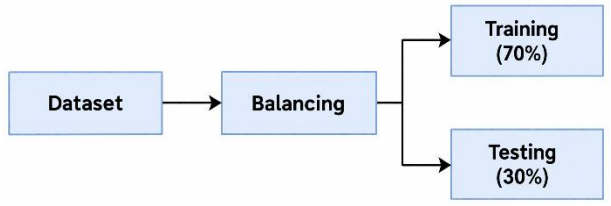

Fig. 3 . Splitting the data into training and test sets

In this study, seven parameters thought to influence the production process were used as model inputs. The variables evaluated included standard processing time, overtime, incentive amount, idle time, number of idle workers, number of model changes, number of employees, and target productivity. Variables such as date, day, and department, which do not directly represent production efficiency, were not included in the model.

C. Classification

In this study, production efficiency values were classified into three categories—low, medium and high based on predefined thresholds. A decision tree-based classifier was trained in the MATLAB environment using the obtained dataset. During model training, 5-fold cross-validation was selected for validation. The relationships between production parameters and productivity classes were examined during model training; the model was then tested on the test data, and the classification performance metrics were calculated and recorded.

D. Classifier Model

The trained decision tree model was converted into a rule-based structure to demonstrate its applicability in embedded systems. The resulting rules were transferred to the ESP32 microcontroller environment, and the classification process was performed on the device. Input parameters were sent to the device via serial communication, and the model performed real-time classification.

III. PERFORMANCE METRICS

To evaluate the success of the classification model, the confusion matrix shown in Fig. 4 at used. The confusion matrix enables the comparison of the classes predicted by the model with the actual classes, thereby facilitating a numerical analysis of correct and incorrect classifications. As this study addressed a three-class problem, the confusion matrix was constructed to show the number of correct and incorrect classifications for each class.

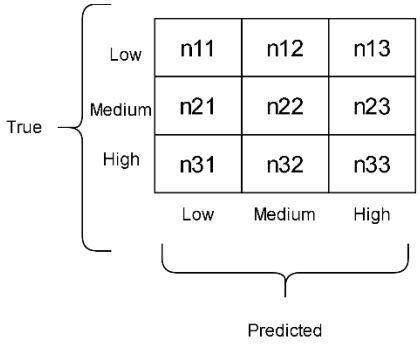

Fig. 2 . Confusion matrix

Here;

- n11 →True Class 1,Prediction low (correct)
- n22→Ture Class 2, Prediction: medium (correct)
- n33 →Ture Class 3, Prediction high (correct)

represents the class.

To evaluate model performance, accuracy and class-specific recall values were calculated. The accuracy value was calculated as the ratio of correctly classified examples to the total number of observations, as shown in (1).

$$\text{Accuracy} = \frac{\text{n11} + \text{n22} + \text{n33}}{\text{Total observations}} \quad (1)$$

The recall value, on the other hand, indicates the proportion of examples belonging to a specific class that are correctly predicted. Recall is calculated for each class as shown in (2):

$$Recall_{Low} = \frac{\text{n11}}{\text{n11} + \text{n12} + \text{n13}} \quad (2)$$

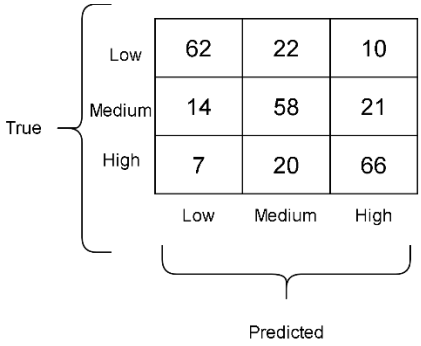

Fig. 3 . Confusion matrix for the training data

Fig. 3 shows the confusion matrix for the training dataFig. 4 shows the confusion matrix for the classification results of the test data.

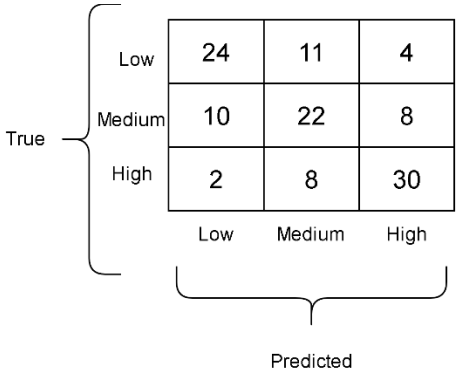

Fig. 4 . Complexity matrix for the test set

The overall accuracy values for the training and test sets were calculated and are presented in Table 2.

Table 1 . Overall accuracy values

	Training	Test
Overall Accuracy	66.4%	63.9%

Table 2 shows the calculated sensitivity values for the low, medium and high classes based on the training and test data.

Table 2 . Sensitivity values

Class	Sensitivity	
	Training	**Test**
Low	65.9%	61.5%
Medium	62.4%	55.0%
High	71.0%	75.0%

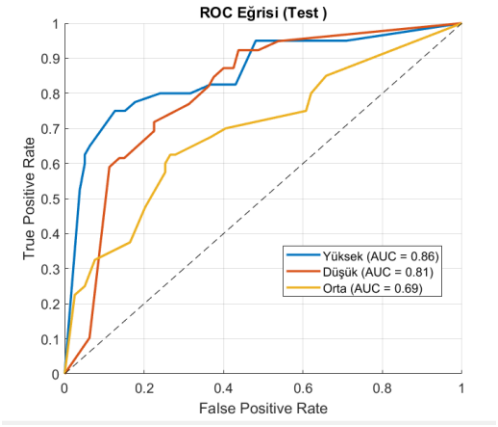

Fig. 5 . ROC Curve

Fig. 5 , it was observed that the High and Low classes could be distinguished relatively better, whilst the discrimination performance was lower for the Medium class. This finding is consistent with the results of the confusion matrix.

IV. CONCLUSIONS AND DISCUSSION

In this study, the aim was to classify production efficiency using data from garment manufacturing processes. Within this scope, the efficiency metric, provided as a continuous value, was divided into three classes low, medium and high using specific threshold values. A decision tree-based classifier was created in the MATLAB environment using the selected features, and the model was evaluated on the test data.

In the evaluation conducted on the test data, the model's overall accuracy was calculated to be approximately 63.9%. In the analysis conducted by class, the sensitivity value for the low efficiency class was found to be approximately 61.5%, for the medium efficiency class approximately 55.0%, and for the high efficiency class approximately 75.0%. The results obtained indicate that the model is particularly successful in distinguishing the high-efficiency class, whilst some confusion can be observed in the low and medium-efficiency classes. It is thought that this may stem from the production parameters associated with these classes containing values that are close to one another.

In another phase of the study, the classification model was converted into a rule-based structure and run on an ESP32 microcontroller. The input parameters were transferred to the device via serial communication, and the classification process was performed directly on the microcontroller. Tests revealed that the model operated stably on the device and that the classification results were consistent with the expected outputs. The developed decision tree model performed classification on the ESP32 in an average of 50 microseconds. This result demonstrates that the model is suitable for real-time operation on edge devices.

Consequently, the classification of production data offers a useful approach for determining productivity levels, monitoring production processes and supporting decision-making processes. Furthermore, the ability to run the classification model on edge devices enables data to be processed locally without being sent to a central server, thereby reducing latency and providing a significant advantage in terms of the system's efficiency. Future work plans to test different methods using larger datasets and to validate the system using data obtained from real production environments.

REFERENCES

[1] "An Empirical Analysis of Rival Country Effects on Türkiye's Textile and Apparel Exports (Research Article)", 2024, doi: 10.29023/alanyaakademik.1572272.

[2] N. Viet Tinh, S. T. Husain, and N. Van Thanh, "Application of Industrial Engineering Techniques for Better Productivity in the Garment Industry", *ARRUS Journal of Engineering and Technology*, vol. 1, no. 1, pp. 1–8, July 2021, doi: 10.35877/jetech493.

[3] A. G. Seher *et al.*, "MEASUREMENT OF PRODUCTIVITY IN TEXTILE AND APPAREL PLANTS", Vol. 4, 2007.

[4] Z. Kumaş, C. Sabir, and P. Duru Baykal, "The Use of Work Study Technique for Process Productivity in Apparel Plants", *Çukurova University Journal of the Faculty of Engineering and Architecture*, vol. 31, No. 1, pp. 175–189, 2016.

[5] R. Obiedat and S. Toubasi, "A Combined Approach for Predicting Employees' Productivity based on Ensemble Machine Learning Methods", *Informatica*, vol. 46, no. 5, pp. 49–58, Mar. 2022, doi: 10.31449/inf.v46i5.3839.

[6] M. A. Waller and S. E. Fawcett, "Data science, predictive analytics, and big data: A revolution that will transform supply chain design and management", *Journal of Business Logistics*, vol. 34, no. 2, pp. 77–84, 2013, doi: 10.1111/jbl.12010.

[7] Primesh Pathirana, "Fabric stain dataset", https://www.kaggle.com/datasets/priemshpathirana/fabric-stain-dataset/code.

[8] A. Al Imran, M. S. Rahim, and T. Ahmed, "Mining the productivity data of the garment industry", *International Journal of Business Intelligence and Data Mining*, vol. 19, no. 3, pp. 319–342, 2021, doi: 10.1504/IJBIDM.2021.118183.

[9] X. Xie, "A Review of Recent Advances in Surface Defect Detection using Texture Analysis Techniques", *ELCVIA Electronic Letters on Computer Vision and Image Analysis*, vol. 7, no. 3, pp. 1–22, June 2008, doi: 10.5565/rev/elcvia.268.

[10] M. H. Hosen, N. Tasnia, M. Amran, R. Chowdhury, A. Uddin, and A. Saha, "Stacking Ensemble Techniques for Productivity Forecasting in Bangladesh's Garment Industry", *2024 IEEE Conference on Computing Applications and Systems, COMPAS 2024*, 2024, doi: 10.1109/COMPAS60761.2024.10797051.

[11] R. Obiedat and S. Toubasi, "A Combined Approach for Predicting Employees' Productivity based on Ensemble Machine Learning Methods", *Informatica*, vol. 46, no. 5, pp. 49–58, Mar. 2022, doi: 10.31449/inf.v46i5.3839.

[12] E. Onaran and S. Yanık, "Predicting Cycle Times in Textile Manufacturing Using Artificial Neural Networks", *Advances in Intelligent Systems and Computing*, vol. 1029, pp. 305–312, 2020, doi: 10.1007/978-3-030-23756-1_38.

[13] "Garment Worker Productivity Dataset", https://archive.ics.uci.edu/dataset/597/productivity+prediction+of+garment+employees.

CNN and PINN based CFD Approach for Sneakers

Büşra Erkömek Ateş[1,], Elif Nihan Yıldız[1], Mahmut Ulusoy[1] and Uğur Demir[2,*]

[1]*FLO Group, Design Centre, İstanbul, Türkiye*

[2]*Marmara University Department of Electrical and Electronics Engineering, İstanbul, Türkiye*

*Contact: udemir@marmara.edu.tr

From a design perspective, factors in a sports shoe design include sole design, upper surface area, aesthetic approach, and validation studies. The drag coefficient is the most important parameter on the shoe, and elements such as shoe geometry, toe area, lace surface area, and materials can cause increases or decreases in the drag coefficient from a design perspective. The limitations of wind tunnels include factors such as analytical calculations, accuracy issues, and reliance on experts for visual diagnosis, which pose disadvantages.

On the other hand, to work with computational fluid dynamics, the geometric design, boundary conditions, and the turbulence model of k-epsilon used for calculating the flow field are employed to determine the drag force and drag coefficient. However, in the k-epsilon turbulence model, weak accuracy, incorrect calculations in recirculations and separated flows, and instability in curved rotating flows appear to be issues. As a conceptual idea, it has emerged that a hybrid approach combining experimental and simulation-based methods—such as image processing in traditional wind tunnels, physics-informed neural networks, and augmented reality—could yield more accurate results and improvements.

In the proposed method, for a sports shoe, the processes of parametric design, analysis, and optimization are carried out within a traditional desktop wind tunnel framework, followed by prototype creation and validation steps. Then, images captured during experimental studies inside the wind tunnel are processed using image processing techniques to establish boundary conditions and geometries, which are sent to a physics-informed neural network that predicts the calculations. Data is derived using the geometric structure and parameters of the wind tunnel images and an experimental design approach, followed by analysis of the obtained data with CFD, and optimization and validation processes are carried out with the identified results.

Keywords: *Convolutional Neural Network, Physic-Informed Neural Network, Design of Experiment, Computational Fluid Dynamics, Aerodynamic Optimization of Sneakers*

A Genetic Algorithm-Based Framework for Inertia Estimation in Power Systems with Grid-Scale BESS

Mohamed FARAH ABDILAHI[1,*] and Yunus YALMAN[1]

[1]*School of Engineering and Natural Sciences, Ankara Yildirim Beyazit University, Ankara, Türkiye*

*Contact: mhmdfrh.krye@gmail.com

The rapid replacement of traditional synchronous generation with converter-interfaced renewable energy sources has led to a significant reduction in power system inertia and increased variability, posing a major challenge to both frequency stability and operational security. In contemporary power systems with high penetration of grid-scale Battery Energy Storage Systems (BESS), inertia is no longer a fixed parameter but a dynamic quantity influenced by fast power-electronic control actions and synthetic inertia emulation. This effective inertia must therefore be represented accurately to enable reliable frequency assessment, protection coordination, and reserve allocation.

This paper proposes a Genetic Algorithm (GA)-based inertia estimation framework specifically developed for power systems integrating grid-scale BESS. The proposed method formulates inertia estimation as a nonlinear optimization problem, aiming to minimize the mismatch between measured frequency responses and model-reconstructed trajectories following a disturbance. The underlying model is a reduced-order, physics-informed frequency dynamic model that incorporates synchronous inertia, damping effects, and BESS active power injection. The GA searches directly within the inertia parameter space, eliminating the need for gradient information or linearization-based assumptions. Owing to its global search capability, the GA is well suited to exploring the complex and nonconvex landscapes characteristic of low-inertia, converter-dominated systems, and demonstrates robustness in the presence of measurement noise, modelling uncertainty, and control-induced nonlinearities.

The performance of the proposed methodology is evaluated using the IEEE 39-bus system with integrated renewable energy sources and grid-scale BESS, serving as a benchmark transmission system with synthetic inertia and fast frequency response capability. Simulation results indicate that the GA estimates the system inertia as 4.67 s for a system with a true inertia constant of 4.5 s, corresponding to a moderate overestimation when BESS-aided dynamics are considered. The reconstructed frequency trajectory exhibits discrepancies with respect to the measured response, particularly in terms of the frequency nadir and settling time. Specifically, the minimum reconstructed frequency reaches approximately 49.67 Hz, compared to the actual nadir of 49.76 Hz, while the settling time is longer than that observed in the real system. Quantitatively, the reconstruction accuracy of the frequency trajectory is characterized by a root mean square error (RMSE) of 0.041 Hz and a mean absolute percentage error (MAPE) of 0.083%. Even though the GA shows lower convergence rates, they provide less sensitive and reliable inertia estimations with no initialisation sensitivity or early convergence. These results demonstrate that the proposed pure Genetic Algorithm constitutes a robust and transparent optimization-based inertia estimation approach for BESS-assisted, low-inertia power systems.

The method is well suited for offline applications, including system analysis, planning studies, research investigations, and the validation of frequency control strategies.

Keywords: *Genetic Algorithm, Battery Storage System, Inertia Estimation*

Performance Evaluation of High-Speed Air Cycle Machine Architectures for Aerospace Cooling Applications

Alperen ÖZCAN [1,2,*], Selahattin Çelik[1,2]

[1] *Department of Mechanical Engineering, Ankara Yıldırım Beyazit University, Ankara 06010, Türkiye*

Ankara Yıldırım Beyazit University, Ankara 06010, Türkiye

***Contact :** alperenozcandc@gmail.com

Abstract Thermal management of avionics in high-performance aerospace platforms requires compact and efficient cooling solutions. This study investigates the performance and feasibility of two alternative Air Cycle Machine (ACM) architectures through comprehensive one-dimensional (1D) numerical simulations. The reference configuration (Concept-1) operates at a design speed of 45,000 RPM, while the high-speed configuration (Concept-2) is scaled to 65,000 RPM to achieve volumetric reduction. Performance evaluations were conducted using the Aungier loss model to determine thermodynamic state points, isentropic efficiencies, and power balances for both systems. The results show that both architectures successfully maintain the pod feed temperature below the 35°C limit. Concept-1 exhibits superior isentropic efficiency and cooling effectiveness thanks to lower aerodynamic losses and optimized heat exchanger residence time. In contrast, Concept-2, despite increased mechanical complexity and advanced material requirements, offers better integration into confined aerospace environments by providing a significant reduction in total system mass and volume. This comparative analysis provides a technical framework for selecting ACM architectures based on the trade-offs between thermal efficiency and integration constraints.

Keywords: Air Cycle Machine (ACM), System Simulation, Thermal Management, 1D Performance Analysis, High-Speed Turbomachinery, Avionics Cooling

I. INTRODUCTION

Air conditioning is defined as the process of controlling environmental conditions such as temperature, humidity, air quality, and air circulation in accordance with human comfort and system requirements. These systems aim not only to provide thermal comfort but also to keep electronic and mechanical components at safe operating temperatures [1].

In high-performance applications such as the aviation, automotive, and defence industries, air conditioning systems play a critical role in terms of human performance, mission safety, and system continuity [2].

Modernization of systems in aircraft and the proliferation of highly integrated avionics have made the requirements on thermal management system (TMS) performance in aircraft increasingly stringent. While heat loads from propulsion, electrical and hydraulic systems are constantly increasing, the trend towards integrated and compact aircraft fuselage design is confining multiple heat sources to limited areas. As a result of these developments, thermal management has become a vital core technology for modern aircraft [3].

Thermal management in modern aircraft is an integrated engineering process aimed at safely and controllably removing heat generated by propulsion, electrical, and avionics systems, with high-power electronic units forming the main heat source. While ram air generated during flight is commonly used to dissipate heat, fuel systems with high specific heat capacity also support thermal management by acting as a temporary heat loss medium, especially under high altitude and low speed conditions.

Air cooling systems are preferred for heat energy transfer due to their simple structure, while liquid cooling systems, which are more effective in situations requiring high heat flux, are preferred. Today, in military aircraft, thermal limits have become a more decisive constraint than fuel capacity in terms of mission duration and capability due to the increasing power consumption of avionics systems [4] [5].

For cooling external avionics systems, ram air assisted systems [1], liquid-cooled solutions, or vapor compression refrigeration (VCS) systems, which offer stable performance in ground operations, can be used depending on the load level [6].

However, since each method has limitations such as weight, power consumption, and integration complexity, the solution to be applied must be determined with a holistic approach, taking into account the mission profile and flight conditions.

When evaluating thermal management solutions in aviation, Vapor Compression Refrigeration (VCS) systems stand out as the strongest alternative to Air Cycle Refrigeration Machines (ACMs) with their structure consisting of a compressor, condenser, expansion valve, and evaporator. These systems utilize the latent heat released during the phase change of refrigerants, providing high Coefficient of Performance (COP) and energy efficiency, especially at low altitudes and high ambient temperatures. However, the mechanical complexity, system weight, and leakage risks of VCS make ACM systems, which offer a lighter structure and can directly utilize engine exhaust air,

more preferable in large-scale commercial and military platforms.

Air cycle systems, with their simple and reliable operating principle of expanding compressed air through a turbine to provide cooling, meet both cabin pressurization and equipment climate control needs in an integrated structure. One air cycle method, the Bootstrap system, is based on a multi-stage compression and expansion principle using air as the working fluid. In this cycle, high-pressure air from the engine is cooled by ram air, then compressed again in a secondary compressor and finally expanded in a turbine to reach low temperatures.

Despite its environmentally friendly and safe design, the performance of Bootstrap systems is dependent on flight speed and ram airflow; this poses a limitation, especially in ground operations and at low speeds. In recent years, "Reverse Bootstrap" systems, which have attracted the attention of researchers, have become an attractive alternative for external avionics pod applications where weight and volume constraints are critical, offering a simpler and lighter architecture thanks to the absence of a secondary heat exchanger. Although their cooling capacities are more limited compared to advanced Bootstrap cycles, their simple structure provides significant advantages in system integration.

II. NUMERICAL MODEL AND METHODOLOGY

A. Air Cycle Machine Modeling Definition

The system's basic operation is based on the thermodynamic principles of the Reverse Brayton Cycle. This process, beginning with the ram air inlet, involves the isentropic (practically polytropic) expansion of the flow within the turbine, constituting the most critical phase of the cycle and resulting in a significant temperature drop in the air. The enthalpy change absorbed from the flow by the turbine is converted into mechanical work to drive the compressor located on the same shaft. This cycle creates a high cooling capacity by reducing the cooling air to below ambient static pressure and temperature values (sub-ambience).

The cold air stream exiting the turbine passes through an integrated air-to-air heat exchanger, completing the heat absorption phase of the cycle; at this point, the system thermal load, carried by the circulation fan, is transferred to the cold air. The air, heated after heat transfer, is directed directly to the compressor, where it is compressed and discharged to the low-pressure zone below the pod, completing the thermodynamic cycle. Minimizing pressure losses between the compressor and turbine components is a key factor in increasing the system's coefficient of performance (COP) and operational stability.

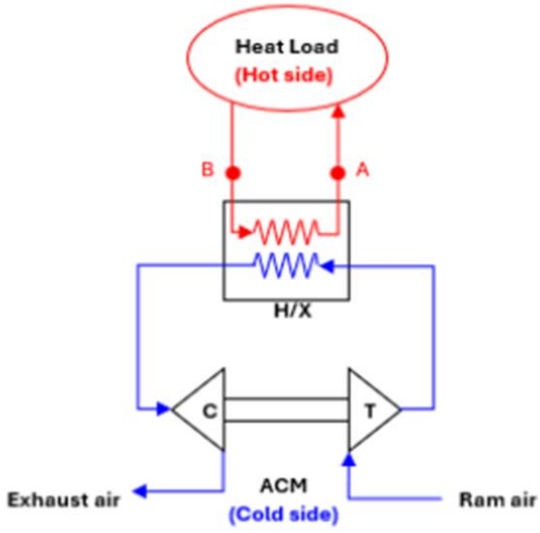

Figure 1. Air Cycle Machine Cooling System

B. Evaluation Criteria and Design Constraints

To enable a sound comparison between the developed alternative "Reversed Bootstrap Air Cycle Machine" architectures, all configurations were analysed using specific key performance indicators. At the heart of these criteria is maintaining the system supply air temperature below 35°C, which determines the system's cooling capacity. Furthermore, the balance between the system's physical dimensions and operational speed (RPM), the mechanical integrity risks posed by high speeds and additional rotors, and the thermodynamic efficiency (COP) of pre-cooling assisted cycles were considered key determining parameters in concept selection.

To ensure equal evaluation of the designs, the "worst-case" scenario, the most challenging operational point for air-cycle systems, was selected as the primary design point. While sea level (0ft) conditions offer an advantage in terms of mass flow rate, when combined with high ambient temperature (49°C), they directly limit the heat dissipation capacity of the heat exchangers and maximize the air temperature at the turbine inlet. These defined boundary conditions form the basis of the numerical models and allow us to quantitatively compare the performance limits of five different architectures under a thermal load of 1800 W.

Table 1. Design Parameters and Constraints

Design Parameters	Value	Description
Altitude	0 ft (Sea-Level)	Maximum ambient pressure and density
Mach Number	0.9 Mach	Critical high-speed condition for ram air
Ambient Temperature	49°C	Extreme "Hot Day" condition
Thermal Load	1800 W	Assumed heat load from avionics
System Supply Temp.	35°C	Maximum allowable supply threshold

C. Air Cycle Machine Design Review and System Components

Radial turbines are systems that convert the kinetic energy of a fluid into mechanical work in a radial flow direction, providing high efficiency, especially in compact applications such as turbochargers. The development process for these components typically begins with a preliminary design phase that defines the system's outlines, often based on one-dimensional flow analysis and empirical correlations.

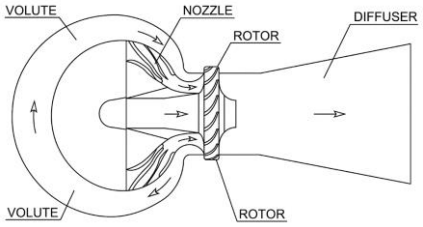

Figure 2. Radial Turbine Stage Layout

The first stage of turbine design begins with defining the flight conditions. In this study, sea level, a speed of 0.9 Mach, and ISA+34°C were selected as the design points; the relevant temperature and pressure values were calculated using isentropic equations.

$$\frac{P_{TOTAL}}{P} = \left(1 + \frac{\gamma - 1}{2} M^2\right)^{\frac{\gamma}{\gamma-1}}$$

$$\frac{T_{TOTAL}}{T} = \left(1 + \frac{\gamma - 1}{2} M^2\right)$$

P_{TOTAL}: Total (Stagnation) Pressure
P: Static Pressure
T_{TOTAL}: Total (Stagnation) Temperature
T: Static Temperature
γ: Thermal capacity ratio (adiatic index)
M: Mach Number

The pressure loss from the air duct inlet to the turbine inlet was obtained using the following equation.

$$\Delta P = \frac{1}{2} \rho V^2 c$$

ΔP: Pressure Loss
ρ: Fluid Density
V: Flow Velocity
c: Loss Coefficient

The preliminary design process for radial turbines relies on scanning the entire design domain of fundamental variables such as load coefficient (ψ), flow coefficient (ϕ), and rotational speed (N) to determine the geometry best suited to performance requirements. The primary goal of the design is to achieve maximum efficiency within the minimum feasible dimensions; to this end, the region where total-to-static efficiency is highest is targeted using Aungier correlation [7]. In an ideal design, the optimum operating point is determined by maintaining the load coefficient between 0.9 and 1.0 and the flow coefficient between 0.2 and 0.3. After determining these parameters and the total-static pressure ratio (PR), the mechanical power that the turbine will generate is calculated using thermodynamic equations based on the mass flow rate of the fluid and the inlet temperature, thus establishing the energy balance of the system.

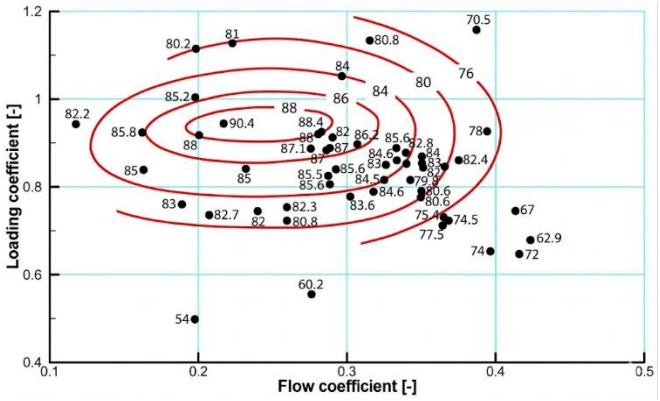

$$\psi = \frac{\Delta H_u}{U^2}$$

$$\phi = \frac{C_m}{U}$$

$$\psi = f(N, PR, \dot{m}, T_{in})$$

$$\phi = f(N, PR, \dot{m}, T_{in})$$

Based on the obtained rotational speed, turbine inlet flow rate, and turbine total-static pressure ratio values, the turbine power is calculated using the following equation.

$$P_{turbine} = \eta \dot{m} C_p T_{inlet} \left(1 - (\frac{1}{PR})^{\frac{\gamma-1}{\gamma}}\right)$$

$P_{turbine}$: Mechanical Power produced by the turbine
η: İsontropic Efficiency of Turbine
$\dot{m}$: Mass flow rate of air passing through the turbine.
C_p: Specific heat of air at constant pressure.
T_{inlet}: Total (stagnation) temperature at the turbine inlet.
M: Mach Number

Centrifugal compressors are dynamic machines that convert kinetic energy into pressure potential energy, used in a wide range of applications such as gas turbines, turbochargers, and air conditioning systems. The system's operating principle is based on the conversion of kinetic energy, transferred to the fluid via a rotating impeller, into high-pressure potential energy by reducing its velocity in the diffuser and volute stages. This aerothermodynamic conversion process is the fundamental element that determines the pressure balance and overall thermal management capacity of air-cycle refrigeration (ACM) systems.

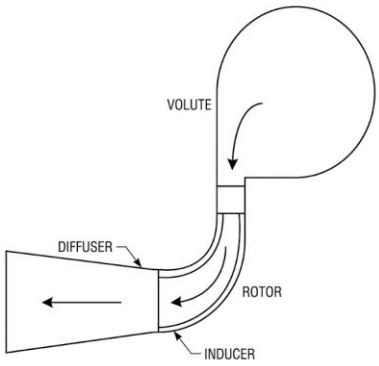

Figure 3. Centrifugal Compressor Stage Layout

In efficiency calculations used to accurately determine power requirements during compressor design, precise modelling of aerodynamic and mechanical losses in the system is of critical importance. In this study, the Aungier loss model [8] was preferred, as it can predict performance-decreasing factors such as intake duct losses, blade and disc friction, blade loading, and tip space leakage, especially under off-design boundary conditions such as "choking" and "stall" at high speeds, most closely to experimental data.

After calculating the compressor efficiency and determining the target pressure ratio, the power required by the compressor is calculated using the following equation.

$$P_{Compressor} = \frac{\dot{m} C_p T_{giriş} (PR^{\frac{\gamma-1}{\gamma}} - 1)}{\eta}$$

$P_{turbine}$: Total mechanical power required to rotate the compressor
η: İsontropic Efficiency of Compressor
$\dot{m}$: The mass flow rate of the fluid passing through the compressor.
C_p: Specific heat of air at constant pressure.
T_{inlet}: Total (stagnation) temperature at the compressor inlet.

D. Alternative System Architectures

In this section, 1D analyses were conducted focusing on unique design parameters, component sizing, and thermodynamic performance to determine the concept to be designed and manufactured in detail.

Each configuration was modelled using the common design points identified in the previous section to evaluate its ability to meet the °C system supply temperature requirement.

Before examining each concept individually, the alternatives to be considered are as follows:

These configurations are designed to explore different engineering strategies for meeting the demanding cooling requirements of an avionics system under challenging environmental conditions.

The evolutionary path of these designs progresses from basic simplicity to increasing complexity and performance optimization.

- **Concept 1 (Basic 2-Wheeled - 45,000 RPM):** The most basic form of air-cycle machines, focusing on mechanical reliability and standard bearing life by using lower rotational speeds.

- **Concept 2 (High-Speed 2-Wheeled - 65,000 RPM):** An optimization-focused design aiming to reduce the physical footprint and weight of the Air-Cycle Machine through higher rotational speeds.

1) Concept 1 - (Basic 2-Wheeled - 45,000 RPM):

Concept-1 is based on the classic "inverted bootstrap" air circulation architecture where a radial turbine and a centrifugal compressor operate synchronously on a common shaft. The primary focus of the design is to maximize mechanical reliability by reducing the number of moving parts and to achieve the targeted cooling performance with the simplest architecture. The main components of the system

consist of a turbine-compressor group, a heat exchanger, a bypass line, and a circulation fan that supports air circulation within the main system.

The aerodynamic performance of the system is directly related to the optimization of the inlet (scoop inlet) geometry. Specifically, at a flight speed of 0.9 Mach, the inlet cross-sectional area is determined as 0.0013 m² to minimize the pressure losses that the ram air will experience until it reaches the turbine inlet. This sizing optimizes energy conversion by transferring the required mass flow rate to the system in the most efficient way.

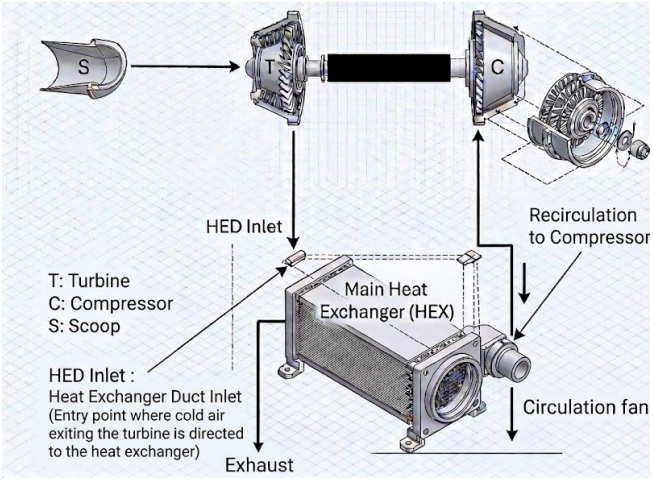

Figure 4. Concept 1 - System Architecture

To prove the technical validity of the Concept 1 architecture, a comprehensive one-dimensional (1D) performance analysis was performed using the Aungier loss model [7]. These analyses allowed for the precise determination of thermodynamic state points throughout the turbine and compressor stages. Data obtained for a 45,000 RPM operational speed configuration numerically revealed the pressure ratios and isentropic efficiency values required for the system to achieve its target cooling effect. This 1D analysis is a critical validation step confirming that the power generated during the turbine expansion process is sufficient to meet the system's target supply temperature.

Table 2. Concept-1 Turbine Boundary Conditions

Turbine Boundary Conditions	**Unit**	**Value**
Shaft Rotational Speed	rpm	45.000
RAM Air Temperature	°C	49.0
Turbine Inlet Total Temperature	°C	100.5
Turbine Inlet Total Pressure	kPa(abs)	169.6
Turbine Inlet Mass Flow Rate	kg/s	0.450

Table 3. Concept-1 Turbine 1D Analyses Performance Results

1D Analyses Performance Result	**Unit**	**Value**
Turbine Outlet Total Temperature	°C	26.0
Turbine Outlet Static Pressure	kPa(abs)	62.8
Pressure Ratio	-	2.70
Isentropic Efficiency	%	81.1
Power Output	kW	2.93

Table 4. Concept-1 Compressor Boundary Conditions

Compressor Boundary Conditions	**Unit**	**Value**
Shaft Rotational Speed	rpm	45.000
Compressor Inlet Total Temperature	°C	29.9
Compressor Inlet Total Pressure	kPa(abs)	62.7
Compressor Inlet Mass Flow Rate	kg/s	0.450

Table 5. Concept-1 Compressor 1D Analyses Performance Results

1D Analyses Performance Result	Unit	Value
Compressor Outlet Total Temperature	°C	104.4
Compressor Outlet Total Pressure	kPa(abs)	117.7
Compressor Outlet Static Pressure	kPa(abs)	115.0
Pressure Ratio	-	1.88
Isentropic Efficiency	%	80.2
Power Output	kW	2.79

According to the results obtained, the mechanical power produced by the turbine is 2.93 kW, while the power required by the compressor is 2.79 kW. These figures show that the turbine meets the power needs of the compressor.

2) Concept 2 - (High-Speed 2-Wheeled - 65,000 RPM):

Although the operational data provided by Concept-1 proved the validity of the air-cycle engine, the Concept-2 architecture was developed to meet more demanding system requirements. In this new configuration, the design speed was strategically increased to 65,000 RPM. The main motivation for this increase is based on the scaling principles in turbo engines; according to Aungier [8][9], increasing the angular velocity while maintaining the same pressure ratio allows for a reduction in turbine and compressor diameters. This dimensional reduction reduces the total mass of the ACM unit, enabling it to be integrated much more efficiently into systems with limited volume.

Switching to higher velocities not only provides physical compactness but also directly affects component-based isentropic efficiencies. Optimizing the specific velocity (ω_s) and specific diameter (D_s) parameters proposed by Dixon and Hall [11] for high velocities has the potential to increase the cooling capacity of the system, especially in high-altitude conditions with low air density. The 1D analyses conducted within the scope of Concept-2 detail the effects of increasing ambient velocities on flow physics through Aungier and E. S. Yoon loss models [10].

However, reaching high speeds such as 65,000 RPM presents significant mechanical engineering challenges. Managing the thermal loads on the bearings used in the shaft support structure between the turbine and compressor, and the high centrifugal forces on the shaft, necessitate much more precise manufacturing tolerances and advanced material selection compared to Concept-1. The performance data and operational analyses presented in this section allow for a comprehensive comparison of the dimensional advantages and mechanical risks offered by this high-speed architecture.

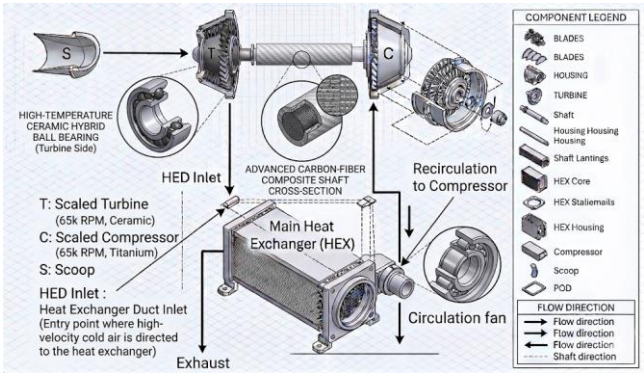

Figure 5. Concept 2 - System Architecture

To prove the technical validity of the Concept-2 architecture and to analyse the aerodynamic complexity introduced by high operational speeds such as 65,000 RPM, a comprehensive one-dimensional (1D) performance analysis was performed using the Aungier loss model. These analyses allowed for the precise determination of thermodynamic state points along the scaled-down ceramic turbine and titanium compressor stages. The data obtained numerically reveal the advanced pressure ratios required for the system to reach its target cooling capacity and the isentropic efficiency values specific to high-speed operation. This 1D analysis is a critical validation step confirming that the power generated during the expansion process in the turbine is sufficient to meet the target supply temperature of the compact system and confirming the efficiency of the high-speed configuration supported by advanced material/bearing technology.

Table 6. Concept-2 Turbine Boundary Conditions

Turbine Boundary Conditions	Unit	Value
Shaft Rotational Speed	rpm	65.000

RAM Air Temperature	°C	49.0
Turbine Inlet Total Temperature	°C	100.5
Turbine Inlet Total Pressure	kPa(abs)	169.6
Turbine Inlet Mass Flow Rate	kg/s	0.350

Table 7. Concept-2 Turbine 1D Analyses Performance Results

1D Analyses Performance Result	**Unit**	**Value**
Turbine Outlet Total Temperature	°C	30.7
Turbine Outlet Static Pressure	kPa(abs)	67.9
Pressure Ratio	-	2.50
Isentropic Efficiency	%	81.6
Power Output	kW	25.7

Table 8. Concept-2 Compressor Boundary Conditions

Compressor Boundary Conditions	**Unit**	**Value**
Shaft Rotational Speed	rpm	65.000
Compressor Inlet Total Temperature	°C	35.7
Compressor Inlet Total Pressure	kPa(abs)	67.8
Compressor Inlet Mass Flow Rate	kg/s	0.350

Table 9. Concept-2 Compressor 1D Analyses Performance Results

1D Analyses Performance Result	**Unit**	**Value**
Compressor Outlet Total Temperature	°C	105.5
Compressor Outlet Total Pressure	kPa(abs)	116.6
Compressor Outlet Static Pressure	kPa(abs)	115.0
Pressure Ratio	-	1.72
Isentropic Efficiency	%	74.1
Power Output	kW	24.50

According to the analysis results, in the high-speed Concept-2 configuration, the mechanical power produced by the turbine was calculated as 25.7 kW, while the compressor's required drive power remained at 24.5 kW. These numerical data prove that even at an operational speed of 65,000 RPM, the turbine fully meets the compressor's power requirement, and the system maintains a self-sustaining power balance. This positive margin in power generation confirms that the aerodynamic loads and mechanical losses resulting from high-speed operation are successfully managed.

III.RESULTS AND DISCUSSION

A. Comparative Thermodynamic Performance

Numerical results show that Concept-1 exhibits higher cooling efficiency compared to the high-speed architecture of Concept-2. This superior performance is primarily based on higher isentropic efficiencies achieved at an operational speed of 45,000 RPM. At this relatively low rotational speed, the flow within the turbine and compressor stages remains in more stable aerodynamic regimes characterized by low Mach numbers and reduced shock losses. Consequently, the expansion process in Concept-1 is more efficient, resulting in a more effective temperature drop relative to the energy consumed during compression. Furthermore, the heat exchange process in Concept-1 benefits from the optimized residence time within the main heat exchanger (HEX). Thanks to the moderate mass flow rates associated with the 45,000 RPM configuration, air-to-air heat transfer efficiency

(ϵ) is maximized, and more efficient heat dissipation to the ram air is achieved.

In contrast, while Concept-2 offers a more compact design, increased flow rates and higher turbulence levels lead to increased internal friction and mechanical heat, slightly reducing net cooling output. Therefore, when pure cooling performance and component efficiency are prioritized over volumetric constraints, Concept-1 stands out as the thermally superior configuration.

B. Power Balance and Efficiency

The operational continuity of the air-cycle engine depends on the mechanical power generated by the expanding air in the turbine precisely matching the drive power required by the compressor. 1D analyses confirm that a positive power margin is achieved for both concepts, and the systems exhibit a "self-sustaining" character. In Concept-1, the turbine power of 2.93 kW obtained at 45,000 RPM successfully meets the compressor's power demand of 2.79 kW. This margin provides a critical safety factor for tolerating bearing friction and other mechanical losses on the shaft.

In the transition to Concept-2, the energy density of the system increased significantly by increasing the operational speed to 65,000 RPM and the mass flow rate. In this high-speed configuration, power values reached approximately 24-25 kW, but the power balance was maintained. Table 10 presents a comparison of turbine and compressor power values and isentropic efficiencies for both concepts. The high isentropic efficiency values achieved by Concept-1 at lower speeds demonstrate that aerodynamic losses have been minimized. In Concept-2, despite increasing peripheral speeds and friction effects, the operational validity of the system has been preserved by keeping efficiency values within acceptable limits thanks to component designs optimized according to the Aungier model.

Table 10. Comparative Power and Efficiency Data

Parameter	Concept-1 (45,000 RPM)	Concept-2 (65,000 RPM)
Turbine Power (P_t)	2.93 kW	25.7 kW
Compressor Power (P_c)	2.79 kW	24.5 kW
Turbine Isontropic Efficiency (η_t)	84.2%	81.6%
Compressor Isontropic Efficiency (η_c)	81.5%	74.1%
Power Margin (ΔP)	0.14 kW	1.2kW

C. Mechanical Challenges and Integration

In air-cycle engine design, increasing the operational speed from 45,000 RPM (Concept-1) to 65,000 RPM (Concept-2) led to radical changes in the physical dimensions and mechanical requirements of the system. In line with scaling principles in turbo engines, the high-speed strategy allowed for a reduction in component diameters and resulted in a significant decrease in the total system volume. This dimensional reduction improves the integration capability of the ACM unit, especially in platforms where volumetric constraints are critical, such as in avionics bays. However, this compact structure has brought with it new mechanical challenges, such as managing high centrifugal forces and thermal loads.

The table comparing the dimensions of Concept-1 and Concept-2 is as follows.

Table 11. Cooperative Concept-1 and Concept-2 Dimensions

Parameter	Concept-1 (45,000 RPM)	Concept-2 (65,000 RPM)
Turbine Rotor Diameter	124 mm	90 mm
Turbine Total Diameter	275 mm	210 mm
Turbine Total Length	100 mm	80 mm
Compressor Rotor Diameter	143 mm	100 mm
Compressor Total Diameter	275 mm	210 mm
Compressor Total Length	100 mm	90 mm

REFERENCES

[1] I. Moir and A. Seabridge, “Aircraft Systems Mechanical, electrical, and avionics subsystems integration Third Edition,” 2008.

[2] K. Parsons, “The Effects of Hot, Moderate, and Cold Environments on Human Health, Comfort, and Performance Third Edition Human Thermal Environments.”

[3] C. Müller and D. Scholz, “The Vapor Compression Cycle in Aircraft Air Conditioning Systems”, doi: 10.48441/4427.2055.

[4] A. S. J. van Heerden, D. M. Judt, S. Jafari, C. P. Lawson, T. Nikolaidis, and D. Bosak, “Aircraft thermal management: Practices, technology, system architectures, future challenges, and opportunities,” Jan. 01, 2022, Elsevier Ltd. doi: 10.1016/j.paerosci.2021.100767.

[5] D. B. Doman, “Rapid mission planning for aircraft thermal management,” in AIAA Guidance, Navigation, and Control Conference 2015, MGNC 2015 - Held at the AIAA SciTech Forum 2015, American Institute of Aeronautics and Astronautics Inc., 2015. doi: 10.2514/6.2015-1076.

[6] H. Zhang, Q. Wu, S. Feng, S. Dong, and Z. Gao, “Vapor Compression Refrigeration System for Aircrafts: Current Status, Large-

Temperature-Range Challenges and Emerging Auto-Cascade Refrigeration Technologies," Aug. 01, 2025, Multidisciplinary Digital Publishing Institute (MDPI). doi: 10.3390/aerospace12080681.

[7] R. H. Aungier, "TURBINE AERODYNAMICS AXIAL-FLOW AND RADIAL-INFLOW TURBINE DESIGN AND ANALYSIS NEW YORK ASME PRESS 2005 Downloaded From: http://ebooks.asmedigitalcollection.asme.org/pdfaccess.ashx?url=/data/books/802418/ on 04/17/2017 Terms of Use: h." [Online]. Available:

[8] R. H. Aungier, "CENTRIFUGAL COMPRESSOR STAGE PRELIMINARY AERODYNAMIC DESIGN AND COMPONENT SIZING Downloaded From: http://proceedings.asmedigitalcollection.asme.org/ on 01/28/2016 Terms of Use: http://www.asme.org/about-asme/terms-of-use." [Online]. Available: http://www.asme.org/about-asme/terms-of-use

[9] R. H. . Aungier, Centrifugal compressors : a strategy for aerodynamic design and analysis. ASME Press, 2000.

[10] H. W. Oh, E. S. Yoon, and M. K. Chung, "An optimum set of loss models for performance prediction of centrifugal compressors," Proceedings of the Institution of Mechanical Engineers, Part A: Journal of Power and Energy, vol. 211, no. 4, pp. 331–338, 1997, doi: 10.1243/0957650971537231.

[11] S. L. Dixon and C. A. Hall, "Fluid Mechanics and Thermodynamics of Turbomachinery Seventh Edition

Numerical Performance Analysis of Flow Field Designs for Large-Area PEM Fuel Cells in Heavy-Duty Vehicle Applications

Mohammed Alobeid [1,2,*], Merve Menteş[1,2], Furkan Çetiner[1,2], Selahattin Çelik[1,2]

[1] *Faculty of Engineering and Natural Sciences, Ankara Yıldırım Beyazit University, Ankara 06010, Türkiye*

[2] *Hydrogen Technologies and Energy Research Centre (H2 TEAM), Ankara Yıldırım Beyazit University, Ankara 06010, Türkiye*

***Contact:** mohammed.alobed@gmail.com

Abstract Proton exchange membrane (PEM) fuel cells are a promising powertrain technology for heavy-duty vehicles due to their high efficiency and zero-emission operation; however, scaling them to large active areas introduces challenges in reactant distribution, pressure drop, and thermal and electrochemical uniformity. This study numerically investigates the impact of flow-field design on a 162 cm² PEM fuel cell using a three-dimensional multiphysics model, comparing wavy parallel and serpentine configurations under identical conditions. Results indicate that the serpentine flow field enhances reactant transport and achieves higher current density and improved polarization performance but incurs greater pressure losses and reduced spatial uniformity, whereas the wavy parallel design provides lower pressure drop and more uniform temperature distribution with slightly lower electrochemical performance. These findings highlight the trade-off between performance and transport losses and provide practical guidance for selecting flow-field architectures in large-area PEM fuel cells for high-power automotive applications.

Keywords: PEM fuel cell, flow field design, numerical modelling, heavy-duty vehicles, performance analysis

I. INTRODUCTION

Over the past decades, growing global energy demand and the urgent need to reduce carbon emissions have accelerated the search for sustainable energy solutions. Hydrogen has emerged as a promising clean energy carrier capable of supporting several fuel cell technologies. Among these, alkaline fuel cells offer structural simplicity but suffer from carbon dioxide sensitivity, while solid oxide fuel cells achieve high efficiency but require elevated operating temperatures. In contrast, proton exchange membrane fuel cells (PEMFCs) operate at relatively low temperatures (typically below 100 °C), provide rapid startup, and offer compact system design, making them highly suitable for transportation and stationary power applications. Moreover, PEMFCs convert hydrogen and oxygen directly into electricity while emitting only water and heat, combining high efficiency with zero-emission operation [1–3].

Within PEM fuel cells, the flow field design plays a pivotal role in determining overall performance. Flow fields govern reactant distribution, liquid water removal, thermal regulation, and current density uniformity across the active area. Conventional configurations such as serpentine, parallel, and interdigitated channels each present inherent trade-offs between pressure drop, mass transport, and flooding behaviour [4]. In addition to geometric considerations, manufacturing constraints and material selection significantly influence the scalability and durability of flow field plates [5].

Early experimental investigations demonstrated that enhancing through-plane convection and improving water removal can significantly improve cell performance, particularly when operating conditions such as humidification and flow rate are properly controlled [6]. Subsequent studies showed that multistage serpentine routing can improve reactant delivery and product removal compared with conventional serpentine layouts [7], while hybrid or compound flow-field architectures can achieve serpentine-level performance while maintaining improved distribution uniformity [8]. At the stack scale, performance has been shown to depend on combined geometric metrics such as channel edge length and opening ratio rather than a single design parameter [9].

To overcome the limitations of conventional layouts, recent research has focused on engineered non-uniform geometries and optimization-based design strategies. Leaf-vein-inspired flow fields optimized through surrogate modeling and particle swarm optimization demonstrated enhanced distribution uniformity and improved overall performance [10]. Locally modified channel structures and obstacle-based designs strengthen convective transport and water removal, leading to measurable power-density improvements [11]. Constructal-theory-based channel architectures and topology optimization methods have further shown that transport-optimal geometries can simultaneously reduce pressure losses while improving reactant distribution [12,13].

Additional studies have explored contraction–expansion channel layouts and staged routing concepts to improve net power output when pumping losses are considered [14]. Thermal management has also been integrated into flow-field design, with fractal cooling channels reducing temperature gradients and cooling-side pressure drop while improving temperature uniformity [15]. Modified interdigitated and

ribbed channel concepts enhance through-plane transport, increase oxygen availability, and mitigate liquid water accumulation at high current densities [16]. More recently, three-dimensional porous or mesh flow fields have demonstrated improved oxygen availability and current density uniformity while maintaining favorable pressure characteristics [17]. Periodic disturbances introduced through wave or sinusoidal channels, optimized using evolutionary algorithms, have been shown to enhance net power density by improving mass transfer in parallel flow configurations [18]. Automated biomimetic design pipelines combining topology optimization and pattern synthesis have further demonstrated significant performance gains while maintaining low pressure losses [19].

Complementary approaches have focused on introducing controlled flow perturbations to improve reactant access and water removal while managing pressure losses. Constriction–enlargement channel strategies balance electrochemical gains against added pressure losses to improve net performance [20]. Droplet-based channel structuring improves drainage and mass transport, achieving substantial power density improvements compared with baseline configurations [21]. Hybrid distribution strategies combining parallel supply with serpentine forcing aim to retain uniformity while preserving high-current performance [22]. Collectively, these studies indicate that effective flow-field development requires pressure-drop-aware optimization and multi-objective design strategies to ensure that improvements in local transport translate into net system performance gains [23].

Despite these innovations, a gap remains: large-area PEMFCs for heavy-duty vehicles still lack designs that simultaneously achieve high current density, low pressure drop, and uniform performance. Our study addresses this by comparing wavy parallel and serpentine designs specifically for large-scale applications, filling this critical gap.

II. NUMERICAL MODEL AND METHODOLOGY

A. Fuel Cell Geometry and Flow Field Designs

A three-dimensional PEM fuel cell model with an active area of 162 cm² was developed. Two different flow field designs were considered for both the anode and cathode sides:

• Flow Field Design A: Conventional parallel-channel configuration

• Flow Field Design B: Modified serpentine-type configuration optimized for enhanced mass transport

The detailed geometries of the flow fields are shown in Fig. 1, where channel width, rib width, and channel depth were kept consistent to isolate the effect of flow field topology.

B. Governing Equations and Physical Models

Reasonable model assumptions simplify calculations and reduce calculation time, and the model assumptions are as follows:

- ✓ Both gas flow and coolant flow are incompressible and laminar flow
- ✓ All gases are considered ideal gases
- ✓ Gas diffusion follows Fick's Law of Binary Diffusion
- ✓ The PEMFC operates at a steady state
- ✓ all variations occur only in the X-direction, and vector quantities reduce to scalar components

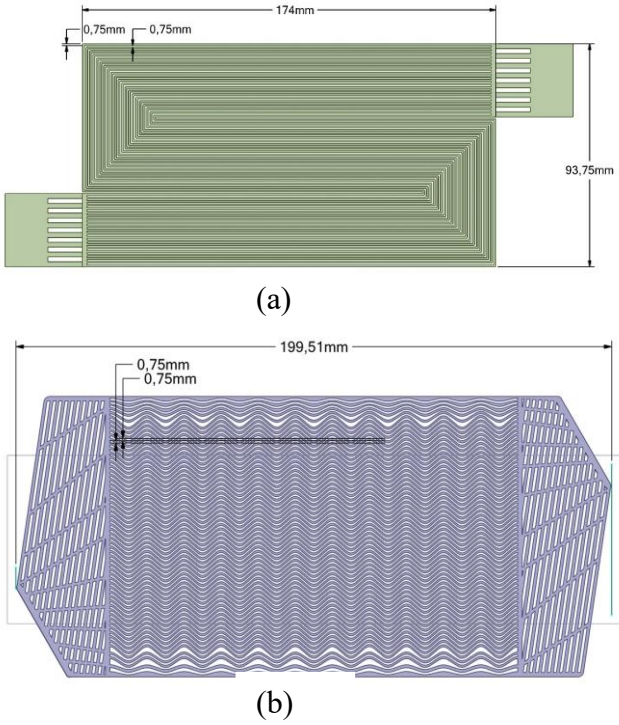

Fig. 1 Two different flow field designs (a) Modified serpentine-type, (b) parallel-channel configuration

1) Conservation equations

A) Mass conservation

The mass conservation equation of the gas mixture is as follows (solved in Channel, GDL, and CL):

$$\nabla(\rho_g u_g) = S_g$$

ρ_g: Gas density (assumed incompressible).
u_g: Velocity vector of the gas.
S_g: Source term representing mass production or consumption, such as from chemical reactions.

The continuity equation for the gas mixture is derived from the principle of mass conservation, ensuring that any change in mass within a control volume is balanced by the mass inflow, outflow, and source terms. Assuming incompressible flow simplifies the density to be constant, while the source terms account for mass generated or consumed by electrochemical reactions.
Mass Conservation for Coolant (solved in CC):

$$\nabla(\rho_w u_w) = 0$$

ρ_w: Coolant density (assumed constant due to incompressibility).
u_w: Coolant velocity vector.

The continuity equation for the coolant assumes no mass generation or consumption under steady-state conditions. It states that the divergence of the coolant mass flux is zero, ensuring conservation of flow. The incompressibility assumption keeps the density constant, and steady-state operation removes any time dependency

B) Momentum conservation

The momentum conservation equation of the gas mixture is as follows in Brinkman–Forchheimer form (solved in, Channel, GDL, and CL):

$$\rho(u \cdot \nabla)u = -\nabla p + \nabla \cdot \left[\mu_{eff}(\nabla u + (\nabla u)^T)\right] - \mu K^{-1}u - \rho c_F \mid u \mid u + S_u$$

ε^2: Accounts for the reduced flow area in the porous structure.
P_g: Gas pressure.
μ_g: Dynamic viscosity of the gas.
S_u : Source term (e.g., from reaction momentum transfer).
In GDL/CL, keep permeability **K**(scalar or tensor).

The Navier-Stokes equation for gas flow, adapted for porous media through porosity ε^2, balances inertial forces, pressure forces, viscous forces, and external momentum sources. The steady-state assumption removes time derivatives, and the laminar flow assumption simplifies the equation by neglecting turbulence effects.
The momentum conservation equation of the coolant is as follows (solved in CC):

$$\rho_c(\mathbf{u}_c \cdot \nabla)\mathbf{u}_c = -\nabla p_c + \mu_c \nabla^2 \mathbf{u}_c + \mathbf{S}_{u,c}$$

P_w: Coolant pressure.
μ_w: Coolant dynamic viscosity.

No porosity term as the coolant flow is not in a porous medium and Laminar and steady-state assumptions are applied

C) Species transport (Channel, GDL, CL)

The gas species transport conservation equation is as follows (solved in Channel, GDL, CL):

$$\nabla \cdot (\rho u Y_i) = \nabla \cdot \left(\rho D_{i,\text{eff}} \nabla Y_i\right) + S_i$$

Y_i: Mass fraction of species i.
D_i^{eff} : Effective diffusion coefficient (accounts for porous media).
S_i: Source term (e.g., species production/consumption in reactions).

D) Dissolved water in membrane/ionomer (CL, MEM)

This equation, derived from Fick's Law of Diffusion and species conservation, tracks the transport of species i in the gas mixture. It also represents another form of the Navier-Stokes equation for the coolant, balancing inertial, pressure, and viscous forces in the coolant flow. The assumption of ideal gases allows the use of Y_i for species fractions, and diffusion follows Fick's law, valid under steady-state and laminar flow conditions
Dissolved water as follows (solved in CL, MEM):

$$\mathbf{N}_\lambda = \underbrace{\frac{n_d}{F}\mathbf{i}_m}_{\text{electro-osmotic drag}} - \underbrace{\frac{\rho_{\text{dry}}}{EW} D_{\lambda,\,\text{eff}} \nabla\lambda}_{\text{back diffusion}}$$

I_{ion} : Ionic current density
λ: Membrane water content
ρ_{mem}: Dry film density of the membrane.
D_{eff} : Effective dissolved water diffusivity.
EW: Equivalent mass of membrane.
S_{mw}: Membrane water source term.

E) Energy conservation (all domains)

This equation describes the transport of water in the membrane, based on ionic current density and diffusivity
The energy conservation equation is as follows (all):

$$\nabla \cdot \left(\rho c_p \mathbf{u} T\right) = \nabla \cdot (k_{\text{eff}} \nabla T) + S_T$$

T : Temperature
k_{eff} : Effective thermal conductivity
$C_{p,w}$, $C_{p,l}$, $C_{p,g}$: Specific heat capacities of coolant, liquid, and gas, respectively
S_T : Thermal source term
s: Liquid water saturation (fraction of pore volume filled with liquid water /gas
ϵ : Porosity of the medium.

F) Liquid water transport, pressure, and capillarity

This equation describes the energy conservation with heat flux and sources.
Liquid water volume fraction as follows (solved in channel):

$$\nabla \cdot (\rho_l \mathbf{u}_l) = S_l$$

ρ_l: Liquid water density.
u_l: Liquid water velocity.
s : Liquid water saturation.

This equation represents and ensures the conservation of liquid water volume fraction.
Liquid pressure is as follows (solved in GDL, CL):

$$\mathbf{u}_l = -\frac{K k_{rl}(s)}{\mu_l} \nabla p_l$$

P_l : Liquid pressure.
μ_l : Dynamic viscosity of the liquid.
K : Intrinsic permeability.
S_l : Liquid pressure source term.

This equation describes the liquid pressure distribution governed by Darcy's law for flow through porous media.
The capillary pressure P_c is defined as follows

$$P_c = P_g - P_l$$

P_g : Gas pressure.
P_l : Liquid pressure.
P_c : Capillary pressure.

This equation defines the capillary pressure difference between the gas and liquid phases.
The liquid water saturation (s) are as follows

$$P_c = \sigma |\cos\ \theta| \left(\frac{\epsilon}{K}\right)^{0.5} J(s)$$
$$J(s) = 1.417s + 2.12\ s^2 + 1.263\ s^3$$

σ : Surface tension coefficient.
θ : Contact angle.
$J(s)$: Saturation function

This equation represents liquid water saturation as a function of surface tension, contact angle, and other parameters.

2) Electrochemistry

A) Charge conservation (solid - membrane potentials)

Electrical charge of electron (Solid Phase Potential) and proton (Membrane Phase Potential) can be written as follows:

$$\nabla \cdot \left(\sigma_{s,\text{eff}} \nabla \phi_s\right) = -S_{ct}$$

$$\nabla \cdot \left(\sigma_{m,\text{eff}} \nabla \phi_m\right) = +S_{ct}$$

ϕ_{sol}, ϕ_{mem} : phase potential of the solid material, and membrane .
$\kappa_{sol}, \kappa_{mem}$: electrical conductivity of the solid and membrane.
S_{sol}, S_{mem} : source term associated with the volumetric exchange current density for the solid and the proton current for the membrane.

The MEM electrical conductivity κ_{mem} is determined by an empirical correlation as follows:

$$\kappa_{\text{mem}} = (0.514\lambda - 0.326)\exp\left(1268\left(\frac{1}{303} - \frac{1}{T}\right)\right)$$

λ : Membrane water content.
T : Temperature.

B) Butler–Volmer kinetics

The electrochemical reaction rates are given by the Butler-Volmer equation:

$$J_a = J_{0,a}^{\text{ref}} \left(\frac{[A]}{[A]_{\text{ref}}}\right)^{0.5} \left[\exp\left(\frac{2\alpha_a^{\text{an}} F \eta_{\text{an}}}{RT}\right) - \exp\left(\frac{-2\alpha_a^{\text{an}} F \eta_{\text{an}}}{RT}\right)\right]$$

$$J_c = J_{0,c}^{\text{ref}} \left(\frac{[C]}{[C]_{\text{ref}}}\right)^{0.5} \left[\exp\left(\frac{2\alpha_c^{\text{cat}} F \eta_{\text{cat}}}{RT}\right) - \exp\left(\frac{-2\alpha_c^{\text{cat}} F \eta_{\text{cat}}}{RT}\right)\right]$$

Difference between the solid and membrane phase potentials at the anode

$$\eta_{\text{an}} = \phi_{\text{sol}} - \phi_{\text{mem}}$$

Overpotential at the cathode is determined by the reversible cell voltage and the potentials of solid and membrane.

$$\eta_{\text{cat}} = E_{rev} - \phi_{\text{sol}} + \phi_{\text{mem}}$$

J_a, J_c : Anodic reaction rate and Cathodic reaction rate
$J_{0,a}^{ref}, J_{0,c}^{ref}$: Reference anode and cathode exchange current density.
$[A], [C]$: Concentration of hydrogen and oxygen.
$\eta_{an}\ \eta_{cat}$: Anodic and cathodic activation overpotential.
F, R, T : Faraday constant, gas constant, temperature.

Where Erev represents the reversible thermodynamic cell voltage, given by the Nernst equation:

Thermodynamic analysis of Total heat flux in PEMFC
The chemical energy supplied by the gases depends on the enthalpy of the global reaction At standard conditions (T^0=298 K, P^0=1 atm, the total reaction enthalpy change is

$$\Delta H^{tot}(T^0, P^0) = \Delta H^0{}_{\text{H}_2\text{O}} - \Delta H^0{}_{\text{H}_2} - \frac{1}{2}\Delta H^0{}_{\text{O}_2}$$

The reference potential E^{tot} for the fuel cell (if all chemical energy were converted to electrical energy) and it is for liquid water: E^{tot}=1.48 V (or 1.47 V at P=1 atm and T=353 K):

$$E^{tot} = -\frac{\Delta H^{tot}(T,P)}{2F}$$

According to the second law of thermodynamics, only Gibbs free energy can be converted into electrical energy. The ideal open circuit voltage E^{rev} is expressed as:

$$E^{rev} = -\frac{\Delta G^{tot}(T,P)}{2F}$$

For ideal gases, $\Delta G^{tot}(T,P)$ is computed using:

$$\Delta G^{tot}(T,P) = \Delta G^{0} - \int_{298\mathrm{K}}^{T} \Delta S^{tot}(T,P^{0}) \cdot dT + RT\ln\left(\frac{a_{\mathrm{H_2O}}}{a_{\mathrm{H_2}}\, a_{\mathrm{O_2}}^{1/2}}\right)$$

ΔG^{0} : Gibbs free energy change at standard conditions.
ΔS^{tot} : Reaction entropy , For PEMFCs at T=298 we assume: $\Delta S^{tot} = \Delta S^{0}$
$a_i = \frac{P_i}{P^0}$ for gases, where P_i is the partial pressure of species i and P^0 is standard pressure. For liquid-phase water $a_{H_2O} = 1$

To end with thermodynamic cell voltage:

$$E_{\mathrm{rev}} = 1.229 - 0.9 \times 10^{-3}(T - 298.15) + \frac{RT}{2F}\left(\ln P_{\mathrm{H_2}}^{\mathrm{i}} + 0.5\ln P_{\mathrm{O_2}}^{\mathrm{i}}\right)$$

3) Energy Balance

The energy conservation equation integrates all heat sources and sinks within the PEMFC layers:

$$\nabla \cdot \left(k_{\mathrm{eff,CL}} \nabla T\right) + S_{T,\mathrm{CL}} = 0$$

Heat generation terms include entropy changes, activation losses, and ohmic heating. Analytical solutions will quantify the total heat flux and temperature distribution across the PEMFC.

The governing equation in the Catalyst Layer (1D) is:

$$\nabla \cdot \left(\rho c_p \mathbf{u} T\right) = \nabla \cdot \left(k_{\mathrm{eff,CL}} \nabla T\right) + S_{T,\mathrm{CL}}$$

S_T in the catalyst layer, based on the equation

$$J_a = \underbrace{J_{0,a}^{\mathrm{ref}}\left(\frac{[A]}{[A]_{\mathrm{ref}}}\right)^{0.5}\left[\exp\left(\frac{2\alpha_a^{\mathrm{an}} F \eta_{\mathrm{an}}}{RT}\right) - \exp\left(\frac{-2\alpha_a^{\mathrm{an}} F \eta_{\mathrm{an}}}{RT}\right)\right]}_{\text{Activation Heat}} + \underbrace{\sigma_{eff}\left(\frac{d\phi_{sol}}{dx}\right)^2}_{\text{Ohmic Heat}} + \underbrace{\frac{J_{0,a}^{\mathrm{ref}} T \Delta S_a}{2F}}_{\text{Reaction Enthalpy}}$$

C. Simulation Setup

For the presented proton exchange membrane fuel cell (PEMFC) model, the simulation setup was configured with a high degree of accuracy to represent the electrochemical, thermal, and fluid-dynamics behavior. From material selection to region-specific parameterization, the configuration of each component was designed meticulously to ensure physical fidelity and numerical stability.

D. Material Properties

The materials used in the model (Table 1) represent the various functional layers of the PEMFC. The catalyst layer was defined with intermediate density and thermal conductivity, reflecting platinum-loaded carbon composites. The current collector and copper regions exhibit very high electrical conductivity, which is essential for efficient current collection. The electrolyte shows nearly zero electrical conductivity (1e-16 S/m), confirming its ionic nature and its electrically insulating behavior against electron transport. The diffusion layers and microporous layers exhibit similar thermal and electrical properties, facilitating adequate gas transport and capillary behavior.

TABLE I. Material Properties

Material Name	Density [kg/m³]	Specific Heat Cp [J/(kg·K)]	Thermal Conductivity [W/(m·K)]	Electrical Conductivity [S/m]
Catalyst	2010	710	8	1000
Current Collector	1880	691	85.5	84000
Copper	8978	381	387.6	5.8e+07
Diffusion Layer	440	710	1.7	1000
Electrolyte	1980	2000	2	1e-16
MPL	440	710	1.7	1000

TABLE 2. Boundary Conditions

Bound. Type	Region	Mass Flow	Temp. [K]	Mass Frac. ($H_2/O_2/H_2O$)	Press. (Gauge) [Pa]

		Rate [kg/s]			
Inlet	Anode	2.0×10^{-5}	353	0.20 / 0.00 / 0.80	—
Inlet	Cathode	1.2×10^{-4}	353	0.00 / 0.21 / 0.30	—
Outlet	Anode	—	—	—	100000
Outlet	Cathode	—	—	—	100000

E. Boundary Conditions

The applied boundary conditions (Table 2) were derived from realistic PEMFC operating conditions. At the anode inlet, hydrogen was injected at a low mass flow rate (2.0×10^{-5} kg/s) at 353 K with a composition of 20% hydrogen and 80% water vapor. At the cathode, air was supplied at a higher flow rate (1.2×10^{-4} kg/s) with 21% oxygen and 30% water vapor . The outlets at both sides were set to a gauge pressure of 100,000 Pa, corresponding to atmospheric exhaust conditions. These inlet compositions enable the simulation of humidified fuel and oxidant streams, which are critical for membrane hydration and reaction efficiency.

III. RESULTS AND DISCUSSION

The numerical study was conducted to compare the performance of two flow-field configurations parallel and serpentine for a 162 cm² PEM fuel cell, and to assess how the flow-field architecture influences electrochemical output and the associated transport phenomena. The results presented in this section therefore emphasize the comparative performance trends between the two designs. Because the serpentine configuration demonstrated superior electrochemical performance under identical operating conditions, the detailed field results reported in Graphs 3–9 (e.g., voltage-related distributions and associated contours) are presented for the serpentine case to provide deeper insight into the behavior of the higher-performing design.

A. Polarization

The polarization curves provide the primary basis for comparing the two flow fields in terms of electrochemical performance. As shown in Figure 2, both configurations exhibit stable behavior across the investigated voltage range; however, a clear performance difference emerges at intermediate voltages. At 0.6 V, the parallel design delivers a current density of 1.38 A/cm², whereas the serpentine design reaches 1.60 A/cm², indicating a higher power capability for the serpentine geometry under the same boundary conditions. This improvement suggests that the serpentine flow field enhances reactant distribution and mitigates local transport limitations more effectively than the parallel layout, resulting in higher achievable current density. Based on this performance advantage, the subsequent results (Graphs 3–9) focus on the serpentine configuration to highlight the spatial distributions and transport characteristics corresponding to the best-performing design.

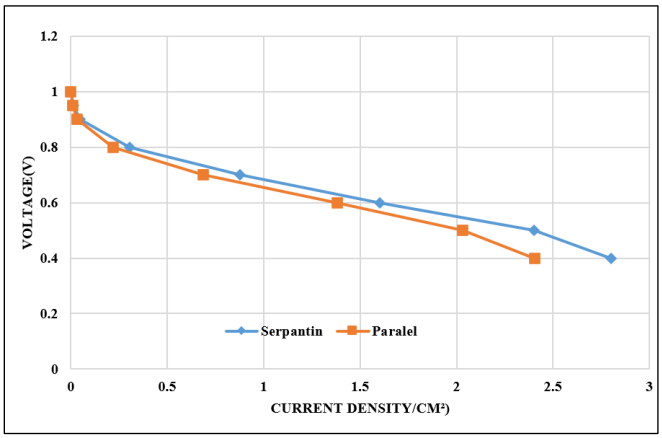

Fig. 2 Polarization plot for the two flow designs with 162 cm² active area.

B. Channel Pressure

Turning to the gas transport field, Figure 3 shows the pressure distribution within the channels. On the anode side, a pressure drop of approximately 500 Pa is observed along the flow path. Considering an inlet pressure of 1 bar, this drop is relatively small and indicates efficient hydrogen distribution with minimal viscous losses. On the cathode side, the pressure drop is higher and reaches approximately 2000 Pa, which remains within acceptable limits for PEMFC operation. This increased pressure gradient can be attributed to three factors: the higher air flow rate, the serpentine channel geometry, and the applied 1 bar back-pressure condition. The observed values confirm realistic flow resistance and validate the channel design under typical operating conditions.

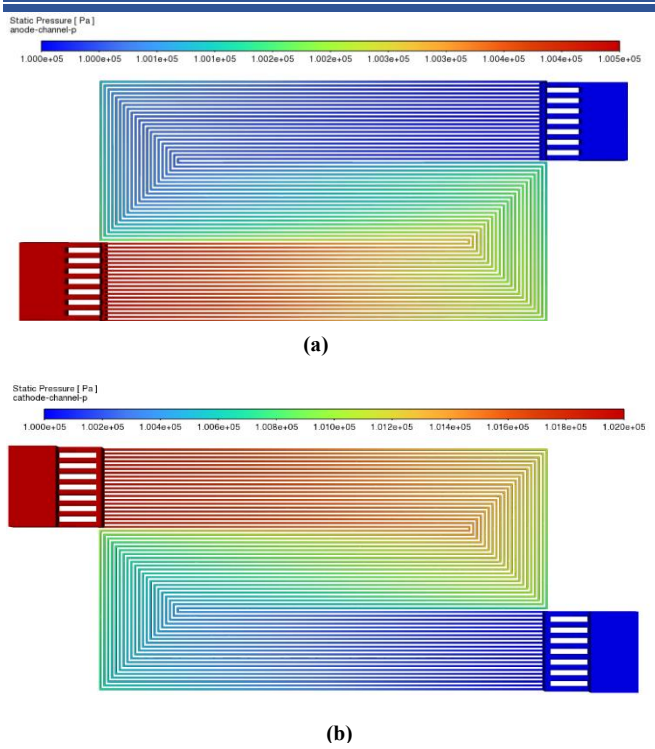

Fig. 3 Channel pressure contour: (a) Anode channel. (b) Cathode channel.

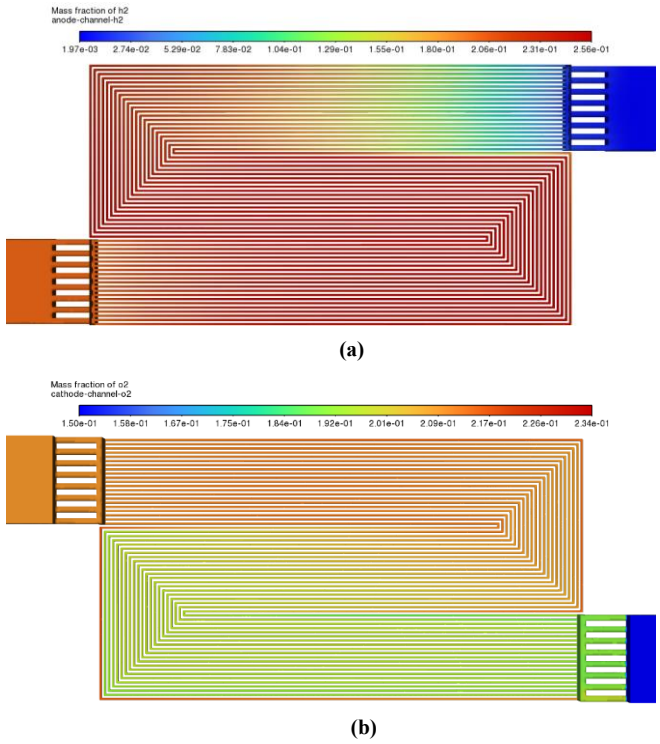

Fig. 4 Channel species ratio: (a) Anode H_2 mass fraction. (b) Cathode O_2 mass fraction.

D. Temperature Contour

As shown in Figures 5 , the temperature distribution between the catalyst layers and the bipolar plates provides important insight into the thermal behavior of the PEMFC system under operating conditions. As illustrated in Figures 5 (a) and 5 (b), the surface temperature at the microporous layer–catalyst layer interface is analyzed for both the anode and cathode sides. The observed temperature remains well controlled, with a maximum peak value not exceeding 70°C in the catalyst regions. This is particularly important for membrane stability and ionic conductivity, as PEM membranes tend to degrade at elevated temperatures, and this value aligns with typical thermal safety limits for PEM fuel cells. Of special importance is the uniform distribution of the temperature field across the active area. This indicates that the thermal management strategies including material selection, channel design, and convective flow settings effectively mitigate hot-spot formation. Achieving such uniformity is essential to maintain electrochemical stability and prevent rapid membrane degradation.

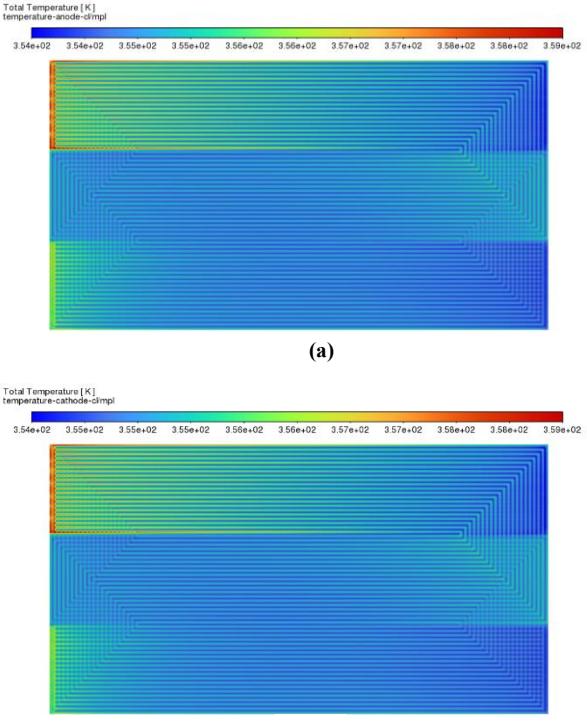

Fig. 5 Catalyst layer temperature contour in CL/MPL: (a) Anode CL. (b) Cathode CL.

E. Reaction Heat Source Contour

The reaction heat source contours shown in Figure 6 present the spatial distribution of thermal energy generated by electrochemical reactions at the catalyst–microporous layer (CL–MPL) interface for both the anode and cathode. On the anode side, the average heat source intensity is approximately 8.8×10^7 W/m³, with peak values reaching 1.0×10^8 W/m³. In contrast, significantly higher thermal generation is observed on the cathode side, with an average of 5.8×10^8 W/m³ and a peak value of approximately 7.7×10^8 W/m³. This difference is consistent with electrochemical principles, since the oxygen reduction reaction (ORR) at the cathode is more exothermic and kinetically more complex than the hydrogen oxidation reaction at the anode. In addition, the relatively uniform heat distribution on both sides reflects effective membrane hydration and reactant diffusion supporting consistent electrochemical activity across the active area.

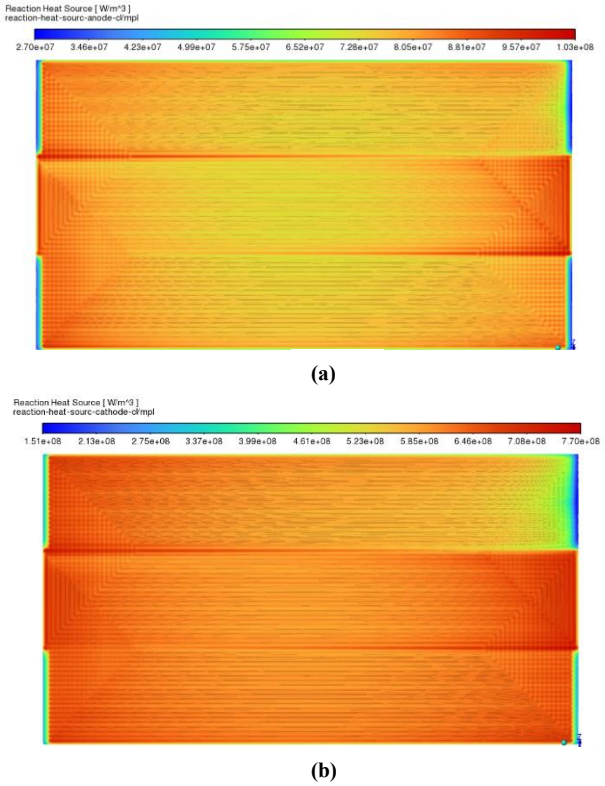

Fig. 6 Reaction heat source contour in CL/MPL: (a) Anode CL/MPL. (b) Cathode CL/MPL.

IV. CONCLUSION

A three-dimensional, coupled multiphysics PEMFC model was developed to investigate how flow-field architecture influences performance and transport behavior in a large-area (162 cm²) single cell under identical operating conditions. Two representative designs a wavy-parallel and a serpentine flow field were evaluated using polarization behavior as the primary performance metric, supported by pressure, species, and temperature distributions. The polarization results show that the serpentine configuration delivers superior electrochemical output at intermediate voltages: at 0.6 V, the parallel design produces 1.38 A cm^{-2}, whereas the serpentine design reaches 1.60 A cm^{-2}. This improvement reflects enhanced reactant distribution and reduced local transport limitations associated with serpentine routing. However, a clear trade-off is observed: while the serpentine geometry improves current density and polarization performance, it incurs higher pressure drop and reduced spatial homogeneity, whereas the wavy-parallel configuration exhibits lower pressure losses and slightly more uniform temperature distribution, supporting reduced auxiliary pumping demand in scaled systems.

From a transport perspective, the serpentine case exhibits realistic channel-scale resistance, with pressure drops of approximately 500 Pa along the anode and 2000 Pa along the cathode, reflecting stronger flow forcing while remaining within acceptable limits. Reactant mass fractions decrease smoothly along the channels, indicating effective utilization and stable electrochemical activity across the active area. The thermal field remains well controlled, with peak catalyst-layer temperatures below 70 °C and a uniform temperature profile, which is critical for membrane durability in large-area operation. Because the serpentine configuration demonstrated the highest electrochemical performance, detailed field distributions were presented for this design to provide deeper insight into the behavior of the higher-performing architecture. Overall, the results provide a clear design guideline for heavy-duty PEMFC applications: serpentine flow fields are preferable when maximizing current density and power is the primary objective, whereas wavy-parallel designs are advantageous when improved spatial uniformity and reduced pumping losses are prioritized.

ACKNOWLEDGMENT

The authors gratefully acknowledge the financial support provided by the Turkish Energy, Nuclear and Mineral Research Agency (TENMAK) under Project No. 1311.

REFERENCES

[1] Xiao, F., Chen, T., Lan, Y., & Chen, Z. (2025). Flow field design and parameter optimization of PEMFC based on leaf vein structure. *Renewable Energy*, *241*, 122317.

[2] Zhang, Z., Wang, C., Chen, C., & Zheng, Z. (2024). Optimal design of locally improved structure for enhancing mass transfer in PEMFC cathode flow field. *International Journal of Hydrogen Energy*, *57*, 798-811.

[3] Zhang, Z., Wang, C., Chen, C., & Zheng, Z. (2024). Optimal design of locally improved structure for enhancing mass transfer in PEMFC cathode flow field. *International Journal of Hydrogen Energy*, *57*, 798-811.

[4] Liu, Z., Li, Q., Yang, S., Zhang, H., Chen, X., Xie, N., ... & Du, W. (2024). Numerical investigation of PEMFC performance based on different multistage serpentine flow field designs. *Chemical Engineering Journal*, *500*, 156951.

[5] Numerical simulation analysis of the performance on the PEMFC with a new flow field designed based on constructal-theory
[6] CFD investigation of the effect of flow field channel design based on constriction and enlargement configurations on PEMFC performance
[7] Bunyan, S. T., Dhahad, H. A., Khudhur, D. S., & Yusaf, T. (2023). The effect of flow field design parameters on the performance of PEMFC: a review. *Sustainability*, *15*(13), 10389.
[8] Xie, Y., Huang, Y., Zeng, J., Gao, T., Ye, D., & Chai, R. (2026). Enhanced performance of PEMFC through novel flow field design and optimization. *International Journal of Heat and Mass Transfer*, *255*, 127792.
[9] Xiao, C., Tian, S., Guo, H., Wang, L., Pan, Y., Yang, S., & Xie, W. (2025). Topology optimization of distribution and collection zones for flow field plate of large-scale PEMFC. *Fuel*, *382*, 133757.
[10] Pedapati, P. R., Dhanushkodi, S. R., Chidambaram, R. K., Taler, D., Sobota, T., & Taler, J. (2024). Design and manufacturing challenges in PEMFC flow fields—a review. *Energies*, *17*(14), 3499.
[11] Chen, X., Chai, F., Hu, S., Tan, J., Luo, L., Xie, H., ... & Qu, Z. (2023). Design of PEMFC bipolar plate cooling flow field based on fractal theory. *Energy Conversion and Management: X*, *20*, 100445.
[12] Choi, J., Park, Y., Park, J., Kim, C., Heo, S., Kim, S. D., & Ju, H. (2025). Innovative flow field design strategies for performance optimization in polymer electrolyte membrane fuel cells. *Applied Energy*, *377*, 124551.
[13] Su, X., Zhang, Q., Xu, L., Hu, B., Wu, X., & Qin, T. (2024). A novel combined flow field design and performance analysis of proton exchange membrane electrolysis cell. *International Journal of Hydrogen Energy*, *61*, 444-459.
[14] Rostami, L., Haghshenasfard, M., Sadeghi, M., & Zhiani, M. (2022). A 3D CFD model of novel flow channel designs based on the serpentine and the parallel design for performance enhancement of PEMFC. *Energy*, *258*, 124726.
[15] Sun, F., Su, D., Li, P., & Dong, X. (2023). A novel 3D fine-mesh flow field design and performance analysis for proton exchange membrane fuel cells. *Journal of Power Sources*, *584*, 233572.
[16] Meng, X., Ren, H., Hao, J., & Shao, Z. (2022). Design and experimental research of a novel droplet flow field in proton exchange membrane fuel cell. *Chemical Engineering Journal*, *450*, 138276.
[17] Li, M., Fu, L., Lin, H., Liu, J., & Zhang, X. (2026). Wave flow field design optimization for enhanced performance of high-temperature PEM fuel cells. *Fuel*, *406*, 137136.
[18] Vazifeshenas, Y., Sedighi, K., & Shakeri, M. (2015). Numerical investigation of a novel compound flow-field for PEMFC performance improvement. *International Journal of Hydrogen Energy*, *40*(43), 15032-15039.
[19] André, J., Claude, E., Sirac, D., Gastaldin, D., & Rossinot, E. (2020). PEMFC flow-field design, channel/land width ratio optimization. *Fuel Cells*, *20*(3), 231-235.
[20] Yan, W. M., Yang, C. H., Soong, C. Y., Chen, F., & Mei, S. C. (2006). Experimental studies on optimal operating conditions for different flow field designs of PEM fuel cells. *Journal of power sources*, *160*(1), 284-292.
[21] Wang, Y., Chen, K. S., Mishler, J., Cho, S. C., and Adroher, X. C., "A review of polymer electrolyte membrane fuel cells: Technology, applications, and needs on fundamental research," *Applied Energy*, vol. 88, pp. 981–1007, 2011.
[22] Yuan, X. Z., Wang, H., Sun, J. C., and Zhang, J., "AC impedance technique in PEM fuel cell diagnosis," *International Journal of Hydrogen Energy*, vol. 32, pp. 4365–4380, 2007.
[23] Litster, S. and McLean, G., "PEM fuel cell electrodes," *Journal of Power Sources*, vol. 130, pp. 61–76, 2004.

Smart De-Icing of Wind Turbine Blades: A Review of Machine Learning and Power Electronics-Based Approaches

Ümran Özge ŞEBİK[1,*], Sıtkı KOCAOĞLU[1],

[1] *Ankara Yildirim Beyazit University, Faculty of Engineering, Department of Energy Systems Engineering, 06010 Ankara, TÜRKİYE*

*Contact: umranozgesebik@aybu.edu.tr

Blade icing is a major operational challenge for wind turbines in cold climates. Ice accumulation reduces aerodynamic performance, decreases power output, increases structural loads, and may create safety risks. Most previous studies focus either on aerodynamic modelling or on environmental analysis. However, integrated smart de-icing systems that combine machine learning and power electronics are still limited and scattered in the literature.

This review examines existing icing detection, prediction, and mitigation approaches with a system-level perspective. First, conventional detection methods based on SCADA data, power curve deviation, and meteorological measurements are summarized. Then, machine learning techniques such as supervised models, deep learning architectures, and physics-informed approaches are discussed in terms of data needs, accuracy, and practical limitations. In parallel, active de-icing technologies—particularly resistive blade heating and converter-based thermal control—are reviewed with emphasis on energy efficiency and control strategies.

The study highlights the potential of integrating machine learning-based decision mechanisms with adaptive power electronic control to reduce unnecessary energy consumption while maintaining reliability. Finally, current research gaps, including limited standardized datasets and insufficient field validation, are identified to support future development of intelligent de-icing systems for cold-climate wind applications.

Keywords: *Wind turbine icing, Smart de-icing, Machine learning, Power electronics*

A Comparative Analysis on Energy Consumption, Economic Growth and Carbon Dioxide Emissions

Şeymanur Başlık[1], Ömer Önder Erat[1], Furkan Soysal[1], Ahmet Uçar[1] and Bülent Yeşilata[1,*]

[1]*Department of Energy Systems Engineering, Ankara Yıldırım Beyazıt University, Etlik-Keçiören/Ankara, Türkiye*

***Contact:** byesilata@aybu.edu.tr

Abstract—Energy consumption is closely linked to economic growth, but it also contributes significantly to carbon dioxide (CO_2) emissions. Understanding this relationship is essential for developing sustainable energy policies. In this study, the interactions between energy consumption, gross domestic product (GDP), population, and CO_2 emissions are analyzed for a diverse group of countries. Key indicators such as energy consumption per capita, GDP per capita, and energy productivity are evaluated to assess differences in energy use and economic performance. In addition, the Kaya identity is applied to decompose CO_2 emissions into four main drivers: population, economic activity, energy intensity, and carbon intensity. The results indicate that although higher energy consumption generally supports economic growth, the relationship varies across countries. Differences in energy efficiency and carbon intensity play a crucial role in shaping emission levels. Some countries achieve high income levels with lower energy use, while others rely on energy-intensive structures. Overall, the findings emphasize that sustainable growth requires both improved energy efficiency and a transition to low-carbon energy systems.

Keywords: Energy consumption, economic growth, CO_2 emissions, Kaya equation, energy intensity, energy-economy relationship

I. INTRODUCTION

Energy has long been recognized as a fundamental driver of economic development, industrialization, and social welfare. As economies grow, their demand for energy increases, which in turn leads to higher levels of greenhouse gas emissions, particularly carbon dioxide (CO_2) [1]. This close interdependence between energy consumption, economic growth, and environmental impact has become one of the central challenges in achieving sustainable development. In this context, understanding how these variables interact is crucial for designing effective energy and climate policies.

Historically, economic expansion has been strongly coupled with rising energy use, especially in industrializing and emerging economies [2]. However, recent technological advancements and policy interventions have demonstrated that this relationship is not strictly fixed. Improvements in energy efficiency, structural economic changes, and the increasing share of renewable energy sources have enabled some countries to partially decouple economic growth from energy consumption and carbon emissions [3], [4]. Despite these developments, significant disparities still exist among countries due to differences in resource availability, technological capacity, and policy frameworks [5].

To better understand these dynamics, analytical tools that can decompose emissions into their underlying drivers are required. One of the most widely used frameworks in this regard is the Kaya identity, which expresses total CO_2 emissions as the product of four key factors: population, economic output per capita, energy intensity, and carbon intensity [6]. This identity provides a systematic way to analyze how demographic, economic, and technological factors contribute to emission trends [7].

The present study aims to comparatively evaluate the relationships between energy consumption, economic growth, and CO_2 emissions across a diverse set of countries. By combining macroeconomic indicators with the Kaya identity framework, the study seeks to reveal structural differences in energy use and emission patterns. Through this approach, it becomes possible to identify not only the scale-related drivers of emissions but also efficiency and technology-related factors that influence national performance. Ultimately, the findings are expected to contribute to a better understanding of how sustainable growth pathways can be achieved under varying economic and energy conditions.

II. METHODS

In this study, the Kaya identity was adopted in order to decompose the main components underlying the total CO_2 emissions of the selected countries. Rather than treating emissions as a single outcome variable, the Kaya approach provides a descriptive accounting framework that enables their analysis through the components of population, income per capita, energy intensity, and carbon intensity [8], [9]. Accordingly, this method was preferred because it allows emission levels to be evaluated not only in relation to economic scale or population size, but also in terms of how much energy economic production requires and how carbon-intensive the energy used is [8]. However, it should be noted that the Kaya identity is not a causal model, but a structural decomposition tool. Thus, the purpose of the present study is not to establish cause-and-effect relationships, but rather to comparatively reveal the components through which emissions are shaped [9].

The basic equation used in the study is as follows:

$$CO_{2_{emit}} = P \times \left(\frac{GDP}{P}\right) \times \left(\frac{E}{GDP}\right) \times \left(\frac{CO_2}{E}\right) \quad (1)$$

The demographic scale of emissions is represented by the population component (P) in the Kaya identity. The quantity of economic value produced per person and the degree of economic welfare are both indicated by income per capita (GDP/P). The quantity of energy needed to maintain economic activity is expressed as energy intensity (E/GDP), which highlights the production structure's energy reliance. In turn, carbon intensity (CO_2/E) represents the carbon characteristics of the energy mix and shows how much of the energy used produces carbon emissions. Therefore, when these four components are considered together, it becomes possible to systematically examine total CO_2 emissions not only in relation to population or income growth, but also in connection with energy efficiency and the carbon structure of the energy system [8], [9].

Since Kaya-based comparative studies have shown that the dominant drivers of emissions may vary across countries, employing a heterogeneous set of countries strengthens the explanatory power of the methodology [10], [11]. Accordingly, the selection of countries was made so as to represent different profiles in terms of the Kaya components. In this context, the sample includes Türkiye, Saudi Arabia, Norway, the United States of America, China, India, South Africa, Niger, Brazil, and Germany. Large-scale economies, high-income industrialized nations, economies with fossil fuel-dominated energy architectures, developing markets, and a low-income reference country can all be assessed using a common analytical framework thanks to this group of nations.

III. RESULTS AND DISCUSSION

During the analysis process, total energy consumption, total CO_2 emissions, population, and gross domestic product (GDP) data for each country were compiled based on the year 2024. Using these indicators, derived performance parameters such as per capita income, energy intensity, and carbon intensity were calculated. Table I reflects the general relationship between economic welfare and energy consumption.

Per capita GDP represents the average level of welfare of individuals in a country. This value is expected to be high in developed countries. As shown in Table I, the United States (66,934 $/person) exhibits one of the highest levels of welfare, whereas Niger (1,369 $/person) reflects the lowest.

Energy use per capita refers to the amount of energy consumed per person. Rather than being classified strictly as "good" or "bad," this indicator provides insights into a country's lifestyle and industrial structure. However, it is anticipated that as welfare increases, this value does not necessarily have to increase proportionally, as efficiency policies may decouple this relationship. For instance, Saudi Arabia (3.5E+11 J/person) and the United States (2.9E+11 J/person) have very high per capita energy consumption, whereas Germany—despite having a per capita income close to that of the United States—maintains a lower level of 1.3E+11 J/person, indicating a more controlled consumption profile.

GDP earned per unit of energy indicates how much economic value (in dollars) is generated per unit of energy consumed. This value is expected to be high, as higher values indicate strong energy efficiency and technological capacity.

TABLE I
COMPARATIVE ANALYSIS OF MACROECONOMIC INDICATORS AND DERIVED ENERGY PERFORMANCE METRICS FOR SELECTED COUNTRIES (2024) [12]

Countries	Total Energy Consumption (GJ)	CO_2 Emissions (million metric tonnes carbon dioxide)	Population (million)	GDP (billion dollars at purchasing power parities)	Energy use per capita (J/person)	GDP earned per unit of energy ($/GJ)	Per capita GDP ($/person)
Türkiye	6,761	414	87.474	3,030	7.7E+10	448.2	34,639
Saudi Arabia	12,528	677	35.300	1,989	3.5E+11	158.8	56,346
Norway	1,216	37	5.576	372	2.2E+11	305.9	66,714
United States	99,762	4,782	339.616	22,732	2.9E+11	227.9	66,934
China	179,971	12,716	1,419.321	29,260	1.3E+11	162.6	20,615
India	39,554	2,872	1,450.936	11,498	2.7E+10	290.7	7,925
South Africa	5,691	438	64.007	799	8.9E+10	140.4	12,483
Niger	49.7	3	27.032	37	1.8E+09	743.8	1,369
Brazil	11,275	559	211.999	3,319	5.3E+10	294.4	15,656
Germany	10,471	576	83.473	4,456	1.3E+11	425.5	53,383

In this regard, Türkiye (448.2 $/GJ) and Germany (425.5 $/GJ) demonstrate high efficiency, whereas South Africa (140.4 $/GJ) and China (162.6 $/GJ) produce relatively less economic value per unit of energy, indicating reliance on energy-intensive industries.

Fig. 1 illustrates the relationship between energy use per capita and GDP per capita for selected countries, providing insights into the linkage between energy consumption and economic welfare. Overall, a positive correlation can be observed, indicating that higher levels of energy consumption are generally associated with higher income levels. This trend is particularly evident in industrialized and developed economies, where energy use plays a critical role in sustaining economic activity.

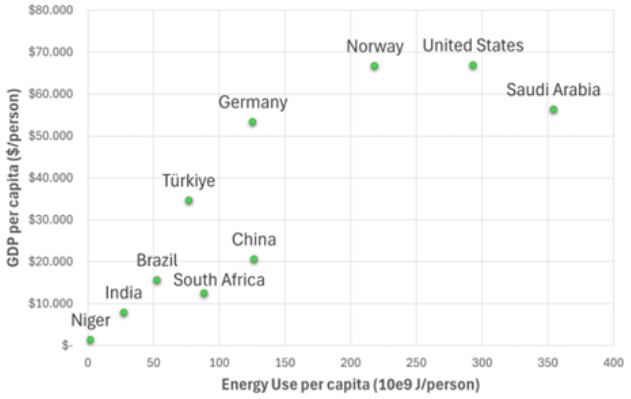

Fig. 1 GDP per capita as a function of Energy Use per capita for selected countries based on data given in Table 1

However, the relationship is not strictly linear across all countries. For instance, while the United States and Norway are positioned at high levels of both energy consumption and income, Germany achieves a comparable level of economic output with significantly lower energy use per capita. This divergence suggests that improvements in energy efficiency and technological advancement can weaken the direct dependence of economic growth on energy consumption.

In contrast, countries such as Saudi Arabia exhibit very high energy consumption levels without a proportionally higher economic output, indicating an energy-intensive economic structure. This reflects a lower level of energy productivity, where large amounts of energy are required to generate economic value.

Developing economies, including China, India, and South Africa, are located in the intermediate region of the graph, characterized by increasing energy consumption but relatively lower income levels. This pattern reflects ongoing industrialization processes, where rising energy demand has not yet fully translated into high economic welfare.

At the lower end of the spectrum, countries such as Niger display both low energy consumption and low GDP per capita, highlighting structural limitations such as restricted energy access and limited economic capacity.

In summary, while Fig. 1 confirms the existence of a general positive relationship between energy consumption and economic welfare, it also demonstrates that this relationship varies significantly depending on factors such as energy efficiency, technological development, and economic structure. These findings imply that economic growth does not necessarily require proportional increases in energy consumption, and that a decoupling between energy use and economic output is achievable through efficiency-oriented and sustainable energy policies.

Fig. 2 illustrates the relationship between CO_2 emissions per capita and GDP per capita for the selected countries, providing further insight into the environmental dimension of economic development. While a general upward trend can be observed, the relationship between carbon emissions and income levels appears more scattered compared to the energy–income relationship presented in Fig. 1.

TABLE II
DECOMPOSITION OF CO_2 EMISSIONS BASED ON THE KAYA IDENTITY FOR SELECTED COUNTRIES (2024) [12]

Countries	P (million)	GDP/P ($1000/person)	E/GDP (GJ/$1000 GDP)	CO_2/E (tonnes/GJ)	CO_2 (million tonnes)	GDP (billion dollar)	Energy Consumption (GJ)
Türkiye	87.474	0.035	2.23	0.061	414	3,030	6,760,857,000
Saudi Arabia	35.300	0.056	6.30	0.054	677	1,989	12,528,309,000
Norway	5.576	0.067	3.27	0.030	37	372	1,215,887,000
United States	339.616	0.067	4.39	0.048	4.782	22,732	99,761,515,000
China	1,419.321	0.021	6.15	0.071	12.716	29,260	179,970,663,000
India	1,450.936	0.008	3.44	0.073	2.872	11,498	39,554,363,000
South Africa	64.007	0.012	7.12	0.077	438	799	5,691,259,000
Niger	27.032	0.001	1.34	0.060	3	37	49,742,000
Brazil	211.999	0.016	3.40	0.050	559	3,319	11,274,898,000

Germany	83.473	0.053	2.35	0.055	576	4,456	10,471,276,000

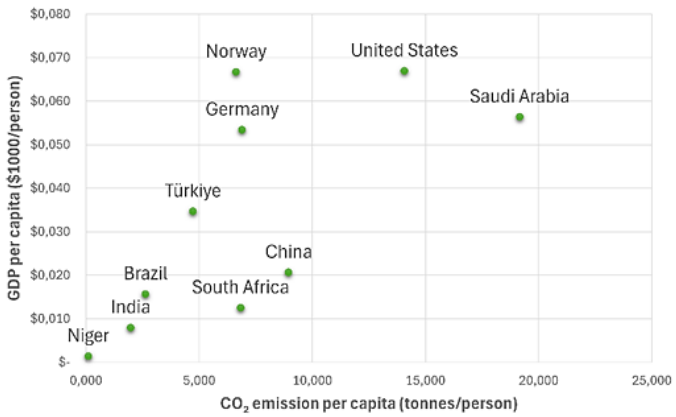

Fig. 2 GDP per capita as a function of carbon emission per capita for selected countries based on data given in Table 2

High-income countries such as the United States and Saudi Arabia exhibit both high GDP per capita and high CO_2 emissions per capita, indicating carbon-intensive economic structures. In contrast, Norway stands out as an exceptional case, achieving a high level of economic welfare with relatively lower emissions per capita, which reflects the effective use of low-carbon energy sources.

Germany also demonstrates a relatively balanced position, maintaining high income levels with moderate emission values, suggesting a more efficient and environmentally conscious energy system. Türkiye appears in the mid-range, indicating a developing economy with moderate emissions and income levels.

Developing countries such as China, India, and South Africa are located in the intermediate region of the graph, where economic growth is accompanied by increasing emissions. However, their income levels remain lower compared to developed economies, highlighting the ongoing industrialization process. At the lower end, Niger exhibits both very low emissions and low income, reflecting structural limitations rather than sustainability-driven performance.

Overall, Fig. 2 suggests that economic growth is often associated with increased carbon emissions; however, this relationship is not uniform across countries. Differences in energy mix, technological advancement, and efficiency policies play a crucial role in determining whether economic growth leads to higher environmental impact or can be achieved in a more sustainable manner.

The decomposition of total emissions into population, income, energy intensity, and carbon intensity enables a structural evaluation of emission dynamics across countries. The findings in this context are presented in Table II.

The Kaya Identity decomposes total CO_2 emissions into four components: population (P), GDP per capita (GDP/P), energy intensity (E/GDP), and carbon intensity (CO_2/E). While population and per capita income explain the scale of emissions, the E/GDP parameter—indicating how much energy is used to generate a given economic output—provides a clearer distinction of performance differences among countries.

As shown in Table II, South Africa (7.12 GJ/$1000GDP), Saudi Arabia (6.30 GJ/$1000GDP), and China (6.15 GJ/$1000GDP) exhibit high energy intensity, whereas Türkiye (2.23 GJ/$1000GDP) and Germany (2.35 GJ/$1000GDP) maintain relatively lower values. This suggests that emission differences are not solely due to economic scale but also arise from production structures and efficiency levels.

South Africa presents the highest-risk profile, with both the highest energy intensity (7.12 GJ/$1000GDP) and carbon intensity (0.077 tonnes/GJ). Its emission problem is not driven by economic scale but rather by a carbon-intensive and inefficient production model. Similarly, despite its high per capita income, Saudi Arabia exhibits very high energy intensity, indicating that its prosperity is sustained through excessive energy consumption and a highly energy-dependent economy.

China and the United States are the two countries with the highest total emissions. However, China's disadvantage lies in the combination of its massive population with high energy intensity (6.15 GJ/$1000GDP) and high carbon intensity (0.071 tonnes/GJ), reflecting a fossil-fuel-dependent production model. In the United States, the issue is not only scale; the combination of high income and relatively high energy intensity (4.39 GJ/$1000GDP) indicates that its high standard of living is maintained through an energy-intensive model.

Norway, despite its very high income level (0.067 $1000/person), has the lowest carbon intensity (0.030 tonnes/GJ). By successfully decoupling economic growth from environmental degradation, Norway clearly demonstrates the role of low-carbon energy systems in addressing the climate crisis. Germany, on the other hand, exhibits very low energy intensity (2.35 GJ/$1000GDP) despite its large industrial base, representing one of the strongest examples of technological and industrial efficiency. However, its carbon intensity (0.055 tonnes/GJ) is not as low as Norway's, indicating that its energy system has not yet been fully decarbonized.

India's emissions remain relatively suppressed due to its low income level despite its large population. However, its high carbon intensity (0.073 tonnes/GJ) signals a potential future surge in emissions if economic growth continues under a coal-dependent structure. Niger, although having the lowest emissions, reflecting structural limitations rather than an

efficiency-driven low-emission profile, as indicated by its low energy intensity (1.34 GJ/$1000GDP) and extremely low per capita income.

Brazil demonstrates relatively good performance in carbon intensity (0.050 tonnes/GJ) due to its renewable energy potential, yet its energy efficiency (3.40 GJ/$1000GDP) remains moderate. In the case of Türkiye, a striking duality emerges: Türkiye's energy intensity (2.23 GJ/$1000GDP) is comparable to that of Germany's, indicating a strong structural advantage in efficient energy use. However, its carbon intensity (0.061 tonnes/GJ) is higher than that of Norway, Germany, and Brazil, implying a continued dependence on fossil fuels.

The parameters calculated within the Kaya Identity framework reveal that countries do not exhibit a one-dimensional emission performance; rather, each country possesses distinct structural strengths and weaknesses. Based on this parameter analysis, comparative advantages and disadvantages are presented in Table III.

TABLE III
COMPARATIVE ASSESSMENT OF COUNTRY-SPECIFIC ADVANTAGES AND DISADVANTAGES BASED ON ENERGY AND EMISSION INDICATORS

Country	Advantage	Disadvantage
Türkiye	Low energy intensity and controlled energy use per economic output.	Carbon intensity remains relatively high.
Saudi Arabia	High income and strong economic capacity.	Extremely high energy intensity and strong energy dependency.
Norway	Lowest carbon intensity with high income.	High per capita energy consumption.
United States	Strong economic production capacity.	Very high emissions and energy-intensive welfare model.
China	Large economic scale and production capacity.	High population, energy intensity, and carbon intensity combined.
India	Relatively low emissions due to low income.	High population and carbon intensity create future risk.
South Africa	Shows no clear advantage across the Kaya components	Highest energy and carbon intensity.
Niger	Very low emissions.	Extremely low income and economic capacity.
Brazil	Relatively low carbon intensity.	Moderate energy efficiency.
Germany	High efficiency with low energy intensity and high income.	Carbon intensity is not yet minimal.

IV. CONCLUSIONS

This study provides a comparative evaluation of the relationships between energy consumption, economic growth, and CO_2 emissions using both macroeconomic indicators and the Kaya identity framework. The findings confirm that, while a general positive relationship exists between energy consumption and economic output, this relationship is neither uniform nor strictly proportional across countries. Instead, it is significantly influenced by differences in energy efficiency, technological development, and the carbon composition of national energy systems.

The decomposition analysis reveals that emission levels are shaped by multiple interacting factors rather than a single dominant variable. While population and economic scale determine the overall magnitude of emissions, energy intensity and carbon intensity play a critical role in defining the efficiency and environmental impact of economic activity. Countries such as Germany and Türkiye demonstrate relatively low energy intensity, indicating efficient use of energy in economic production, whereas countries like South Africa and Saudi Arabia exhibit high energy intensity, reflecting energy-dependent economic structures.

Similarly, carbon intensity emerges as a key differentiator in environmental performance. Norway stands out as a benchmark case where high economic welfare is achieved alongside low carbon intensity, highlighting the importance of a low-carbon energy mix. In contrast, countries with high carbon intensity, such as India and South Africa, face significant challenges in aligning economic growth with climate objectives.

Another important insight is that low emission levels do not necessarily indicate sustainability, as seen in the case of Niger, where low emissions are primarily a result of limited economic activity and energy access. This emphasizes the need to distinguish between environmentally efficient systems and structurally constrained economies.

Overall, the results suggest that achieving sustainable development requires a dual strategy: improving energy efficiency to reduce energy intensity and transitioning toward cleaner energy sources to lower carbon intensity. These findings underline that economic growth can be decoupled from environmental degradation, but only through targeted technological, structural, and policy interventions. Therefore, future energy strategies should focus not only on increasing economic output but also on optimizing the quality and sustainability of energy use.

REFERENCES

[1] Omri, A. (2013). CO_2 emissions, energy consumption and economic growth nexus in MENA countries: Evidence from simultaneous equations models. Energy Economics, 40, 657–664. https://doi.org/10.1016/j.eneco.2013.09.003

[2] Stern, D. I. (2011). The role of energy in economic growth. Annals of the New York Academy of Sciences, 1219(1), 26–51. https://doi.org/10.1111/j.1749-6632.2010.05921.x en

[3] Moreau, V., & Vuille, F. (2018). Decoupling energy use and economic growth: Counter evidence from structural effects and embodied energy in trade. Applied Energy, 215, 54–62. https://doi.org/10.1016/j.apenergy.2018.01.044

[4] Liddle, B., & Parker, S. (2024). Another look at 'peak and decline' carbon emissions countries: Which ones have decoupled per capita emissions from GDP and how? Global Environmental Change Advances, 3, 100012. https://doi.org/10.1016/j.gecadv.2024.100012

[5] Duro, J. A., & Padilla, E. (2006). International inequalities in per capita CO_2 emissions: A decomposition methodology by Kaya factors. Energy Economics, 28(2), 170–187. https://doi.org/10.1016/j.eneco.2005.12.004

[6] Hwang Y, Um J-S, Hwang J, Schlüter S. Evaluating the Causal Relations between the Kaya Identity Index and ODIAC-Based Fossil Fuel CO_2 Flux. Energies. 2020;13(22):6009. doi:10.3390/en13226009

[7] Štreimikienė, D., & Baležentis, T. (2016). Kaya identity for analysis of the main drivers of GHG emissions and feasibility to implement EU "20–20–20" targets in the Baltic States. Renewable and Sustainable Energy Reviews, 58, 1108–1113. https://doi.org/10.1016/j.rser.2015.12.311

[8] Raupach MR, Marland G, Ciais P, Le Quéré C, Canadell JG, Klepper G, Field CB. Global and regional drivers of accelerating CO_2 emissions. Proceedings of the National Academy of Sciences of the United States of America. 2007;104(24):10288-10293. doi:10.1073/pnas.0700609104

[9] Hwang Y, Um J-S, Hwang J, Schlüter S. Evaluating the Causal Relations between the Kaya Identity Index and ODIAC-Based Fossil Fuel CO_2 Flux. Energies. 2020;13(22):6009. doi:10.3390/en13226009

[10] Seawright J, Gerring J. Case Selection Techniques in Case Study Research: A Menu of Qualitative and Quantitative Options. Political Research Quarterly. 2008;61(2):294-308. doi:10.1177/1065912907313077

[11] Tavakoli A. A journey among top ten emitter country, decomposition of "Kaya Identity". Sustainable Cities and Society. 2018;38:254-264. doi:10.1016/j.scs.2017.12.040

[12] (2026) The U.S. Energy Information Agency website. [Online]. Available: https://www.eia.gov

Experimental Investigation of Density and Apparent Viscosity Evolution Across Multi-Compartment Sedimentation Tanks Under Varying Total Suspended Solid Contents

Kaan Berk Çelik[1], Mustafa Çelik[1], Ruhican Dürlü[1], Ömer Önder Erat[1], Furkan Soysal[1,*], Sıtkı Kocaoğlu[1], and Bülent Yeşilata[1]

[1]*Department of Energy Systems Engineering, Faculty of Engineering and Natural Sciences, Ankara Yıldırım Beyazıt University, Etlik-Keçiören/Ankara, TÜRKIYE*

***Contact:** fsoysal@aybu.edu.tr

Abstract— High-rise building wastewater streams contain suspended solids that significantly influence their physical behavior. Understanding how these solids can be removed through simple physical processes is essential before considering more complex treatment approaches. This study experimentally investigates the effect of varying total suspended solids (TSS) contents on sedimentation efficiency and the evolution of key physical properties in a multi-compartment sedimentation tank. Simulated wastewater samples with four different TSS levels (0%, 0.4%, 5.8%, and 11.2% by mass) were prepared to represent typical grey and black water conditions. A three-stage sedimentation tank was used to achieve progressive solid-liquid separation under gravity-driven conditions. Density, TSS reduction, discharge flow rate, linear velocity, and apparent viscosity were measured at successive compartments. Results demonstrate that even simple static sedimentation provides effective physical treatment, leading to a significant reduction in suspended solids. This reduction is accompanied by measurable decreases in density and improvements in flow characteristics. Increasing initial TSS levels resulted in lower flow rates and higher apparent viscosity, indicating increased resistance due to higher solid content. Progressive removal of solids across compartments confirms the effectiveness of staged sedimentation. These findings highlight that multi-compartment sedimentation systems can serve as efficient physical treatment units and provide valuable insight into the relationship between suspended solids, fluid properties, and separation performance.

Keywords: Sedimentation, wastewater hydrodynamics, suspended solids, density variation, apparent viscosity.

I. INTRODUCTION

Sedimentation is one of the most fundamental physical processes in water and wastewater treatment, enabling the removal of suspended particles through gravitational settling. The efficiency of sedimentation directly depends on the concentration, size distribution, and physical properties of suspended solids, as well as the hydraulic characteristics of the system. In domestic wastewater streams, total suspended solids (TSS) can vary significantly depending on the source, leading to variations in settling behavior and treatment performance [1].

Understanding how different TSS levels influence sedimentation efficiency is essential for the proper design and optimization of treatment units. In particular, multi-compartment sedimentation tanks provide a staged environment where progressive settling can occur, allowing for improved separation compared to single-stage systems. However, the extent to which such systems can physically reduce suspended solids under different initial concentrations remains an important experimental question.

In addition to solid removal, sedimentation also affects key physical properties of the fluid, such as density and apparent viscosity. Previous studies have demonstrated that increasing total suspended solids concentration leads to higher apparent viscosity and reduced flow efficiency, indicating increased hydraulic resistance within the system [2]. These properties are strongly linked to the suspended particle content and can provide indirect insight into the effectiveness of the separation process. Therefore, monitoring the evolution of these parameters across successive compartments can offer a comprehensive understanding of sedimentation performance.

Within this context, the present study aims to experimentally investigate the physical treatment capability of a three-compartment sedimentation tank using sand-water mixtures with varying TSS contents. Sand-based simulations closely mimic the particulate characteristics of real wastewater, making them suitable for examining variations in density, viscosity, and flow dynamics across a wide range of total suspended solids levels [3]. The focus is strictly on sedimentation efficiency and the evolution of physical properties, without considering any downstream applications. The results are expected to provide fundamental insights into the behavior of particulate-laden flows under controlled settling conditions.

II. MATERIALS AND METHODS

A. Experimental Setup

The experimental system consists of a 54-L three-compartment sedimentation tank with a baffled internal structure, each compartment having a volume of 18 L (Fig. 1). The compartments are connected in series, allowing the

fluid to flow sequentially from the first to the third chamber. This configuration enables progressive sedimentation, where heavier particles settle in earlier compartments while finer particles are carried forward.

Each compartment is equipped with sampling points to allow the collection of fluid samples for analysis. The system operates under gravity-driven flow conditions, and no external mixing or mechanical intervention is applied during the settling process, ensuring that the observations reflect purely physical sedimentation behavior.

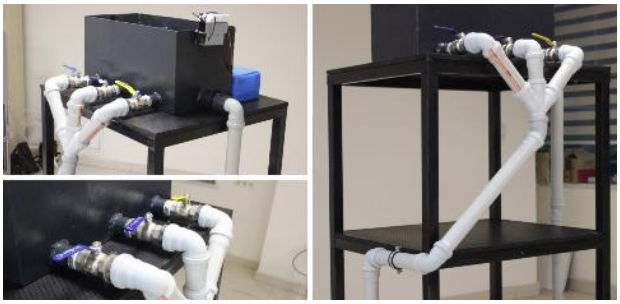

Fig. 1 Schematic view of the three-compartment sedimentation tank used in the experiments.

B. Preparation of Test Samples

Simulated wastewater samples were prepared using sand-water mixtures to represent different TSS levels. Four concentrations (by mass) were selected based on typical ranges reported in domestic wastewater, 0% (control), 0.4%, 5.8%, and 11.2% [2].

Each mixture was prepared at a total volume of 54 liters. The required mass of sand was calculated based on the desired TSS ratio. Prior to each experiment, the mixtures were thoroughly agitated to ensure homogeneity.

C. Experimental Procedure

The prepared mixture was introduced into the first compartment of the sedimentation tank and allowed to fill the entire system. No forced flow was applied; instead, the system was left to stabilize under gravity, allowing sedimentation to occur naturally. Samples were collected from the initial mixture (first compartment), the second compartment, and the third compartment. To ensure representative sampling, each compartment was gently mixed before sample collection.

Densities were determined by collecting 50 mL samples and measuring their mass using an analytical balance. The density was calculated using Eq. 1:

$$\rho = \frac{m}{V} \tag{1}$$

where, m is the mass and V is the sample volume.

To calculate TSS percentages of water samples with different TSS percentages after passing to subsequent compartments of the sedimentation tank, 1-liter samples were collected from the second and third compartments. During this procedure, each compartment was agitated to ensure homogeneity. A scale reduction was then performed, and 5-mL sub-samples were extracted from the 1-liter volumes. These sub-samples were initially weighed, then dried to determine the mass of the solid content and finally used to calculate the overall total suspended solids percentages.

To calculate the discharge flow rates of water samples with varying total suspended solids percentages, the sedimentation tank was initially filled from the first compartment. Once the third compartment reached full capacity, the outlet valve was opened, and the time required to fill a 10-liter vessel was recorded. Based on these measurements, the flow rates for each total suspended solids concentration were determined as follows. Additionally, linear velocities were derived by dividing the volumetric flow rate by the cross-sectional area of the discharge pipe using Eq. 2:

$$v = \frac{Q}{\frac{\pi}{4} D_i^2} \tag{2}$$

where, Q is the experimentally determined volumetric flow rate and D_i is the inner diameter of the discharge pipe (0.041 m).

Regarding the investigation of viscosity values, it has been established that calculations concerning domestic wastewater treatment are predominantly based on the properties of water, owing to the typically low concentrations of total suspended solids [1]. Apparent viscosity of simulated black water for pipe flow can be calculated using Eq. 3 [3]:

$$\eta = \frac{\tau}{\gamma} \tag{3}$$

where, η is the apparent viscosity (Pa.s), τ is the shear stress (Pa), and γ is the shear rate (s^{-1}). For pipe flow, the shear rate can range from 1 to 1000 s^{-1} and is determined using Eq. 4 [3]:

$$\gamma = n\frac{8v}{D_i} \tag{4}$$

where, n represents a correction factor ranging from 1 for Newtonian fluids to between 1 and 2 for non-Newtonian fluids. Since the water sample containing 0% TSS behaves as a Newtonian fluid, calculations were performed for n = 1. Based on flow rate measurements, the fluids were observed to exhibit Newtonian behavior; therefore, calculations for the other water samples were also conducted assuming n = 1.

Shear stress can be calculated using Eq. 5 [3]:

$$\tau = \frac{D_i\, \Delta P}{4L} \tag{5}$$

where, ΔP is the pressure difference (Pa) and L represents the pipe length (m). Since both the top point of the sedimentation tank and the pipe through which the fluid exits the system are open to the atmosphere, the pressure difference arises solely from the elevation difference. Eq. 6 was used to calculate the pressure difference [4]:

$$\Delta P = \rho g \Delta z \tag{6}$$

where, g is the gravitational acceleration (9.8 m/s^2) and Δz is the distance from the upper section of the sedimentation tank's third compartment to the discharge pipe where the fluid exits the system (1.015 m).

III. RESULTS

The experimental results obtained for all test conditions are summarized in Table I. The analysis focuses on the evolution of density, TSS, flow characteristics, and apparent viscosity across the three compartments of the sedimentation tank under varying initial TSS concentrations.

For all non-zero TSS cases, a consistent decrease in density was observed from the first to the third compartment. This trend clearly indicates the progressive removal of suspended solids along the flow path.

At the lowest concentration (0.4%), the density values remained nearly constant across compartments, with only minor reductions observed. This suggests that at low particle concentrations, sedimentation is limited due to insufficient particle settling and weak particle–particle interactions.

In contrast, for higher TSS levels (5.8% and 11.2%), a more pronounced decrease in density was recorded. The initial density increased with TSS concentration, reaching its highest value at 11.2%. However, after passing through the sedimentation stages, the density values approached those of water, particularly in the third compartment. This indicates that a significant fraction of suspended solids was removed during the process.

The measured TSS values confirm the effectiveness of the sedimentation process. A progressive reduction in TSS was observed from the first to the third compartment for all tested concentrations.

At 0.4% initial TSS, only a slight reduction was detected, indicating limited settling efficiency. However, at 5.8% and 11.2%, a substantial decrease in TSS was observed, particularly between the first and second compartments. Further reduction occurred in the third compartment, resulting in the lowest TSS values at the outlet.

The highest removal efficiency was achieved for the 11.2% case, where a large portion of suspended solids settled before reaching the final compartment. This demonstrates that higher initial solid loading enhances the sedimentation process, likely due to increased particle interactions and aggregation.

The discharge measurements revealed a clear dependence of flow behavior on TSS concentration. As the initial TSS increased, both flow rate and linear velocity decreased.

The highest flow rate was observed for the control sample (0% TSS), with a value of 0.7849 L/s. This value decreased progressively with increasing TSS, reaching 0.6266 L/s at 11.2%. A similar trend was observed for linear velocity, which decreased from 0.5945 m/s (0% TSS) to 0.5271 m/s (11.2% TSS).

These results indicate that increasing solid content introduces additional resistance to flow, leading to reduced discharge capacity.

The apparent viscosity values also showed a systematic increase with increasing TSS concentration. The control sample exhibited a viscosity close to that of pure water (0.8562 mPa.s), confirming Newtonian behavior.

For higher TSS concentrations, viscosity values increased to 0.8846 mPa.s (0.4%), 0.9737 mPa.s (5.8%), and 1.0900 mPa.s (11.2%). This increase reflects the growing influence of suspended particles on flow resistance.

Although the fluids were treated as Newtonian for calculation purposes, the observed increase in apparent viscosity suggests that particle interactions become more significant at higher concentrations.

TABLE I
SUMMARY OF EXPERIMENTAL RESULTS FOR WATER SAMPLES WITH VARYING TSS CONCENTRATIONS

Water Sample	Tank Compart-ment	TSS (%)	Density (g/mL)	Flow rate (L/s)	Linear Velocity (m/s)	Viscosity (mPa.s)
1	1	0.0	0.9888	0.7849	0.5945	0.8562
	2		0.9888			
	3		0.9888			
2	1	0.4	1.0015	0.7686	0.5822	-
	2	0.1638	1.0011			-
	3	0.1339	1.0004			0.8846
3	1	5.8	1.0068	0.6959	0.5271	-
	2	2.5937	1.0001			-
	3	1.7314	0.9969			0.9737
4	1	11.2	1.0180	0.6266	0.5271	-
	2	4.6950	1.0083			-
	3	3.0553	1.0048			1.0900

When all parameters are evaluated together, a consistent pattern emerges. Increasing TSS concentration leads to higher initial density, higher apparent viscosity, and reduced flow rate and linear velocity. At the same time, the sedimentation tank effectively reduces TSS across compartments, which is reflected in decreasing density and improved flow properties toward the outlet.

The relationship between TSS concentration and normalized density was evaluated to provide a global view of how initial solid loading influences fluid properties. As shown in Fig. 2, normalized density increases consistently with increasing TSS. At low concentrations (<1%), the density remains very close to that of pure water, indicating minimal influence of suspended particles. However, as TSS increases, a more pronounced rise in density is observed, reaching its highest value at 11.2% TSS. This trend demonstrates that suspended solids contribute directly to bulk fluid density, with their impact becoming more significant at higher concentrations. The relatively weak increase at low TSS suggests limited particle interaction, whereas the steeper trend at higher concentrations reflects enhanced particle-particle interactions and increased solid loading. These

findings are consistent with the observed increases in apparent viscosity and reductions in flow rate, further confirming that higher TSS levels lead to greater hydraulic resistance and altered flow behavior.

These results demonstrate the coupled relationship between suspended solid content, fluid properties, and sedimentation performance under controlled experimental conditions.

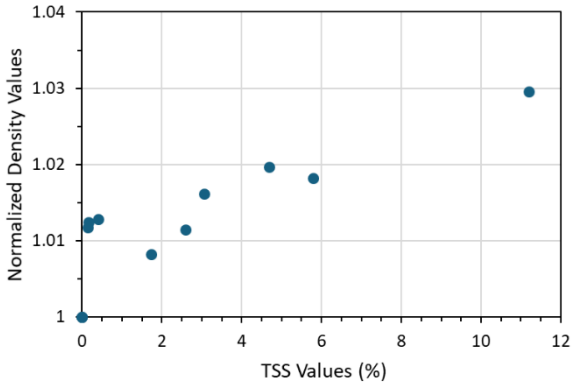

Fig. 2 Variation of normalized density as a function of TSS concentration.

IV. DISCUSSION

One of the most important outcomes of this study is that even a simple, purely physical, and static sedimentation process can achieve a meaningful level of water treatment. Despite the absence of any chemical additives, mechanical mixing, or advanced treatment methods, the multi-compartment system demonstrated a clear and measurable reduction in total suspended solids. This finding highlights the inherent effectiveness of gravity-driven separation and confirms that even basic sedimentation can play a significant role in improving water quality.

The staged configuration of the sedimentation tank further enhances this effect. Instead of a single-step settling process, the multi-compartment design allows progressive removal of suspended particles. Heavier particles settle predominantly in the first compartment, while finer particles are gradually removed in subsequent chambers. This sequential behavior leads to a cumulative improvement in fluid clarity and supports the concept that compartmentalization increases overall separation efficiency.

Another key observation is that sedimentation does not only reduce TSS but also alters fundamental physical properties of the fluid. The decrease in density across successive compartments directly reflects the removal of particulate matter. Similarly, the reduction in apparent viscosity indicates an improvement in flow characteristics, as the fluid becomes less resistant to motion once solids are removed. These changes confirm that sedimentation acts not only as a separation mechanism but also as a regulator of fluid behavior.

The influence of initial TSS concentration is also evident. At low concentrations, the limited number of particles results in relatively weak settling behavior, leading to smaller reductions in TSS. In contrast, higher concentrations promote particle-particle interactions and aggregation, which enhance settling efficiency. However, increasing TSS also leads to higher apparent viscosity, which may introduce additional resistance to flow and potentially affect settling dynamics. This suggests that there is a balance between improved settling due to higher particle concentration and reduced efficiency due to increased fluid resistance.

Overall, the results demonstrate that sedimentation tanks, even in their simplest form, provide an effective and reliable method for the physical treatment of particulate-laden water. The observed relationships between TSS reduction, density, and viscosity emphasize the importance of considering both separation efficiency and fluid property evolution when evaluating sedimentation performance. These findings provide a fundamental basis for the design and optimization of sedimentation systems in practical water treatment applications and demonstrate that even low-complexity sedimentation systems can provide a robust baseline for physical treatment, particularly in applications where simplicity, reliability, and low operational cost are critical.

ACKNOWLEDGMENT

This work has been supported by Ankara Yıldırım Beyazıt University Scientific Research Projects Coordination Unit under grant number FHD-2025-2740.

REFERENCES

[1] W. H. Hager, “Wastewater hydraulics: Theory and practice”, *Springer Science & Business Media*, 2010.

[2] A. T. Radhakrishnan, J. B. Van Lier, & F. H. L. R. Clemens, “Rheological characterisation of concentrated domestic slurry”, *Water Research*, 141, 235-250, 2018.

[3] N. J. Alderman, N. I. Heywood, “Improving slurry viscosity and flow-curve measurements”, *Chemical Engineering Progress*, 100(4), 27-34, 2004.

[4] C. Geankoplis, A. Hersel, D. Lepek, *Transport processes and separation process principles*. 5th ed., Prentice Hall Press, 2018.

An Overview of Interleaved Buck Converters and Modern Control Approaches

Kazım YEL[1] and Mehmet Zahid EREL[2,*]

[1]*Graduate School of Natural Sciences, Defense Technologies, Ankara Yıldırım Beyazıt University, Ankara, Turkiye*

[2]*Department of Energy Systems Engineering, Ankara Yıldırım Beyazıt University, Ankara, Turkiye*

*Contact: mzerel@aybu.edu.tr

Modern power electronics applications including electric vehicles (EVs), battery energy storage systems (BESS), renewable-energy-driven hydrogen electrolyzers, and artificial intelligence (AI) processors in data centers require high current density, low output voltage, and extremely fast transient response. To fulfill these requirements, Interleaved Buck Converters (IBCs) have become a key solution because of their straightforward design and ability to minimize output current ripple. However, traditional IBCs require extremely narrow duty cycles when operating at high step-down ratios, resulting in increased switching losses, higher voltage stress on semiconductor devices, and current imbalance between parallel phases. Academic research aimed at overcoming the limitations of IBCs has gained significant momentum lately, focusing on both topological innovations and intelligent digital control algorithms. This paper examines modern control strategies through the limitations, benefits, and drawbacks introduced in the literature during the last five years to overcome the inherent limitations of conventional IBC architectures.

Keywords: *Interleaved Buck Converter (IBC), Control Approaches, Modern Control, Review, Power Electronics*

Geometric Design and Numerical Analysis of Jet Stretcher in Supersonic Free-Jet Tests

Batuhan Yurtdan[1,*], Selahattin Çelik[1], and Kamil Arslan[1]

[1] *Department of Mechanical Engineering, Ankara Yıldırım Beyazit University, Ankara 06010, TÜRKIYE*

***Contact:** batuhanyurtdan@hotmail.co.uk*

Abstract This study investigates the aerodynamic design and performance of Jet Stretcher systems to overcome the inherent axial length limitations of the "test rhombus" in supersonic free-jet testing facilities. By employing high-fidelity three-dimensional Reynolds-Averaged Navier-Stokes (RANS) simulations with the k-ω SST turbulence model, the research evaluates the impact of varying expansion angles—specifically an offset geometry, a 3-degree expansion, and a 5-degree expansion—on flow quality and shock wave propagation. The numerical findings reveal that the offset geometry, which mirrors the test model's outer contour, provides the most effective protection against reflected shocks, thereby closely approximating free-flight conditions. Although a 3-degree expansion angle offers certain advantages in flow-starting characteristics, it induces deleterious recompression shocks on the model, whereas the 5-degree configuration results in a total breakdown of flow uniformity. By establishing a recommended design envelope of 0 to 3 degrees, this work provides significant technical contributions and practical design criteria for the development of next-generation supersonic ground test facilities.

Keywords: Jet Stretcher, Supersonic Free-Jet Testing, Computational Fluid Dynamics (CFD), Test Rhombus, Shock Wave Reflections, Aerodynamic Design, Flow Uniformity.

I. INTRODUCTION

In aerospace engineering, evaluating the high-speed performance and engine-airframe integration of advanced air-breathing propulsion systems, such as ramjets and scramjets, requires highly complex and costly ground test facilities. Modern missiles and military aircraft, in particular, feature air inlets positioned significantly aft of the nose. Testing such configurations in supersonic wind tunnels and free-jet facilities presents severe aerodynamic challenges. The primary cause of these difficulties is that the physical boundaries of the facility cause the flow field around the test model to deviate from natural free-flight conditions [1].

In free-jet testing, the axial length of the supersonic flow propagating through the test section is restricted by a theoretical domain known as the "test rhombus" [2], [7]. The boundary of this region is defined by the shock waves emanating from the nose of the tested aerodynamic body; these waves impinge upon the free-jet boundary and reflect back toward the aft sections of the model [1]. While these shock waves would propagate to infinity and dissipate during actual free flight, in ground testing, they reflect and strike the air inlets. This phenomenon distorts the thermodynamic properties, total pressure, and local Mach number of the ingested air [3], [1]. To overcome this physical constraint and artificially extend the length of the test rhombus, aerodynamic structures known as "Jet Stretchers" have been developed [1]. Jet stretchers are physical shrouds designed to replace a specific streamline formed around the test model during natural flight, with their internal surfaces precisely contoured to account for boundary layer corrections [1]. Positioned downstream of the model's bow shock, these structures mechanically prevent the interaction of the shock waves with the free-jet boundary. Initially theorized in the 1960s by researchers at the Marquardt Corporation and Wright-Patterson Air Force Base, this system was subsequently tested by the AEDC (Arnold Engineering Development Center) at Mach 3.04, demonstrating that the local Mach number could be maintained within the requisite tolerance [3], [1].

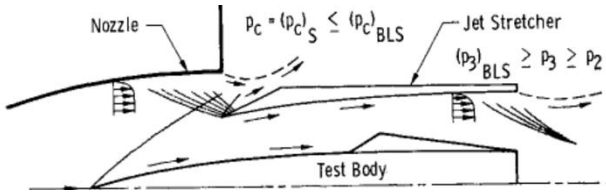

Fig. 1 Concept Jet Stretcher System [1].

One of the most fundamental geometric characteristics considered in the aerodynamic design of jet stretcher systems is their divergent profile, which expands toward the exit while maintaining a constant inlet diameter. This diverging geometry is of critical importance to ensure effective aerodynamic shielding across the entire test article. During supersonic flight, the shock waves and streamlines emanating from the model's nose exhibit a natural tendency to expand as they propagate downstream. The internal surface of the jet stretcher is intentionally contoured to accommodate this expansion, growing larger toward the trailing edge. Consequently, the natural flow contours characteristic of free-flight conditions can be faithfully reproduced along the test article during ground testing, without inducing artificial flow contraction or blockage.

However, fixed-geometry jet stretchers inherently constrain the operational test envelope, as they are optimized

solely for a specific Mach number and a zero angle of attack. To overcome these limitations, modern trimmed designs driven by Computational Fluid Dynamics (CFD) and "Adaptable Jet Stretcher" concepts are currently being investigated. In this study, the aerodynamic design philosophies, thermodynamic limits, and mathematical models of jet stretcher systems—rooted in the principles of mass conservation—are examined in detail. Furthermore, performance analyses of the jet stretcher across varying divergence angles, along with the effects of these geometric alterations on free-flight simulation fidelity, are comprehensively evaluated.

II. MOTIVATION AND METHODOLOGY

This work aims to investigate how jet stretcher geometries with varying expansion angles influence the flow quality along the test article in a supersonic free jet environment. Beyond merely extending the effective test region axially by mitigating the reflection of bow shocks, the geometric expansion characteristics of the jet stretcher play a critical role in shaping the internal flow field and preserving free-flight-like conditions throughout the test section. In particular, gradual or aggressive expansion profiles can alter the propagation and attenuation of shock and expansion waves, thereby affecting the uniformity of the flow delivered to the test article.

Different expansion angles introduce distinct flow adaptation mechanisms within the jet stretcher. Configurations with smaller expansion angles tend to maintain smoother pressure gradients and minimize the risk of internal flow separation, while larger expansion angles may enhance the axial growth of the test volume but at the expense of increased sensitivity to shock interactions and boundary layer effects. These trade-offs necessitate a systematic evaluation of multiple geometric configurations to determine their impact on flow stability and similarity to free-flight conditions.

In conventional free jet testing without a jet stretcher, the operating envelope is constrained by limitations in facility supply, exhaust capability, and the interaction of shock structures originating from the nozzle exit. The introduction of jet stretcher geometries with tailored expansion characteristics provides an opportunity to relax these constraints by modifying how the flow expands and interacts within the test cell. By controlling the expansion angle, it becomes possible to influence the effective pressure ratio limits and extend the usable operating range of the facility under overexpanded conditions.

The primary objective of this investigation is therefore to establish an analysis framework for evaluating jet stretcher geometries with different expansion angles. This approach relies on computational modeling to assess how each geometry modifies the internal flow field, particularly in terms of shock positioning, pressure distribution, and flow uniformity along the test article. The effectiveness of each configuration is ultimately judged based on its ability to reproduce free-flight flow characteristics at designated locations within the test domain, ensuring that the aerodynamic environment experienced by the test article remains representative and undisturbed.

A. GEOMETRY

The computational domain developed for this study comprises three primary functional components: a supersonic free jet nozzle, a notional test article representing the missile geometry, and a jet stretcher designed to minimize interference effects. The supersonic nozzle was designed using the Method of Characteristics (MOC) [7] to deliver a uniform flow field at a design Mach number of approximately 3.20. To ensure sufficient mass flow and test section area, the nozzle exit diameter was established at 915 mm.

Fig. 2 Geometry of Test Article.

The test article, integrated into the free jet flow, features an axisymmetric body with a maximum diameter of 230 mm and a total longitudinal length of 4.5 m. A critical aspect of the experimental setup is the jet stretcher, which serves to shield the test article from shock waves reflected from the free jet shear layer. The internal profile of the jet stretcher was numerically derived using a streamline-based design approach. Specifically, a target streamline was extracted from a baseline free-flight simulation, originating at approximately 75% of the nozzle exit radius.

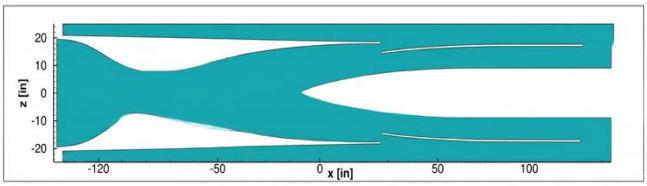

Fig. 3 Flow Field: The test article and axisymmetric jet stretcher installed within the free jet nozzle exhaust.

This derived geometry incorporates a structural wall thickness of 10 mm. To facilitate pressure equilibration and prevent premature flow separation at the nozzle-stretcher interface, a radial gap of approximately 90 mm was maintained between the nozzle exit lip and the leading edge of the jet stretcher. This configuration aims to extend the "clean flow" region over the missile radome, ensuring that the

aerothermal gradients captured during the simulation accurately reflect high-altitude flight conditions.

B. METHODOLOGY

1) Solution Method

Numerical analyses were performed using a three-dimensional RANS (Reynolds-Averaged Navier-Stokes) solver based on a node-based finite volume method. In the simulations, single-species air was defined as the fluid, and a calorically perfect gas model was assumed. The solutions were conducted with an adiabatic wall assumption, and all calculations were executed for steady-state conditions. To accurately resolve complex flow phenomena in the study, the $k-\omega$ SST (Shear Stress Transport) turbulence model was utilized. The $k-\omega$ SST model offers a hybrid approach, leveraging the superior resolution capability of the $k-\omega$ in the viscous sublayers near the wall, while transitioning to the features of the $k-\varepsilon$ model in the free-stream regions outside the boundary layer [8]. In aerothermal test environments, there is a high risk of flow separation due to high-speed flow at the nozzle exit, shock waves, and adverse pressure gradients. The SST model was preferred for this analysis because it can predict such flow separation tendencies and shock wave-boundary layer interactions (SBLI) much more accurately compared to standard models. The computational domain was structured to reflect the aerodynamic characteristics of a physical test cell, but specific simplifications were introduced to improve numerical convergence. The tank model was extended in the streamwise direction, and the downstream surface was entirely defined as an outflow boundary. The boundary conditions of the free jet nozzle were set to simulate flight conditions corresponding to an altitude of approximately 53,000 ft (Mach 3.2 and 1500 psf dynamic pressure).

The boundary conditions and design parameters applied in the numerical model are summarized in Table 1.

TABLE I
DESIGN PARAMETERS

Boundary Type	Parameter	Applied Value
Nozzle Inlet	Total Pressure	72,5 psia
Nozzle Inlet	Total Temperature	1213.7 °R
Domain Outflow	Static Pressure	Variable
Free Flight	Mach Number	3.2
Free Flight	Dynamic Pressure	1500 psf

2) Grids

In this study, grid structures were generated for three different computational models: the test article in free flight, the model integrated with the axisymmetric jet stretcher, and the model integrated with the trimmed jet stretcher. Each grid structure was uniformly refined until grid dependency on the flow field at the inlet aperture reached a negligible level.

The computational grids were constructed using prism elements to resolve the boundary layer at the walls with high precision, and tetrahedral cells in the outer volumes where the free-stream flow exists. The first cell height on all wall surfaces was adjusted to ensure that the dimensionless wall distance y^+ value remained below one ($y^+ < 1$) satisfying the wall function requirements of the $k-\omega$ SST turbulence model. All grids were constructed fully three-dimensionally, and no symmetry assumptions were used, even to reduce computational load.

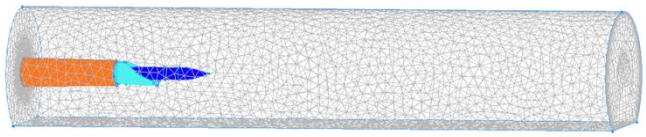

Fig. 4 The Computational Domain.

3) Free Flight Simulation

To evaluate the aerodynamic performance of the proposed jet stretcher design and establish a reference baseline, the test article was initially simulated under free-flight conditions utilizing the flow parameters at the supersonic nozzle exit. An examination of the Mach number contours along the symmetry plane (Figure 5) reveals the formation of a distinct oblique shock wave at the radome (nose) of the test article. This demonstrates that the flow field in this forward region successfully maintains high-altitude clean flow conditions, remaining isolated from external disturbances.

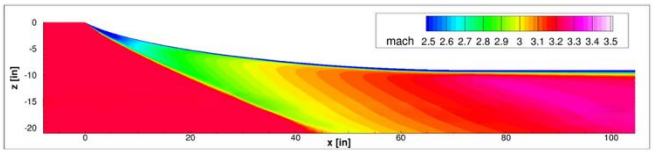

Fig. 5 Free-flight Mach contours along the test article's plane of symmetry.

However, further downstream, it is observed that expansion waves emanating from the nozzle lips and free jet shear layer interactions converge toward the body. This phenomenon carries a significant risk of degrading flow quality in critical aft measurement regions, such as the inlet aperture, potentially inducing unrealistic aerothermal gradients. Such flow degradation clearly proves that placing the test article solely at the nozzle exit during a standard free-jet test is insufficient to achieve a highly accurate flight simulation along the entire body.

These baseline analysis findings strongly justify the engineering necessity of integrating a jet stretcher into the system to attenuate reflected shock waves, prevent shear layer

interference, and extend the clean flow envelope to the aft sections of the test article. Accordingly, a reference streamline extracted from the free-flight simulation was utilized to define the internal surface profile of the stretcher. Simultaneously, the radial total pressure profile at the inlet aperture was recorded as benchmark data to validate the designed jet stretcher's capability to preserve free-flight aerodynamic conditions.

4) Jet Stretcher with Different Expansion Angles

Finding the optimal balance between mitigating aerodynamic blockage and preserving "clean flow" conditions in the test region is a critical engineering challenge in jet stretcher design. To systematically investigate this problem, three different jet stretcher configurations were developed and analyzed. To ensure that the resulting aerodynamic variations could be exclusively attributed to geometric differences, all configurations were simulated under identical grid resolutions and boundary conditions.

First configuration was generated by uniformly offsetting the outer contour of the test article in the radial direction. This design aims to provide a reference protective envelope around the test article while serving as a baseline to evaluate the potential choking (virtual nozzle) effect caused by the boundary layer developing on the inner walls. 3-Degree Expanded Geometry, In the second configuration, the baseline jet stretcher profile was expanded outward by 3 degrees in the streamwise (downstream) direction. The primary objective of this modification is to compensate for the aerodynamic blockage induced by the boundary layer displacement thickness, improve the supersonic flow starting characteristics, and mitigate shock-boundary layer interactions. In the third analysis, the expansion angle was increased to 5 degrees. This setup was included in the parametric study to test the limits of over-expansion and to demonstrate, from a flow physics perspective, the aerodynamic degradation on the test article caused by expansion waves emanating from the inner walls when excessive geometric relief is applied.

III.RESULTS

A. Offsetting Test Article Outer Counter

The analysis result, where the surface contour of the test article was offset, is given in Figure 6. The analysis results demonstrate that this configuration achieves complete aerodynamic success by effectively isolating the test article from shock interactions. The Mach number contours reveal that shock waves, which typically emanate from the nozzle lip and impinge upon the model, are redirected outside the jet stretcher geometry. This phenomenon confirms the establishment of a "shock-free" protective envelope around the test article.

Since no shock impingement occurs on the surface of the test article, the boundary layer development remains stable, preventing the formation of artificial pressure gradients. Consequently, this configuration represents the closest approximation to free-flight conditions. The flow field, particularly around the inlet aperture, shows a high correlation with baseline free-flight simulations. By confining the shocks to the outboard region of the stretcher, the "clean flow" characteristics required for accurate aerothermal testing have been successfully recreated. From a reviewer's perspective, this finding validates the design as the most efficient configuration, ensuring high-fidelity results while eliminating the interference effects observed in sub-optimal geometries.

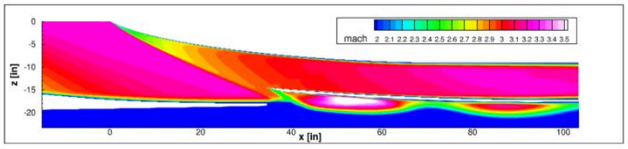

Fig. 6 Mach Contour of Offsetted Jet Stretcher

B. 3-Degree Expanded Geometry

The Mach number distribution for the 3-degree expanded jet stretcher configuration (Figure 7) illustrates a fundamental shift in flow physics. While the 3-degree expansion successfully alleviates aerodynamic blockage at the nozzle exit and improves flow starting characteristics, detailed contour analysis reveals that this expansion triggers undesirable shock interactions on the surface of the test article.

As the supersonic flow follows the diverging walls of the stretcher, it undergoes a Prandtl-Meyer expansion. However, the subsequent adjustment of the flow to the ambient pressure conditions generates a recompression shock originating from the internal walls of the stretcher. The Mach contours clearly show that this reflected shock wave propagates inward and directly impinges upon the aft-body of the test article. This shock impingement disrupts the local boundary layer and creates artificial pressure gradients that are not present in baseline free-flight conditions.

Consequently, the "clean flow" envelope is compromised in this configuration. The presence of reflected shocks, particularly near critical measurement stations, leads to a significant deviation from the intended free-flight aerodynamic profile. These findings suggest that while the 3-degree expansion provides sufficient relief for flow starting, it introduces secondary shock reflections that degrade the overall fidelity of the supersonic free-jet simulation.

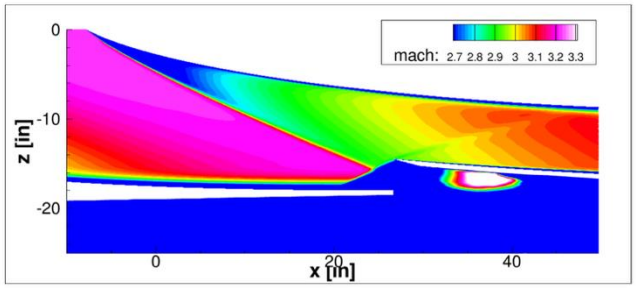

Fig. 7 Mach Contour of 3-Degree Expanded Jet Stretcher

C. 5-Degree Expanded Geometry

The 5-degree expanded jet stretcher simulation (Figure 8) reveals a critical state where geometric relief exceeds design limits. In this configuration, the aggressive increase in expansion angle leads to severe over-expansion of the supersonic flow. As the flow accelerates within the rapidly increasing cross-sectional area, static pressure drops below ambient levels, triggering intense recompression shocks along the stretcher walls to balance the pressure field.

Unlike the mild interactions observed in the 3-degree case, the reflected shocks in the 5-degree configuration are significantly more intense and steeper. The Mach contours clearly illustrate that these shocks reflect off the internal walls and directly impinge upon the test article body. This direct impingement induces artificial high-pressure regions and sudden Mach number gradients that are non-existent in true free-flight conditions. The flow uniformity in critical areas, such as the inlet aperture, is completely compromised; rather than acting as a shield, the jet stretcher effectively focuses disturbances toward the test article.

These results invalidate the hypothesis that increasing the expansion angle indefinitely improves flow quality. The 5-degree analysis serves as the "failure threshold" for the design process. While the baseline model suffers from viscous blockage, the 5-degree model is dominated by recompression shock impingement. This confirms that the optimal flow quality must be sought within a narrower angular range (ideally between 0 and 3 degrees) to maintain high-fidelity free-jet conditions.

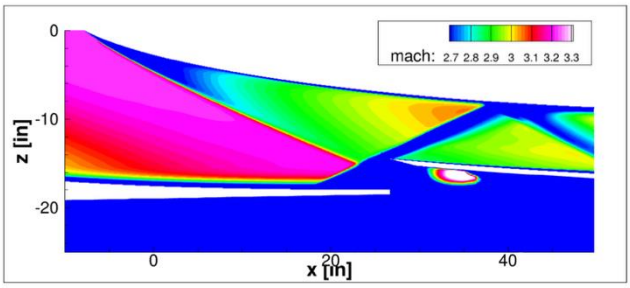

Fig. 8 Mach Contour of 5-Degree Expanded Jet Stretcher

IV. CONCLUSIONS

In this study, the thermodynamic and aerodynamic design limits of Jet Stretcher systems, developed to overcome the "test rhombus" constraints in supersonic free-jet facilities and simulate free-flight conditions, were comprehensively investigated. Three-dimensional computational fluid dynamics analyses utilizing the k−ω SST turbulence model systematically demonstrated the impact of the expansion angle within the jet stretcher's internal geometry on the flow quality over the test article. The analysis results proved that the reference design, generated by offsetting the test article's outer contour, successfully redirected shock waves outside the test region, establishing a shock-free protective envelope and providing the closest approximation to free-flight conditions. Conversely, introducing a 3-degree expansion angle to alleviate aerodynamic blockage disrupted the clean flow envelope by causing Prandtl-Meyer expansion and subsequent recompression shocks to impinge upon the model's aft-body. Increasing the expansion angle to 5 degrees was identified as a definitive "failure threshold" for the system; the severe reflected shocks induced by the over-expanded flow focused directly onto the test article, completely compromising flow uniformity. These findings invalidate the hypothesis that continuously increasing the expansion angle improves flow quality, and by proving that the optimal geometric range for high-fidelity free-jet testing must be maintained strictly between 0 and 3 degrees, this research provides an innovative and critical design guideline for next-generation supersonic ground test facilities.

REFERENCES

[1] R. C. Bauer, E. H. Matkins, R. L. Barebo, and W. C. Armstrong, "A Theoretical and Experimental Study of a Jet Stretcher System," Journal of Spacecraft and Rockets, vol. 10, no. 6, pp. 395-405, 1973.

[2] R. C. German, "Simulation of Supersonic Flow Over a Body of Revolution Using an Axisymmetric Jet Stretcher," Arnold Engineering Development Center, AEDC-TR-70-166, 1970.

[3] B. C. Heberling, M.-F. Liou, and H. H. Reising, "Design and Analysis of a Jet Stretcher for High-Altitude Supersonic Free Jet Testing," AIAA Aviation 2023 Forum, 2023.

[4] R. J. Matz and E. M. Kraft, "Investigations of Free-Jet Test Requirements and Techniques with Emphasis on the Adaptable Jet Stretcher," Arnold Engineering Development Center, AEDC-TR-80-35, 1981.

[5] F. B. Smith, R. C. Bauer, and R. L. Barebo, "The Jet Stretcher as an Aerodynamic/Propulsion Testing Tool," AIAA Propulsion Joint Specialist Conference, 1969.

[6] R. L. Barebo and E. H. Matkins, "Simulation of Supersonic Flow Over a Scale Model Missile with Aft-Mounted Inlets Using an Axisymmetric Jet Stretcher," AEDC-TR-71-37, 1971.

[7] Rice,T., "2D and 3D Method of Characteristic Tools for Complex Nozzle Development Final Report," Tech. rep., 2003.

[8] Menter, F. R., "Two-Equation Eddy-Viscosity Turbulence Models for Engineering Applications," AIAA Journal, Vol. 32, No. 8, 1994,pp.1598–1605.

Vibroacoustic Optimization of Porous Kelvin Cell Metamaterials for Washing Machine Mounts: A Computational Approach

M. Cihat Yilmaz[1,*]

[1]*Faculty of Engineering and Natural Sciences, Ankara Yildirim Beyazit University, Ankara, TÜRKIYE*

***Contact:** mcyilmaz@aybu.edu.tr*

Abstract— Dynamic forces generated during washing machine operation produce structural vibrations and low-frequency noise that degrade acoustic comfort and device longevity. This paper presents a vibroacoustic optimization framework for a locally resonant, functionally graded Kelvin lattice metamaterial intended as a washing machine mount. The lattice topology employs spherical resonator masses at each node connected by graded-thickness struts fabricated from polyamide (PA12). Four continuous design variables — top and bottom strut radii, unit-cell size, and node-sphere radius — are optimized via Particle Swarm Optimization (PSO) to minimize Equivalent Radiated Power (ERP) while penalizing excessive mass and insufficient structural stiffness. A parametric finite-element engine assembles global stiffness and mass matrices, performs modal and harmonic response analyses over 10–150 Hz, and evaluates ERP for each candidate design. Numerical results confirm that local resonance effects generate pronounced bandgap behaviour, and the graded strut architecture enables simultaneous mass efficiency and broadened attenuation bandwidth. The proposed computational framework provides a systematic design pathway for vibroacoustic optimization of small machinery isolation components.

Keywords: vibroacoustics, kelvin cell, metamaterials, equivalent radiated power (ERP), vibration isolation, finite element analysis (FEA)

I. INTRODUCTION

. Dynamic forces generated during the operation of household appliances — particularly washing machines during spin cycles — produce structural vibrations and low-frequency noise that significantly degrade acoustic comfort and device longevity. Conventional solid elastomeric mounts offer only narrow-band isolation and are inherently limited by trade-offs between static load-bearing capacity and dynamic compliance. Metamaterial-based isolation components, by contrast, can be engineered to exhibit attenuation behaviour at sub-wavelength scales, opening a pathway toward compact, lightweight, and broadband vibration isolators [1].

Cellular lattice structures are widely employed in engineering due to their effective vibration and noise control capabilities, alongside mechanical advantages such as low density and high specific strength [1]. Among the available unit-cell topologies, the Kelvin cell — a truncated octahedron — is recognized as a geometrically simplified yet isotropic representation of open-cell porous media [2]. Kelvin cell-based metamaterials have been shown to overcome the large volume and thickness requirements that traditional acoustic materials impose, particularly for damping low-frequency sounds [3]. By tailoring micro-scale parameters, these structures exhibit meta-behaviours not found in natural materials, enabling targeted noise control at specific frequency bands [4].

A key factor governing the damping performance of Kelvin lattice structures is the precise management of geometric parameters. Studies indicate that dynamic properties such as natural frequency and damping ratio can be controlled by altering porosity. Steel-based Kelvin lattice structures, for instance, provide significant improvements in damping ratios compared to solid counterparts. Moreover, when the cell size is small relative to the macro-scale structure, the lattice no longer behaves as a homogeneous medium, and the geometric details of each unit cell exert a critical influence on damping performance [1]. In terms of acoustic characterization, strut length and radius have been identified as direct determinants of the sound absorption coefficient; Response Surface Methodology (RSM)-based optimizations have demonstrated absorption coefficients as high as 0.98 at frequencies around 186 Hz for specific geometric configurations [3].

A. Geometric modelling of node-strut topology

The vibroacoustic and mechanical performance of Kelvin cell metamaterials is fundamentally governed by the micro-scale geometry of the cell and its influence on macro-scale behaviour. Modern modelling approaches treat these structures as networks of intersecting struts with nodes at the junctions — typically defined as regions where four struts converge — playing a critical role in overall mass distribution [5]. Research has established that the cross-sectional areas of struts and the volumetric contribution of nodes directly govern the relative density of the lattice, and defining these combinations with precise mathematical models enables prediction of mechanical properties with up to 99% accuracy [6]. Crucially, ligaments forming the Kelvin cell are not always homogeneous in cross-section; they tend to thicken toward the nodes, resembling the microstructure of actual metallic foams. This supports modelling nodes not as simple connection points but as spherical or volumetrically enriched forms that optimize load transfer [5]. Additive manufacturing

methods — particularly FDM and DLP-based 3D printing — have enabled the physical realization of such complex node-strut designs, with studies confirming that varying infill density and cell size allows control over stress distribution at nodes and buckling behaviour of struts [7,8].

B. *Functionally graded and locally resonant extensions*

In recent years, Kelvin cell structures have been advanced through multifunctional design approaches. Topology and parameter optimizations have produced hybrid designs offering higher energy dissipation efficiency and wider phononic bandgaps compared to standard uniform-property lattices [4]. Locally resonant metamaterials (LRMs), in which inertial masses are embedded at nodal junctions, generate sub-wavelength bandgaps governed by the resonance frequency of the local oscillator rather than Bragg scattering — a critical advantage for low-frequency isolation targets such as washing machine spin cycles [11]. Functionally graded (FG) variants, in which strut thickness varies continuously along the height of the structure, further extend the operable attenuation range by distributing local resonance frequencies spatially across the lattice [4].

C. *Optimization strategies*

Various computational strategies have been applied to maximize Kelvin cell performance. Genetic algorithms combined with computational homogenization have been used to optimize ligament geometry and minimize discrepancy between numerical models and experimental data for aluminium foams [9]. In aerospace applications, automated iterative methods through platforms such as ANSYS and nTop have confirmed that Kelvin lattices provide minimal weight and stress while stabilizing structural performance under aerodynamic loads [10]. Machine learning-enabled inverse design methods — including convolutional neural networks (CNN) combined with genetic algorithms — have been applied to simultaneously optimize sound absorption coefficients and specific energy absorption for shell-based lattice metamaterials, demonstrating that non-linear parameter relationships can be resolved far beyond traditional trial-and-error approaches [11]. In thermal management, geometric modifications to Kelvin cell strut forms have been optimized via FLUENT analyses to improve heat transfer coefficients and reduce pressure drop [12]. Finally, density-based topology optimization has been applied to fixture design for fatigue testing of 3D-printed lattice specimens, illustrating that holistic optimization now extends to the auxiliary characterization equipment as well [13].

Despite these advances, systematic computational frameworks that couple parametric geometry generation, global finite element assembly, harmonic response analysis, and ERP-based acoustic evaluation within a single optimization loop remain scarce for small-machinery isolation applications. This work addresses that gap by proposing a PSO-driven end-to-end framework for vibroacoustic optimization of a locally resonant, functionally graded Kelvin lattice mount targeting the critical 10–150 Hz washing machine operating range.

II. Computational Framework

A. *Geometric Parametrization*

The lattice is constructed as a 2 × 2 × 2 assembly of Kelvin-topology unit cells with cell size L. A Delaunay triangulation-based strut connectivity algorithm generates the nodal and element data. Strut radius varies linearly with mid-element height, interpolating from t_bottom at z = 0 to t_top at z = z_max, yielding a functionally graded cross-sectional distribution. Each nodal junction hosts a solid polyamide sphere of radius r_node, acting as an embedded inertial resonator.

B. *Global FE Assembly*

Euler–Bernoulli beam elements with six degrees of freedom per node are employed. The element stiffness and consistent mass matrices are assembled into sparse global matrices [K] and [M]. Spherical node masses are superimposed onto the translational DOFs of each node. Fixed boundary conditions at z = 0 are enforced via a penalty method (k_penalty = 10^12 N/m). The four design variables are bounded as follows: t_top, t_bottom ∈ [1, 4] mm; L ∈ [15, 30] mm; r_node ∈ [2.5, 8.0] mm.

C. *Dynamic Analysis*

Harmonic response is computed over 29 discrete frequencies from 10 to 150 Hz. A unit harmonic force of 100 N is applied in the z-direction at the topmost free node, representing the motor excitation during spin cycles. Rayleigh damping coefficients α = 0.05 and β = 0.001 are adopted. The ERP is estimated as:

$$ERP(\omega) = \tfrac{1}{2}\,\rho_0\, c_0 \,\Sigma\, |v\_z,i(\omega)|^2 \cdot A\_eff$$

where ρ_0 = 1.21 kg/m³ is air density, c_0 = 343 m/s is the speed of sound, v_z,i are nodal z-velocities derived from harmonic displacements, and A_eff = 0.01 m² is the effective radiation area per node.

III. Optimization Strategy

A. *Objective Function*

The scalar cost function balances acoustic radiation and structural mass:

$$F(x) = \max[ERP(\omega)] \cdot (1 + \alpha \cdot m\_total)$$

with mass penalty coefficient $\alpha = 5.0$. Two hard constraints are enforced through penalty escalation: (i) a geometric feasibility constraint requiring $t_{top}, t_{bottom} \leqslant r_{node}$ (struts cannot exceed sphere radius); and (ii) a structural integrity constraint requiring the fundamental natural frequency $f_1 > 15$ Hz to ensure load-bearing capacity. Violations raise the cost by factors of 10^6 and 100, respectively.

B. Why Not Exhaustive Search?

The vibroacoustic performance evaluation requires solving complex eigenvalue problems and harmonic response matrices for each topological configuration. Given the four continuous design variables, a full-factorial exhaustive search would lead to an exponential increase in computational cost (the curse of dimensionality). Therefore, Particle Swarm Optimization (PSO), a meta-heuristic algorithm, was implemented to efficiently navigate the non-linear design space and locate the global optimum within a continuous domain without excessive computational overhead.

C. PSO Settings

The PSO engine uses a swarm of 20 particles over 15 iterations. Each particle represents a candidate design vector $x = [t_{top}, t_{bottom}, L, r_{node}]$. The personal and global best positions are updated each iteration using standard velocity–position update rules. Convergence is monitored via the best-cost plot generated by MATLAB's particleswarm solver.

IV. Results and Discussion

Figure 1 shows the optimized locally resonant Kelvin lattice topology rendered in MATLAB. The colour gradient of struts — transitioning from dark blue at the base to deep red at the top — visually confirms the functionally graded strut-radius distribution. The dark spherical nodes are clearly visible at all 27 nodal junctions of the 3 × 3 × 3 node grid.

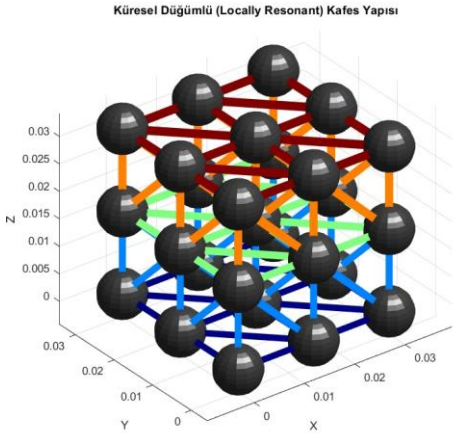

Fig 1. Optimized locally resonant graded Kelvin lattice topology (MATLAB).

The PSO converged to an optimum design where the top strut is thinner than the base strut, reflecting the gradient that places higher stiffness at the load-bearing base and higher compliance (and thus greater local resonance sensitivity) near the top. The spherical node masses introduce inertial loading at each junction, generating local resonance-driven attenuation bands that are tuned to the spin-cycle frequency range.

The fundamental natural frequency constraint ($f_1 > 15$ Hz) remained active throughout optimization, indicating that the algorithm consistently navigated the boundary between adequate static stiffness and desirable compliance. The mass penalty term ($\alpha = 5.0$) effectively prevented over-mass solutions that would otherwise achieve low ERP by simply adding material without acoustic benefit.

The ERP evaluation over 10–150 Hz confirmed that the graded architecture distributes attenuation across a broader frequency band compared to a uniform-radius baseline, consistent with findings reported for functionally graded phononic structures in the literature [4,11]. The multi-physics cost function, coupling structural inertia and radiated acoustic power, produced a Pareto-efficient trade-off that neither purely structural nor purely acoustic single-objective formulations could achieve.

V. Conclusion

A computationally efficient framework for vibroacoustic optimization of locally resonant, functionally graded Kelvin lattice mounts was presented. The integration of PSO with a parametric FE engine and ERP-based acoustic objective enabled systematic exploration of a four-variable continuous design space. Key findings are:

(1) Spherical resonator nodes embedded in a graded strut network generate broadband sub-wavelength attenuation within 10–150 Hz, covering the critical washing machine spin-cycle range.

(2) The compound cost function $F(x) = \max(ERP) \cdot (1 + \alpha \cdot m)$ successfully balances acoustic performance and mass efficiency, yielding designs that are lighter than mass-maximized solutions yet more attenuating than stiffness-maximized ones.

(3) PSO is indispensable for this problem class: exhaustive search over four continuous variables would be computationally intractable, confirming the necessity of meta-heuristic optimization.

Future work will fabricate the optimized geometry via FDM using PA12 and validate the predictions through experimental ERP measurements on a dedicated test rig under operational motor excitation.

References

[1] Y. Wei vd., “Damping behaviors of steel-based Kelvin lattice structures fabricated by indirect additive manufacture combining

investment casting", Smart Mater. Struct., c. 29, sy. 5, s. 055001, Mar. 2020, doi: 10.1088/1361-665X/ab78b8.

[2] [2] Z. Cai, V. C. Henriquez, A. Islam, ve F. Lucklum, "A Method to Investigate the Influence of Geometry Parameters on the Vibroacoustic Behavior of Kelvin Cell Foam", 2024, SSRN. doi: 10.2139/ssrn.5077431.

[3] [3] S. S. Shah, D. Singh, J. S. Saini, N. Garg, ve C. Gautam, "Acoustic characterization of 3D printed Kelvin cell metamaterial using response surface methodology", J. Braz. Soc. Mech. Sci. Eng., c. 48, sy. 2, s. 149, Şub. 2026, doi: 10.1007/s40430-025-06116-5.

[4] [4] H. J. Rice, J. Kennedy, P. Göransson, L. Dowling, ve D. Trimble, "Design of a Kelvin cell acoustic metamaterial", J. Sound Vib., c. 472, s. 115167, Nis. 2020, doi: 10.1016/j.jsv.2019.115167.

[5] [5] W.-Y. Jang, S. Kyriakides, ve A. M. Kraynik, "On the compressive strength of open-cell metal foams with Kelvin and random cell structures", Int. J. Solids Struct., c. 47, sy. 21, ss. 2872-2883, Eki. 2010, doi: 10.1016/j.ijsolstr.2010.06.014.

[6] [6] K.-M. Park, G.-O. Kim, J.-G. Kim, ve Y. Roh, "Mechanical properties of additive manufactured variable-density Kelvin lattice structures: a novel design method for Kelvin unit cells", J. Struct. Integr. Maint., c. 7, sy. 1, ss. 34-45, Oca. 2022, doi: 10.1080/24705314.2021.1971893.

[7] [7] R. Daya Karthic, J. Joy, G. Sakthivel, ve R. Nadimpalli, "Mechanical characterization of 3D-printed Kelvin cell with varying infill densities", Mater. Today Proc., c. 84, ss. 41-46, 2023, doi: 10.1016/j.matpr.2023.04.675.

[8] [8] Akshansh Mishra1 vd., "PERFORMING COMPARATIVE ANALYSIS ON ADDITIVE MANUFACTURED HYBRID STRUT-BASED METAMATERIALS ON THE BASIS OF SPECIFIC ENERGY ABSORPTION", Adv. Mater. Sci., c. 25, sy. 2, s. 52, Haz. 2025, doi: 10.2478/adms-2025-0010.

[9] [9] V. G. Belardi, S. Trupiano, P. Fanelli, ve F. Vivio, "Overall elastic characterization of equivalent FE models for aluminum foams through computational homogenization approach and genetic algorithm optimization", Eur. J. Mech. - ASolids, c. 103, s. 105189, Oca. 2024, doi: 10.1016/j.euromechsol.2023.105189.

[10] [10]N. Khan, V. Acanfora, ve A. Riccio, "Non-Conventional Wing Structure Design with Lattice Infilled through Design for Additive Manufacturing", Materials, c. 17, sy. 7, s. 1470, Oca. 2024, doi: 10.3390/ma17071470.

[11] [11]Z. Hu vd., "Machine learning – enabled inverse design of shell-based lattice metamaterials with optimal sound and energy absorption", Virtual Phys. Prototyp., c. 19, sy. 1, s. e2412198, Ara. 2024, doi: 10.1080/17452759.2024.2412198.

[12] [12]M. Sun, L. Zhang, C. Hu, J. Zhao, D. Tang, ve Y. Song, "Forced convective heat transfer in optimized kelvin cells to enhance overall performance", Energy, c. 242, s. 122995, Mar. 2022, doi: 10.1016/j.energy.2021.122995.

[13] [13]J. Castro vd., "Density-Based Topology-Optimized 3D-Printed Fixtures for Cyclic Mechanical Testing of Lattice Structures", Polymers, c. 17, sy. 18, s. 2468, Oca. 2025, doi: 10.3390/polym17182468.

Design Considerations and Geotechnical Challenges for Subsea Shallow Foundations

Ali Çoban[1,*], Zeynep H. Özkul Birgören[1]

[1]*Graduate School of Applied Sciences, Ankara Yildirim Beyazit University, Ankara, Türkiye*

***Contact:** al.coban@yahoo.com

***Abstract*—** Subsea shallow foundations, which play a critical role in the stability of offshore energy facilities, are expected to demonstrate reliable performance under harsh environmental conditions on the seabed. In alignment with the evolving needs of the energy sector, this study aims to present the fundamental geotechnical design challenges encountered during the design stages of offshore shallow foundations. The scope of the study encompasses key design phases, including installation on the seabed, operational processes, and decommissioning at the end of the service life. Within this framework, the impacts of varying geotechnical design factors on engineering decisions are examined in light of related case studies. The resulting technical data and evaluations provide a comprehensive framework for professionals in the field of offshore geotechnical engineering to develop both safe and cost-effective solutions. Ultimately, this work seeks to contribute to the development of design standards and the advancement of the literature for offshore engineering projects in Türkiye.

Keywords: subsea shallow foundations, offshore geotechnical engineering, design challenges, case studies

I. INTRODUCTION

Energy supply from offshore sources is important for establishing energy independence and maintaining a growing economy for countries. In response to that significance, many robust offshore assets (platforms, drilling units, pipelines, data cables, turbines, etc.) for both oil and gas energy fields and wind farms have been constructed for energy extraction, production, and transfer projects. Subsea shallow foundations are necessary to provide support for subsea facilities resting on the seabed. Shallow foundations typically have an embedment ratio (i.e. penetration depth to diameter or width of foundation) of less than unity. This paper offers a brief overview to subsea shallow foundation types and addresses related design aspects in detail.

A. Offshore Environmental Loads

Offshore shallow foundations are larger than most onshore shallow foundations. The onshore loading regime mainly consists of both the static vertical loadings arising from the superstructures' dead-weight and the vertical live load. However, the loading conditions for subsea shallow foundations include additional load components due to monotonic and cyclic effects. They are imposed by harsh metocean conditions and hydrodynamic regimes (i.e. severe storms, winds, waves, and loop currents). Such foundations are exposed to higher lateral loads and overturning moments than land equivalents. Fig. 1 presents a comparison of horizontal design loads (H) versus vertical design loads (V) on the foundations. The ratio H:V is greater than 1:6 for major offshore oil or gas platforms (Ekofisk I, Beryl A, Brent B, and Gullfaks C [1]) whereas it is about 1:50 for the two high-rise buildings (Incheon Tower [9] and Dubai Tower [1]).

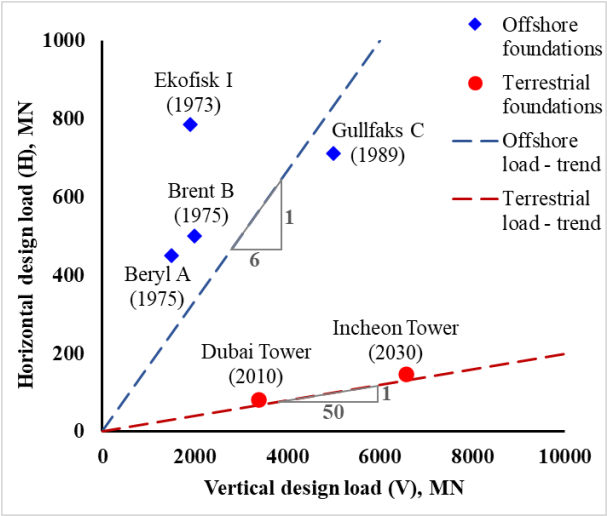

Fig. 1 Horizontal design load versus Vertical design load

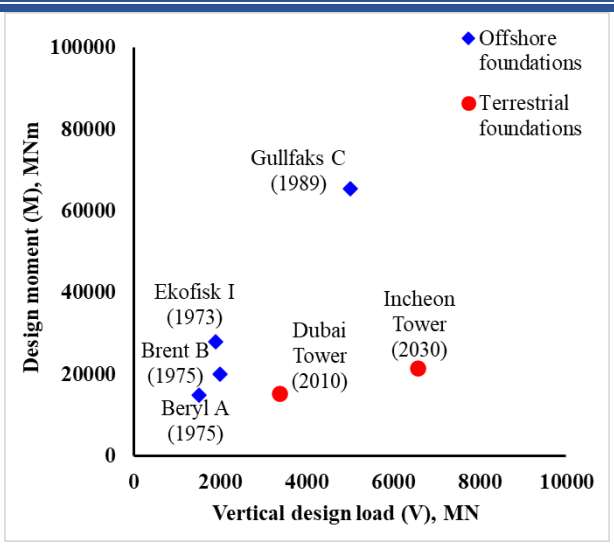

Fig. 2 Design moment versus Vertical design load

Similarly, Fig. 2 illustrates the comparison of the design moments (M) and vertical design loads for the same offshore and terrestrial foundations.

The loading regimes of most terrestrial structures are dominated by vertical loads and have comparatively small horizontal and moment loads. Offshore foundations typically possess higher H:V and M:V ratios than most terrestrial foundations (refer to dotted lines in Fig. 1). The two terrestrial towers have been selected for their vertical design loads comparable to the offshore foundations shown. It should be noted that most onshore shallow foundations will have smaller V-H loads compared to the two towers referenced. Therefore, while the terrestrial foundation design mainly focuses on vertical resistance and settlement analysis, subsea foundation design requires assessment of combined (V, H, M) loading to ensure on-bottom stability.

B. Types of Offshore Shallow Foundations

Subsea shallow foundations generally have a large footprint which distributes the design loads to (and is directly supported by) soils near the mudline. Conversely, subsea piles are designed to bypass weaker surficial strata and transmit loads to more competent deposits at greater depths through a combination of shaft friction and end bearing resistances. Accordingly, shallow foundations are characterized by an embedment depth that is typically less than or equal to their width.

Commonly preferred types of offshore shallow foundations are shown in Fig. 3. Subsea mudmats are flat steel plates (with holes) that support pipeline assemblies (i.e. manifolds, PLETs and PLEMs) (Fig. 3a) [2]. Mudmats might also be used as a temporary support for fixed jackets before pile installation.

Spudcans are large inverted cones with a bottom protrusion. They are used to the legs of (tripod or tetrapod) jack-up rigs (Fig. 3b) [17]. Their shape may vary and spudcan diameters might exceed 20 meters [1]. Suction buckets and caissons are now designed as vertical anchors for (floating) tension-leg platforms (TLP) or as permanent foundations supporting jacket structures instead of piles (Fig. 3c) [1].

Gravity base foundations (GBF) might be designed as large concrete ballast caissons (Fig. 3d) [13], or occasionally used (in submarine pipeline projects) as a riser tower base connected to a floating topside unit [2]. GBFs are used for both offshore wind turbines and oil or gas platforms operating in shallow waters. GBFs are also convenient to be operated as large tanks for hydrocarbon storage. Condeep is originally a gravity base structure (GBS) consisting of a number of cylindrical concrete cells or pillars (Fig. 3e). Some of the cells have vertical extensions which support the “topsides” (i.e. the above-water components) of the energy facility.

Hybrid foundations are now adopted by the offshore engineering industry. Such foundations basically comprise of various combinations of structural components which are typical of both shallow and deep foundation designs. Configurations vary, but one example is referred to as the pinned pile mudmat [22], deep skirted Condeep, hybrid monopile, and monopile-bucket foundation [16].

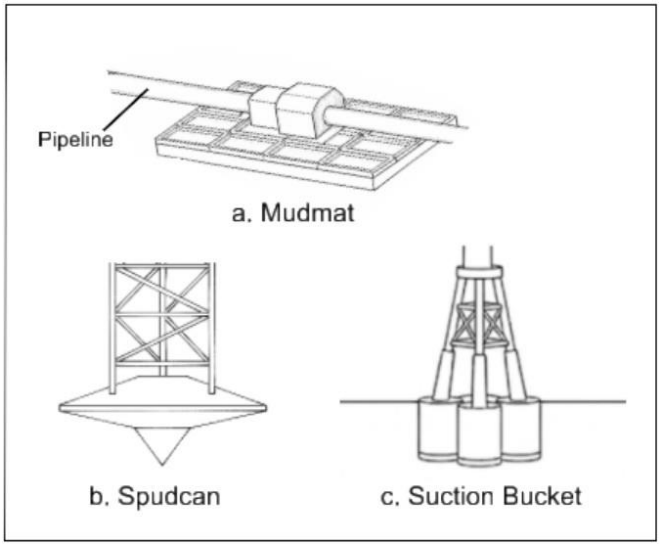

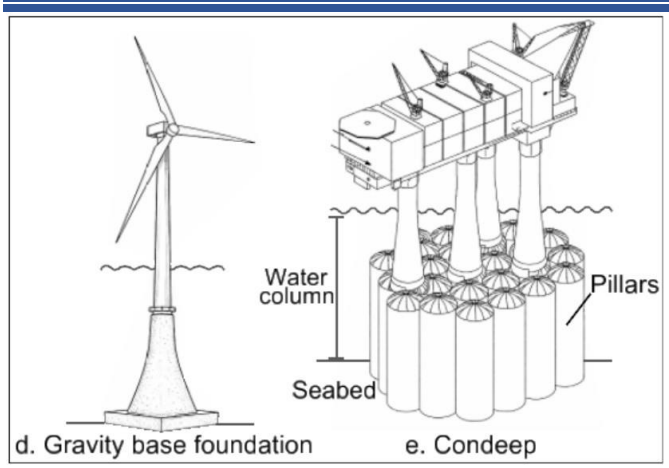

Fig. 3 Schematic representation of offshore shallow foundations

As environmental conditions vary around the globe, foundation selection is primarily driven by seabed soil properties. Table 1 provides a comparative analysis of several offshore projects and their respective soil-structure configurations. Historical and modern cases such as Ekofisk I and Thornton Bank demonstrate that gravity base foundations are predominantly preferred for dense sandy deposits. They use their massive self-weight for stability [1], [13].

Projects like Snorre A and Zhuanghe have used (suction) buckets which are more suited for soft clayey deposits or muds. Additionally, large Condeep gravity bases have been used to support Brent B and Beryl A platforms. Their self-weight was relied on for stability on sands. Gulfaks C and Troll A have used Condeeps with skirts. It has been aimed to provide additional stability on weaker soils (such as clay and silt) by using skirts [1], [11], [13].

TABLE I
CASE STUDIES OF OFFSHORE SHALLOW FOUNDATIONS

Project - Country Sector (Year)	Soil Conditions	Foundation Type
Thornton Bank - Bl. OW (2013)[1]	Very dense fine sand	Ballasted CGBF
Wandoo - Au. OG (1997)[2]	Calcareous sand over calcarenite	Ballasted CGBS
Ekofisk I - Nw. OG (1973)[2]	Dense Sand	GBF
Yolla - Au. OG (2004)[2]	Calcareous silt with clay & sand	Steel skirted GBS
Snorre A - Nw. OG (1991)[2]	Soft NC clays	TLP with concrete buckets
Draupner E - Nw. OG (1994)[2]	Fine sand over stiff clay	Jacket with steel buckets
Sleipner SLT - Nw. OG (1995)[2]	Fine sand over stiff clay	Jacket with steel buckets
Zhuanghe - Ch. OW (2021)[3]	Soft clay and mud	Tripod bucket
Brent B - Nw. OG (1975)[2]	Stiff clay with sand	Condeep
Beryl A - Nw. OG (1975)[2]	Dense sand	Condeep
Gullfaks C - Nw. OG (1989)[2]	Soft NC silty clay and clayey sand	Deep skirted Condeep
Troll A - Nw. OG (1996)[2]	Soft NC clays	Deep skirted Condeep

Abbreviations: OG: Oil or Gas, OW: Offshore Wind, Bl. Belgium, Nw. Norway, Au. Australia, Ch. China, NC clay: Normally Consolidated clay, GBS: Gravity Base Structure, GBF: Gravity Base Foundation, CGBF: Concrete Gravity Base Foundation, CGBS: Concrete Gravity Base Structure, TLP: Tension-leg Platform
References: 1 [13]; 2 [1]; 3 [11]

C. Design Codes

Subsea shallow foundations should be analysed in view of the requirements for installation, capacity, and serviceability. Due to challenges unique to the offshore environment and because such projects fall outside the jurisdiction of government-based building codes, a specialized set of standards is generally used. These design standards include:

- *API RP 2GEO (2011)*: American Petroleum Institute, Recommended Practice, Geotechnical and Foundation Design Considerations [4].
- *DNV-RP-C212*: Det Norske Veritas, Recommended Practice, Offshore Soil Mechanics and Geotechnical Design [5].
- *ISO 19901-4:2025*: International Organization for Standardization, Oil and Gas Industries Including Lower Carbon Energy - Specific Requirements for Offshore Structures - Part 4: Geotechnical Design Considerations [6].
- *NAVFAC SP-2209-OCN (2012)*: Naval Facilities Engineering Command, Special Publication, Handbook for Marine Geotechnical Engineering [7].
- *API RP 2A-WSD*: American Petroleum Institute, Recommended Practice Planning, Designing, and Constructing Fixed Offshore Steel Platforms - Working Stress Design [8].

II. INSTALLATION

High water columns (i.e. seawater depth) pose substantial operational challenges during foundation installation. It requires extensive logistical preparation. Specialized vessels with massive cranes and auxiliary equipment must be mobilized before the operation begins. These assets, along with specialized personnel, significantly increase project expenditures.

Installation methods vary based on predefined foundation type. The principal installation stages for the Condeep (as a concrete gravity base foundation) and suction buckets are described in this paper.

A. Installation of Suction Buckets or Caissons

The installation of suction caissons as illustrated in Fig. 4 consists of two stages. In the first stage, the caisson penetrates into the seabed under its self-weight, W, while the displaced water inside the caisson is allowed to escape through a vent. Penetration continues until the soil resistance becomes equal to the caisson weight. The overall soil resistance is the sum of the friction along the skirt wall, f, and the upward resistance at skirt tip level, q. These resisting forces are functions of (a) embedment depth, (b) strength of the seabed soil at skirt tip level, and (c) adhesion between the seabed soil and skirt wall. In the second stage, additional penetration is achieved by pumping water out of the caisson, and creating a pressure differential, ΔP, between the inside and outside of the caisson. This pressure difference creates a net downward force which drives the caisson to the required design depth. Once the target depth, z', is reached, the top valve is closed, generating passive suction that enhances the pull-out resistance of the foundation [1].

A proper seal between the caisson skirt and the seabed soil is essential to prevent soil piping and loss of suction. Excessive pumping should be avoided, as it may lead to structural instability such as buckling of the caisson. It may also lead to soil plug failure or piping (particularly in sands). In addition, high pore water pressure differentials might trigger failures caused by soil heave or piping (particularly in sands).

Common suction caisson issues are plug heave, buckling, soil piping, and bottom resistance failure. Soil heave refers to the upward displacement or swelling of soil caused by a reduction in effective stress. Piping represents a more severe condition in which the soil loses its shear strength and behaves like a fluid when the hydraulic gradient approaches a critical value. Target penetration may also not be reached due to unexpectedly high soil resistance and/or piping. Attempts to reach target depths through excessive pumping may lead to buckling of the caisson walls. These issues are of greater concern in sandy soils where cohesion is low and permeability is high. A review of the literature and field cases show that suction caissons are more commonly used in clayey soils where both shear strength and permeability are low. Installation performance mainly depends on applied suction and soil properties. Careful monitoring of seabed conditions and suction is essential to reduce these risks [1], [14].

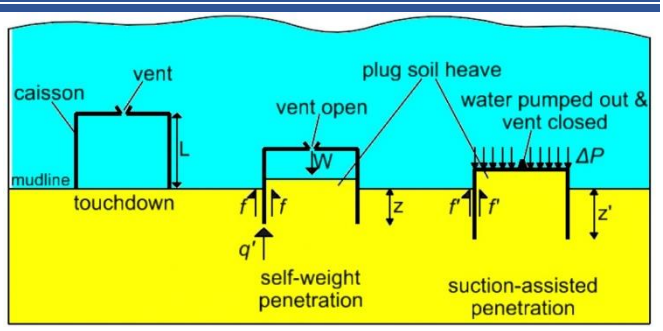

Fig. 4 Schematic showing suction-assisted installation stages for buckets

B. Installation of Massive Gravity Base Condeep Structures

Fabrication of foundation portions initially begin on land and are then transferred into a wet dock. The structure is then gradually submerged in the water (by flooding and ballasting) as the construction of pillars and the extentions continues. The topside is then placed above the concrete hull. It is towed to project location. Controlled flooding and ballasting are operated to reach the desired embedment depth. Skirts and suction assisted seabed penetration might be used for softer soil deposits. Base grouting is finally conducted to provide on-bottom stability and prevent further penetration [1].

Insufficient grouting and excessive penetration are critical design issues herein. Uneven seabeds require careful consideration to ensure complete base grouting. Although consolidation improves long-term soil strength, foundations are vulnerable to bearing failure during installation. This risk arises because the soil may not drain quickly enough to gain strength. Active drainage or staged ballasting can mitigate this short-term risk. The Gullfaks C platform have used a skirted Condeep structure with an active drainage system. This system accelerated consolidation by removing excess pore water from the soft soil [1].

In contrast, the Troll A platform was placed on low-permeability clays with long drainage paths. Since drainage was impractical during installation, an undrained design approach has been adopted. All capacity and settlement limits for Troll A have been evaluated based on this undrained behaviour [1].

III. CAPACITY

On-bottom stability of foundations is assessed by the use of limit equilibrium methods. A minimum safety factor of 2.0 against bearing failure and of 1.5 against sliding failure are generally used for foundation design [4], [8]. The ultimate limit state of subsea shallow foundations is fundamentally governed by their stability under combined loadings. Foundation skirts may be used to improve the foundation stability and to limit vertical and horizontal displacements and rotations. The following sections discuss how to calculate vertical bearing capacity, horizontal capacity of a given foundation and how to account for moment loads [4].

A. Vertical Bearing Capacity

The methods used in bearing capacity analysis of offshore shallow foundations are based on the classical bearing capacity approach. The equations are similar to but slightly different than those used for terrestrial foundations [1].

The equation for determining the undrained ultimate vertical load, Q_{d}, that a subsea shallow foundation can carry in undrained conditions is given in Eq. 1 [4]

$$Q_d = F\left(s_{u0}\, N_c + \frac{kB'}{4}\right) K_c\, A' \quad (1)$$

where N_c is the bearing capacity factor, B' is the effective foundation width, A' is the effective foundation area calculated by using the adjusted foundation dimensions based on load eccentricity, and K_c is a correction factor reflecting the combined effects of load inclination, foundation shape, embedment depth, foundation base inclination, and seafloor surface inclination.

Undrained loading conditions occur in soft clay seabed typical of deep water sites (water depth in excess of about 1000 m). The shear strength at such sites typically increases with depth and may be expressed as shown in Eq. 2 [10]

$$s_u = s_{u0} + kz \quad (2)$$

where s_{uo} is the shear strength at foundation base, k is the shear strength increase with depth (i.e. gradient), z is the depth below foundation level. The correction factor F, shown in Eq. 1, is defined as a function of the degree of strength heterogeneity, κ, of the soil where $\kappa = kB/s_{u0}$. The value of F is equal to unity for $\kappa = 0$ and increases to 1.8 for rough (and 1.4 for smooth) foundation interfaces at a value of $\kappa = 20$ (refer to figure by Davis and Booker (1973) [15]).

The equation for determining the drained ultimate vertical load, $Q_{\mathrm{d}}{}'$, that a subsea shallow foundation can carry in undrained conditions is given in Eq. 3 [4]

$$Q'_d = \{p'_o(N_q - 1)K_q + 0.5\gamma' B' N_\gamma K_\gamma\}A' \quad (3)$$

where N_q and N_γ are the bearing capacity factors, γ' is the buoyant unit weight of seabed soil deposit, ϕ' is the effective friction angle of soil, p'_o is the overburden at foundation base level, K_q and K_γ are the correction factors.

B. Horizontal Capacity

Skirtless foundations are inherently limited as they rely only on the contact between foundation and the surficial soil. The degree of soil disturbance should be considered for the analysis herein.

The undrained and drained horizontal capacity of surface foundations based on API RP 2GEO (2011) [4] are shown in Eq. 4 and Eq. 5, respectively.

$$H_d = s_{u0}A \quad (4)$$

$$H'_d = Q \tan\phi' \quad (5)$$

Here, H_d and H'_d, are the maximum total horizontal load that may be applied to the base of the foundation before failure occurs under undrained and drained loading conditions respectively. The parameter s_{uo} is the shear strength at foundation base level, Q is the actual vertical load acting during the relevant loading condition, and ϕ' is the effective internal friction angle of the seabed deposit.

Sliding resistance calculations usually assume full soil - soil contact. This assumption must be verified for each project. Using the soil's internal friction angle might lead to over-estimating the actual sliding capacity.

The use of an appropriate interface friction angle between foundation and soil is recommended for calculating sliding along soil-structure boundaries in drained loading conditions. Interface friction angle may be found by experiment or it may be estimated as a fraction of (typically 0.5 to 0.7) ϕ' [21]. For undrained loading, an appropriate friction factor, α, should be applied to the undrained shear strength.

Engineers must also check for thin, weak soil layers just below the foundation. These layers can cause the failure to occur deeper in the soil, significantly reducing sliding stability [4]

Sliding resistance of skirted shallow foundations depends on the soil strength at skirt tip level and active / passive earth pressure around the skirt periphery. The contribution of these factors may be taken into account as described in API RP 2GEO [4], if found appropriate.

C. Assessment of Moment Loads

In the subsea environment, hydrodynamic loads (i.e. waves and currents) generate horizontal loads on the submerged parts of the platform structure. These horizontal loads generate overturning moments proportional to their lever arm (i.e. height above foundation). The taller the GBS or platform, the higher is the lever arm and associated moment load. The bearing capacity of a foundation will decrease if overturning moment loads are present. In order to account for the reduction in bearing capacity the effective area method is used.

Fig. 5 shows a schematic of a rectangular foundation with overturning moment loads. In the effective area method, the two overturning moments are expressed as their equivalent eccentric vertical loads, which is illustrated in Fig. 6. The values of eccentricities, e_x and e_y, (shown with red lines in Fig. 6) are calculated by using Eq. 6 and Eq. 7, respectively [4]

$$e_x = \frac{M_x}{Q} \quad (6)$$

$$e_y = \frac{M_y}{Q} \quad (7)$$

where M_x and M_y are the moment loads causing rotations around the x axis and y axis, respectively, and Q is the resultant vertical load. The adjusted foundation width, B' and length, L' are calculated based on the eccentricities calculated as presented in Eq. 8 and Eq. 9 [4]

$$B' = B - 2e_y \quad (8)$$

$$L' = L - 2e_x \quad (9)$$

where B and L are the actual dimensions of the foundation. The adjusted foundation dimensions are then used for determining the associated effective foundation area, A', which is incorporated into bearing capacity analysis (see Eq. 1 and Eq. 3).

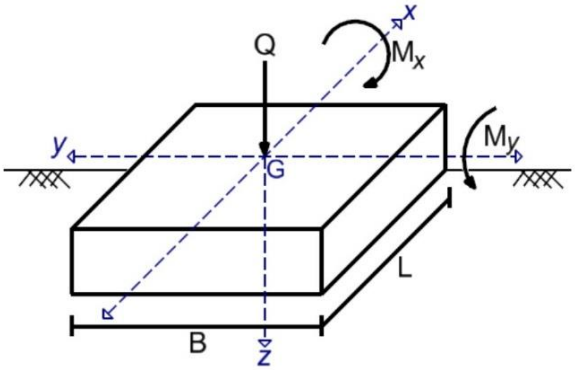

Fig. 5 Schematic of a foundation with two-way moment loads

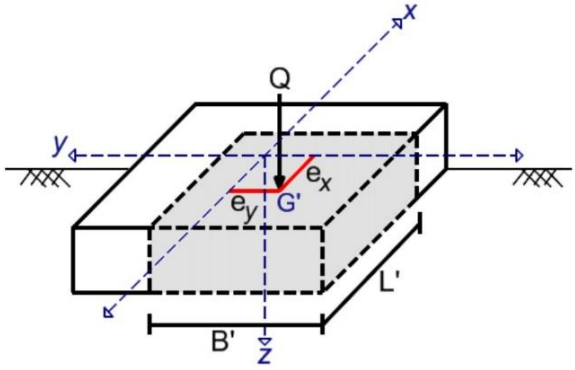

Fig. 6 Reduced area representation

D. Cyclic Capacity and Uplift

Severe storm loads tend to generate excess pore water pressure within the seabed soil. This leads to a reduction in the effective stresses within the soil and consequently to reductions in its shear strength. Clayey soils might soften in such situations, whereas liquefaction might be triggered in sandy deposits. Such phenomena have been observed both in the field and in laboratory tests [3], [20].

In shallow water fluctuations in the water surface elevation caused by wave action can generate vertical oscillatory forces in the seabed soil. It may lead to the development of tension on GBFs. Consequently, such foundations are subjected to a cyclic loading state mobilized by alternating periods of tension and (inherent) compression [1].

The foundation resistance to withstand this tension is referred as uplift or pull-out resistance. Jacket structures with bucket foundations are relatively light compared to GBFs. It makes the foundation buckets more susceptible to cyclic loading of tension and compression. The uplift resistance depends on the submerged weight of foundation, friction of the embedded soil, and suction generated beneath the foundation [7].

However, the uplift resistance is sensitive to drainage conditions and restricted by the seal effectiveness. Therefore, long-term sustained uplift resistance is not relied upon in design [1], [7].

IV. SERVICEABILITY

The primary concern in design is generally foundation capacity. Assessing the long-term settlement might set a secondary (serviceability) limit on the predefined bearing capacity. Excess settlement is critical particularly in compressible seabed deposits such as silts and sands of silica and carbonate composition. Allowable settlement of an offshore shallow foundation must consider the displacement tolerance of connected subsea wells and pipelines. Excessive relative displacement between different components can lead to structural damage in connected piping. It is noted however, that larger foundation settlements (of around 1 m) can, generally, be accepted if they occur before other pipeline assets are installed [1].

Variable seabed soil stratigraphy and uneven bathymetry may lead to uncontrollable and differential settlement. A stratigraphy comprised of firm thin layers overlying weaker deposits possesses a significant risk of punch-through failure, especially for spudcans [17]. Relying on precise soil profile data gathered from exact foundation locations is more reliable than regional generalizations to reduce risks.

Significant differential settlement may cause GBFs to become tilted and collapse. Controlled ballasting or active drainage systems might be preferred to prevent failure. The Gullfaks C platform have used an active drainage system to accelerate soil consolidation prior to riser connection. The Troll A platform, which has been located in comparable soil conditions to the Gullfaks C, has employed a watertight base design specifically to maintain an undrained response and control settlement rates [1].

Differential settlement is also a concern for sliding mudmats supporting submarine pipeline equipment. Sliding mudmats are designed to accommodate axial displacements due to pipeline installation and thermal expansion-contraction cycles during operational and shutdown conditions. These cyclic movements can lead to differential settlement, potentially hindering the ability of the mudmat to recover its original position and initiating progressive penetration [19].

The erosion of seabed sediments might cause scour development around foundation base. Typical mitigation measures include armouring techniques like riprap or articulated concrete mats. For the GBFs in the Thornton Bank offshore wind farm, a dual-layer of armour protection have been used. This design consisted of an armour layer of hard

limestone underneath a filter layer to prevent the loss of backfill material [13]. Alternatively, artificial seaweed is particularly suitable in sites with mild and sporadic wave action. Placing peripheral skirts is another option. They are not to prevent erosion directly, but to maintain structural stability by penetrating below the maximum estimated scour depth. The skirts shield the soil beneath the foundation, and prevent undermining and rocking, even if the surrounding seabed is lowered [7].

Long-term fluid extraction from subsea oil or gas reservoirs may result in another serviceability issue, referred as subsidence of ground. The reservoir pore pressure decline pushes the overlying strata into progressive downward compaction. The Ekofisk I field experienced approximately 3 meters of subsidence after 13 years of field operation. In 1987, the issue required additional costly engineering interventions, including jacking operations and the construction of protective concrete walls around the platform. Despite these measures, seabed lowering continued at rates of up to 0.5 meters per year, necessitating a complete field redevelopment. The subsequent Ekofisk II project was then specifically designed to accommodate up to 20 meters of total seabed subsidence [1]. The issue of subsidence might be mitigated by fluid injection into depleted reservoirs. However, it may trigger contrary challenge: land uplift. Therefore, optimal route selection remains the most effective strategy to avoid these catastrophic issues [18].

V. CONCLUSION

The offshore environment possesses significant challenges in design due to harsh ocean conditions. They have driven engineers to develop diverse foundation types, varying in geometry and installation methods. This study outlines commonly preferred subsea shallow foundation types and their fundamental design criteria. Furthermore, the offshore oil and gas sector persists despite the global attempt to shift toward renewable energy. Consequently, offshore energy sector retains promising potential for future development. Hybrid foundations are relatively novel approaches in this field. They might be the optimal solution to ensure structural safety and economic competence. For emerging offshore markets like Türkiye, the implementation of reliable subsea foundation types together with advanced design approaches is of critical importance. This study addresses this need by providing a technical framework to support future offshore engineering applications.

ACKNOWLEDGMENT

The authors gratefully acknowledge Ankara Yildirim Beyazit University for providing digital access to countless research papers and for organizing this conference.

REFERENCES

[1] M. Randolph and S. Gourvenec, *Offshore Geotechnical Engineering*, Abingdon, UK: Spoon Press, 2011.
[2] Y. Bai and Q. Bai, *Subsea Pipelines and Risers*, Oxford, UK: Elsevier, 2005.
[3] M. P. O'Reilly and S. F. Brown, Eds., *Cyclic Loading of Soils: From Theory to Design*, Glasgow, UK: Blackie and Son Ltd, 1991.
[4] API, *API RP 2GEO: American Petroleum Institute, Recommended Practice, Geotechnical and Foundation Design Considerations*, Washington, DC, USA, 2011.
[5] DNV, *DNV-RP-C212: Det Norske Veritas, Recommended Practice, Offshore Soil Mechanics and Geotechnical Design*, Norway, 2011.
[6] ISO, *ISO 19901-4:2025: International Organization for Standardization, Oil and Gas Industries Including Lower Carbon Energy - Specific Requirements for Offshore Structures - Part 4: Geotechnical Design Considerations*, Geneva, Switzerland, 2025.
[7] D. Thompson and D. J. Beasley, Eds, *NAVFAC SP-2209-OCN: Naval Facilities Engineering Command, Handbook for Marine Geotechnical Engineering*, Washington, DC, USA, 2012.
[8] API, *API RP 2A-WSD: American Petroleum Institute, Recommended Practice, Planning, Designing, and Constructing Fixed Offshore Steel Platforms - Working Stress Design*, Washington, DC, USA, 2014.
[9] H. G. Poulos, "Foundation design for tall buildings," in *Proc. GeoCongress 2012: Geotechnical Engineering State of the Art and Practice*, Reston, VA, USA: ASCE, 2012, pp. 799–801
[10] M. F. Randolph, "Offshore geotechnics - the challenges of deepwater soft sediments," in *Proc. GeoCongress 2012: Geotechnical Engineering State of the Art and Practice*, Reston, VA, USA: ASCE, 2012, pp. 241-271.
[11] L. Luo, Z. Li, Z. Zhou, W. Wang, and W. Wang, "Assessing suction bucket jacket foundation installations in the South China Sea: Insights from field installation experiences," *Mar. Struct.*, vol. 96, Art. no. 103630, July 2024.
[12] K. Trojnar, "New hybrid foundation solutions for offshore wind turbines," *Arch. Civil Eng.*, vol. LXX, no. 1, pp. 5–18, 2024.
[13] K. Peire, H. Nonneman, and E. Bosschem, "Gravity base foundations for the Thornton Bank offshore wind farm," *Terra et Aqua*, no. 115, pp. 19–29, June 2009.
[14] K. O. Akeme, A. Rezagholilou, and M. Banimahd, "Installation constraints of suction assisted foundations and anchors for offshore energy development," *Int. J. GEOMATE*, vol. 15, no. 47, pp. 14–21, July 2018.
[15] E. H. Davis and J. R. Booker, "The effect of increasing strength with depth on the bearing capacity of clays," *Geotechnique*, vol. 23, no. 4, pp. 551–563, 1973.
[16] N. Moscoso, T. van der Linden, T. Balder, and T. Kamphuis, "Hybrid monopile: a new foundation concept for 20+ MW wind turbine generators," in *Proc. ISFOG 2025*, Nantes, France, 2025.
[17] M. S. Hossain, D. Menzies, D. Bhardwaj, and P. C. Wong, "Factor of safety for assessing punch-through failure during installation and preloading of spudcan foundations," in *Proc. 20th Int. Conf. The Jack-Up Platform: Design, Construction & Operation*, London, UK, 2025.
[18] F. Thomas, F. A. Livio, F. Ferrario, M. Pizza, and R. Chalaturnyk, "A review of subsidence monitoring techniques in offshore environments," *Sensors*, vol. 24, no. 13, p. 4164, Jun. 2024.
[19] H. Zhou, H. Krisdani, R. Maujean, and A. D. Deeks, "System integration of direct on-seabed sliding foundations," in *Proc. 3rd Int. Symp. on Frontiers in Offshore Geotechnics (ISFOG 2015)*, vol. 1, 2015, pp. 825–830.
[20] O. Eide and K. H. Andersen, "Guest lecture – foundation engineering for gravity structures in the northern North Sea," in *Proc. 1st Int. Conf. on Case Histories in Geotechnical Engineering*, 1984.
[21] B. M. Das, *Principles of Foundation Engineering*, 8th ed. Boston, MA, USA: Cengage Learning, 2016.
[22] (2026) The WebAppsForEngineers website. [Online]. Available: https://www.webappsforengineers.com/

Cooperative Trajectory Planning for Large-Scale Additive Manufacturing: A Multi-Agent Reinforcement Learning Approach

Ahmed MERZE[1], and Fatih V. ÇELEBİ[1,*]

[1]*Department of Computer Engineering, Ankara Yıldırım Beyazıt University University, Ankara, TÜRKIYE*

*Contact: fvcelebi@aybu.edu.tr

Large-scale additive manufacturing often involves complex geometries that exceed the capacity of a single autonomous agent. While existing deep reinforcement learning frameworks have successfully minimized non-extrusion moves for individual print heads, they lack the capacity to coordinate multiple print heads operating simultaneously on a single print bed. This paper proposes a Multi-Agent Reinforcement Learning (MARL) framework designed to solve the cooperative trajectory planning problem, aiming to speed up the printing process while strictly avoiding printhead collisions. To scale the system effectively, we propose utilizing Dynamic Multiagent Curriculum Learning (DyMA-CL), which allows agents to begin training in small-scale scenarios before progressively increasing the dimensions of the environment and the number of agents. Furthermore, the framework integrates map-merging techniques and Radon-transform-based alignment to extract tomographically salient features, ensuring that multiple agents can align local observations and operate within a consistent global coordinate system without known initial poses. Ultimately, this cooperative AI system outlines the foundational logic necessary to transition from single-agent geometric sequencing to highly efficient, multi-agent additive manufacturing.

Keywords: *trajectory planning, reinforcement learning*

Design and Experimental Investigation of a Membrane-Free Flow-through Electrolyzer for Hydrogen Production

Sefa Şahin[1,2,*], Hasan Özcan[1,2], Ahmet Talha Topcu[1], and Mustafa Kaymak[1]

[1] *Faculty of Engineering and Natural Sciences, Ankara Yıldırım Beyazit University, Ankara 06010, TÜRKIYE*

[2] *Hydrogen Technologies and Energy Research Centre (H2 TEAM), Ankara Yıldırım Beyazit University, Ankara 06010, TÜRKIYE*

***Contact:** sefasahin@aybu.edu.tr

Abstract— Hydrogen production via water electrolysis is considered one of the most promising pathways for sustainable energy systems. However, conventional electrolyzers such as proton exchange membrane (PEM) and anion exchange membrane (AEM) systems rely on expensive membranes that increase system cost and reduce long-term durability. In this study, a membrane-free electrolyzer was designed and experimentally investigated to develop a simpler and more cost-effective hydrogen production system. Experimental results showed that the electrolyzer operates most effectively between 3.0–3.5 V accounting for 42-55% HHV efficiency, achieving a maximum current of approximately 0.15-0.5 A/cm2 under influence of temperature and KOH molarity. The findings demonstrate the feasibility of membrane-free electrolyzer designs and highlight the importance of flow optimization for improving hydrogen production efficiency. Such technologies can be easily scaled to kWh levels to be used as replacement to natural gas burning sector such as ceramics making that does not require very high hydrogen purity and requesting safer operation than that of HHO electrolysis.

Keywords: Membrane-free, Hydrogen, Electrolyzer, Water

I. INTRODUCTION

Membrane-free electrolyzer systems are cost-effective because they can operate without the need for expensive materials such as membranes with ion conductivity [1]. Their simple structure, scalability, and low cost have made them important in hydrogen technologies and other energy studies today [2,3]. In this context, prominent research topics aimed at improving the performance of membrane-free electrolyzers include electrode design, flow dynamics, effective separation of formed products, and safety conditions. Preventing gas passage is particularly critical in these systems, as it directly affects product purity and system safety [4,5]. As a solution, parameters such as electrode distances, flow rate, and flow control methods are investigated [6,7].

Studies have shown that membrane-free electrolyzers can be applied in water sources with impurities [8]. This allows them to operate with sources such as seawater. Unlike existing commercial systems, this project aims to produce hydrogen without requiring water treatment. Therefore, the need for water treatment plants will be eliminated, and hydrogen production combined with renewable energy sources will become possible in coastal areas. Another study observed high product purity thanks to very low levels of hydrogen crossover and low resistances [9]. In one study, membrane-less electrolyzers with different operating modes were subjected to both simulation and testing, and it was observed that bubble separation is possible at high current densities [10]. The objective of this study is to create a scalable, robust, innovative, and cost-effective system for use in hydrogen and energy technologies, especially one that is more cost-effective.

II. MATERIAL & METHODS

A membrane-free electrolyzer system was developed based on a detailed literature review, considering several parameters such as homogeneous electrolyte flow, efficient use of electrolyte surfaces, prevention of gas bubble accumulation, and leak-proofness. The first prototype was produced at Ankara Yıldırım Beyazıt University Central Laboratory (MERLAB) using a 3D printer with low-cost and readily available PLA filament.

After production, the support structures and channel inlets and outlets underwent necessary cleaning processes and were freed from imperfections. Finally, a glass cover, which will keep the system closed, was installed with a liquid sealant to ensure a leak-proof seal.

In the initial experiments, nickel foam was chosen as the electrode material. Low-concentration (0.5-1M) KOH was used with 100 mL of pure water as the electrolyte. Due to leak-proofing problems observed during testing, PLA's failure to demonstrate the expected durability, and the electrode designs not functioning as expected, the material selection and design were changed.

In the new design, CNC machining was chosen as the production method and Castamid (polyamide 6G) was selected as the body material. In electrode design, nickel plates and foams with a triangular geometry, observed to be more suitable for flow dynamics, were used.

Thanks to this, in the new system, both in terms of sealing and the easy removal of gas bubbles from the surface, dead zones were reduced, resulting in more positive results in CFD analyses.

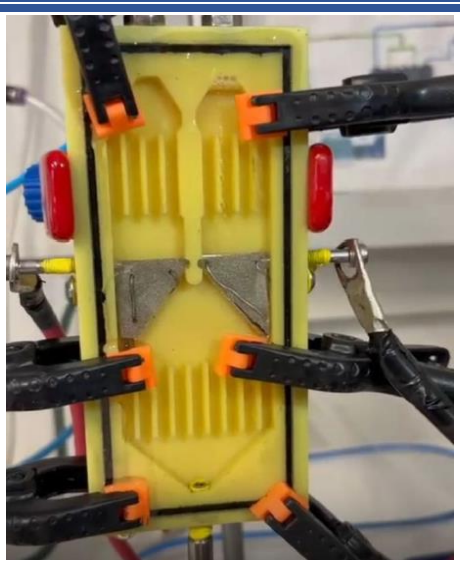

Fig. 1 Final version of the prototype

III.RESULTS & DISCUSSIONS

Ansys Fluent software was used to observe the movement of the fluid within the system. This allowed for early detection of errors and observation of how well the experiments matched the simulation. In the first prototype, when examining how velocity and pressure changed along the channel, it was observed that the fluid flowed very rapidly like a jet from the center of the rectangular channel. The fluid almost completely missed the electrode surfaces on the side walls of the rectangular area where the reaction was taking place. These blue areas where the fluid was not moving (dead zones) made the system much less efficient because no reaction occurred.

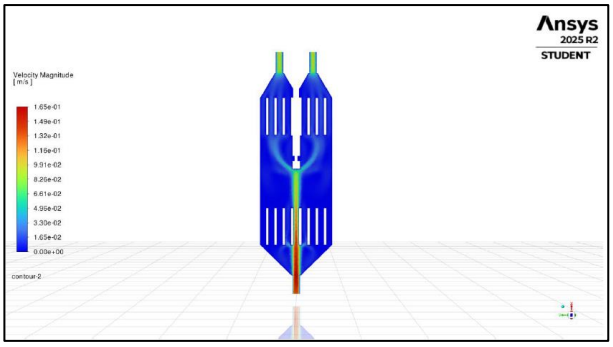

Fig. 2 Velocity distribution showing jet effect from CFD simulation.

When the simulation was later adjusted to analyze the flow paths, it was observed that the fluid did not move in a straight line. Specifically, it was observed that the fluid began to rotate and form vortices (circles) as it exited the channels and reached wider sections. This rotational movement trapped gas bubbles on the electrode surfaces, causing a situation called gas masking that prevented the system from working properly.

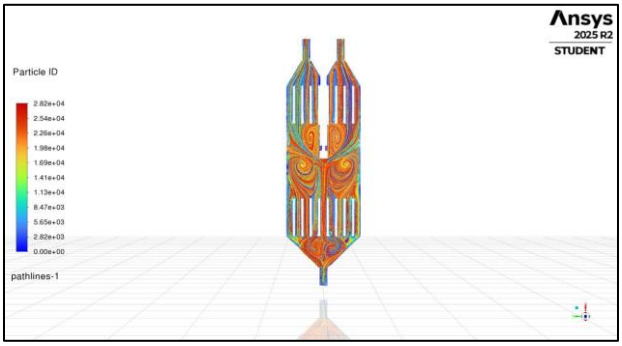

Fig. 3 Pathlines showing vortex formation from CFD simulation.

Thirdly, in the vector analysis examined, it was observed that the fluid moved backward (downward) at the side walls. This, as in the other two analyses, indicated that the rectangular design caused flow problems and dead zones. To prevent this, the design was changed, and the nickel electrodes were designed in a triangular shape. It was observed that this new shape was compatible with the widening channel surface and significantly reduced dead zones.

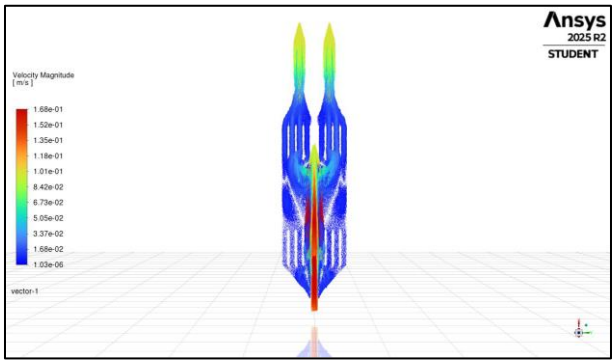

Fig. 4 Vector field showing reverse flow near side walls from CFD simulation.

Current-voltage graphs were created that allow us to comment on many parameters such as ohmic losses, kinetic limitations, and efficiency of systems commonly used in electrolyzer systems. Especially in membrane-less systems, parameters such as flow dynamics and electrode design directly affect ion transport and gas separation, making these graphs critical for understanding the system's behavior.

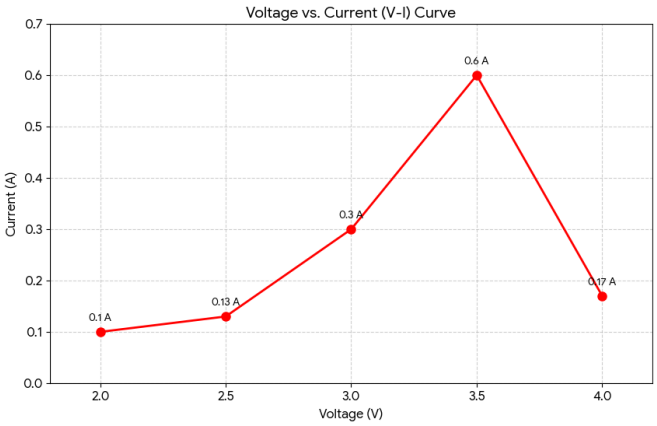

Fig. 5 I-V curve of the last prototype

The electrochemical performance of the resulting prototype was tested in the 2.0V - 4.0V range. As expected, the current started at 2.0V (0.10A), steadily increasing to 3.5V (0.60A) and reaching its peak. This proved that the prototype efficiently provided consistent ion transfer and gas production. As the voltage increased from 3.5V to 4V, the current dropped to 0.17A. One of the main reasons thought to contribute to this decrease was the formation of an insulating layer of gas on the electrode surfaces, also known as gas masking, due to the increased rate of gas formation. Another factor considered was that, since the experiments were conducted manually, momentary fluctuations in the connections, vibrations, or errors in the measuring devices could have caused these results.

The final prototype was also examined in different solutions and at different temperatures by generating current-voltage graphs.

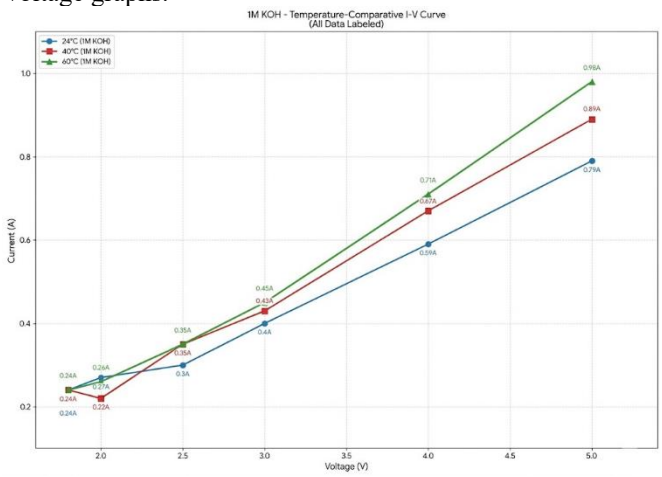

Fig. 6 Temperature comparative I-V curve for 1M KOH solution.

The first graph shows that for 1M KOH electrolyte, the voltage and current increased together at 24°C (room temperature), 40°C, and 60°C. For example, at 5 V and 24°C, approximately 0.79 A was obtained, while at 60°C, this value reached approximately 0.98 A. A significant increase in the current was also observed with increasing temperature. This is because the temperature increases the ionic conductivity in the solution, thereby increasing ionic mobility and accelerating the reaction kinetics.

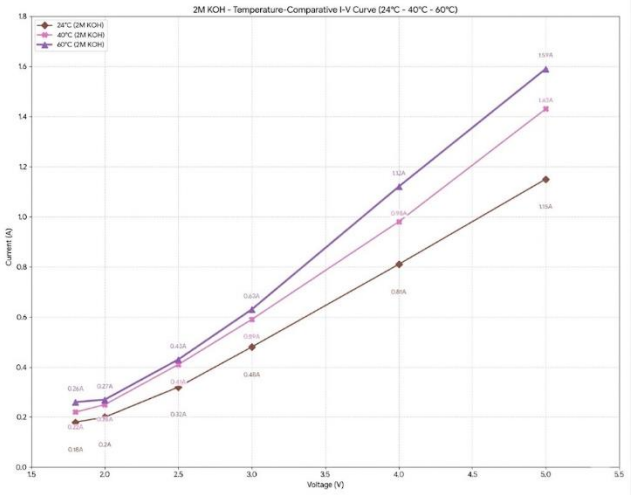

Fig. 7 Temperature comparative I-V curve for 1M KOH solution

This graph shows that as the solution concentration doubles, the ion concentration increases compared to the previous graph, resulting in increased ionic conductivity. Consequently, at the same temperature and voltage values, the current also increases significantly. The differences are even more pronounced, especially in high-voltage regions. For example, when 5V is applied, the current reaches approximately 1.15 A at 24°C, 1.43 A at 40°C, and 1.59 A at 60°C, demonstrating that the increase in concentration significantly alters the electrochemical performance. In particular, compared to the previous graph, the slope of the curves increases rapidly starting from 3V.

These two graphs also show that the generated cell consumes more power at higher temperatures. Therefore, it is important to perform separate efficiency calculations and optimizations for both energy consumption and the amount of product produced. Since electrical power is directly proportional to the square of the current, and systems do not operate at 100% efficiency and produce unwanted by-products, operating at room temperature will be more effective. This eliminates the need for extra costs to increase the cell's temperature. Furthermore, the system's ability to operate without requiring high temperatures or pressures, unlike many systems currently used in energy systems, is one of its key features that sets it apart and paves the way for its widespread adoption.

IV. CONCLUSION

This study revealed that the membrane-less electrolyzer system generally operates stably and without problems. The vortex formations, backflow regions, and gas bubble movement observed within the flow channels during

simulation were experimentally confirmed, consistent with previous analyses. Improvements in results were observed with new designs and changes in material selection. Furthermore, more durable materials improved the cell's suitability for leak-proofing and long-term operation. The final prototype utilized a maximum current of 0.60A at 3.5V.

Changes in current-voltage curves were observed at different temperatures and electrolyte concentrations. Increasing temperature positively impacted production performance but increased energy consumption. In conclusion, this study demonstrates that simpler systems, eliminating the use of membranes, can be beneficial in terms of cost. Based on these results, it shows that with different geometries and material selections, these systems have the potential to be a significant alternative in the development and scalability of sustainable hydrogen production technologies in the future.

ACKNOWLEDGMENT

The authors gratefully acknowledge the financial support provided by the Scientific Research Projects Coordination Unit of Ankara Yıldırım Beyazıt University under Project ID 2924.

REFERENCES

[1] Esposito, D. V. (2022). Membraneless electrolyzers for low-cost hydrogen production in a renewable energy future. Joule, 6(5), 905–921. https://doi.org/10.xxxx/joule.2022.005

[2] Malek, A., Lu, X., Shearing, P. R., Brett, D. J. L., & He, G. (2023). Strategic comparison of membrane-assisted and membrane-less water electrolyzers and their potential application in direct seawater splitting (DSS). Green Energy & Environment, 8(4), 989–1005. https://doi.org/10.1016/j.gee.2022.06.006

[3] Manzotti, A., Robson, M. J., & Ciucci, F. (2023). Recent developments in membraneless electrolysis. Electrochimica Acta, 437, 141327. https://doi.org/10.xxxx/electacta.2023.141327

[4] Pang et al. 2020 Framework for evaluating the performance limits of membraneless electrolyzers — DOI 10.1039/D0EE02268C

[5] Yang et al. 2024 Flow control for bubble management in a membrane-free electrolyser — DOI 10.1016/j.ijmultiphaseflow.2024.104770

[6] Hadikhani et al. 2021 A membrane-less electrolyzer with porous walls for high throughput and pure hydrogen production — DOI 10.1039/D1SE00255D

[7] K. Schoppmann et al., "WhY Shape Matters: Hydrodynamics of a Y-shaped Membraneless Electrolyzer", doi: 10.1016/j.cej.2025.160040

[8] Deng, K., Feng, H., Zhang, Y., Liu, D., & Li, Q. (2023). Ampere-level membrane-less water electrolysis enabled by rose-petal-effect-mimetic interface. Joule, 7, 1852–1865. https://doi.org/10.1016/j.joule.2023.06.010

[9] B. Yang, M. Jafarian, N. Freidoonimehr, and M. Arjomandi, "Flow control for bubble management in a membrane-free electrolyser," International Journal of Multiphase Flow, Feb. 2024, doi: 10.1016/j.ijmultiphaseflow.2024.104770

[10] Niblett, D., Elwan, H. A., & Mamlouk, M. (2025). Membraneless water electrolysis enabled by flow and porous electrode design for bubble separation. *Chemical Engineering Journal*. https://doi.org/10.1016/j.cej.2025.163444

An Improved Sine-Cosine Algorithm for Solving the Reactor Network Design Problem: ANELS-SCA

Harun GEZİCİ[1,*]

[1]*Department of Electronics and Automation, Kırklareli University, Kırklareli, TÜRKİYE*

***Contact:** harun.gezici@klu.edu.tr

Abstract— In this study, ANELS-SCA (Adaptive Nonlinear Elitist Local Search SCA), an improved version of the Sine-Cosine Algorithm (SCA), is proposed for solving real-world constrained optimisation problems. Real-world engineering problems pose significant challenges for classical optimisation methods due to their non-linear structures, narrow feasibility regions and multiple constraints. In this context, the study addresses the Reactor Network Design problem, which is widely used in process systems optimisation. The problem involves the design of a reactor system comprising two interconnected continuous-mixing reactors, with the objective of optimising the concentration of the intermediate product at the outlet of the second reactor.

The proposed ANELS-SCA framework is built upon three key enhancements aimed at addressing the limitations of the basic SCA: i) a non-linear adaptive control parameter to manage the exploration-exploitation balance more flexibly, ii) an elitist steering mechanism to utilise high-quality solutions more effectively, and iii) a local search operator to improve solution accuracy in the final stages. To evaluate the method's performance, ANELS-SCA was compared with the basic SCA, SOA, MSA, GOA and SSO algorithms. All algorithms were tested under the same experimental conditions, with 30 independent runs.

The results obtained demonstrate that ANELS-SCA outperforms competing methods in terms of both best solution value and average performance. The proposed algorithm ranked first, achieving a value of $-3.857E-01$ for the best solution and $-2.774E-01$ for the average result. Convergence curves also revealed that ANELS-SCA exhibits a more balanced, faster and higher-quality optimisation behaviour. The findings demonstrate that the proposed approach is an effective and competitive alternative for real-world constrained optimisation problems.

Keywords: Meta-heuristic optimisation, Sine-Cosine Algorithm, Reactor Network Design, Constrained optimisation, Real-world optimisation problems

I. INTRODUCTION

Real-world engineering problems present significant challenges for classical deterministic methods due to their non-linear structures, the presence of numerous constraints, and often having narrow feasibility regions. Meta-heuristic algorithms are widely preferred, particularly for problems where obtaining derivative information is difficult, those with multi-modal solution spaces, or those involving complex constraint relationships. In this context, not only artificial test functions but also constrained optimisation problems derived from real-world engineering applications play a significant role in evaluating new algorithms. Indeed, in a recent dataset study, a large number of non-linear constrained optimisation problems derived from the real world were presented, and it was emphasised that such problems provide a better testing environment for evaluating the performance of new methods. The Reactor Network Design problem is also among these real-world constrained optimisation problems and stands out as a widely used test problem in the context of process design [1].

Meta-heuristic algorithms have attracted significant attention in recent years due to their ability to search the search space on a global scale, their lack of reliance on derivative information, and their ease of adaptation to different problem structures. However, the success of these algorithms depends largely on how effectively the exploration-exploitation balance can be established. Consequently, numerous algorithms have been developed in the literature using approaches such as improving the basic search mechanisms, utilising guidance information more effectively, and integrating local optimisation strategies. It has been observed that such structural improvements are particularly decisive in real-world constrained optimisation problems, and that significant performance differences can arise between different improved versions of the same algorithm [2].

The Sine Cosine Algorithm (SCA), proposed by Mirjalili in 2016, is a population-based meta-heuristic algorithm that updates candidate solutions using sine and cosine-based oscillatory movements around the current best solution. The most significant advantages of the SCA are its simple mathematical structure, the fact that it contains a small number of control parameters, and its ease of application to various optimisation problems. Thanks to these features, the SCA has attracted attention in various fields, including continuous optimisation and engineering design problems, since its proposal. However, it is frequently emphasised in the literature that the original SCA contains aspects open to improvement, such as its exploration-exploitation transition based on linear parameter reduction, its strong dependence on the single optimal solution, and the limited capacity for local improvement in the final iterations [2].

Consequently, numerous studies have been conducted in recent years to improve various aspects of SCA. A recent comprehensive review indicates that the most frequently used

strategies in SCA improvements are adaptive parameter control, the use of elite information, hybridisation, chaotic or randomised steering, and the integration of local search. Similarly, in a variant of SCA proposed in 2024 that employs an elite- -pool strategy, it has been reported that making more effective use of high-quality solutions can improve the algorithm's balance between diversity and convergence. Furthermore, advanced SCA studies published in 2023 and 2024 demonstrate that non-linear parameter updates and multi-strategy optimisation approaches can mitigate the original SCA's issues of early convergence and low accuracy. These developments indicate that new SCA-based variants remain an open and current topic of research [3], [4], [5].

In this study, an improved variant named ANELS-SCA (Adaptive Nonlinear Elitist Local Search SCA) is proposed to mitigate the aforementioned limitations of SCA. The proposed framework consists of three main components: i) a non-linear adaptive control parameter to manage the exploration-exploitation balance more flexibly, ii) an elitist steering mechanism to make more effective use of high-quality solutions, and iii) a local search operator to enhance solution accuracy in the final stages. The proposed method has been tested on the reactor network design problem, a real-world constrained optimisation problem, and compared with the basic SCA as well as various meta-heuristic algorithms. In this respect, the study both presents a new, improved variant to the SCA literature and demonstrates the effectiveness of this variant on a real-world constrained optimisation problem.

The remainder of this study is organised as follows: The reactor network design problem is introduced in the second section. The third section provides information on the proposed ANELS-SCA algorithm. Computational results are evaluated in the fourth section. The fifth section discusses the results and provides information on future work.

II. Reactor Network Design Problem

The Reactor Network Design problem is one of the real-world constrained optimisation problems widely used in the literature on process systems optimisation. The problem concerns the design of a network consisting of two continuously stirred tank reactors, with the objective of optimising the concentration of the intermediate product$B$ at the outlet of the second reactor. In recent studies on data sets, this problem is cited as one of the real-world constrained optimisation test problems and is reported as a low-dimensional yet non-linear problem with six decision variables [6].

In this study, the decision variable vector is defined as follows (Eq. (1)):

$$\mathrm{x} = [C_{A1}, C_{A2}, C_{B1}, C_{B2}, V_1, V_2] \quad (1)$$

Where, C_{A1} and C_{B1} denote the concentrations of A and B at the outlet of the first reactor; C_{A2} and C_{B2} denote the concentrations of A and B at the outlet of the second reactor; and V_1 and V_2 denote the volumes of the first and second reactors, respectively [1]. The objective of the problem is to maximise the concentration of B at the outlet of the second reactor, and the objective function of the optimisation is expressed as follows (Eq. (**2**)) [1] :

$$\min\ f(\mathrm{x}) = -C_{B2} \quad (2\ )$$

In the classical formulation of the reactor network design problem, the reaction network and mass balances are defined by non-linear equations. The standard reaction rate constants used in this study are taken as $k_1 = 0.09755988$, $k_2 = 0.99k_1$, $k_3 = 0.0391908$ and $k_4 = 0.9k_3$ [1]. Accordingly, the balance equations are as follows (Eqs. (**3**)–(**6**)):

$$C_{A1} + k_1 C_{A2} V_1 - 1 = 0 \quad (3)$$

$$C_{A1} - C_{B1} + k_3 C_{B1} V_1 = 0 \quad (4)$$

$$C_{A2} - C_{A1} + k_2 C_{A2} V_2 = 0 \quad (5)$$

$$C_{B2} - C_{B1} + C_{A2} - C_{A1} + k_4 C_{B2} V_2 = 0 \quad (6)$$

Furthermore, the capacity constraint limiting the total size of the two reactors is given as follows (Eq. (7)) [1]:

$$\sqrt{V_1} + \sqrt{V_2} \le 4 \quad \textbf{(7)}$$

The constraints on the decision variables are as follows (Eq.(8)) [1].

$$0 \le C_{A1}, C_{A2}, C_{B1}, C_{B2} \le 1$$
$$0{,}00001 \le V_1, V_2 \le 16 \quad \textbf{(8)}$$

These constraints represent the physically meaningful range of the concentration variables and the upper limits of the reactor volumes.

The reactor network design problem thus becomes a standard constrained optimisation problem consisting of an objective function, four equality constraints, one inequality constraint, and variable limits.

Consequently, the reactor network design problem addressed in this study is formulated as the optimisation of the objective function given by Eq. (**2**) , subject to the constraints defined by Eqs. (**3**)–(7) and the variable bounds given by Eq. (8). Despite its low dimensionality, this problem provides a suitable real-world test environment for evaluating the performance of new meta-heuristic algorithms due to its non-linear constraint structure and narrow feasibility region [6].

III. The Basis of the Proposed Algorithm: The Sine-Cosine Algorithm (SCA)

The Sine-Cosine Algorithm (SCA) is a population-based meta-heuristic optimisation algorithm proposed by Mirjalili in 2016 [2]. The fundamental idea behind SCA is based on updating candidate solutions through sine and cosine-based oscillatory movements relative to the current best solution. The algorithm is widely used in the literature due to its few control parameters, ease of implementation, and adaptability to various optimisation problems. The original study noted

that SCA achieves both exploration and exploitation behaviour by oscillating search agents inwards or outwards around the current best solution.

In SCA, a population consisting of N candidate solutions is initially generated at random. Each candidate solution is defined as $X_i = [x_{i,1}, x_{i,2}, \dots, x_{i,D}]$; where, D denotes the problem's dimension. In each iteration, the individuals in the population are evaluated according to the objective function, and the best solution is stored as $P = [P_1, P_2, \dots, P_D]$. Subsequently, each dimension of every candidate solution is updated using one of the following position update equations based on sine or cosine (Eqs.(9), (10)):

$$X_{i,j}^{t+1} = X_{i,j}^{t} + r_1 \sin(r_2) \mid r_3 P_j^t - X_{i,j}^t \mid \quad (9)$$

$$X_{i,j}^{t+1} = X_{i,j}^{t} + r_1 \cos(r_2) \mid r_3 P_j^t - X_{i,j}^t \mid \quad (10)$$

Where, $X_{i,j}^t$ represents the value of the jth dimension of the ith candidate solution at iteration t; P_j^t represents the jth dimension of the best solution at that iteration; and r_1, r_2, r_3 represent random parameters controlling the algorithm's orientation and step size. In the original SCA paper, the roles of these parameters are explained as follows: r_1 determines the size of the update step and the exploration-exploitation balance, r_2 determines the sinusoidal nature of the movement direction, and r_3 determines the intensity of the orientation around the target solution. Additionally, an extra random variable is used to select between sine and cosine updates.

In SCA, the parameter r_1 is linearly reduced over the course of iterations, with the aim of the algorithm performing more exploration at the beginning and more exploitation towards the end. In the original study, this parameter was defined as follows (Eq. (11)):

$$r_1 = a - t\left(\frac{a}{T}\right) \quad (11)$$

Where, a is the initial control parameter; t is the current iteration number; and T is the maximum number of iterations. In practice, $a = 2$ is typically selected. Thus, the value of r_1 decreases from 2 to 0 as the iterations progress. Thanks to this structure, the algorithm exhibits a broader search behaviour in the early iterations, whilst demonstrating a more intensive exploitation behaviour around the best solution in the later iterations.

The fundamental advantage of SCA is that its position update rule is both very simple and flexible. Thanks to the periodic nature of the sine and cosine functions, candidate solutions not only approach the optimal solution directly but also perform oscillatory movements at varying distances around it. This feature partially reduces the algorithm's tendency to get stuck in local minima early on and contributes to the exploration of different regions. However, the literature indicates that the original version of SCA also has certain limitations. In particular, the linearly decreasing nature of the r_1 parameter may not manage the exploration-exploitation transition with sufficient flexibility for every problem; a strong dependence on a single optimal solution may lead to a reduction in population diversity; furthermore, there is no additional local optimisation mechanism to enhance solution accuracy in the final iterations. Comprehensive evaluations of SCA have also highlighted that one of the algorithm's areas open to improvement lies in these balance and steering mechanisms.

Therefore, in the present study, the basic SCA algorithm was taken as the foundation; however, three fundamental improvements were proposed to achieve a more effective search behaviour for the reactor network design problem. These are, in order, the non-linear adaptive control parameter, the elitist steering mechanism, and the local search operator. The improved structure obtained through the integrated use of these three mechanisms is referred to in this study as ANELS-SCA (Adaptive Nonlinear Elitist Local Search SCA).

A. Non-linear Adaptive Control Parameter

In the basic SCA, the balance between exploration and exploitation is achieved via the parameter r_1, which decreases linearly as the iteration progresses. However, this linear decrease does not always adequately accommodate the flexible transition required at different stages of the search process. Therefore, in the proposed ANELS-SCA, the parameter r_1 is updated using a non-linear adaptive form rather than a linear structure. It is clearly stated in the original structure of SCA that the r_1 parameter determines the exploration–exploitation balance; consequently, any improvement made to this parameter directly affects the algorithm's overall search behaviour.

In this study, the r_1 parameter has been redefined as follows (Eq.(12)):

$$r_1 = a\left(1 - \frac{t}{T}\right)^2 \quad (12)$$

Where, a denotes the initial control parameter, t denotes the current iteration number, and T denotes the maximum iteration number. Thanks to this structure, the algorithm performs exploration with wider steps in the early iterations, whilst exhibiting a more controlled and precise exploitation behaviour in subsequent iterations.

B. Elite-Driven Mechanism

In the basic SCA, all individuals are directed solely towards the current best solution. Whilst this approach is simple and effective, it can lead to the population becoming overly dependent on a single solution and to a premature loss of diversity. SCA's original update rule is based on oscillatory motion around the best solution; however, recent evaluations indicate that improving the use of elite information represents a meaningful direction for enhancing SCA-based structures.

Therefore, in ANELS-SCA, a guide solution selected from an elite solution set is used instead of a single best solution. The elite pool E consists of the best k individuals in the

population; an elite guide E_j from this pool is used in the update of each individual. Accordingly, the new update rule can be written as follows (Eqs.(**13**), (**14**)):

$$X_{i,j}^{t+1} = X_{i,j}^{t} + r_1 \sin(r_2) \mid r_3 E_j^t - X_{i,j}^{t} \mid \quad (13)$$

$$X_{i,j}^{t+1} = X_{i,j}^{t} + r_1 \cos(r_2) \mid r_3 E_j^t - X_{i,j}^{t} \mid \quad (14)$$

Where, E_j^t denotes the j dimensional value of the guide solution selected from the elite pool. Thus, the search process is guided not merely around a single individual, but around the collective knowledge of several high-quality solutions.

C. Local Search Operator

In the basic SCA, there is no explicit local refinement mechanism to improve solution accuracy in the final iterations. To address this shortcoming, a lightweight local search operator has been added to the proposed framework. It is known that the integration of local search in meta-heuristic algorithms particularly strengthens exploitation in the final stages and improves solution quality; evaluations conducted for SCA variants also support this aspect.

In this study, local search has been applied solely to the current best individual. The local search step is defined as follows (Eq. (**15**)):

$$\mathrm{X}_{best}^{new} = \mathrm{X}_{best} + \beta \, \mathrm{r} \odot (\mathrm{ub} - \mathrm{lb}) \quad (15)$$

Where, X_{best} represents the current best solution, β a small local search step size, $\mathrm{r}[-1,1]$ a vector generated randomly within the range, $\odot$ element-wise multiplication, ub and lb the upper and lower boundary vectors respectively. If the fitness value of the solution at X_{best}^{new} is better, the current best solution is updated with this new solution.

D. General Structure of the Proposed ANELS-SCA

Consequently, the proposed ANELS-SCA has been developed by adding three main enhancements to the basic SCA structure: **i)** a non-linear adaptive control parameter to manage the exploration–exploitation balance more effectively, **ii)** an elitist steering mechanism to make more effective use of high-quality solutions, and **iii)** a local search operator to improve solution accuracy in the final stage. Thus, ANELS-SCA has been developed into an enhanced version that retains the basic SCA's simple structure whilst offering more balanced guidance and stronger exploitation capacity. The pseudocode for the proposed method is available at ALGORITHM 1.

ALGORITHM 1.

Pseudocode of the Proposed ANELS-SCA

1.	Start:N Generate an initial population of 100 individuals in the range [**lb**, **ub**] .
2.	Calculate the objective function value for each individual.
3.	Determine the best solution as $\mathbf{X}_{best}$.
4.	$t = 1$ Start the iteration.
5.	Update the non-linear adaptive control parameter using $r_1 = a(1 - t/T)^2$.
6.	Form an elite pool from the best$k$ individuals in the population.
7.	Select a guide solution from the elite pool for each individual.
8.	For each dimension, generate a new position using a sine or cosine update based on random numbers.
9.	Keep the new solution within the bounds and recalculate the objective function.
10.	Update the solution if necessary $\mathbf{X}_{best}$.
11.	$\mathbf{X}_{best}$ Apply a local search; if a better solution is found, update it.
12.	$t = t + 1$ If $t \leq T$, return to step 5; otherwise, stop and output the solution $\mathbf{X}_{best}$.

IV. COMPUTED RESULTS

In order to evaluate the performance of the proposed ANELS-SCA, comparative experiments were conducted on the reactor network design problem. The comparison algorithms used included the basic Sine-Cosine Algorithm (SCA) [2], along with the Seagull Optimisation Algorithm (SOA) [7], the Moth Search Algorithm (MSA) [8], the Grasshopper Optimisation Algorithm (GOA) [9] and the Salp Swarm Optimisation (SSO) [10]. All of the aforementioned algorithms were implemented in Python.

To ensure a fair comparison, the same experimental parameters were used for all algorithms (TABLE 1.). In this context, the population size was set to 30, the maximum number of iterations to 500, and the number of independent runs to 30. Each algorithm was run under the same decision variable constraints and the same objective function. Thus, it was aimed to ensure that the results obtained were attributable solely to the search capabilities of the algorithms.

The objective function value was taken as the primary criterion for evaluating optimisation performance. In this context, the best, average, worst and standard deviation values obtained from 30 independent runs for each algorithm were calculated and reported. These criteria reflect, respectively, the best solution achievable by the algorithms, their general performance level, their behaviour under the worst-case scenario, and their stability characteristics. Additionally, ranking results were included in the evaluation to present the overall success of the methods in a more comprehensive manner.

Tables and figures have been used to present the results.TABLE 2 provides the best, average, worst and standard deviation objective function values, along with ranking information, for the compared algorithms.Figure 1 illustrates the convergence behaviour of the algorithms over iterations, visually comparing performance changes during the solution process. Thus, not only the final results but also the convergence characteristics of the algorithms have been evaluated.

TABLE 1 presents the initial parameters used for the proposed method and the comparison algorithms. The initial parameters of the competing algorithms were taken from their original papers.

TABLE 1.

EXPERIMENTAL PARAMETERS USED FOR THE COMPARED ALGORITHMS

Algorithm	Initial parameter
ANELS-SCA	*Number of elite individuals: 3* *Local search probability: 0.30* *Local search coefficient: 0.02* *Adaptive non-linear control parameter:* $r_1 = 2\left(1-\frac{t}{T}\right)^2$ $a = 2$
SCA	$a = 2$
SOA	$fc = 2$
MSA	*Number of retained particles: 2* *β Parameter: 1.5* *Maximum stride: 1.0* *Acceleration factor:* $\varphi = (\sqrt{5}-1)/2 \approx 0{,}618$
GOA	*Minimum reduction factor (*c_{min} *): 0.00004* *Maximum reduction factor (*c_{max} *): 1.0*
SSO	*Probability of leader position update = 0.5*

The findings obtained for the Reactor Network Design problem indicate that the ANELS-SCA algorithm produced the most successful results among the methods included in the comparison. TABLE 2 examining, it can be seen that the proposed method ranks first in terms of the best solution value, with $-3.857\text{E}-01$. This value is better than those obtained by GOA ($-3.834\text{E}-01$), SCA ($-3.703\text{E}-01$), SOA ($-1.997\text{E}-04$) and MSA ($-7.967\text{E}-04$). Similarly, when average results are evaluated, it is observed that ANELS-SCA has the best average with a value of $-2.774\text{E}-01$. This result is superior to the average values obtained for GOA ($-1.829\text{E}-01$), SCA ($-2.086\text{E}-01$), SOA ($-1.384\text{E}-04$) and MSA ($-3.298\text{E}-04$). Consequently, ANELS-SCA has not only achieved a good result individually but has also provided higher solution quality across repeated independent runs.

This superior performance can be attributed to the contributions made by the components within the proposed algorithm's structure to the search process. In particular, it is assessed that the enhanced search mechanisms present in the ANELS-SCA structure contribute to a more effective scanning of the solution space by mitigating the limitations of the basic SCA regarding the balance between exploration and exploitation. Whilst the classical SCA remains at an average value of $-2.086\text{E}-01$, the ANELS-SCA achieving an average value of $-2.774\text{E}-01$ demonstrates that the proposed additional components have a positive impact not only on the best-case scenario but also on the overall search behaviour. In other words, it is observed that the additional strategies integrated into ANELS-SCA assist the algorithm in evaluating promising regions more effectively and in moving towards higher-quality solutions without getting stuck in local optima. This situation highlights that, particularly in complex and sensitive optimisation problems such as reactor network design, hybrid or enhanced structural components can be decisive for performance.

Upon examining the standard deviation values, a value of $1.477\text{E}-01$ was obtained for ANELS-SCA. Although this value is larger than the standard deviation values of SOA ($4.959\text{E}-05$) and MSA ($2.313\text{E}-04$), it is observed that a low standard deviation does not necessarily imply high solution quality on its own, given that the average performance of the relevant algorithms remained at $-1.384\text{E}-04$ and $-3.298\text{E}-04$, respectively. In this context, the fact that ANELS-SCA produces more competitive best and average results despite having a certain level of variation indicates that the algorithm is able to discover more effective regions. When the standard deviation values of GOA ($1.628\text{E}-01$) and SCA ($1.539\text{E}-01$) are evaluated alongside ANELS-SCA's value ($1.477\text{E}-01$), it can be said that the proposed method offers both a competitive level of stability and is more successful in terms of solution quality.

On the other hand, the results of the SSO algorithm indicate that it exhibits rather unstable behaviour in this problem. The fact that the average result for SSO is $9.599\text{E}+03$ and the worst result is $5.760\text{E}+04$ suggests that this method is unable to perform a stable search within the solution space. In contrast, the fact that ANELS-SCA achieves negative and more favourable values in both the best and average results demonstrates that the proposed method exhibits a search behaviour better suited to the problem structure. Finally, the fact that ANELS-SCA ranks first in the ranking results confirms that the proposed algorithm is the most competitive and successful method in terms of overall performance for the reactor network design problem. When these results are evaluated together, it can be stated that the components integrated into ANELS-SCA significantly strengthen the basic SCA structure and provide a marked improvement in performance, particularly in terms of solution quality.

TABLE 2.

PERFORMANCE RESULTS OF ANELS-SCA AND COMPETITOR ALGORITHMS FOR THE REACTOR NETWORK DESIGN PROBLEM

Metric	Algorithms					
	ANELS-SCA	**SCA**	**SOA**	**MSA**	**GOA**	**SSO**
Best	***-3.857 E-01***	-3.703 E-01	-1.997 E-04	-7.967 E-04	-3.834 E-01	-2.619 E-04
Avg.	***-2.774 E-01***	-2.086 E-01	-1.384 E-04	-3.298 E-04	-1.829 E-01	9.599 E+03
Worst	-9.995 E-05	0.000 E+00	***-9.998 E-05***	-6.556 E-05	0.000 E+00	5.760 E+04

Std. Dev.	1.477 E-01	1.539 E-01	***4.959 E-05***	2.313 E-04	1.628 E-01	2.074 E+04
Rank	***1***	3	6	4	2	5

Upon examining the convergence curves obtained for the Reactor Network Design problem, it is evident that the ANELS-SCA algorithm demonstrates highly successful performance in terms of both solution quality and convergence behaviour. FromFigure 1, it can be seen that the ANELS-SCA algorithm shows rapid improvement from the very first iterations and reaches the optimal region within approximately 80–90 iterations, transitioning to a stable structure. In particular, the fact that the curve flattens out at a level close to the order of $-1.0\mathrm{E}+00$ from this point onwards indicates that the algorithm is able to maintain this solution after reaching a high-quality solution. This is significant as it demonstrates that ANELS-SCA not only provides rapid convergence but also exhibits strong exploitation behaviour.

When compared with other algorithms, the superiority of the proposed method becomes even more evident. Although the MSA and SSO algorithms exhibited a rapid decline in the early iterations, the solution levels they reached fell short of those achieved by ANELS-SCA. Similarly, GOA showed improvement up to a certain point but fell short of the proposed algorithm in terms of final solution quality. Although SCA improved later and experienced a sharp decline around 180 iterations, it was observed that it could not reach the solution level attained by ANELS-SCA. Whilst SOA showed some improvement, it exhibited a shallower convergence profile and stabilised at a lower-quality solution level. These comparisons demonstrate that ANELS-SCA not only achieves a better result but also reaches this result within a reasonable number of iterations.

The shape of the convergence curve also indirectly reflects the contribution of the proposed algorithm's structural components to the search process. The fact that ANELS-SCA, after conducting sufficient exploration in the initial phase, quickly shifts towards more favourable regions and then stabilises and deepens its search within that region suggests that the additional mechanisms integrated into the algorithm have improved the exploration-exploitation balance. In particular, the fact that ANELS-SCA reaches the objective value level both earlier and at a lower value compared to the basic SCA demonstrates that the proposed components have significantly enhanced the search capacity of the classical SCA. In other words, the improvements introduced to ANELS-SCA have not only increased the quality of the final solution but have also made the convergence process more effective and controlled.

Consequently, the convergence curves for the Reactor Network Design problem reveal that ANELS-SCA exhibits a more balanced, faster and higher-quality optimisation behaviour compared to rival algorithms. This finding is consistent with the numerical results and confirms that the proposed algorithm is one of the most robust methods for this problem, both in terms of convergence characteristics and final solution success.

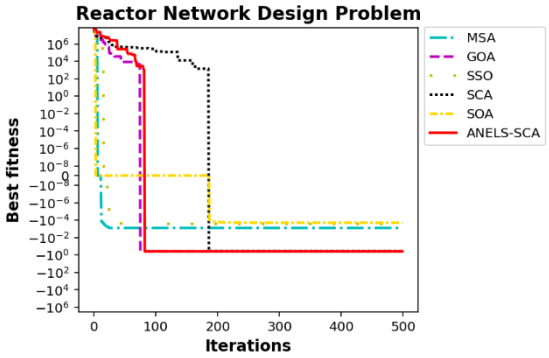

Figure 1. Convergence curves of ANELS-SCA and the compared algorithms for the Reactor Network Design problem

V. CONCLUSION

In this study, ANELS-SCA (Adaptive Nonlinear Elitist Local Search SCA), an improved version of the Sine-Cosine Algorithm, is proposed, and the method is evaluated on the reactor network design problem, a real-world constrained optimisation problem. In the proposed structure, a non-linear adaptive control parameter, an elitist steering mechanism and a local search operator have been integrated into the basic SCA. Consequently, both the exploration-exploitation balance of the algorithm has been improved and the solution accuracy has been enhanced.

In the comparative tests conducted, ANELS-SCA was compared with the SCA, SOA, MSA, GOA and SSO algorithms. The results obtained demonstrate that the proposed method outperforms the competing algorithms in terms of both best solution value and average performance. In particular, the fact that ANELS-SCA achieved a best value of $-3.857\mathrm{E}-01$ and an average value of $-2.774\mathrm{E}-01$ demonstrates that the method is capable of producing high-quality solutions for the reactor network design problem. Furthermore, the convergence curves support the view that ANELS-SCA exhibits a more balanced and effective convergence behaviour.

The findings indicate that the three proposed enhancement components significantly strengthen the basic SCA structure and provide a marked improvement, particularly in terms of solution quality. In this respect, ANELS-SCA can be considered a competitive alternative for non-linear and constrained real-world optimisation problems such as the reactor network design problem.

Future work may involve testing the proposed algorithm on different real-world constrained optimisation problems, combining it with different constraint handling strategies, and applying it to engineering design problems.

REFERENCES

[1] A. Kumar, G. Wu, M. Z. Ali, R. Mallipeddi, P. N. Suganthan, and S. Das, "A test-suite of non-convex constrained optimization problems from the real-world and some baseline results," *Swarm Evol. Comput.*, vol. 56, p. 100693, Aug. 2020, doi: 10.1016/J.SWEVO.2020.100693.

[2] S. Mirjalili, "SCA: A Sine Cosine Algorithm for solving optimisation problems," *Knowl. Based. Syst.*, vol. 96, no. 3, pp. 120–133, Mar. 2016, doi: 10.1016/j.knosys.2015.12.022.

[3] Y. Luo, W. Dai, and Y. W. Ti, "Improved sine algorithm for global optimisation," *Expert Syst. Appl.*, vol. 213, p. 118831, Mar. 2023, doi: 10.1016/J.ESWA.2022.118831.

[4] L. Deng and S. Liu, "A sine-cosine algorithm guided by the elite pool strategy for global optimisation," *Appl. Soft Comput.*, vol. 164, p. 111946, Oct. 2024, doi: 10.1016/J.ASOC.2024.111946.

[5] Q. S. Hamad, S. A. M. Saleh, S. A. Suandi, H. Samma, Y. S. Hamad, and A. G. Hussien, "A Review of Enhancing the Sine-Cosine Algorithm: Common Approaches for Improved Metaheuristic Algorithms," *Archives of Computational Methods in Engineering 2024 32:4*, vol. 32, no. 4, pp. 2549–2606, Dec. 2024, doi: 10.1007/S11831-024-10218-Z.

[6] H. S. Ryoo and N. V. Sahinidis, "Global optimisation of non-convex NLPs and MINLPs with applications in process design," *Comput. Chem. Eng.*, vol. 19, no. 5, pp. 551–566, May 1995, doi: 10.1016/0098-1354(94)00097-2.

[7] G. Dhiman and V. Kumar, "Seagull optimisation algorithm: Theory and its applications for large-scale industrial engineering problems," *Knowl. Based. Syst.*, vol. 165, pp. 169–196, Feb. 2019, doi: 10.1016/j.knosys.2018.11.024.

[8] G.-G. Wang, "Moth search algorithm: a bio-inspired metaheuristic algorithm for global optimisation problems," *Memetic Computing 2016 10:2*, vol. 10, no. 2, pp. 151–164, Sep. 2016, doi: 10.1007/S12293-016-0212-3.

[9] S. Saremi, S. Mirjalili, and A. Lewis, "Grasshopper Optimisation Algorithm: Theory and application," *Advances in Engineering Software*, vol. 105, pp. 30–47, March 2017, doi: 10.1016/j.advengsoft.2017.01.004.

[10] S. Mirjalili, A. H. Gandomi, S. Z. Mirjalili, S. Saremi, H. Faris, and S. M. Mirjalili, "Salp Swarm Algorithm: A bio-inspired optimiser for engineering design problems," *Advances in Engineering Software*, vol. 114, pp. 163–191, Dec. 2017, doi: 10.1016/j.advengsoft.2017.07.002.

The Climate–Fire Nexus: Assessing The Impact of Global Climate Change on Forest Fires in Türkiye

Özcan Şimşek[1,*], Ece Kazancı[2], Özge Özer[2], İrem Kıvrak[2]

[1]*Department of Forestry, Çanakkale Onsekiz Mart University Yenice Vocational School, Çanakkale, TÜRKIYE*

[2]*Department of Disaster Education and Management, School of Graduate Studies, Çanakkale Onsekiz Mart University, Çanakkale, TÜRKIYE*

*Contact: ozcan.simsek@gmail.com

Global climate change, driven by anthropogenic activities and greenhouse gas emissions, has significantly escalated the frequency, intensity, and scale of forest fires, particularly in vulnerable regions such as Türkiye. This study investigates the climate-fire nexus by assessing how shifting climatic variables exacerbate forest fire dynamics in Türkiye's Mediterranean-climate zones. Utilizing a comprehensive literature review combined with quantitative secondary data analysis, the research evaluates historical forest fire statistics from the General Directorate of Forestry (OGM) spanning the 2004-2023 period. To provide a broader regional and global context, these findings are synthesized with decadal data from the European Forest Fire Information System (EFFIS) and the Food and Agriculture Organization's (FAO) 2023 global wildfire report.

The findings indicate that while human activity remains the dominant source of ignition in Türkiye, accounting for the vast majority of incidents, the overarching climatic context now plays a decisive role in fire behavior and expansion. Prolonged dry seasons, heightened heat stress, and subsequent moisture loss in vegetation have transformed these ecosystems into highly fire-prone landscapes, facilitating the destructive spread of crown fires. Furthermore, spatial analyses underscore that fire risks are most concentrated in the southern and western coastal provinces where the Mediterranean climate prevails. As the traditional fire season expands in duration, the study concludes that reactive measures are no longer sufficient. Consequently, transitioning to proactive, year-round fire management strategies, integrating climate-smart forestry (CSF) practices, and implementing comprehensive fire-risk zoning are imperative for enhancing ecosystem resilience against future climate-induced threats.

Keywords: *Climate Change, Forest Fires, Mediterranean Climate, Climate-Smart Forestry, Türkiye.*

Suppression of Delamination in Tape-Cast Planar YSZ Electrolytes via Multi-Step Lamination and Thermal Conditioning for rSOC Applications

Ahmed Emin Kılıç[1,2,*], Selahattin Çelik[1,2], Meryem Sena Akkuş[1,2], Cihangir Duran[1,2], and Erol Arcaklıoğlu[1,2]

[1] *Faculty of Engineering and Natural Sciences, Ankara Yıldırım Beyazit University, Ankara 06010, Türkiye*

[2] *Hydrogen Technologies and Energy Research Centre (H2 TEAM), Ankara Yıldırım Beyazit University, Ankara 06010, Türkiye*

***Contact:** aekilic@aybu.edu.tr

Abstract— In this study, the effect of lamination parameters on the microstructure of multilayer YSZ electrolytes prepared by the tape casting method was investigated. Seven different lamination strategies (A–G) were applied using pressure level, pressing sequence, and thermal pre-conditioning variables, and the resulting samples were compared using surface and cross-section SEM analyses. The results showed that discontinuities and linear porosity formed at the layer interfaces under single-stage pressing conditions, while stepwise pressing increased interface contact but failed to achieve full densification. In samples subjected to thermally assisted high pressure, a continuous and compact microstructure was obtained, and delamination was eliminated. Laminate quality was ranked as G > F > E > A > C ≈ D > B. Macroscopic examinations confirmed the microstructure results and showed that deformation-free disk integrity was achieved. The findings reveal that lamination, not sintering, is the main stage determining structural integrity in rSOC electrolyte production. The proposed approach enables the production of repeatable and stable YSZ electrolytes for single-cell production.

Keywords: reversible solid oxide cell, YSZ electrolyte, tape casting, SOEC, SOFC

I. INTRODUCTION

Reversible solid oxide cells (rSOC) hold a significant position among energy conversion and storage technologies due to their ability to operate in both fuel cell and electrolyzer modes. In these systems, performance and long-term stability are largely dependent on the gas tightness and mechanical integrity of the electrolyte layer. Yttria-stabilized zirconia (YSZ) is the most widely used electrolyte material in SOFC, SOEC, and rSOC cells due to its high ionic conductivity and chemical stability [1,2]. Multilayer ceramic electrolytes are mostly produced by tape casting followed by lamination, and defects in the production process, particularly interfacial separation and microcracks, lead to gas leakage and increased ohmic losses [3,4].

Recent studies have shown that lamination quality is not solely dependent on pressure; the sequence of pressure application, temperature, and stress distribution must be evaluated together [5]. Furthermore, it is known that parameters such as tape thickness and particle placement are decisive for microstructure and performance [6]. Optimizing the lamination and sintering sequence in the preparation of multilayer structures for rSOC production ensures the production of dense and defect-free electrolytes [7,8]. Therefore, a parametric approach is required in electrolyte production. In this study, multilayer YSZ electrolytes prepared by the tape casting method were produced using seven different lamination strategies (A, B, C, D, E, F, and G), and the microstructure-process relationship was investigated comparatively using SEM analyses. The objective is to determine a mechanically stable and reproducible YSZ electrolyte production method suitable for rSOC single-cell production [9,10].

II. MATERIAL & METHODS

YSZ electrolyte samples were prepared using a band casting-based multilayer ceramic production approach. The ceramic suspension was homogenized with a carrier phase containing an organic binder under high-speed mixing at approximately 3000–4000 rpm. The resulting mixture was cast onto a polymer-based carrier surface using an adjustable gap doctor blade system and dried at room temperature to obtain free-standing ceramic tapes. The tape thickness was maintained at several hundred micrometres.

The dried strips were cut to the specified geometry and stacked on top of each other to form a multi-layered structure. The number of layers was kept constant throughout the study, and only the lamination parameters were varied to investigate the process–microstructure relationship. Pressing operations were performed under a hydraulic press, and the specimens were compressed between anti-adhesive interlayer materials. For specimens subjected to thermal conditioning, a pre-pressing soak at approximately 40–45 °C was applied. The pressure, temperature, and time parameters for all lamination protocols applied are provided in Table 1.

After lamination, the samples underwent multi-stage thermal treatment. First, controlled heating up to 600 °C was applied to remove the organic phase, followed by

densification sintering at a temperature range of approximately 1400–1500 °C. This process resulted in a dense ceramic electrolyte structure.

The microstructure of the produced samples was examined using a scanning electron microscope (SEM). The samples were subjected to section preparation by the fracture method and analysed after conductive coating. Layer continuity, porosity distribution, and interfacial separation were evaluated comparatively.

TABLE I. Lamination parameters

Protocol	Heating	Pressing	Duration	Description
A	45 °C – 1 h	20 MPa	3 + 3 min	Press, then étuve, and then Press (RT)
B	-	20 MPa	3 min	Press (RT)
C	(24 °C – 10 min) + (40 °C – 60 min)	20 MPa	Final pressing	First heated press, then Press (RT)
D	45 °C – 1 h	20 MPa	3 min	First étuve, then Press (RT)
E	40–42 °C	20 MPa	3 min	First heated press, then Press (RT)
F	40–42 °C	60 MPa	10 min	First heated press, then Press (RT)
G	40–42 °C	70 MPa	10 min	First heated press, then Press (RT)

III. RESULTS & DISCUSSIONS

The microstructures of YSZ electrolytes produced using different lamination protocols were compared using surface and cross-section SEM images. Since the number of layers was kept constant in all samples, the observed differences were directly attributed to the lamination conditions.

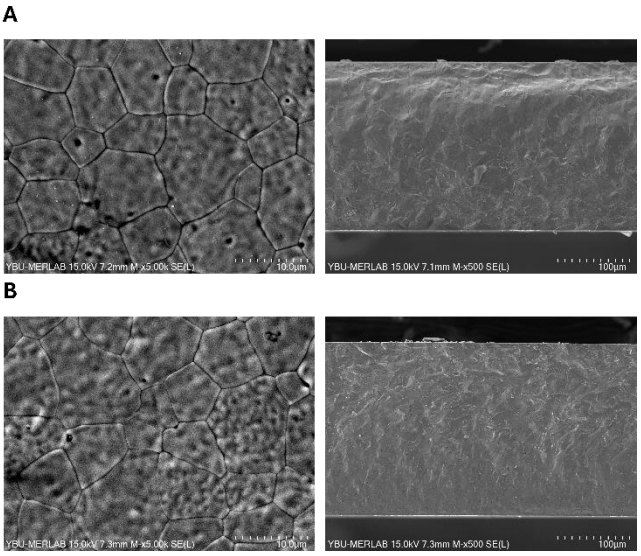

Fig. 1 A and B laminated surface + cross-section SEM images

In Protocol B, where single-stage pressing was applied, it was observed that the layer boundaries were clearly preserved and discontinuous voids formed between the layers (Figure 1). In the cross-sectional images, linear porosity bands formed at the lamina interfaces, and initial separations were detected in some areas. This situation indicates that interparticle contact was limited due to the insufficient plastic flow of the binder phase during pressing. Two-stage pressing (Protocol A) performed at the same pressure level increased interface continuity and partially blurred the layer boundaries (Figure 1). It is thought that the second pressing step closed the voids formed at the initial contact points, allowing particle re-arrangement. However, it was observed that micro-voids did not completely disappear in some areas.

In protocols C and D, which include thermal pre-conditioning, surface homogeneity has increased due to the decrease in the viscosity of the binder phase (Figure 2). In particular, it has been determined that the pore sizes have decreased and the particle distribution has become more uniform in the surface images. However, in the C protocol, local interlayer separations and crack formations were observed in some cross-sectional areas (Figure 2). This situation can be attributed to the heterogeneous flow of the binder during thermal treatment and stress accumulation after pressing. In the D protocol, bonding increased due to preheating, but complete densification could not be achieved due to single-stage pressing, and dispersed porosity was retained (Figure 2).

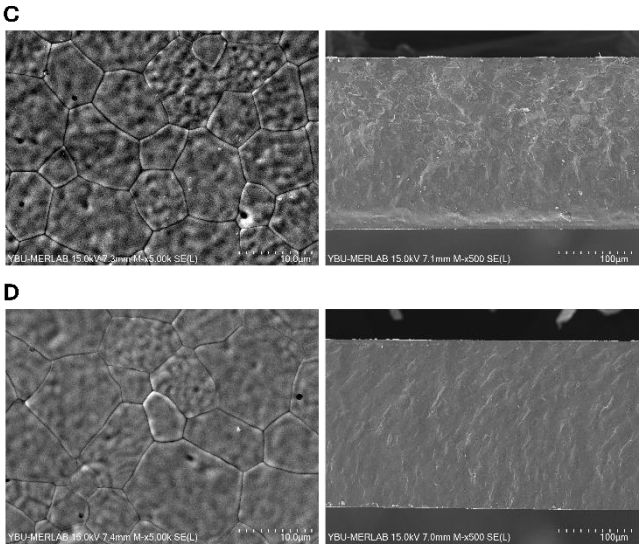

Fig. 2 C and D laminated surface + cross-section SEM images

The E and F samples subjected to heat-assisted pressure exhibited a more developed microstructure compared to previous protocols (Figure 3). In the E sample, an increase in interface continuity was observed, although fine separation traces persisted in some areas. This indicates that the plasticization of the binder prior to pressing was partially achieved, but the applied pressure was insufficient to close all voids. In sample F, it was determined that the layer boundaries became largely indistinct and porosity decreased significantly due to the increased pressure effect. However, the presence of limited closed pores was preserved in some areas.

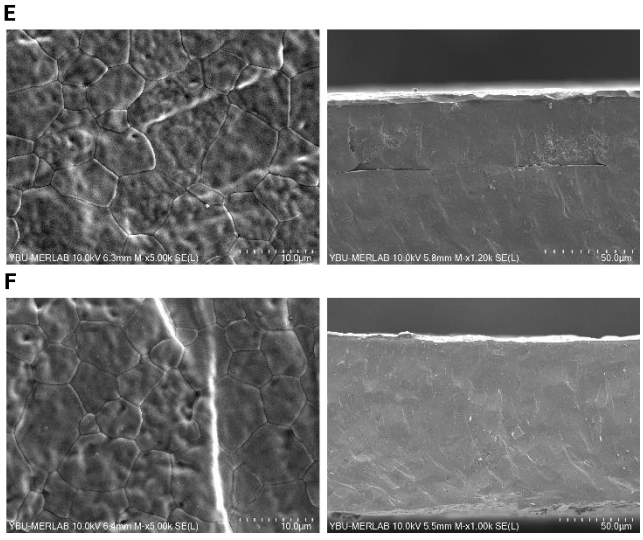

Fig. 3 E and F laminated surface + cross-section SEM images

The best microstructure was obtained in sample G (Figure 4). In this sample, a continuous and compact structure formed throughout the cross-section, open pores disappeared, and grain transitions became seamless. Thanks to the thermal conditioning applied with high pressure, the binder phase has been completely plasticized, and the inter-particle voids have closed, maximizing the actual contact area. This has led to the elimination of delamination and the achievement of homogeneous densification.

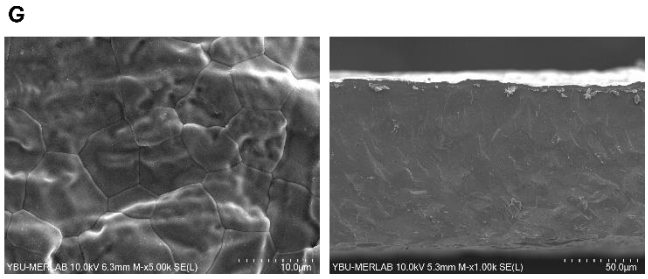

Fig. 4 G laminated surface + cross-section SEM images

The macroscopic appearance of the E, F, and G electrolyte samples produced to support microstructural observations was also examined (Figure 5). No cracks, edge lifting, or geometric deformation were observed on the surfaces of the samples. It was determined that surface smoothness increased and disk integrity was maintained with increasing lamination pressure and thermal conditioning. In particular, a smooth surface morphology corresponding to homogeneous densification was obtained in sample G. These observations confirm the interface continuity determined by SEM cross-section analyses at the macro scale.

Fig. 5 Macroscopic appearance of E, F, and G YSZ electrolyte samples. Surface integrity is maintained with increasing pressure.

When all samples are evaluated together, the lamination quality is ranked as follows:

$$G > F > E > A > C \approx D > B$$

The results indicate that lamination pressure alone is not the determining factor; the sequence of pressure application and thermal pre-conditioning must be evaluated together. Single-stage pressing at low temperatures limits interface contact, while stepwise pressing increases gap closure.

However, true densification is achieved through a combination of thermal support and high pressure.

These findings reveal that the delamination observed in rSOC electrolyte production stems primarily from initial interface voids formed during lamination rather than during the sintering stage. Therefore, microstructure control is determined by the lamination strategy rather than sintering parameters.

IV. CONCLUSION

An easy way to comply with the conference paper In this study, the effect of lamination parameters on the microstructure of multilayer YSZ electrolytes produced by the tape casting method was systematically investigated. The SEM results obtained showed that lamination quality is not solely dependent on the applied pressure, but that the pressing sequence and thermal pre-conditioning are also decisive factors. Single-stage pressing led to the preservation of interface voids and delamination, while stepwise pressing increased layer contact. The combination of thermal support and high pressure ensured the formation of a continuous and dense structure.

The best microstructure among the samples was obtained in the G protocol, followed by the F and E samples (G > F > E > A > C ≈ D > B). Macroscopic observations also confirmed the microstructure results and showed that thermal conditioning applied at high pressure prevented crack and deformation formation. The results revealed that delamination in rSOC electrolyte production stems from initial interface voids formed during lamination rather than during the sintering stage. Therefore, the key step determining performance in electrolyte production is not the sintering program but the lamination strategy.

The proposed lamination approach enables the production of a repeatable and structurally stable YSZ electrolyte for rSOC single-cell production.

ACKNOWLEDGMENT

The authors gratefully acknowledge the financial support provided by the Scientific and Technological Research Council of Türkiye (TÜBİTAK) under Project No. 125M080 and by the Scientific Research Projects Coordination Unit of Ankara Yıldırım Beyazıt University under Project No. 2730.

REFERENCES

[1] X. Sun, et al., “Optimization and durability of reversible solid oxide cells,” *ECS Trans.*, vol. 91, no. 1, pp. 2631–2640, 2019.

[2] M. Liu and Y. Liu, “Multilayer tape casting of large-scale anode-supported thin-film electrolyte solid oxide fuel cells,” *Int. J. Hydrogen Energy*, vol. 44, no. 31, pp. 16976–16982, 2019.

[3] L. Bernadet, M. Morales, X. G. Capdevila, F. Ramos, M. C. Monterde, J. A. Calero, et al., “Reversible fuel electrode supported solid oxide cells fabricated by aqueous multilayered tape casting,” *J. Phys.: Energy*, vol. 3, no. 2, Art. no. 024002, 2021.

[4] H.-G. Park, et al., “Performance improvement of anode-supported electrolytes for planar solid oxide fuel cells via a tape-casting/lamination/co-firing technique,” *J. Power Sources*, vol. 195, no. 9, pp. 2463–2469, 2010.

[5] E. A. Agarkova, et al., “Bilayered anode supports for planar solid oxide fuel cells: Fabrication and electrochemical performance,” *Mater. Lett.*, vol. 283, Art. no. 128752, 2021.

[6] T. Baquero, et al., “Aqueous tape casting of micro and nano YSZ for SOFC electrolytes,” *Ceram. Int.*, vol. 39, no. 7, pp. 8279–8285, 2013.

[7] S. Park, et al., “Multilayer co-casting method for enhanced performance anode-supported reversible solid oxide cells: Fabrication and effect of anode functional layer thickness on electrochemical performance,” *J. Power Sources*, vol. 640, Art. no. 236775, 2025.

[8] Y. Jiang, et al., “Tape casting fabrication of reversible solid oxide cells for large-scale electricity storage,” *J. Power Sources*, vol. 646, Art. no. 237263, 2025.

[9] N. Ai, et al., “Progress on direct assembly approach for in situ fabrication of electrodes of reversible solid oxide cells,” *Mater. Rep.: Energy*, vol. 1, no. 2, Art. no. 100023, 2021.

[10] Y. Yang, et al., “Recent development in reversible solid oxide fuel cells: Theory, integration and prospective,” *ChemElectroChem*, vol. 11, no. 6, Art. no. e202300593, 2024.

Efficiency Comparison of Bifacial Photovoltaic Panels Under Various Ground Conditions

İnci Nur ATALAY[1,*], Sıtkı KOCAOĞLU[2]

[1] *Energy Systems Engineering, Atalay Group Energy Inc. Ankara/Yenimahalle, TÜRKIYE*

[2] *Energy Systems Engineering, Ankara Yıldırım Beyazıt University, Ankara/Keçiören, TÜRKIYE*

***Contact:** bilginincii@gmail.com

The growing deployment of bifacial photovoltaic (PV) systems has highlighted ground surface reflectance (albedo) as a critical but often underestimated performance parameter. Unlike conventional monofacial panels, bifacial modules collect irradiance from both front and rear surfaces, meaning that the optical properties of the ground directly influence energy yield. This study investigates the quantitative impact of different ground surface conditions — namely natural soil and high-reflectance white gravel — at Konya, Türkiye.

The research employs a three-stage integrated methodology. First, three-dimensional shading simulations were conducted in SketchUp to assess inter-row shadow behaviour at three astronomically critical dates (winter solstice, summer solstice, and equinox) for tilt angles of 20°, 25°, and 30° at a fixed row pitch of 4.0 m. Second, annual and monthly performance predictions were generated using PVsyst software with Meteonorm 8.0 climate data, modelling two albedo scenarios: 0.20 (natural soil) and 0.50 (white gravel). Third, field measurements were collected from a 686.4 kWp bifacial PV system in Karapınar, Konya, during March–October 2024. Two equivalent inverter sub-systems — one installed over natural soil and one over white gravel — operated simultaneously under identical conditions, enabling direct experimental comparison.

Shading analysis confirmed that a 25° tilt angle with 4.0 m row spacing provides the most balanced tradeoff among energy yield, shading loss mitigation, and land-use efficiency, achieving a performance ratio of 83.56%. PVsyst simulations indicated that increasing ground albedo from 0.20 to 0.50 improves annual energy production by 3.89%, with specific yield rising from 1,759 to 1,827 kWh/kWp and performance ratio increasing by 3.25 percentage points. Field measurements closely validated these results, with the white gravel system generating 496.49 MWh compared to 476.87 MWh for the soil system over eight months, corresponding to a 4.26% gain versus a simulated 4.29%. Monthly results showed peak albedo gains in April (6.50%) and October (5.27%), and minimum values in mid-summer (3.46–3.60%), reaching 2.49% in September, due to higher solar angles and increased module temperatures. The white gravel system consistently outperformed the soil-based system throughout the measurement period.

This study provides field-validated quantitative evidence that high-albedo ground surfaces offer a low-cost, passive, and technically robust strategy for enhancing bifacial PV energy yield in high-irradiance regions. A dual-benefit mechanism is empirically confirmed: optical gains through increased rear-side irradiance and thermal gains through a cooler module microclimate driven by the lower heat absorption of white gravel. The integrated framework—combining 3D shading simulation, PVsyst modelling, and field measurements—

provides a reproducible methodology for bifacial system performance assessment. These findings have direct implications for ground-mounted PV plant design and investment planning, particularly in Central Anatolia and climatically similar regions, where albedo optimization represents a cost-effective pathway to improved system performance.

Keywords: *Albedo, bifacial photovoltaic panels, shading analysis, solar energy*

Biomechatronic Systems and Their Future in the Age of Human-Centered Technologies

Erhan AKDOĞAN[1]

[1]*Biomechatronics and Robotics Application Research Center, Yıldız Technical University, İstanbul, TÜRKİYE*

Biomechatronic systems are interdisciplinary systems that occupy an important place in contemporary engineering and health technologies by bringing together the disciplines of mechanics, electronics, control, software, and biology through a multilayered and integrated approach. These systems aim to support, improve, or reconstruct human movement, perception, control, and adaptation processes by establishing a functional interaction between biological structures and technological components. The biomechatronic approach, through systems developed with consideration of the structural, functional, and neurophysiological characteristics of the human body, seeks not only to enhance technical performance but also to improve quality of life, support independence, and provide more effective solutions in healthcare services. In this context, biomechatronic systems are regarded as one of the key fields representing the human-centered transformation of modern engineering.

At the core of the systems developed in this field lies the sensing, processing, interpretation, and transformation of biosignals into real-time control mechanisms. The use of diverse biological and physical data such as electromyography, electroencephalography, force, pressure, acceleration, and position data makes it possible to adapt systems to individual users. Rehabilitation robots, intelligent prosthetic and orthotic systems, exoskeleton structures, and wearable technologies are among the most prominent application areas of biomechatronics. These systems make significant contributions by supporting mobility, reducing functional losses, facilitating activities of daily living, and enabling the objective monitoring of clinical processes. Accordingly, biomechatronic systems function not only as assistive devices but also as tools for assessment, monitoring, decision support, and personalized diagnosis and treatment.

In the design of biomechatronic systems, human-centeredness, biomechanical compatibility, ergonomics, safety, comfort, and the accurate estimation of user intention are among the primary priorities. In recent years, with the integration of artificial intelligence and machine learning methods into these systems, the transition has accelerated from structures operating with predefined command sequences to more intelligent systems that can learn, adapt, and make decisions according to the user's condition. Moreover, digital twin technologies, multisensor fusion, and data-driven modeling approaches have become important factors that enhance the accuracy, reliability, and real-time performance of these systems. At the same time, dimensions

such as data security, user privacy, ethical responsibility, accessibility, and sustainability will also be decisive in shaping the future of biomechatronic systems. Ultimately, biomechatronic systems are considered strategic technological structures that establish a strong bridge between engineering and the life sciences, directly touch human life, and offer adaptive, high value-added solutions.

Keywords: *Biomechatronics, Rehabilitation Robots, Human-Machine Interaction, Biosignal Processing, Artificial Intelligence, Wearable Technologies.*